Development and Testing of a Diamond Calorimeter Heat Transfer Gauge



Rowland Penty Geraets

Balliol College

University of Oxford

A thesis submitted for the degree of

Doctor of Philosophy

Michelmas 2019

Abstract

Surface heat flux measurements in hypersonic pulse-flow facilities, such as Reflected Shock Tunnels and Expansion Tunnels, provide vital information for the design of hypersonic and hypervelocity vehicles and for the understanding of these complex flow environments. However, test-times in these facilities are on the order of microseconds to milliseconds, and by nature of their operation, the flow contains particles of metal diaphragms, resulting in damage to instrumentation. Additionally, at high flow enthalpies, ionised species and free electrons are present in the gas. Given these significant challenges, this thesis describes the design and manufacture of a new surface heat flux gauge, called the Diamond Heat Transfer Gauge (DHTG), and presents new data reduction methods, the results of calibration experiments, and two experimental campaigns in pulse-flow facilities. The DHTG is shown to overcome limitations of current instrumentation by increasing robustness, and improving response time, electrical isolation, and accuracy.

Four types of DHTG have been manufactured, consisting of a 2.5 mm diameter disk of synthetic diamond, either 75 µm, 150 µm, 220 µm or 325 µm thick, mounted into a cylindrical steel housing, with a platinum thin-film resistance temperature detector sputtered on the rear surface of the diamond to measure its temperature rise. An analysis of the gauge as a calorimeter showed that the rise-time of the four types of DHTG are 2.4 µs, 11.6 µs, 36.3 µs, and 54.4 µs respectively, and that the measurement error due to the data reduction method grows with time, limiting measurements to 500 µs for a 1 % drop in accuracy. While the rise-time is sufficiently fast for use in pulse-flow facilities, in order to extend the useful test-time and enable accurate measurements in a wider range of facilities, a non-linear implementation of the Sequential Function Specification Method (SFSM) was developed as an alternative data reduction method. This method deconvolves the impulse response of the gauge from a measured temperature rise to estimate the surface heat flux, and using a numerical study is shown to be accurate to within 0.5 % over a typical 2.5 ms Reflected Shock Tunnel test-time. Additionally, for high signal-to-noise ratio measurements, the SFSM method can improve the rise-time of the DHTG.

The typical experimental measurement uncertainty of the DHTG was calculated to be 7.5 % and is primarily driven by uncertainty in the specific heat capacity of diamond. This is comparable to or better than values of uncertainty for existing techniques, such as thin-film gauges and coaxial thermocouples. An experiment to measure the impulse response of the DHTG to reduce measurement uncertainty further was performed using a laser to provide a short-duration pulse

of heat flux. Issues stemming from spatial non-uniformity of the laser intensity and measurement uncertainty meant that the measured response was unsuitable for direct use in the SFSM data reduction method. No significant difference was found between the specific heat capacity of diamond estimated from this experiment and values given in the literature.

Experimental measurements in the X2 expansion tunnel on blunt- and sharp-nosed wedge models showed that the DHTG is a viable method for measuring heat fluxes in an expansion tunnel, but is more susceptible to damage from diaphragm fragments than surface junction thermocouples. The five flow conditions used had total enthalpies ranging from $25\,\mathrm{MJ{\cdot}kg^{-1}}$ to $70\,\mathrm{MJ{\cdot}kg^{-1}}$, resulting in DHTG heat flux measurements of up to $129\,\mathrm{MW{\cdot}m^{-2}}$. Agreement better than 12 % was seen between the heat fluxes measured by the two types of gauge for the majority of the conditions. Across the set of tests, DHTGs were mounted on surfaces at angles of attack from 0° to 90°. No DHTGs were damaged at 0°, whereas those mounted at higher angles of attack survived between 1 and 17 shots, with half still operational at the end of the experimental campaign, but with significant signs of surface damage.

In a second experimental campaign, a DHTG, a coaxial thermocouple, and a thin-film heat transfer gauge were used to make stagnation point heat flux measurements in the T6 Reflected Shock Tunnel at a flow total enthalpy of $2.5\,\mathrm{MJ{\cdot}kg^{-1}}$. The DHTG and the thermocouple were undamaged after three shots, while the thin-film gauge was damaged beyond use after one shot. The DHTG measurements agree with the Fay and Riddell correlation, but are 20 % lower than the thermocouple measurement. The difference is believed to be a result of error in the effective thermal effusivity used in the data reduction of the thermocouples: the junctions were formed by abrasion using sandpaper, whereas for the experiments in X2 the junctions were created by making two larger-scale scratches. For stagnation point measurements in a Reflected Shock Tunnel, the DHTG is shown to be the preferred measurement technique, demonstrating significant improvements in robustness versus thin-film gauges, and in measurement uncertainty versus surface junction thermocouples.

List of Publications

Work published by the author relevant to this thesis:

Penty Geraets, R. T., McGilvray, M., Doherty, L., Morgan, R. G., James, C. M., Vanyai, T, and Buttsworth, D. R. "Development of a Fast-Response Diamond Calorimeter Heat Transfer Gauge". In: Journal of Thermophysics and Heat Transfer 34:1 (2020), p. 193-202 DOI: 10.2514/1.T5688.

Collen, P. L., Doherty, L., McGilvray, M., Naved, I., Penty Geraets, R. T., Hermann, T. A., Morgan, R. G. and Gildfind, D. "Commissioning of the T6 Stalker Tunnel". In: AIAA Scitech 2019 Forum. 2019, p. 1941. DOI: 10.2514/6.2019-1941.

Subiah, S., Collen, P., Doherty, L., Penty Geraets, R. T., Hyslop, A., and McGilvray, M. "Condition Development and Commissioning of the Oxford T6 Stalker Tunnel in Reflected Shock Tunnel Mode". In: International Conference on Flight vehicles, Aerothermodynamics and Re-entry Missions and Engineering, Monopoli, Italy. ESA Conference Bureau. 2019.

Penty Geraets, R. T., McGilvray, M., Williams, B., Shah, P. "Laser-based Calibration and Processing Technique for a Robust Fast-Response Surface Heat Transfer Gauge". In: 2018 Joint Thermophysics and Heat Transfer Conference. 2018, p. 3772. DOI: 10.2514/6.2018-3772.

Penty Geraets, R. T., McGilvray, M., Doherty, L., Morgan, R. G., James, C. M., Vanyai, T, and Buttsworth, D. R."Development of a fast-response calorimeter gauge for hypersonic ground testing". In: 33rd AIAA Aerodynamic Measurement Technology and Ground Testing Conference. 2017, p. 3238. DOI: 10.2514/6.2017-3238.

Other work published by the author during DPhil candidacy:

Penty Geraets, R. T., McGilvray, M., Loehle, S., Hufgard, F. "Stagnation Point Heat Flux Measurements in a Plasma Wind Tunnel Using a Diamond Heat Transfer Gauge". In: AIAA Scitech 2019 Forum. 2019. DOI: 10.2514/6.2019-0535.

Hermann, T., Ifti, H. S., McGilvray, M., Doherty, L., Penty Geraets, R. T. "Mixing characteristics in a hypersonic flow around a transpiration cooled flat plate model". In: HiSST: International Conference on High-Speed Vehicle Science Technology. Moscow, Russia, 2018.

Acknowledgements

Many thanks to my supervisor Matthew McGilvray, for encouraging me to embark on this PhD. Your support and enthusiasm during it have been invaluable. The tireless work you put in that enables us to do such exciting research is truly appreciated.

Everyone in the Oxford hypersonics group has been a huge source of help and advice over the last four years. In particular I would like to thank Luke Doherty, for his endless work getting the hypersonics facilities operational, for helping with the experiments in X2, and for encouraging me to think more about uncertainty; Peter Collen, for his amazing efforts commissioning (sanding) T6, and for being conveniently located a turn of a chair away to hear my thoughts and questions; Tobias Hermann, for the discussions about heat transfer, noise, and deconvolution; Suria Subiah, for commissioning RST mode for T6; and Seb Wylie, for providing the pizza and the toothbrush.

I would also like to thank all of the students and staff at the Centre for Hypersonics at the University of Queensland, without whom the experiments in X2 would not have been possible. In particular Chris James, for keeping the work fun, and putting in late nights far beyond requirement.

Undoubtedly, this work would not have been possible without all the staff at the Osney Thermofluids Institute, those who have helped explicitly, and those who keep the lab running. Thanks to Trevor Godfrey, for helping develop the first prototype gauges, and to Gregory King, for all his design input and meticulous

work on the subsequent iterations that contributed massively to the success of the gauges. Thanks to James Cater, Duncan Blake, and Harry Kachika, who manufactured the models and gauge bodies used in this research.

To my parents, Jane and Patrick, thanks for your interest and numerous discussions about my work over the years, and in particular to Jane for helping me with my writing, which I have found to be a challenging aspect of this PhD.

I am grateful for the financial support of the EPSRC which enabled this research. Grant reference EP/N009037/1.

Finally, thanks to all my friends, for all the good times and climbing trips which have helped sustain me over the last four years.

Contents

1 Introduction **1**

1.1 Motivation 1

1.2 Aero-thermal Heating 2

1.3 Sources of Heat Transfer Data 5

1.4 Thesis Objectives 8

1.5 Thesis Structure 9

2 Review of Surface Heat Flux Instrumentation for Pulse-Flow Facilities **11**

2.1 One-Dimensional Semi-Infinite Analysis 11

2.2 Thin-Film Heat Transfer Gauges 12

2.2.1 Design and Operation 12

2.2.2 Data Reduction 14

2.2.3 Calibration and Measurement Uncertainty 16

2.3 Surface-Junction Thermocouples 17

2.3.1 Design and Operation 17
2.3.2 Data Reduction 18
2.3.3 Calibration and Measurement Uncertainty 21
2.4 Calorimeters 22
2.4.1 Theory and Data Reduction 22
2.4.2 Implementations 24
2.4.3 Calibration and Measurement Uncertainty 26
2.5 Global Measurement Techniques 28

3 Development of the Diamond Heat Transfer Gauge 30
3.1 Introduction 30
3.2 Design Objectives 31
3.3 Review of Existing Diamond-Based Heat Transfer Gauges 33
3.4 Analysis of a One-Dimensional Calorimeter Gauge 34
3.4.1 Calorimeter Data Reduction Equations 34
3.4.2 Transient Error and Rise-Time 36
3.5 Theoretical Calorimeter Design 38
3.5.1 Material Properties 38
3.5.2 DHTG Types 40
3.5.3 Amplitude-Frequency Response 40
3.5.4 Sensitivity 44
3.6 Mechanical Design 46
3.6.1 Calorimeter 46
3.6.2 Housing and Assembly 47
3.7 Evaluation of DHTG Performance 50
3.7.1 Finite Element Model 50
3.7.2 Temperature Response 51
3.7.3 Heat Flux Results 53

3.8 Heat Flux Measurement Uncertainty 56
3.9 Chapter Summary 59

4 Development of an Impulse-Response Based Data Reduction Method 61
4.1 Introduction 61
4.2 The Inverse Heat Conduction Problem 62
4.2.1 The IHCP 62
4.2.2 Regularisation 63
4.2.3 The Forward Problem 64
4.3 The SFSM Algorithm 65
4.4 Obtaining Impulse Response 68
4.4.1 Models for Obtaining Impulse Response 69
4.4.2 Comparison of Impulse Responses 71
4.5 Comparison of Data Reduction Methods 72
4.5.1 Producing Mock Experimental Data 74
4.5.2 Solution Without Noise, $N_F = 0$ 78
4.5.3 SFSM Solutions With Noise 81
4.5.4 Selection of the Optimum Regularisation Parameter 81
4.5.5 Design of an Optimal Low-Pass Filter 86
4.5.6 Comparison of Final Heat Fluxes 88
4.6 Chapter Summary 91

5 Experimental Measurement of Impulse Response 92
5.1 Introduction 92
5.2 Experimental Set-up 93
5.3 Data Reduction 96
5.4 Experimental Measurement Uncertainty 97
5.5 Experimental Results 99

5.5.1 Experimental Temperature Response 99
5.5.2 Beam Non-Uniformity 100
5.6 Tuning FE Model to Experimental Data 102
5.6.1 Modifications to FE Model 102
5.6.2 Results from FE Model 103
5.7 Chapter Summary 106

6 Experiments in the X2 Expansion Tunnel 108
6.1 Introduction 108
6.2 Experimental Set-up 109
6.2.1 Facility and Conditions 109
6.2.2 Model and Instrumentation 110
6.3 Data Reduction and Measurement Uncertainty 111
6.4 Heat Flux Results 112
6.4.1 Example Measurement 112
6.4.2 Results at Each Flow Condition 113
6.4.3 Results for Condition A2 115
6.4.4 A Note on Thermocouple Effective Thermal Effusivity 118
6.5 Robustness Results 118
6.6 Chapter Summary 122

7 Experiments in the T6 Reflected Shock Tunnel 123
7.1 Introduction 123
7.2 Experimental Set-Up 124
7.2.1 The T6 Facility 124
7.2.2 Heat Transfer Instrumentation 125
7.2.3 Probe Design 126
7.2.4 Experimental Installation 127

7.3 Fill Conditions, Flow Conditions, and Test-Time 127
7.4 Data Reduction and Measurement Uncertainty 131
7.5 Robustness Results 133
7.6 Heat Flux Results 137
7.6.1 Fay and Riddell Heat Flux Estimation 137
7.6.2 Experimental Heat Flux Results 138
7.6.3 Noise and Filtering 144
7.7 Chapter Summary 145

8 Conclusions and Recommendations **147**
8.1 Conclusions 147
8.1.1 Development of the DHTG 147
8.1.2 Experiments in an Expansion Tunnel 149
8.1.3 Experiments in a Reflected Shock Tunnel 150
8.2 Recommendations for Future Work 151

References **152**

Appendix A Solution of Heat Diffusion Equations **171**
A.1 Temperature Solution 171
A.2 Heat Flux at $x = L$ 173
A.3 Solution with Constant Surface Heat Flux 174
A.3.1 Temperature 174
A.3.2 Time Derivative of Temperature 175

Appendix B Table of DHTG Details **176**

Appendix C Uncertainty Analysis **179**
C.1 Uncertainty in a Calculated Value 179
C.2 Numerical Evaluation of Sensitivity Coefficients 181

C.3 Non-Dimensional Uncertainty 182
C.4 Uncertainty in a Linear Regression 182

Appendix D RTD Operation and Calibration 184

D.1 RTD Operation 184
D.2 RTD Calibration 185
D.3 Uncertainty in Calibrated Parameters 187

Appendix E The Fay and Riddell Stagnation Point Heat Flux Equation 188

E.1 Hemispherical and Cylindrical Bodies 188
E.2 Correction Factors for Non-Hemispherical Bodies 190

List of Figures

1.1 Flow around a generic hypervelocity vehicle. 3

1.2 Typical altitude-velocity entry profiles and ground-testing facility operational envelopes with the point at which important thermochemical effects become significant. Adapted from Collen et al. [18]. 6

2.1 Schematic of a one-dimensional two-layer semi-infinite heat transfer gauge, from Schultz and Jones [30]. 13

2.2 Schematic of a thin film gauge on a semi-infinite substrate from Oldfield [36]. 14

2.3 Schematic of an abraded surface-junction thermocouple from Li et al. [64]. . 17

2.4 The ratio of inferred to applied heat flux for three junction thicknesses from a numerical study performed by Li et al. [64]. 20

2.5 Micrograph of an interference-fit thermocouple cross-section from Marineau and Hornung [17], but originally from Davis [68]. Annotations have been added by the author. 21

LIST OF FIGURES

2.6 Schematic of an isolated thin-skin (slug) calorimeter gauge from Gülhan [72]. 23
2.7 Thin-skin calorimeter with distributed measurements from Starner and Varwig [82]. 25

3.1 Schematic of a DHTG. 32
3.2 Domain for one-dimensional semi-infinite analysis of a calorimeter gauge. . . 34
3.3 Rear surface temperature gradient error plotted against non-dimensional time for increasing substrate thermal effusivity. 37
3.4 Variation of specific heat capacity and thermal conductivity with temperature for CVD diamond. 39
3.5 The approximate rise-time of an ideal calorimeter at room temperature as a function of thickness for the material properties shown in Table 3.1. 41
3.6 The ratio of measured heat flux to actual heat flux as a function of frequency for the four types of DHTG in Table 3.3, using material properties at room temperature. Solid lines are for a perfectly insulating substrate, dashed lines are for an epoxy substrate. 43
3.7 Sensitivity of the four types of DHTG compared to a typical thin-film gauge on a quartz substrate and a Type-E surface-junction thermocouple. 46
3.8 Drawing of the diamond calorimeter with dimensions in mm. Dimensions other than thickness are standard across gauge types. 47
3.9 Drawings of version 1 and version 2 of the DHTG housing. 49
3.10 Photographs of the two versions of the DHTG sensor with the serpentine platinum RTD track visible through the transparent PCD diamond calorimeter layer in both. 49
3.11 The simulation domain for the Type 1 DHTG with material regions labelled. 52
3.12 Spatially averaged temperature rise across the front and rear surface of the diamond layer in the FE model, in response to a $1\,\mathrm{MW{\cdot}m^{-2}}$ step in heat flux applied at the surface. 52

3.13 The estimated heat flux for the Type 1 DHTG, calculated from the rear surface temperature rise shown in Fig. 3.12. 54
3.14 Relative measurement error for all four types of DHTG in response to a $1\,\mathrm{MW{\cdot}m^{-2}}$ step in surface heating. 55
3.15 Measurement uncertainty as a function of time. 58
3.16 Uncertainty superimposed upon data reduction error for the Type 1 DHTG in response to a step in surface heat flux. 59

4.1 Schematic of the SFSM algorithm showing the real heat flux and the discretised components of estimated heat flux. 66
4.2 The domain used for the FE model. The axis of symmetry is at $r = 0$. . . . 71
4.3 The unit impulse response for three time-scales, representing typical test-times of three types of hypersonic facility. 73
4.4 The unit impulse response of a Type 2 DHTG from the FE model, plotted for a range of initial isothermal temperatures. 74
4.5 A flow chart of the study performed to compare the calorimeter and SFSM reduction methods. 75
4.6 Input heat flux and temperature response from the FE model. 76
4.7 Experimentally recorded temperature noise and its Power Spectral Density, i.e. for $N_f = 1$. 78
4.8 Heat flux solutions without any noise added to the temperature signal. . . . 79
4.9 Relative measurement error in the heat flux solutions without any noise added to the temperature signal. 80
4.10 Heat flux solutions using the SFSM method for a spectrum of values of the regularisation parameter, for $N_F = 1$. 82
4.11 Root-Mean-Squared Error, Bias, and Variance as a function of the regularisation parameter for $N_F = 1$. The point of minimum RMSE is labelled. . . . 83
4.12 L-Curves with the point of maximum curvature labelled. 85

4.13 PSD of the heat flux solution $S_{\widehat{q}_s\widehat{q}_s}$, of the noise ν, and of the applied heat flux $S_{q_sq_s}$. 87
4.14 PSD of the heat flux solution $S_{\widehat{q}_s\widehat{q}_s}$, of the noise ν, and of the applied heat flux $S_{q_sq_s}$. 88
4.15 Design of the optimal filter $\Phi(f)$. 89
4.16 Final heat fluxes from the SFSM method and the calorimeter method for $N_f = 1$. Both signals have been low-pass filtered using the optimal filter Φ. . 90

5.1 Schematic of the experimental set-up for the impulse response measurement. 94
5.2 Cross-sectional view of the DHTG mounted in its heater. 95
5.3 Unit impulse response of DHTG24 at three initial temperatures. Bold lines represent the average across all pulses at the indicated temperature. 100
5.4 (a) Two-dimensional map of beam intensity taken immediately after experiments were performed. The edge of the diamond is indicated by the 2.5 mm diameter circle. (b) The intensity map averaged and projected onto a line of radius. 101
5.5 The discretisation of the thin-film track into N elements of equal arc-length. Each element measures a temperature T_n and is located at a radial distance r_n from the centre-point. 103
5.6 The unit impulse response at three initial temperatures with the tuned response from the FE model. 104
5.7 Values of specific heat capacity from the current experiments compared to the mean of values from the literature. 105
5.8 Impulse responses from the FE model with both a spatially uniform heating profile, and the non-uniform heating profile given in Fig. 5.4b. 106

6.1 Photos of the model used for experimental testing in X2 with hole numbers labelled. 110

6.2 Pitot pressure from shot x2s3485. Stagnation point temperature rise and heat flux for DHTG7, shot x2s3504. 113
6.3 Measured heat flux from a DHTG and a thermocouple for one shot at each condition. 115
6.4 Stagnation point heat flux from DHTG11 and the Fay-Riddell prediction for three shots at Condition A2. 116
6.5 Heat flux from a DHTG and a TC for Condition A2, normalised by the Fay and Riddell stagnation point value. Each column is a distinct shot number. Each row is a constant axial distance from the leading edge. 117
6.6 Electrical resistance measured immediately before the labelled shot number. 120
6.7 Photos of the surface of DHTG7. 120
6.8 Photos of the surface of DHTG10. 121
6.9 Photos of the surface of DHTG11, which was located on the stagnation point. 121

7.1 CAD schematic of T6 configured as a reflected shock tunnel, adapted from McGilvray et al. [24]. 125
7.2 Drawings of the stagnation point probe caps. 127
7.3 Photograph of the rake in the T6 test-section with rake positions and gauge types labelled. The nozzle exit can be seen on the left. 128
7.4 Pitot pressure from the PCB on the centre-line of nozzle (location 6 in the rake). 131
7.5 Frames recorded by the high-speed camera from shot T6s89. The first frame, marked $t = 0\,\mu s$, is the last frame before the flow is seen to arrive at the rake. The steady test-time is from $300\,\mu s$ to $800\,\mu s$. 132
7.6 Change in resistance, measured before and after each shot, referenced to the pre-T6s87 measurement. 134
7.7 Microscope photographs of the surface of DHTG31 before and after testing in T6. 136

7.8 Microscope photographs of the surface of a new TFG, and the TFG used in T6 after testing. Note that these are not the same gauge but have nominally identical construction. 136

7.9 A microscope photograph of the surface of the TC before and after testing in T6. 137

7.10 Experimental heat fluxes normalised by the heat flux calculated using the Fay Riddell equation. 142

7.11 Test-time average heat fluxes. 143

7.12 a) Power-spectral density of the signal and of the noise before the flow arrives. b) Design of the optimal low-pass filter. 145

D.1 Typical water-bath calibration data and results. 186

E.1 Stagnation point flow-field with states labelled for the Fay-Riddell equation. 189

Nomenclature

Acronyms

AOA	Angle of Attack
AR	Area Ratio
CVD	Chemical Vapour Deposition
DHTG	Diamond Heat Transfer Gauge
OPCD	Opaque Polycrystalline Diamond
PCD	Polycrystalline Diamond
PSD	Power Spectral Density
RST	Reflected Shock Tunnel
RTD	Resistance Temperature Detector
SFSM	Sequential Function Specification Method
SCD	Single Crystal Diamond
TC	Thermocouple
TFG	Thin-Film (Heat Transfer) Gauge
TPCD	Transparent Polycrystalline Diamond
TPS	Thermal Protection System
UMF	Uncertainty Magnification Factor
UPC	Uncertainty Percentage Contribution

Roman Letters

a	Ratio of Thermal Diffusivities
b	Systematic Uncertainty
c	Calibrated RTD Intercept, Ω
c_p	Specific Heat at Constant Pressure, $J{\cdot}kg^{-1}{\cdot}K^{-1}$
e	Internal Energy, $J{\cdot}kg^{-1}$
f_c	Filter Cut-Off Frequency, Hz
f_s	Sampling Frequency, Hz

h	Unit Impulse Response, K
h	Local Enthalpy, $\mathrm{J{\cdot}kg^{-1}}$
h_0	Total Enthalpy, $\mathrm{J{\cdot}kg^{-1}}$
I_c	Constant Current Supplied to RTD, A
k	Thermal Conductivity, $\mathrm{W{\cdot}m^{-1}{\cdot}K^{-1}}$
L, l, s	Calorimeter Thickness, m
m	Calibrated RTD Sensitivity, $\Omega{\cdot}\mathrm{K^{-1}}$
M	Mach Number
N_F	Noise Factor
p	Pressure, Pa
q	Heat Flux, $\mathrm{W{\cdot}m^{-2}}$
$\widehat{q}$	Estimated Heat Flux, $\mathrm{W{\cdot}m^{-2}}$
q_{FR}	Heat Flux Calculated using the Fay and Riddel Equations, $\mathrm{W{\cdot}m^{-2}}$
R	Electrical Resistance, Ω
R	Regularisation Parameter
R_0	RTD Resistance at 0 °C, Ω
R_{eff}	Effective Nose Radius, m
R_n	Nose Radius, m
S_{qq}	Power Spectral Density of q, $(\mathrm{W{\cdot}m^{-2}})^2{\cdot}\mathrm{Hz^{-1}}$
t	Time, s
T	Temperature, K
U	Absolute Uncertainty
V	Velocity, $\mathrm{m{\cdot}s^{-1}}$
V_{ss}	Shock Speed, $\mathrm{m{\cdot}s^{-1}}$
Y	Measured Temperature, K
$\mathcal{X}$	Relative Uncertainty, %

Greek Letters

α	Thermal Diffusivity, $\mathrm{m^2{\cdot}s^{-1}}$
α_R	Temperature Coefficient of Resistance, $\mathrm{K^{-1}}$
η	RMS Magnitude of Heat Flux Solution, $\mathrm{W{\cdot}m^{-2}}$
γ	Ratio of Specific Heats
λ_R	Dimensional Regularisation Paramter, s
ν	Power Spectral Density of Noise
ρ	Density, $\mathrm{kg{\cdot}m^{-3}}$
ρ	Temperture Solution Residual, K
τ	Dummy Variable for Time, s
τ_r	Rise-Time, s
Φ	Optimal Filter
χ	Mole Fraction

Subscripts and Superscripts

1	RTD Reference Condition
1	Layer 1

2	Layer 2
e	Boundary Layer Edge Condition
L	At $x = L$
n	Layer Index 1,2
s	Surface
s	Post-Shock Condition
∞	Free-stream Condition

CHAPTER 1

Introduction

1.1 Motivation

Thermal management is a key design consideration for hypersonic flight vehicles. In fact, the hypersonic flight regime is defined by the fact that the physics of the flow are dominated by aerodynamic heating [1]. For this reason, a major goal since the start of aerospace research has been to accurately predict the heating rates, and integrated heat loads, of vehicles flying at hypersonic speeds, either during atmospheric (re-)entry, or sustained flight.

Atmospheric entries from low-earth orbit are around $7.5\,\mathrm{km{\cdot}s^{-1}}$, and the fastest man-made object to enter the Earth's atmosphere was the Stardust sample-return capsule at $12.9\,\mathrm{km{\cdot}s^{-1}}$ [2]. At these velocities, the temperature behind the strong bow-shock which forms in front of the vehicle reaches thousands of degrees, and peak heating rates to the fore-body of the vehicle can exceed $10\,\mathrm{MW{\cdot}m^{-2}}$ [2]. Protection of the crew, cargo, and the vehicle itself from this extreme environment requires ablative Thermal Protection Systems (TPS). In general, faster entries require more TPS, and can constitute significant mass-fractions of an entry vehicle. The Apollo and Hayabusa capsules had 13.7 % and 43 % TPS mass

fractions respectively [3], and future missions to, and returning from, Mars will be limited by the amount of TPS they have to carry. For atmospheric flight, the fastest speed achieved was Mach 9.6 ($3.1\,\mathrm{km{\cdot}s^{-1}}$) by NASA's X-43A, requiring the use of a carbon-composite TPS on its leading edges to withstand the extreme heat load.

As weight minimisation is critical for both space-faring vehicles and hypersonic aircraft, the safe reduction of TPS mass is vital to push the envelope of what is possible for future missions and vehicles. This can be achieved firstly by reducing uncertainties in the prediction of heat flux, and secondly by developing and validating new methods of thermal protection and management. The latter may have the additional benefit of enabling re-usability. Both of these avenues of improvement require accurate knowledge of heat transfer rates, for the validation of numerical models and new vehicle designs. Despite advances in computational methods, experimental measurements in hypersonic wind tunnels continue to be essential sources of heat transfer data. Continual development of instrumentation used in these facilities is therefore needed to keep improving the accuracy and the spatial and temporal resolution of measurements.

1.2 Aero-thermal Heating

Before presenting the sources of heat transfer data used for design and validation, the origin of the heat flux experienced by the generic hypersonic vehicle shown in Fig. 1.1 is discussed. In front of the vehicle a strong bow shock develops, which from the vehicle's frame of reference rapidly decelerates the incoming flow. Total enthalpy h_0 as defined by Eq. (1.1) is conserved across a shock, resulting in a transfer of energy from kinetic energy to local enthalpy h, where $h = e + p/\rho$, thus increasing both temperature and pressure. It is the strength of the shock and the resulting post-shock temperature and thermochemistry that defines the hypersonic and hypervelocity flow regimes, and the interaction of this post-shock gas with the vehicle that drives heat transfer.

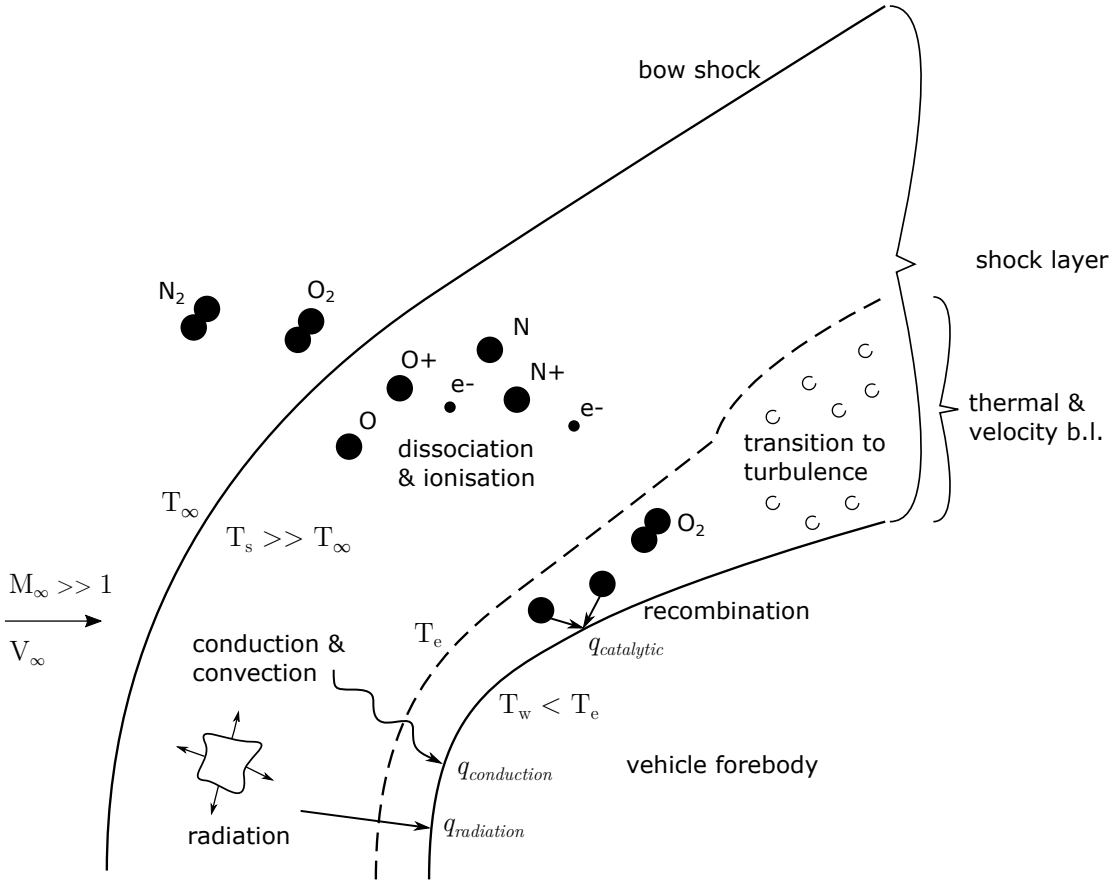


Figure 1.1: Flow around a generic hypervelocity vehicle.

$$h_0 = h_\infty + \frac{V_\infty^2}{2} = h_s + \frac{V_s^2}{2} \tag{1.1}$$

The transition from the supersonic to the hypersonic flow regime begins when the post-shock temperature is high enough that the gas can no longer be considered calorically perfect due to the excitation of vibrational energy modes. For flight in air, this transition begins at around Mach 5 [4], but is greatly dependent on vehicle geometry and does not occur at a well-defined boundary. Unlike for supersonic flow, the post-shock properties for hypersonic flow cannot be calculated assuming perfect gas relations with a constant ratio of specific heats, γ.

The hypervelocity flow regime begins when the post-shock temperature is sufficient to produce significant levels of dissociation. For flight in air, this begins at around $3\,\mathrm{km{\cdot}s^{-1}}$ [5,

6], but again is dependent vehicle geometry. At higher velocities still, and hence higher post-shock temperatures, atoms begin to ionise. These effects represent even further deviation from calorically perfect gas assumptions and, along with vibrational excitation, are collectively known as real-gas effects. Figure 1.2 gives an indication of the relationship between entry velocity, post-shock temperature, and the point at which each of these real-gas effects become significant. The recombination of dissociated and ionised species proceed at finite rates which depend on the probability of collisions: in lower density flows, a higher degree of post-shock non-equilibrium can be expected. The degree of local non-equilibrium can be estimated by comparing the chemical reaction time to a characteristic flow passage duration.

Incident heat flux to the vehicle is a result of conductive, radiative, and catalytic heating, as labelled on Fig. 1.1. Conductive heat transfer, $q_{conduction}$, mainly driven by convection, is a result of a temperature gradient between the hot flow and the relatively cooler vehicle wall. Radiative heating, $q_{radiation}$, is driven by the temperature difference between the post-shock gas and the vehicle wall, and is strongly influenced by the species composition of the post-shock gas and the distribution of its internal modes of energy. A third source of heat flux, catalytic heat flux, is present when a chemical non-equilibrium state exists near the wall. This is a result of the wall catalysing recombination reactions, thus releasing the latent heat of dissociation. The magnitude and proportions of these three components of heat flux depend on the vehicle geometry and materials, the vehicle velocity, and the atmospheric gas state and composition. For example, for a given velocity, the normal shock at the stagnation point of a blunt body will result in a higher post-shock temperature than the oblique shock of a slender vehicle, resulting in higher levels of dissociation and ionisation [7]. Also, the ratio of radiative to convective heating is greater for larger vehicles: for Earth entry at $10\,\mathrm{km{\cdot}s^{-1}}$, 20 % of the heat load comes from radiation for a 1 m diameter vehicle, whereas for a 5 m diameter it is 55 % [8]. Although not labelled on Fig. 1.1, heat transfer is also affected by material response, given that at high temperatures thermal protection materials can out-gas, pyrolyse, and ablate, resulting in coupled flow interactions.

1.3 Sources of Heat Transfer Data

There are three possible sources of data to inform the thermal design of hypersonic vehicles: flight testing, computational models, and ground-based testing. Flight test data requires the least approximations, assumptions, and scaling, but it is difficult to obtain high quality data because it is hard to integrate instrumentation into flight vehicles. Additionally, flight tests are too complex, time-consuming, and expensive to be used as the primary source of data. Computational Fluid Dynamics (CFD) can be used for much of the design of a vehicle. However, high-fidelity simulations can be very computationally expensive and are inherently only as good as the underlying physical models. CFD studies and numerical models require benchmarking and validation against high quality experimental data, particularly for: flows where real-gas effects are significant [9]; coupled material-flow interactions [10]; unsteady processes such as shock-boundary layer interactions [11]; modelling of strongly radiating flows [12]; the effect of rough surfaces on heat transfer [13] and boundary layer transition [14]. The importance of ground test facilities to provide high quality heat transfer data for use in the validation of models and for the design of hypersonic and hypervelocity vehicles is clear. Additionally, heat transfer measurements are necessary to characterise the performance of the test facilities themselves [15, 16, 17].

Despite decades of development, and in part due to physical and financial constraints [19], no single ground-based facility is capable of fully replicating the hypersonic and hypervelocity flight environment. Instead, results from a number of complementary facilities, each simulating different aspects of the flight environment, must be carefully combined to inform the overall design. This is demonstrated in Fig. 1.2, where the typical velocity-altitude profiles for re-entry vehicles and a scramjet ascent to orbit are seen to span the operational envelope of multiple facilities.

With the use of sub-scale models and appropriate scaling of flow conditions [6, 20], so-called pulse-flow facilities (Reflected Shock Tunnels (RST), shock tubes, expansion tunnels)

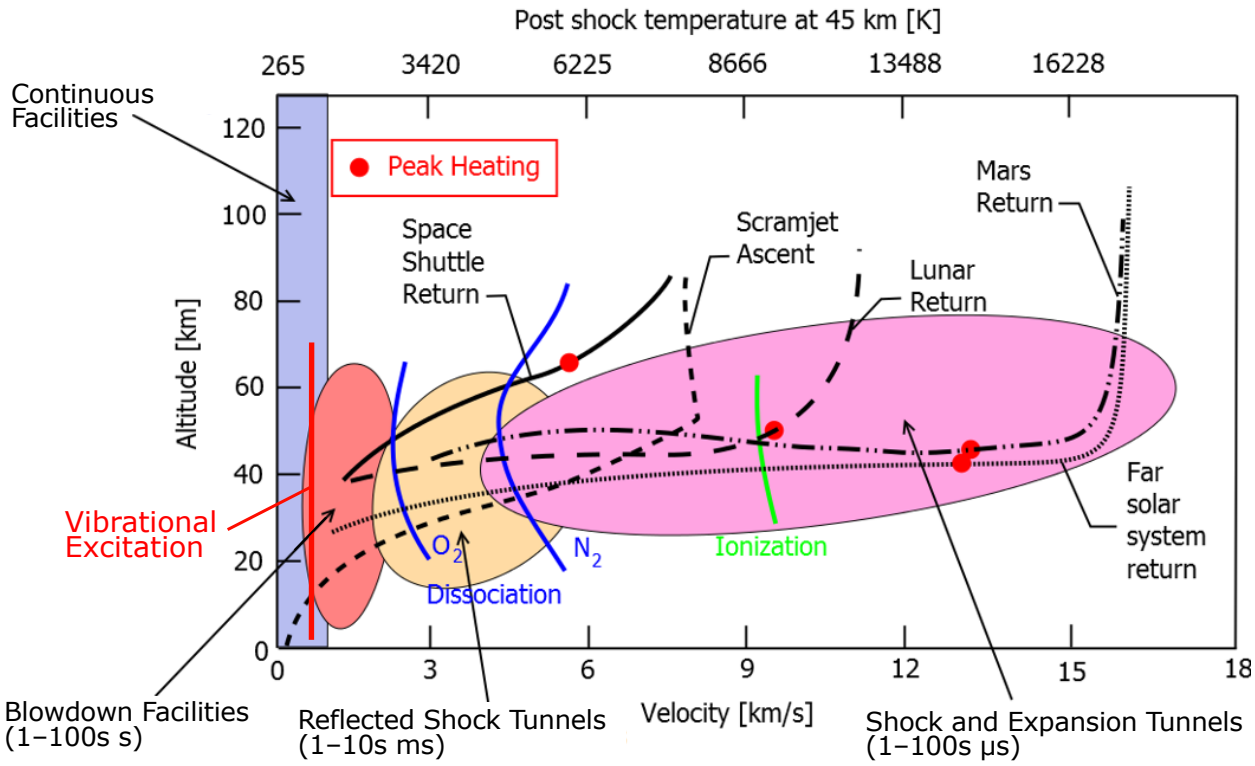


Figure 1.2: Typical altitude-velocity entry profiles and ground-testing facility operational envelopes with the point at which important thermochemical effects become significant. Adapted from Collen et al. [18].

can replicate the post-shock aero-thermodynamic environment for much of a vehicle's entry or ascent profile. However, as indicated on Fig. 1.2, test-times are limited. RSTs typically have test-times of 0.5 ms to 2.5 ms for higher enthalpy shots and smaller facilities [21, 22, 23, 24], extending up to 10 ms for lower enthalpy shots in large facilities [21, 25]. Expansion tunnel test-times, depending on flow conditions, can range from tens of microseconds to hundreds of microseconds [26, 27, 24], and shock tube test-times are even shorter. These pulse-flow facilities operate by bursting a diaphragm, fragments of which are entrained in the flow and can hit models and instrumentation at high speeds, causing serious damage even to hardened steel models. Additionally, at extreme speeds, and hence extreme stagnation temperatures, free electrons in the ionised gas can cause significant disruption to electronics. Instrumentation for use in pulse-flow facilities must not only be able to survive this harsh flow environment, but must also be capable of acquiring high-quality, high-accuracy heat

transfer rates within the short test-durations. Development of heat flux instrumentation for this environment is the focus of this thesis.

In an experiment in a hypersonic pulse-flow wind tunnel in which surface heat transfer is to be measured, a model or probe placed in the flow typically begins at ambient temperature, and experiences a heat flux resulting in a temperature rise. The test-duration is sufficient for the flow to fully develop around the model, but not sufficient for thermal equilibrium to be reached within that model. In fact, despite extreme heating rates, surface temperature rises can be small, on the order of a few to a few hundred degrees Celsius, depending on the materials used. From a measurement of the temperature rise, the heat flux can be calculated by implementing a data reduction scheme based on a mathematical model of the conduction of heat in the vicinity of the temperature measurement(s). The data reduction scheme typically involves parameters such as the thermophysical properties and physical dimensions of a gauge. The accuracy of the heat flux measurement therefore depends on the accuracy of the temperature measurement, the accuracy of the parameters fed into the model, and how conceptually accurately the model represents the conduction of heat in the real gauge. There is no existing surface heat transfer measurement technique which is used ubiquitously, partly because the requirements of specific experiments in specific facilities can vary widely. The general requirements are:

- Fast response, to get transient data within microsecond and millisecond test-times;
- Robust, to survive many experiments without needed replacing;
- Small package size, to obtain high density measurements in small models;
- Electrically isolated from ionised flow;
- Accurate and repeatable measurements.

Currently the most widely used methods to measure heat transfer in pulse-flow facilities are thin-film gauges and surface-junction thermocouples. Both of these can be de-

signed to give microsecond response times, and can measure just a few millimetres in diameter. However, thin-film gauges, by nature of their construction, are extremely fragile. The thin ($< 1\,\mu m$) metallic resistance temperature detector is directly exposed to the damaging flow environment, and can be destroyed after a single tunnel shot. While surface-junction thermocouples are extremely robust, even in the most destructive of experimental facilities, they have also been shown to have large transient uncertainties, particularly on the short time-scales of expansion and shock tubes. A recent development, the Atomic-Layer-Thermopile [28] has enabled measurements of high-frequency flow phenomena, but suffers from damage even in facilities that do not use diaphragms. The limitations of these existing techniques motivate the development of new instrumentation.

1.4 Thesis Objectives

This chapter has outlined the need for high quality heat transfer measurements in experimental facilities. To this end, the overarching aim of this thesis is: *to design, develop, and test, a heat transfer gauge, primarily for use in short-duration hypersonic and hypervelocity wind tunnels, which improves on the short-comings of existing surface heat flux measurement techniques.*

The overall aim can be broken down into the following objectives:

Objective A: To design and manufacture a new heat transfer gauge to improve on the limitations of existing techniques, specifically in terms of response time, accuracy, robustness.[1];

Objective B: To determine the measurement uncertainty of the gauge to a high level of accuracy, and attempt to reduce it where possible, including through the development of improved data reduction methods;

[1]Specific design criteria for the gauge are given in Chapter 3.

Objective C: To define the operating envelope of the gauge in terms of free-stream flow conditions, facilities, test durations, and robustness;

Objective D: To perform experiments that compare the new gauge to existing techniques, both in terms of measurements and usability.

1.5 Thesis Structure

The objectives stated above were pursued through multiple iterations of design, development, and experimental testing described in the chapters of this thesis as follows:

Chapter 2 presents a review of the current state of the art for surface heat transfer measurement techniques for pulse-flow ground-test facilities, discussing the benefits and limitations of the most widely used techniques.

Chapter 3 covers the development and design of a novel heat transfer gauge, named the Diamond Heat Transfer Gauge (DHTG). The design objectives are explained, followed by a theoretical analysis of the performance of the gauge, used to define a calorimeter-based data reduction method, its rise-time, amplitude-frequency response, and sensitivity. A study using an axisymmetric Finite Element model of a DHTG to provide a temperature response to a step in surface heat flux is used to estimate the transient measurement accuracy of the calorimeter-based data reduction method.

Chapter 4 introduces the use of the non-linear Sequential Function Specification Method (SFSM) as an alternative data reduction method for the DHTG and compares numerical models to obtain the impulse response as a function of temperature required for this method. A study is performed to compare the SFSM method to the calorimeter-based method (presented in Chapter 2) using the simulated temperature response of a DHTG, obtained from a axisymmetric Finite Element model with the addition of typical experimental noise.

Chapter 5 covers a calibration experiment aiming to directly measure the impulse response of a DHTG, with the goal of using the result with the SFSM method to provide

parameter-free data reduction for experimental measurements. The temperature response of the DHTG is measured following a short-duration pulse of heat applied to its surface using a laser. From the experimental data, the material properties of the diamond and substrate are estimated and compared to values given in the literature.

Chapter 6 is the first of two chapters in which experimental results from the use of the DHTG in hypersonic pulse-flow facilities are analysed. This chapter details an experimental campaign in the X2 expansion tube at the University of Queensland, Australia. Heat flux measurements are made on a wedge model, at multiple angles of attack, using both DHTGs and surface-junction thermocouples. Measured heat fluxes are compared for five flow conditions, and the robustness of the gauges is evaluated in this very destructive environment.

Chapter 7 describes the second set of wind tunnel experiments, performed in the T6 Reflected Shock Tunnel at the University of Oxford. A DHTG, a surface-junction thermocouple, and a thin-film gauge, were each mounted on the stagnation point of cylindrical probes in the test-section of T6. Transient and test-time average heat flux measured during three tunnel shots is presented and compared. Damage to the gauges is evaluated, and microscope photos of the gauge surfaces before and after testing are shown.

Chapter 8 presents conclusions regarding the development and calibration of the DHTG, and the two experimental campaigns it has been used in. Recommendations for future efforts to build on the work presented in this thesis are given.

CHAPTER 2

Review of Surface Heat Flux Instrumentation for Pulse-Flow Facilities

In this chapter, literature relating to the most common surface heat flux measurement techniques used in hypersonic pulse-flow facilities is reviewed. The focus is on thin-film heat transfer gauges, surface-junction thermocouples, and calorimeters. The chapter concludes with a brief overview of global measurement techniques, focusing on the difficulties of using these methods in pulse-flow facilities. A wider perspective on heat flux measurements is given by Diller [29]. For each technique, the general construction and operation is given, data reduction methods are described, and the way in which these relate to the measurement uncertainty and operational envelope of the gauge is discussed.

2.1 One-Dimensional Semi-Infinite Analysis

Before discussing specific techniques, an overview of the general problem is given, as described in greater detail by Schultz and Jones [30]. Although more complex analysis can be applied, the basic operation of all the techniques in this chapter is on the so-called semi-infinite principle. The problem is that of transient heat conduction into a one-dimensional two-layer

medium, as shown in Fig. 2.1. The second layer is considered to be of semi-infinite depth if the temperature rise on its rear surface is negligible. If the first and second layer are $n = 1$ and $n = 2$, then the transient conduction of heat through the gauge with constant thermophysical properties is described by:

$$\frac{\partial T_n}{\partial t} = \frac{1}{\alpha_n} \frac{\partial^2 T_n}{\partial x^2} \tag{2.1}$$

The solution to this equation for the temperature at any depth x given a boundary condition heat flux q_s is given in Appendix A. For a heat transfer gauge, the inverse problem must be solved, meaning that an estimate of surface heat flux, $\widehat{q_s}$, must be found from a given temperature measurement. This is the Inverse Heat Conduction Problem (IHCP), which can be stated as: "the estimation of a surface heat flux boundary condition given an in-depth temperature measurement". The IHCP is discussed further in Chapter 4 and in detail by Becket et al. [31] and Woodbury [32] amongst many others. The techniques described in this chapter avoid the main issues of the IHCP by simplifying the problem, either by assuming that the top layer has negligible thermal capacity (thin-film gauges and surface-junction thermocouples), or by assuming that the top layer is isothermal (calorimeters). These assumptions are discussed for specific gauges in the following sections.

2.2 Thin-Film Heat Transfer Gauges

2.2.1 Design and Operation

Thin-film heat transfer gauges have been used since 1956, by Vidal [33] and Rabionwicz et al. [34], and are still one of the most widely used methods in low-enthalpy facilities and for measurements on flat plates and leeward faces in high enthalpy facilities, where robustness is not an issue. A schematic of a thin-film gauge is shown in Fig. 2.2. The gauge consists of a thin metallic strip, painted or sputtered onto the surface of a homogenous substrate. The

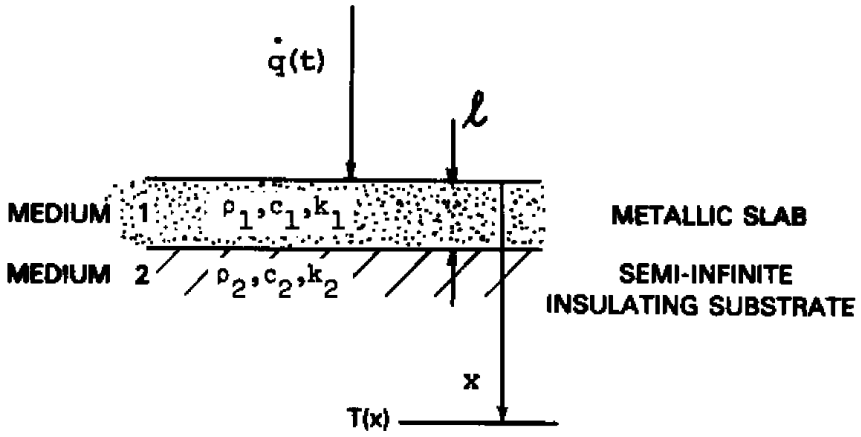


Figure 2.1: Schematic of a one-dimensional two-layer semi-infinite heat transfer gauge, from Schultz and Jones [30].

film is made of a material such as platinum or nickel; materials with a large temperature coefficient of resistance. If a heat flux is applied to the surface of the gauge, the temperature rise of the film can be detected as a change in resistance according to Eq. (2.2), where α_R is the temperature coefficient of resistance and R_0 is the resistance at a reference temperature. Equation (2.2) assumes a linear relationship between temperature and resistance, which is valid for platinum for temperature rises less than 100 °C. This type of temperature transducer is commonly known as an Resistance Temperature Detector (RTD). The change in resistance is typically measured by supplying the film with constant current and measuring the voltage response [30]. Although the sensitivity of the gauge increases with supply current, it must be limited such that self-heating is negligible [35]. A typical value of temperature sensitivity for a thin-film gauge is $1\,\mathrm{mV{\cdot}K^{-1}}$ [30].

$$\Delta R = \alpha_R R_0 \Delta T \tag{2.2}$$

Generally, thermally insulating substrates such as quartz, ceramics, and plastics are used for thin-film gauges. This is a benefit for most testing because it results in large surface temperature rises, thus increasing heat flux sensitivity. However in high enthalpy testing

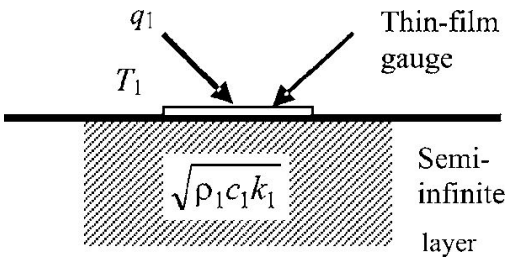


Figure 2.2: Schematic of a thin film gauge on a semi-infinite substrate from Oldfield [36].

this can be a problem: Neely and Morgan [7] used thin-film gauges on quartz to measure stagnation point heat fluxes in an expansion tube, and at the highest velocity condition of $12.4\,\mathrm{km{\cdot}s^{-1}}$, the platinum film melted during the test-time.

The poor robustness of thin-film gauges is their main drawback for use in high enthalpy facilities and on stagnation points due to impacts from fragments of metallic diaphragms in the flow [37, 38]. In high enthalpy facilities, when mounted on blunt bodies or at high angles of attack, a thin film gauge will be destroyed after a single shot [39]. Even in facilities that do not use diaphragms, the electrical resistance of gauges can be seen to change during test-times due to impacts from small particulates such as dust [40].

Jahn and Weimer [41] found that thin-film gauges are susceptible to interference from ionisation in shock tube flows, due to the exposed electrically conductive thin-film element. Marrone and Hartunian [42] found the same problem, and were able to reduce the interference by applying a thin layer of SiO_2 over the surface to electrically isolate the gauge from the flow. This procedure is now common practice, but reduces the response time of the gauge [43] and the thin insulating layer suffers from the same robustness issues as the resistive layer itself.

2.2.2 Data Reduction

If the substrate is homogenous and semi-infinite, and the metallic layer is thermally thin, then the two-layer system given in Fig. 2.1 reduces to one layer and the surface temperature is purely a function of the heat flux history and the thermophysical properties of the

substrate. Given these conditions, an expression for the surface heat flux in terms of the surface temperature can be found by solving Eq. (2.1) for the boundary condition, as given in Appendix A.2. Schultz and Jones [30] give a form of the solution as:

$$\widehat{q_s}(t) = \frac{\sqrt{\rho_1 c_1 k_1}}{\sqrt{\pi}} \left[\frac{T_1(t)}{\sqrt{t}} + \int_{\tau=0}^{t} \frac{T_1(t) - T_1(\tau)}{(t-\tau)^{3/2}} d\tau \right] \tag{2.3}$$

Many methods to solve Eq. (2.3) have been developed over the years because it cannot be solved exactly due to a singularity when $\tau = t$. In the 1960s, numerical discretisation methods were developed, the most well-know of which is by Cook and Felderman [44] where heat flux is assumed to be a piece-wise linear function. Hartunian and Varwig [45] developed an update to the Cook and Felderman algorithm allowing for the variation of thermophysical properties with temperature rise during a test, thus broadening its scope of applicability. More recently, Oldfield [36] developed an impulse-response processing method allowing computationally cheap data reduction for gauges consisting of one or more substrate layers, but only for constant thermophysical properties. Finite Element (e.g. Bertolazzi et al. [46]) and finite difference (e.g. [47]) methods are more computationally expensive than Oldfield's method, but allow arbitrary geometries with temperature dependent properties.

The data reduction methods described above are only valid if the temperature measurement is assumed to be at the surface of the material, at the same location as the incident heat flux. Whether this is a valid assumption depends on whether or not the metallic thin film layer is thermally thin, which depends on the magnitude and rate of change (i.e. frequency content) of the heat flux. Buttsworth and Jones [48] provide a lower bound of frequency at which the influence of a given film can no longer be ignored, defined as the point at which the measurement error without a correction exceeds 1 %. For a typical sputtered platinum film with a thickness of 100 nm this is 100 kHz and for painted films with a typical thickness of 1 µm this is 10 kHz. With a correction for thermal storage, the limit can be extended to 310 kHz and 31 kHz respectively. Despite this, the response time of thin-film gauges without a correction applied is often quoted to be less than 1 µs [49].

Measuring the temperature at the same location as the heat flux is a special case of the IHCP which allows the relatively simple solutions mentioned above. However, a fundamental limitation still exists, as for any solution to the IHCP: increased sampling rate and noise level lead to greater instability [50]. All of the methods presented thus far may produce unstable solutions in the presence of imperfect temperature data, i.e. noise, and only avoid instability by limiting sampling rates and applying low-pass filters. Frankel and Chen [50] provide a methodology for the data reduction of temperature data from thin-film gauges which can help maximise information without leading to unstable solutions.

2.2.3 Calibration and Measurement Uncertainty

The measurement uncertainty of a thin-film gauge depends on the parameters used in the data reduction equations. Firstly, this depends on the values of α_R and R_0 used in the calculation of temperature rise. These parameters are typically found by calibration in an isothermal water bath (e.g. Collins et al. [51]) or oven (e.g. Miller [40]). However, it is the thermal effusivity ($\sqrt{\rho c_p k}$) that is the main source of uncertainty in the measured heat flux. To measure this, a known heat flux is applied to the surface of the gauge and the thermal effusivity is deduced from the surface temperature rise. The heat flux can be applied using the thin-film itself, through ohmic heating [45, 52], or using radiation based source such as a laser [53, 54]. These calibration experiments are vital, as not only can the results show deviation from typical bulk properties [52], but additionally, uncertainty in these parameters is rarely given by material manufacturers.

Some typical values of quoted heat flux measurement uncertainties for thin film heat transfer gauges that use the results of these typical calibration experiments are: Epstein, ±7 % [55]; Capra, ±8.5 % [56]; Kinnear and Lu ±10 %[57]; and Wise, ±5.8 % to ±11.9 % [43][1].

[1]Depending on overall temperature rise, and therefore changes in substrate thermophysical properties

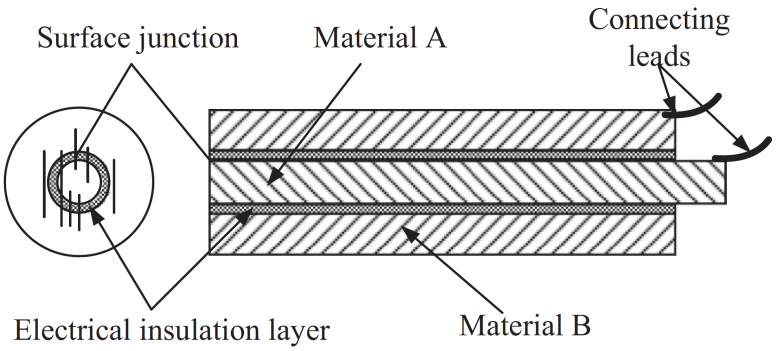


Figure 2.3: Schematic of an abraded surface-junction thermocouple from Li et al. [64].

2.3 Surface-Junction Thermocouples

2.3.1 Design and Operation

Like thin-film gauges, surface-junction thermocouples have been in use since the 1960s [58]. Their robustness and fast response-time makes them well-suited to measurements in high-enthalpy facilities, particularly for measurements on blunt bodies and stagnation points [37]. The most common construction arrangement is coaxial. A hollow tube and solid rod of differing metals are separated by layer of electrical insulation and an electrical junction is then formed at the surface either by abrasion [59, 56, 60, 61], as shown in Fig. 2.3, or by interference fit using a tapered central element [62, 63]. The temperature sensitivity of a thermocouple is up to $68\,\mu V \cdot K^{-1}$ for a Type E, which is more than an order of magnitude lower than that of a thin-film gauge.

Abraded junction thermocouples can have response times as fast as 1 µs [56] while interference-fit thermocouples are around 10 µs [63]. The excellent robustness of these sensors is achieved because the entire portion of the gauge exposed to flow is made from solid metal. Junctions made by abrasion can require re-abrading between shots, as the flow erodes the strands of metal which form the junction. In more destructive facilities, at high enthalpy, impacts from diaphragm particles can even produce new junctions [26].

2.3.2 Data Reduction

After calculating temperature rise from the voltage measured across the thermocouple, many sources in the literature apply the same one-dimensional semi-infinite data reduction techniques to calculate heat flux as presented for thin-film gauges in the previous section (Section 2.2.2). To apply these methods, the same assumptions apply: the temperature measurement must be at the surface, and the substrate must be homogenous. However, the nature of a thermocouple means that two dissimilar metals are needed, and depending on the construction, whether or not the temperature measurement is on the surface is in question. Commonly, an effective value of thermal effusivity is used, taken to be the average of the two metals. This assumption is only valid if the two metals and the insulation all have identical thermal properties, or if the temperature distribution within the gauge closely resembles that which a gauge made from homogenous material would have.

Buttsworth showed using both a computational study [65] and an experimental study [66, 61] that if the two metals have different values of thermal effusivity, such as for a Type K thermocouple, then using an effective thermal effusivity which is the average of the two metals to calculate heat flux will lead to over-predictions of up to 50 % on millisecond time-scales, and that the over-prediction decreases with time. It was concluded, contrary to similar investigations such as Kovacs and Mesler [58], that the junction does not lie above the insulation layer, but in fact lies in close proximity to the insulation on one of the metals. The effective thermal product is therefore affected by four factors:

1) Which thermocouple element the junction lies on;

2) The proximity of the junction to the insulation layer;

3) The depth of the junction;

4) Time.

Buttsworth [66] finds that the effective thermal product of a thermocouple with a junction formed by scratching the surface with a scalpel is much closer to the average of the two metals than junctions formed by abrasion with sandpaper. The difference is due to the geometry of the scratch, and therefore factors 2) and 3) given above. A conclusion is drawn that the shallower the junction, the closer the junction lies to the insulation, and therefore the greater the effect of the insulation layer on the effective thermal effusivity. However, the drawback to using scratched junctions is that the response times are significantly longer, around 10 µs, and less predictable.

Even if the metals have similar values of thermal effusivity, as is the case for Type E thermocouples (to within 10 % [67]), the effect of even a relatively thin thermally insulating layer between the metals produces local overheating in the vicinity of the junction and leads to over-estimates of heat flux. A numerical study by Li et al. [64] modelled the thermocouple junction as a annular disk, located directly above the insulation layer, and investigated how the thickness (depth) of the junction leads to an error in heat flux measured. How this junction geometry relates to that of real gauge is not stated. The ratio of inferred (calculated) to applied heat flux as a function of time for a Type E thermocouple is shown in Fig. 2.4, where the measured temperature is taken to be the volume average of the junction. The conclusion agrees with Buttsworth [66], in that a thinner junction leads to higher levels of error: a junction 2 µm thick leads to an over-prediction in heat flux of 30 % after 100 µs, reducing to 18 % after 1 ms, whereas a junction thickness of 10 µm has an error of 5 % after 100 µs and is much the same after 1 ms. The reason for the decrease in error with a thicker junction is that it has better thermal contact with the bulk material which reduces the overheating effect. However, it can also be seen in Fig. 2.4 that increasing the junction thickness increases the response time to tens of microseconds.

Marineau and Hornung [17] and Sanderson and Sturtevant [62] presented data reduction techniques accounting for a sub-surface junction (for measured depths of 5 µm and 1.5 µm respectively), but both methods still assume that the gauge is a one-dimensional homogenous

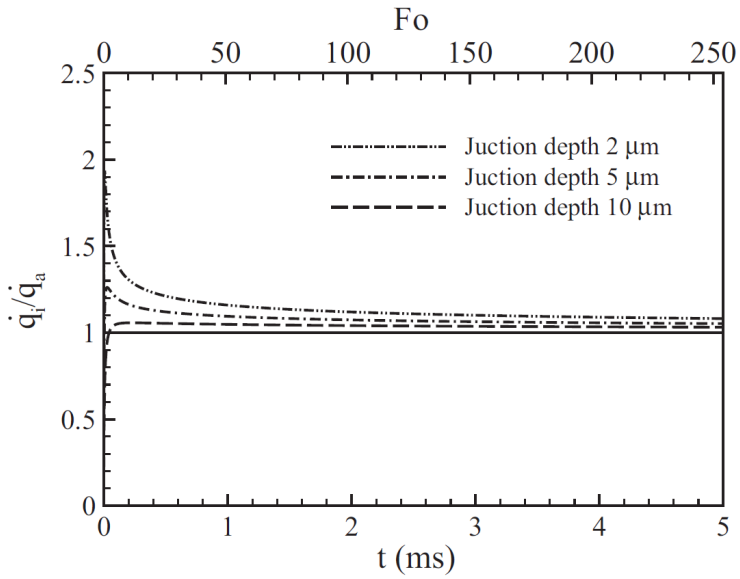


Figure 2.4: The ratio of inferred to applied heat flux for three junction thicknesses from a numerical study performed by Li et al. [64].

medium, i.e. the insulating layer is not accounted for. Marineau [63] performed a study using a Finite Element model of an interference-fit surface-junction thermocouple. The junction geometries were based on the micrograph images of a cross-sectional cut of a real gauge shown in Fig. 2.5. This figure clearly demonstrates the proximity of the junction to the epoxy adhesive. The study showed that in response to a step in surface heat flux the layer of epoxy reduces heat conduction from the junction compared to a fully metallic gauge. Applying a data reduction technique based on one-dimensional conduction with an effective thermal effusivity taken to be the average of the two metals, the over-prediction is greater than 60 % for $t < 100\,\mu s$, falling to 25 % at $t = 1\,ms$. For longer durations, the temperature distribution within the gauge homogenises, and the over-prediction of heat flux reduces. Note that it is not clear exactly how the temperature response of the simulated thermocouple is defined. Experimental results from a shock tube supported the findings of the numerical study, finding that the heat flux was over-predicted by as much as 30 % for $t < 30\,\mu s$, and 20 % for $t = 1.5\,ms$.

Mohammed et al. [69] and Sundqvist [67] both show that the metallurgical composition

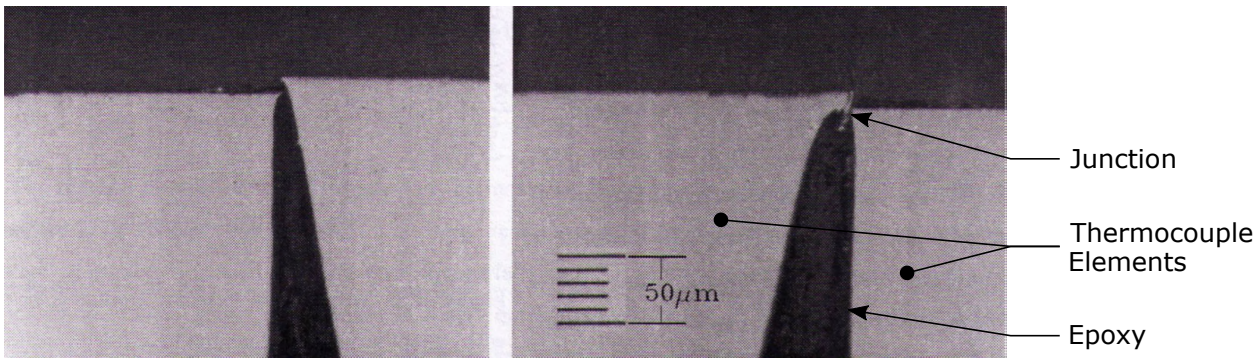


Figure 2.5: Micrograph of an interference-fit thermocouple cross-section from Marineau and Hornung [17], but originally from Davis [68]. Annotations have been added by the author.

of thermocouple metals from different manufacturers is not consistent, meaning that neither standard values of the generic material thermal properties nor the Seebeck coefficient should be used, but instead should be found through calibration. Measurements of the bulk thermal properties of chromel and constantan, forming a Type-E thermocouple, vary by up to 15 % [56, 70].

A conclusion made by Li et al. [64] sums up the issues presented above succinctly: "the effective thermal effusivity is not an inherent, invariant property of a surface thermocouple, but rather is connected with the junction and the time".

2.3.3 Calibration and Measurement Uncertainty

Calculation of temperature rise of a thermocouple can either be found from thermocouple tables, or more accurately using the results of a calibration experiment to determine voltage as a function of temperature in an isothermal water-bath [56, 71], similar to that used for the temperature calibration of thin-film gauges.

Calibration experiments to determine the effective thermal effusivity of coaxial thermocouples can be performed using shock tubes [66, 63], water-droplet experiments [66], and by applying a surface heat flux with a laser [61]. Despite the fact that there exists a large spread of results from these experiments, particularly on short time-scales as discussed in the previous section, this error is generally not included in quoted values of overall measurement

uncertainty in the literature. This is presumably because the error is transient, and because it is difficult to determine the exact geometry of the thermocouple junction of each gauge, especially when it may change during an experiment either due to impacts from diaphragm fragments, or manual re-abrading of the surface. With this caveat, a sample of heat flux measurement uncertainties quoted in the literature is: Capra [56], ±7 %; Sanderson [62], ±8.9 %; Mohammed [60], ±10%; Marineau [63], ±11 %. Following the studies discussed above, reported measurements that have not been calculated using a value of effective thermal effusivity calibrated for the specific gauge on the specific time-scale presented could have additional errors ranging from 5 % to 60 %.

2.4 Calorimeters

2.4.1 Theory and Data Reduction

The basic operation of a calorimeter is an energy balance into a control volume of material. The net heat flux across all boundaries is equal to the energy stored, and the energy stored results in a measurable temperature rise. A schematic of a slug calorimeter is shown in Fig. 2.6, where a thermocouple junction on the rear surface of the calorimeter is used to measure temperature. Gauges operating on the "thin-skin" principle, including slug calorimeters, assume 1) that the calorimeter is isothermal; and 2) that the heat lost from the calorimeter to the surroundings is negligible [72]. Using the notation given in Fig. 3.2, the basic calorimeter data reduction equation for the surface heat flux can be written for constant thermophysical properties as

$$q_s = \rho c_p s \frac{dT(s,t)}{dt} \tag{2.4}$$

where ρ, c_p, and s are the density, specific heat capacity, and thickness of the calorimeter respectively.

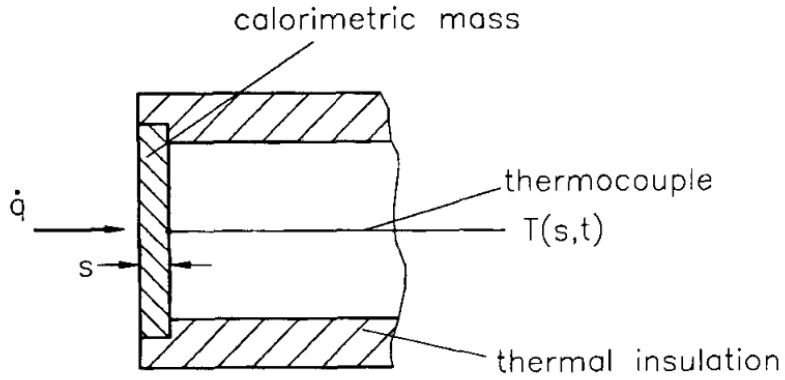


Figure 2.6: Schematic of an isolated thin-skin (slug) calorimeter gauge from Gülhan [72].

The validity of the two assumptions above is investigated by Schultz and Jones [30] for a calorimeter modelled as the two-dimensional geometry given in Fig. 2.1, where layer 1 is the calorimeter and layer 2 is a semi-infinite backing material. In response to a step in surface heat flux, the rise time can be defined as the time taken for the measured temperature gradient to come within 1 % of the mean temperature gradient of the calorimeter. If the temperature is measured on the rear surface of the calorimeter as in Fig. 2.6, then Schultz and Jones [30] give the rise time as

$$\tau_r = 0.5 s^2 \frac{\rho c_p}{k} = 0.5 \frac{s^2}{\alpha} \tag{2.5}$$

The validity of the assumption that negligible heat is lost limits the accuracy of measurements with calorimeters and the useful test-time which they can be used for. Heat loss in terms of both axial [30] and radial [73] conduction can be modelled assuming semi-infinite media, and both should either be minimised or accounted for in the energy balance to improve the accuracy of Eq. (2.4).

For a thick-skin calorimeter, the calorimeter is not assumed to be isothermal. In general, any in-depth measurement in a material can be considered a thick-skin calorimeter, but apart from the implementation developed by Rose [74] discussed below, they are generally not used in pulse-flow facilities due to slow response-times. However, thick-skin data reduction

techniques can also applied to thin-skin calorimeters and thin-film gauges, and can even improve the accuracy of measurements from them because it is not necessary to make the assumptions that the top layer is isothermal or that the temperature measurement is on the surface. For example, Frankel et al. [75, 76, 77] have developed an integral-based approach to heat flux data reduction which is applicable for arbitrary geometries, and can provide an entirely parameter-free data reduction method when used in conjunction with a calibration experiment [78].

2.4.2 Implementations

Palmer [79, 73] produced slug calorimeters, similar to that shown in Fig. 2.6 and those used by Ledford [80], with a response time of 2 µs by using 25 µm thick copper with a butt-welded thermocouple junction on the rear surface. These were used to measure stagnation point heat fluxes in the X1 expansion tube of over $100\,\mathrm{MW{\cdot}m^{-2}}$. While the measurements were successful, the survival rate was low in this extremely destructive environment, with only "a number" of the sensors surviving two or three shots, implying some only survived one shot. The measured heat flux exhibited a large dip upon flow arrival in the expansion tube, which is attributed to interference from ionisation. However, this was fixed by using the model in the test section as the electrical ground for the amplifier and data acquisition systems.

A distributed-measurement thin-skin calorimeter is a commonly used extension of the slug calorimeter concept which can improve measurement density when compared to discrete gauges [72, 81]. Thermocouple junctions are formed on the internal surface of a thin sheet of metal which can be curved or flat. By assuming that lateral heat flux gradients are small, each temperature measurement can be analysed as a one-dimensional thin-skin slug calorimeter. Starner and Varwig [82] produced the thin-skin calorimeter shown in Fig. 2.7. The model was built to investigate the effect of varying surface roughness on heat transfer in a shock tunnel with a test-time of milliseconds. This example demonstrates one of the main advantages of thin-skin calorimeters; as long as the thermal capacity of the calorimeter can

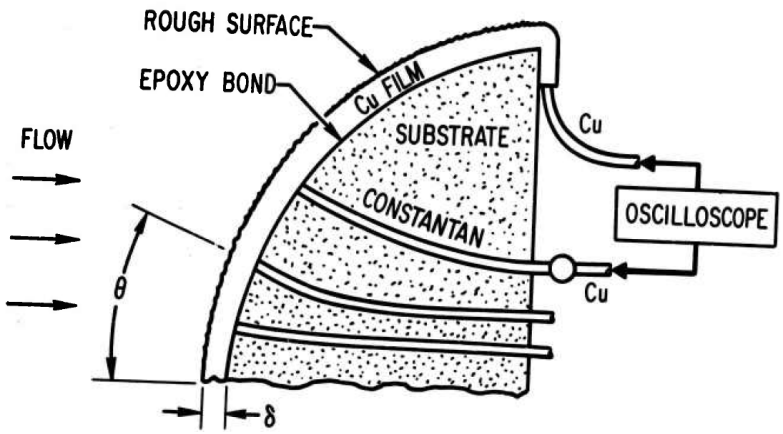


Figure 2.7: Thin-skin calorimeter with distributed measurements from Starner and Varwig [82].

be found, the shape and size of the surface roughness can be arbitrarily complex without affecting the measurement.

A study by Miller [40] comparing the use of thin-film gauges and thin-skin calorimeters in short-duration hypersonic facilities found that, although a higher measurement density could be achieved with the calorimeters, it was difficult to accurately measure the local thickness of the metal hemisphere, leading to inferior measurement uncertainty. However, the thin-film gauges required re-calibrating between experiments due to damage from the flow, while the thin-skin calorimeter were not damaged.

Rose [74] developed platinum thick-skin calorimeters for use in shock tubes with test-times of around 50 µs, where heat fluxes of over $10\,\mathrm{MW{\cdot}m^{-2}}$ would result in damaging surface temperature rises to standard thin-film gauges on thermally insulating substrates. The gauges were designed around specific experimental conditions, tailoring the thickness of the calorimeter according to the thermal penetration depth of the experimental heat pulse such that essentially all of the heat remained in the calorimeter, and the temperature distribution across the calorimeter layer was as even as possible. Rose showed that the temperature measured by treating the film as a standard RTD (albeit with a supply current of 700 A) was sufficiently close to the mean temperature of the calorimeter, and thus could be used as the temperature in Eq. (2.4) to calculate heat flux.

2.4.3 Calibration and Measurement Uncertainty

Beyond the calibration of the temperature transducer used, calibration involves determining the heat capacity of the calorimeter and possibly the backing material. Many of the methods presented for the calibration of thin-film gauges and thermocouples can be applied to calorimeters, as fundamentally they are all experiments to determine thermal properties.

Starner [82] used a pulse of radiation of known magnitude from a graphite strip to determine both the calorimeter heat capacity during the heating phase, and the substrate thermal properties from the rate of decay of temperature during the subsequent cooling phase. An absorbing paint was applied to the calorimeters to provide a known absorptivity, but how this additional layer affected the calibration is not discussed, and no indication of measurement uncertainty is given. Palmer [73] used a constant heat flux of arbitrary magnitude (due to unknown reflectivity) from a laser to determine the effect of conduction from the copper calorimeter described in Section 2.4. From this, the validity of neglecting conduction losses from the calorimeter to the gauge body and thermocouple wire in the data reduction equations was determined. The time at which the response had decayed by 5 % from its peak was taken as the maximum useful measurement time of the gauges.

Sprinks [83] describes a method to determine the heat capacity of a calorimeter by sudden immersion into a heated liquid bath of known temperature and thermal properties. The resulting transient heat conduction equations can be solved over the two coupled regions, the liquid and the calorimeter, to find the thermal capacitance of the calorimeter. Palmer [73] employed this method for copper calorimeters, and additionally applied a deconvolution technique to calculate the temperature at the top surface of the calorimeter, i.e. the interface between the two media, from the rear surface thermocouple measurement. However, suitable data from the calibration experiment could only be obtained for 20 % of the gauges manufactured.

Perhaps the most unique calibration technique in the literature is that of Rose [74]. The

method is essentially the same as the electrical discharge method described to determine the thermal effusivity of standard thin-film gauges. However, that a copper-clad bullet was fired through two parallel metal plates to complete an electrical circuit for around 250 µs, thus allowing a large current to flow through the thick-film calorimeter. The thermal capacitance of the calorimeter was determined from a calculation of the energy delivered to the calorimeter through ohmic heating and the resulting temperature rise.

Although developed for longer-duration facilities such as high enthalpy plasma wind tunnels, Löhle et al. have applied a novel method called Non-Integer System Identification (NISI) [84, 85] to find the impulse response of both null-point calorimeters [86] and slug calorimeters [87], including the DHTG [88][2]. The method involves using a laser to apply a known heat flux to a gauge, measuring the temperature response, and subsequently identifying the impulse response from this information. The impulse response can be used to solve the inverse heat conduction problem for experimental data without the need to make further assumptions such as thermophysical or geometric properties of the gauge, thus providing a parameter-free data reduction method. There is no fundamental limitation preventing this approach from being applied to gauges operating on shorter test-times.

None of the publications regarding calorimeters cited in this section include an explicit evaluation of measurement uncertainty, and the wide range of types and implementations of calorimeter make it difficult to make direct comparisons. However, Palmer [73] states that ±15 % is a "good indication" of uncertainty. Rose [38] suggests that a calibration result used in the data reduction process varies by around 15 %, and states that "extreme recording accuracy can be achieved at very considerable expenditure of effort" [74]. Only Miller [40] gives estimated values of uncertainty for thickness and specific heat capacity of 2.5 % and 2 % respectively, but also presents a host of other factors leading to increased uncertainty which are not quantified.

[2]The calibration of the DHTG using the NISI method is not presented in this thesis as the result was not applicable to the test-durations of pulse-flow facilities, but can be found in Penty Geraets et al. [88]

2.5 Global Measurement Techniques

Global measurement techniques make use of a camera to record a three-dimensional map of intensity which can be converted into a map of surface temperature. Two popular global measurement techniques are Infrared thermography and Temperature Sensitive Paints (TSP). For infrared Thermography, the surface of a model is imaged using an infrared camera, and the temperature is calculated from the recorded intensity and knowledge of the emissivity of the material. Temperature Sensitive Paints contain a luminophore, which when excited at specific wavelengths, re-emit radiation at a different wavelength, with the intensity of the emission related to temperature. Model surfaces can be painted with a thin layer of this paint and the emission can be imaged with a standard camera through a band-pass filter to remove the excitation light.

From a measurement of surface temperature, surface heat flux can then be calculated for each pixel by applying, for example, the one-dimensional analysis presented in Section 2.1. The clear advantage of global methods over discrete methods is spatial resolution. However, they are generally limited to use on model surfaces which are smooth, without high curvature, with good optical access, and to experiments where the flows themselves are not radiating.

Temperature sensitive paints have been used widely in hypersonic facilities [89, 90, 91, 92, 93, 94]. Response times as short as 200 µs are reported [89], making them a feasible measurement option for test-time average heat fluxes, but not for high speed transient measurements. Drawbacks of TSP include: limited durability in high enthalpy facilities, perhaps only lasting one tunnel shot [91], the need for in-situ calibrations, degradation of the luminophore over a time-scale of hours [95], and uncertainties due to variability in the paint thickness [96].

Infrared thermography has been used successfully in long duration cold flow hypersonic facilities, e.g. by Choudhury [97], and in ballistics ranges, e.g. by Reda [98]. However, due to camera limitations and short test-times in pulse flow facilities, Infra-Red Thermography is currently limited to low resolution line-scans [99, 100]. For example, a high-end high-

speed IR camera such as a Telops FAST M100k at its fastest frame-rate of 120 kHz has a resolution limited to 64x2 pixels, thus reducing somewhat the main advantage of global methods: spatial resolution. In addition, radiation from the flow itself can pose significant challenges to the use of IR thermography in pulse-flow facilities [101].

CHAPTER 3

Development of the Diamond Heat Transfer Gauge

Contents

3.1 Introduction **30**
3.2 Design Objectives **31**
3.3 Review of Existing Diamond-Based Heat Transfer Gauges . . **33**
3.4 Analysis of a One-Dimensional Calorimeter Gauge **34**
3.5 Theoretical Calorimeter Design **38**
3.6 Mechanical Design **46**
3.7 Evaluation of DHTG Performance **50**
3.8 Heat Flux Measurement Uncertainty **56**
3.9 Chapter Summary **59**

3.1 Introduction

This chapter presents the design and development of a new heat flux gauge, the Diamond Heat Transfer Gauge (DHTG). The DHTG uses a piece of synthetic diamond as a calorimeter, and was created primarily for the measurement of heat fluxes in hypersonic pulse-flow facilities such as Reflected Shock Tunnels and Expansion Tunnels. The chapter begins by

outlining the design objectives which must be achieved if the gauge is to be useful for making heat transfer measurements in pulse-flow facilities, and presents a schematic of the DHTG. This is followed by a review of literature where synthetic diamond is used as a part of a heat transfer gauge, thus introducing the work that the DHTG builds upon. Then, a theoretical analysis of the operation of the DHTG as a one-dimensional slug calorimeter is presented, leading to a data reduction method for the gauge. The detailed design of four types of DHTG, distinguished by the grade of diamond they use and their thickness, including an evaluation of rise-time, amplitude-frequency response, and sensitivity is then presented. Subsequently, the mechanical design and the assembly process are described. Finally, a study using a Finite Element model of the DHTG is used to assess the theoretical heat flux measurement uncertainty due to conceptual error in the application of the data reduction method and uncertainty in material properties.

3.2 Design Objectives

As discussed in Chapter 1, the main challenges to instrumentation in pulse-flow facilities are having sufficient fast rise-time to make measurements within short test-times which can be on the order of tens of microseconds, and being sufficiently robust to survive impacts from metallic particles of diaphragm entrained in the flow. While overcoming these two obstacles, the gauge must also make accurate measurements and not be negatively affected by free electrons and ionised species in the flow. With these requirements in mind, and considering the current state of the art of instrumentation presented in Chapter 2, the following objectives for the design of a new gauge were defined:

1. **Response time:** The sensor should, at minimum, be capable of measuring test-time average heat fluxes in Expansion Tunnels and Reflected Shock Tunnels (RST), where the test-times are on the order of 50 µs to 250 µs and 0.5 ms to 10 ms respectively, although many smaller RSTs have maximum test-times of around 2.5 ms. Ideally, the

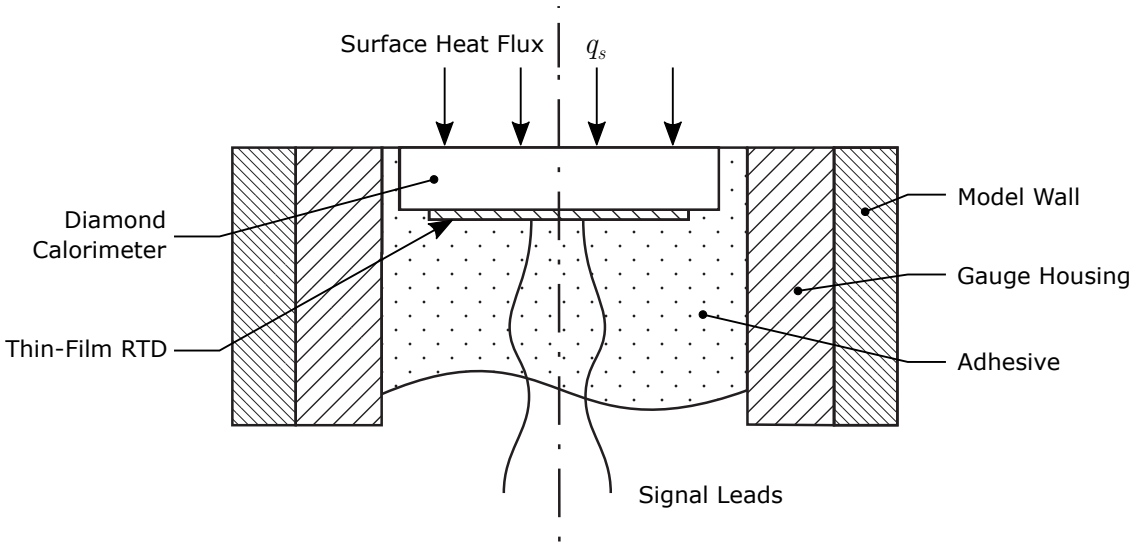


Figure 3.1: Schematic of a DHTG.

sensor should be able to resolve transient heat transfer phenomena during these tests.

2. **Accuracy:** The accuracy of the sensor should be comparable or better than the currently most widely used heat transfer gauges in pulse-flow facilities, surface junction coaxial thermocouples and thin-film gauges which have reported uncertainties in the range 5 % to 11 % (see Chapter 2 for further discussion).

3. **Robustness:** The sensor should last multiple shots without significant damage, or any other need for intervention, on a windward surface or stagnation point in pulse-flow facilities, thus achieving an improvement over thin-film gauges and surface-junction thermocouples which can require re-abrading.

A calorimeter heat flux gauge using a piece of synthetic diamond as the calorimeter and a thin-film resistance-temperature detector (RTD) on the rear surface was identified as a design that might meet the objectives stated above. A schematic of the proposed DHTG design is shown in Fig. 3.1. The following section presents previous studies to develop similar gauges, and the subsequent sections detail the investigation of the design and theoretical performance of the DHTG, with the aim of achieving the design objectives.

3.3 Review of Existing Diamond-Based Heat Transfer Gauges

The first mention in the literature regarding the use of diamond in the construction of a heat transfer gauge is by Follador [102]. The stated aim of this study was to develop a calorimeter gauge for use in hypersonic wind tunnels. However, the focus is on the growth of diamond onto an existing thin-film gauge substrate using the Chemical Vapour Deposition (CVD) process, and no heat flux measurements are presented, nor is an indication of the success of the work as a heat transfer gauge given.

Clark [103] investigated the use of a piece of polycrystalline CVD diamond acting as a protective layer on top of a thin-film gauge to improve robustness in pulse-flow facilities. Two versions were manufactured: The first version consisted of a painted thin-film gauge on a Macor (ceramic) substrate with a 350 µm thick piece of diamond bonded on top. For the second version, the film was sputtered onto the diamond itself. However, the film exhibited poor adhesion and could easily be rubbed off by hand. An interstitial layer of chromium was used which formed a strong bond to the diamond as a result of a layer of chromium carbide. This extra layer lowered the performance of the platinum film as an RTD. Despite the nominal success of the manufacture of both versions of the gauge, an attempt to measure heat flux with them in a low-enthalpy shock tube ($h_0 < 0.5\,\mathrm{MJ{\cdot}kg^{-1}}$) was unsuccessful. However, it is believed that a poor choice of data reduction method was at fault, rather than a fundamental problem with the gauges themselves.

The work of Clark was continued by Vanyai [104], who also manufactured heat transfer gauges by sputtering a platinum thin-film onto a piece of CVD diamond with an interstitial chromium layer. However, no heat transfer measurements using the gauge were presented.

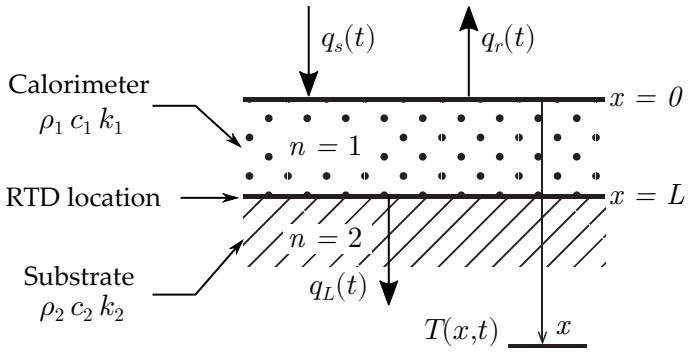


Figure 3.2: Domain for one-dimensional semi-infinite analysis of a calorimeter gauge.

3.4 Analysis of a One-Dimensional Calorimeter Gauge

3.4.1 Calorimeter Data Reduction Equations

This section builds on the review of calorimeter heat transfer gauges given in Section 2.4 to develop a data reduction equation for the DHTG which includes temperature-dependent thermophysical properties and a correction for heat lost through conduction to a semi-infinite substrate. Figure 3.2 shows a simplification of the DHTG schematic in Fig. 3.1 as a one-dimensional two-layer system with a semi-infinite substrate and negligible radial conduction. The first layer is the calorimeter and the second layer is an adhesive substrate. The effect of the RTD, which lies at the interface between the two layers, is not considered because its effect is negligible: the typical thickness of 100 nm is around three orders of magnitude less than the calorimeter layer. For $n = 1, 2$, the equation governing the diffusion of heat through these two layers is:

$$\frac{\partial T_n}{\partial t} = \frac{1}{\rho_n(T_n) c_{p,n}(T_n)} \frac{\partial}{\partial x}\left(k_n(T_n)\frac{\partial T_n}{\partial x}\right) \tag{3.1}$$

Performing an energy balance on the boundaries of layer 1, the net conductive surface heat flux q_s is defined as:

$$q_s(t) = \int_{x=0}^{x=L} \rho_1(T) c_{p,1}(T) \frac{\partial T}{\partial t} dx + q_L(t) + q_r(t) \tag{3.2}$$

where $q_r(t)$ is the radiative heat flux lost to the surroundings, and $q_L(t)$ is the conductive heat flux at the boundary between the two layers. With certain types of calorimeter design it may be possible to make temperature measurements inside the calorimeter, and even at multiple depths, but for the case of the DHTG it is only feasible to measure the temperature on the rear surface of the diamond calorimeter at $x = L$. To make use of Eq. (3.2) with a single temperature measurement, T_L, an assumption that the measured temperature is equal to the mean temperature of the calorimeter must be made:

$$T(L,t) = T_L = \int_{x=0}^{x=L} T(x,t) dx = \overline{T} \tag{3.3}$$

and therefore by definition:

$$\frac{dT_L}{dt} = \frac{d\overline{T}}{dt} \tag{3.4}$$

The radiative loss term q_r can be neglected because short test-times in pulse flow facilities mean absolute temperature rises of model surfaces and gauges are small, typically less than 100 °C, resulting in radiative losses orders of magnitude smaller than incident heating. Introducing the standard notation of the hat operator to denote an estimated value, the equation for the estimated surface heat flux becomes:

$$\widehat{q}_s = \rho_1(T_L) c_{p,1}(T_L) L \frac{dT_L}{dt} + \widehat{q}_L \tag{3.5}$$

Since the temperature at the interface between the diamond and substrate is known, the heat flux lost into the semi-infinite substrate can be found by applying the semi-infinite analysis presented for a standard thin-film gauge in Section 2.2. An expression for the heat flux loss term q_L can be found following the analysis give in Appendix A.2. The resulting

expression, written in a form applicable to numerical implementation is given as Eq. (3.6), and repeated here for clarity:

$$\widehat{q}_L = \sqrt{\frac{\rho_2 c_{p,2} k_2}{\pi}} \left[\frac{T_L(t) - T_L(t=0)}{\sqrt{t}} + \int_0^t \frac{T_L(t) - T_L(\tau)}{(t-\tau)^{3/2}} d\tau \right] \tag{3.6}$$

Equations (3.5) and (3.6) provide the calorimeter data reduction equations for the DHTG. Equation (3.6) can be implemented numerically using any of the techniques discussed in Section 2.2, such as the numerical algorithm by Cook and Felderman [44] or the impulse-response processing developed by Oldfield [36].

3.4.2 Transient Error and Rise-Time

The error resulting from the use of the rear surface temperature instead of the mean temperature of the calorimeter in the data reduction equations is given by Eq. (3.7). This is equivalent to the error in measured heat flux for $T = T_L$ if the term in the data reduction equation accounting for losses from the calorimeter is accurate, i.e. if $\widehat{q}_L = q_L$.

$$e_q = \left(\frac{dT_L}{dt} - \frac{d\overline{T}}{dt} \right) \Big/ \frac{d\overline{T}}{dt} \tag{3.7}$$

An analysis given in Appendix A leads to an expression for $dT(x,t)/dt$, which can be used to evaluate Eq. (3.7). Note that the equivalent equations in Schultz and Jones [30] contain typographical errors. Figure 3.3 shows e_q evaluated using Section A.3.2 in response to a step in surface heat flux against non-dimensional time (Fourier Number, $Fo = \alpha t / L^2$). The error for four values of a is shown, where a is the ratio of the thermal effusivity of the calorimeter to substrate, i.e. $a = \sqrt{\rho_2 c_{p,2} k_2} / \sqrt{\rho_1 c_{p,1} k_1}$. Increasing a represents increasing the thermal effusivity of the substrate while holding the calorimeter properties constant. A substrate with a higher thermal effusivity removes heat more effectively from the calorimeter.

Immediately following the step in heat flux at $t = 0$, the gradient error for the rear surface is arbitrarily large and negative because the rear surface temperature takes time to

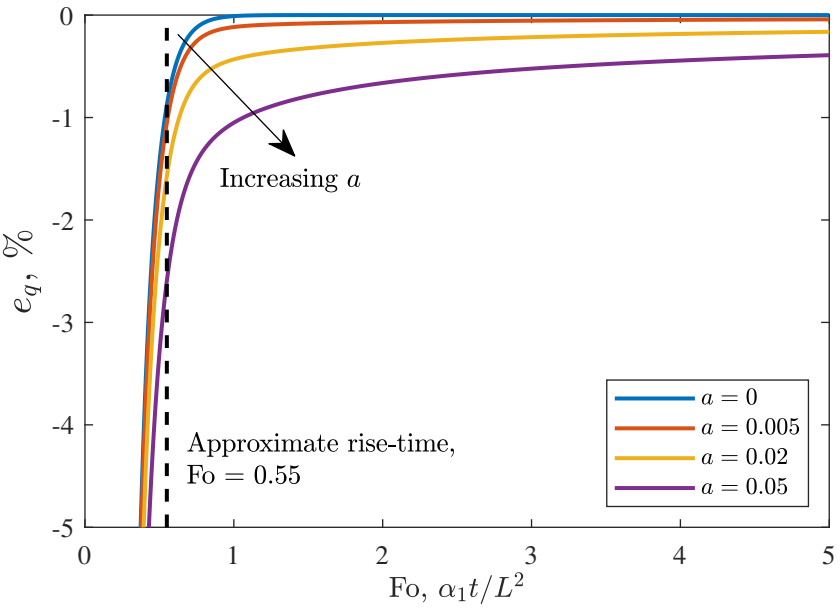


Figure 3.3: Rear surface temperature gradient error plotted against non-dimensional time for increasing substrate thermal effusivity.

respond to the heat flux applied at the surface. For all values of a the error asymptotes to zero, however the response is faster for smaller values, meaning the response is faster for substrates with a comparatively lower thermal effusivity. A rule-of-thumb for the rise-time, defined as the approximate time taken to reach 99 % of the steady state value, is given by Eq. (3.8) and is also marked on Fig. 3.3. Following a similar analysis, but assuming losses from the calorimeter to the substrate are not accounted for in a data reduction scheme, Schultz and Jones [30] give slightly faster estimation of $Fo = 0.5$. The rule given by Eq. (3.8) increasingly under-predicts the rise-time of gauges with larger values of a.

$$\tau_r \approx 0.55\frac{L^2}{\alpha_1} = 0.55L^2\left(\frac{\rho_1 c_{p,1}}{k_1}\right) \tag{3.8}$$

Equation (3.8) leads to intuitive conclusions about the design of a calorimeter gauge: to minimise response time, the thickness of the calorimeter should be minimised and the thermal diffusivity of the calorimeter material should be maximised. However, as one of the design objectives is to improve durability, the relationship between thickness and robustness

must also be considered. Exploring this relationship is one of the aims of the experiments presented in Chapters 6 to 7. With these conclusions in mind, the next section presents the material properties and design of the four types of DHTG.

3.5 Theoretical Calorimeter Design

This section describes the design of the DHTG based on the theoretical performance of a calorimeter gauge. Firstly, material properties are given for synthetic diamond and adhesive substrates, followed by the definition of the four types of DHTG. Finally, an analysis of the amplitude-frequency response and the sensitivity of the DHTG is presented.

3.5.1 Material Properties

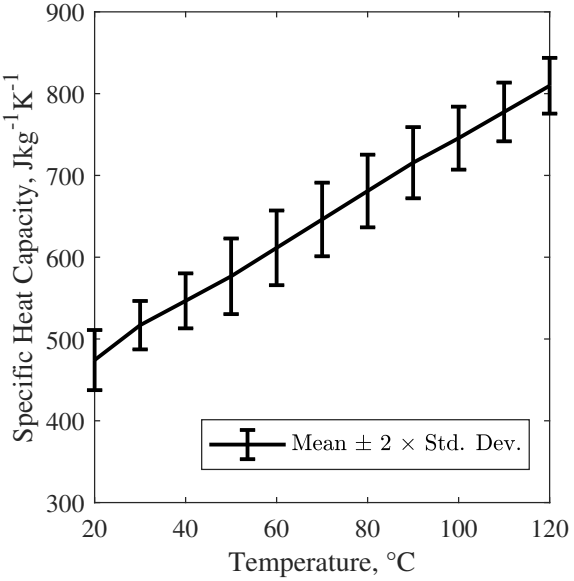
The room temperature thermophysical properties of three grades of synthetic diamond are given in Table 3.1. For reference, the properties of copper (Cu) are also shown because it has been used for calorimeter gauges described in the literature (e.g. Palmer [73]). The three grades of diamond are all produced by the Chemical Vapour Deposition (CVD) process. Single Crystal Diamond (SCD), as the name suggests, consists of a single crystal structure. Transparent Polycrystalline (TPCD) and Opaque Polycrystalline Diamond (OPCD) have microstructures made up of multiple crystals, with OPCD having a finer grain structure than TPCD. The crystal size of OPCD makes it opaque in the visible spectrum and appear black in colour. Additionally, as the grain size of diamond increases, moving from OPCD to TPCD and finally SCD, the thermal conductivity increases.

The specific heat capacity is constant across all grades of diamond [109, 106], and is shown in Fig. 3.4a as a function of temperature, given as the mean and a 95 % confidence interval based on multiple sources in the literature. The confidence interval is roughly constant at ± 7 % across the temperature range shown. Thermal conductivity is also a strong function of temperature, as shown in Fig. 3.4b. The density of diamond is not plotted because it shows

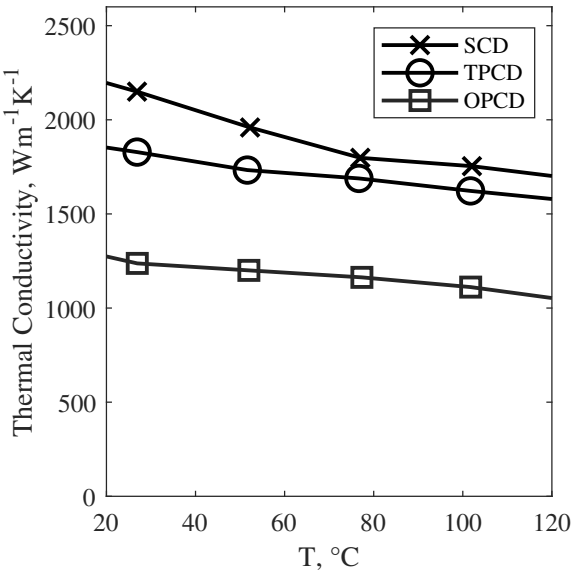
Table 3.1: Thermal properties of possible calorimeter materials at 20 °C [105, 106, 107, 108].

Material	ρ, kg·m^{-3}	c_p, J·kg^{-1}·K^{-1}	k, W·m^{-1}·K^{-1}	α, m^2·s^{-1}	$\sqrt{\rho c_p k}$, J·m^{-2}·K^{-1}·s$^{-1/2}$
SCD	3514	495	2195	1265×10^{-6}	61 800
TPCD	3514	495	1852	1064×10^{-6}	56 800
OPCD	3514	495	1274	732×10^{-6}	47 100
Copper	8960	385	380	11×10^{-6}	36 200

insignificant temperature dependence over the range of interest and is constant to within 1 % across many grades of synthetic diamond [106].



(a) The temperature-dependent mean and uncertainty of specific heat capacity from Refs. [105, 109, 110, 111, 112, 106].



(b) Thermal conductivity [107].

Figure 3.4: Variation of specific heat capacity and thermal conductivity with temperature for CVD diamond.

Thermophysical properties of four adhesives are given in Table 3.2. These adhesives were identified as possible candidates for use in the manufacture of DHTGs based on adhesion to diamond and steel, ease of use in the assembly process, low thermal effusivity, and maximum operating temperature. Details of the adhesive used in each individual DHTG are given in Table B.1.

Table 3.2: Thermal properties of adhesive substrate materials used in construction of DHTGs.

Material Property	ρ, kg·m^{-3}	c_p, J·kg^{-1}·K^{-1}	k, W·m^{-1}·K^{-1}	$\sqrt{\rho c_p k}$, J·m^{-2}·K^{-1}·s$^{-1/2}$	Degrad. Temp., °C
Araldite 5861[113]	1170	1100	0.22	532	80
EPO-TEK H77 [114]	2331	1100	0.70	1340	405
Permabond ES550 [115]	1500	1100	0.55	953	200
Ceramabond 670 [116]	1875	1000	1.0	1370	1650

3.5.2 DHTG Types

Figure 3.5 shows the 99 % rise-time of calorimeters as a function of thickness, calculated using Eq. (3.8) with the thermophysical properties of the three grades of synthetic diamond and copper given in Table 3.1. For a given thickness of calorimeter, using any grade of synthetic diamond can give order-of-magnitude reductions in response time. From this analysis, the four types of DHTG given in Table 3.3 were defined, with thicknesses spanning 75 µm to 325 µm, and response times spanning 2.4 µs to 54.4 µs. The response times of each type of DHTG are also indicated on Fig. 3.5.

Comparing the rise-times given here to the test-times of pulse-flow facilities, Type 1 and Type 4 DHTGs able to measure heat fluxes in the shortest of expansion tube test-times which may only be tens of microseconds. The thicker two types of DHTG, Type 2 and Type 3, are able to measure heat fluxes in longer duration expansion tubes, and all four types are able to make transient measurements in Reflected Shock Tunnels. Experiments presented in this thesis use Types 1, 2 and 3. Type 4 DHTGs have been manufactured and used to make measurements in low-enthalpy hypersonic facilities [117], but results from these studies is beyond the scope of this thesis and are therefore not presented.

3.5.3 Amplitude-Frequency Response

The ratio of measured heat flux to incident surface heat flux as a function of frequency, otherwise known as the amplitude-frequency response, provides insight into how useful the

Table 3.3: Details of the four types of DHTG.

DHTG Type	Diamond thickness, µm	Diamond Type	τ_r, µs[(a)]	DHTG Numbers
Type 1	150	TPCD	11.6	1 – 5, 16, 17
Type 2	220	OPCD	36.3	6 – 10, 19, 23 – 25, 29, 31, 32
Type 3	325	TPCD	54.4	11 – 15, 18, 20, 26 - 28, 30, 33
Type 4	75	SCD	2.4	21, 22

[(a)] Estimated response times calculated using Eq. (3.8).

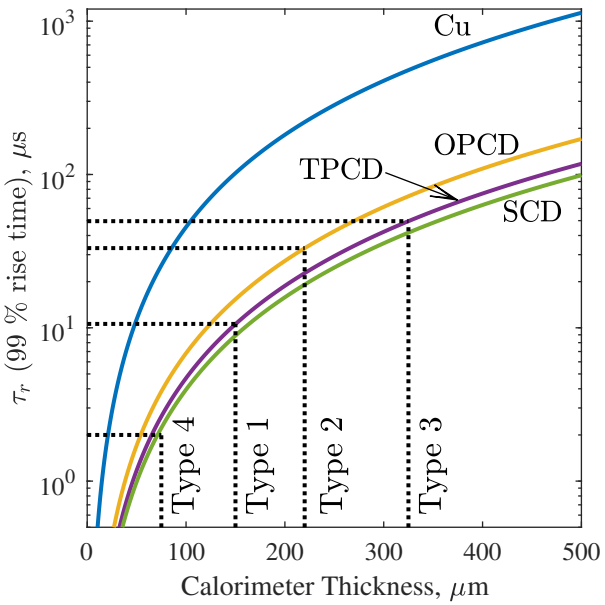


Figure 3.5: The approximate rise-time of an ideal calorimeter at room temperature as a function of thickness for the material properties shown in Table 3.1.

gauge will be in applications where measurement of phenomena at specific frequencies is of interest. Denoting the Laplace transform in general as $\mathscr{L}(f(t)) = \mathscr{F}()$, and taking the Laplace transform of the calorimeter equation for surface heat flux (Eq. (3.5)), with the expression for $\widehat{q}_{loss}$ in Eq. (A.17), gives:

$$\widehat{\mathcal{Q}}_s = \rho_1 c_{p,1} L s \mathscr{T}_L + \sqrt{\rho_2 c_{p,2} k_2} \sqrt{s} \mathscr{T}_L \tag{3.9}$$

Substituting the expression for T at $x = L$ from Eq. (A.13) or Eq. (A.14) and rearranging gives:

$$\frac{\widehat{\mathcal{Q}}_s}{\mathcal{Q}_s} = \frac{2\sqrt{\alpha_1}\left(\rho_1 c_{p,1} L s + \sqrt{s}\sqrt{\rho_2 c_{p,2} k_2}\right)}{k_1\sqrt{s}\left((1+a)\exp(L\sqrt{s/\alpha_1}) + (1-a)\exp(-L\sqrt{s/\alpha_1})\right)} \tag{3.10}$$

Moving from the Laplace domain to the Fourier domain ($s \to j\omega$) and taking the magnitude of Eq. (3.10) gives the amplitude-frequency response shown in Fig. 3.6 for the four types of calorimeter in Table 3.3. The response is shown for both an insulating substrate ($a = 0$) and for the properties of an epoxy (Permabond ES550) substrate. The value of a ranges between 0.0217 and 0.0285 depending on the grade of diamond, with SCD (i.e. Type 4 DHTG) having the lowest value of a, and TPCD(i.e Type 3 DHTG) having the highest.

It is common to define the bandwidth of a system as the frequency at which the amplitude response drops to $-3\,\mathrm{dB}$ ($\widehat{q}_s/q_s = 0.707$ of the peak value). This cut-off is useful for comparison and characterisation of a gauge, but is essentially arbitrary. In the context of measuring surface heat flux, if the magnitude of an oscillating signal is to be measured accurately, a criterion of $\widehat{q}_s/q_s = 0.99$ is more appropriate. These two criteria are shown on Fig. 3.6, and the values of the cut-off points are shown in Table 3.4. For the 99 % criterion, the effect of the substrate is more significant. The use of a substrate with a higher thermal effusivity would reduce these values further.

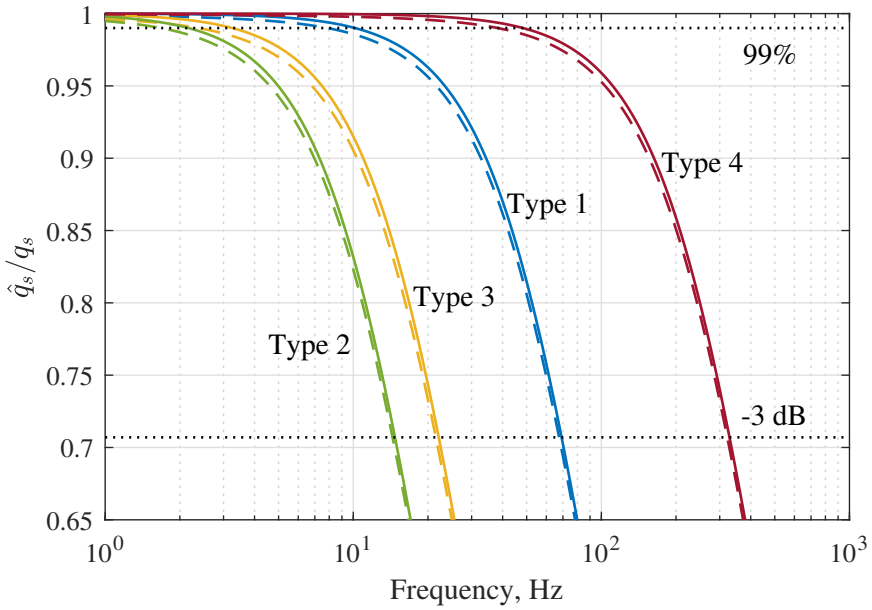


Figure 3.6: The ratio of measured heat flux to actual heat flux as a function of frequency for the four types of DHTG in Table 3.3, using material properties at room temperature. Solid lines are for a perfectly insulating substrate, dashed lines are for an epoxy substrate.

Table 3.4: Amplitude-frequency response cut-off frequency for two criteria, with and without an epoxy substrate (Permabond ES550).

	-3 dB (kHz)		99 % (kHz)	
DHTG Type	No substrate	With substrate	No substrate	With substrate
Type 1 (150 µm)	69.1	67.6	10.2	7.9
Type 2 (220 µm)	22.1	21.5	3.2	2.3
Type 3 (320 µm)	14.7	14.4	2.2	1.7
Type 4 (75 µm)	328.5	321.8	48.34	38.27

3.5.4 Sensitivity

Sensitivity of any measurement technique is an important design parameter which defines the magnitude of the measured response per unit input. For a heat transfer gauge, improving sensitivity improves the Signal-to-Noise Ratio (SNR) by increasing the temperature response to given surface heat flux. This can be especially important for short-duration facilities where absolute temperature rises are small, and interference noise from vacuum pumps and other electrical equipment can be significant.

The calorimeter data reduction equation contains the derivative of temperature with respect to time, so the temperature sensitivity is a function of the thermal capacity of the calorimeter, the substrate properties, and frequency. Rearranging Eq. (3.9), the Laplace transform of the data reduction equation, gives:

$$\frac{\mathscr{T}_L}{\widehat{\mathcal{Q}}_s} = \frac{1}{\rho_1 c_{p,1} L s + \sqrt{\rho_2 c_{p,2} k_2}\sqrt{s}} \tag{3.11}$$

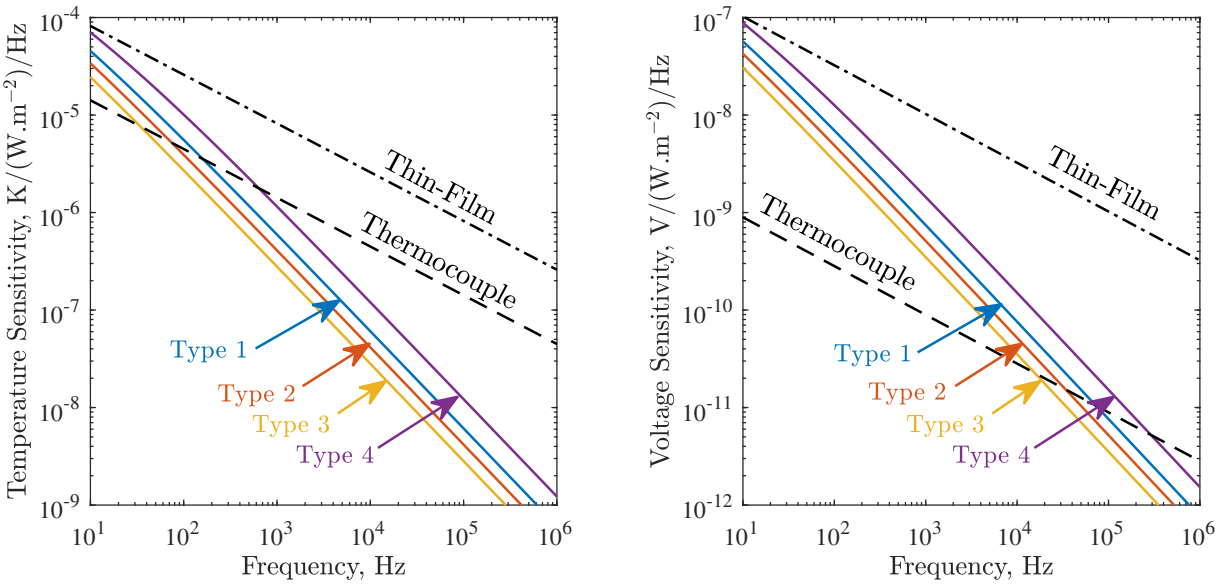
For a calorimeter with an insulating substrate, the temperature sensitivity scales inversely with the thermal capacity of the calorimeter, i.e. $\propto 1/(\rho_1 c_{p,1} L)$. Fortunately, this means that maximising sensitivity and minimising the rise-time of a calorimeter gauge are not competing design aims. For a substrate that is not perfectly insulating, the sensitivity is maximised by minimising its thermal effusivity $\sqrt{\rho_2 c_{p,2} k_2}$.

Figure 3.7a shows the temperature sensitivity for the four types of DHTG given in Table 3.3 as a function of frequency, i.e. using Eq. (3.11) with $s \to j\omega$. The properties of Permabond ES550 epoxy (see Table 3.2) are used for the substrate. The temperature sensitivity of a quartz-based thin-film gauge and Type-E surface-junction thermocouple are also shown, calculated by substituting $L = 0$ into Eq. (3.11) and using typical values of thermal effusivity from the literature: $\sqrt{\rho_2 c_2 k_2} = 1540\,\mathrm{J{\cdot}m^{-2}{\cdot}K^{-1}{\cdot}s^{-1/2}}$ for a quartz thin-film gauge [43] and $\sqrt{\rho_2 c_2 k_2} = 8900\,\mathrm{J{\cdot}m^{-2}{\cdot}K^{-1}{\cdot}s^{-1/2}}$ for a Type-E thermocouple [56].

As frequency increases, the sensitivity of all types of gauge decreases. The sensitivity of

the DHTGs decays at double the rate of the thin-film and surface-junction thermocouple for the frequency range shown because Eq. (3.11) is dominated at high frequencies by the $1/s$ term for the calorimeter while for the thin-film and thermocouple it is dominated by the $1/\sqrt{s}$ term. In the 10 Hz to 100 Hz range the influence of the substrate on the sensitivity of the DHTGs is just noticeable as a deviation from the straight line trend. The thin-film gauge is shown to have the highest temperature sensitivity across the frequency range shown and the thermocouple is shown to have higher temperature sensitivity than all types of DHTG at frequencies above 1 kHz.

In an experiment, it is voltage that is recorded, and therefore the voltage sensitivity that is the important factor when considering experimental signal-to-noise ratios. Figure 3.7b shows the voltage sensitivity of the same gauges as in Fig. 3.7a, calculated using typical values for the temperature-to-voltage sensitivity: $1.25\,\mathrm{mV{\cdot}K^{-1}}$ for the RTD used by the thin-film gauge and the DHTGs [51], and $62.5\,\mu\mathrm{V{\cdot}K^{-1}}$ for the Type-E thermocouple. A significant change in relative sensitivity between the DHTG and thin-film gauge, and the surface-junction thermocouple is seen because the temperature-to-voltage sensitivity of the thermocouple is around 20 times lower than an RTD. Given the same experimental noise for all types of gauge, a thin-film gauge has the best SNR across the frequency range shown. DHTGs have superior SNR compared to surface-junction thermocouples up to a limit of 10 kHz for a Type 3 DHTG and 300 kHz for a Type 4 DHTG. This analysis demonstrates the significant advantage of using an RTD over a thermocouple to measure the temperature rise of the diamond in the DHTG, and shows how the DHTG is, up to a limit, a more sensitive measurement technique than surface-junction thermocouples.



(a) Temperature sensitivity.

(b) Voltage sensitivity.

Figure 3.7: Sensitivity of the four types of DHTG compared to a typical thin-film gauge on a quartz substrate and a Type-E surface-junction thermocouple.

3.6 Mechanical Design

3.6.1 Calorimeter

A drawing of the calorimeter element of the DHTG is shown in Fig. 3.8. It consists of a disk of CVD diamond with a 100 nm thick track of platinum sputtered on its rear surface, acting as a thin-film RTD. The track was designed to give around 50 Ω resistance at room temperature and to maximise surface coverage of the diamond to provide an average temperature measurement. At the track terminations in the centre of the diamond are two gold pads to which 60 µm gold wires are ball-bonded. Details of the operation and calibration of the RTD element can be found in Appendix D.

As discussed in Section 3.3, previous attempts by Clark [103] and Vanyai [104] to deposit a platinum film directly onto diamond required an interstitial layer of chromium to provide satisfactory adhesion. This was not required for the DHTG. The calorimeter element was

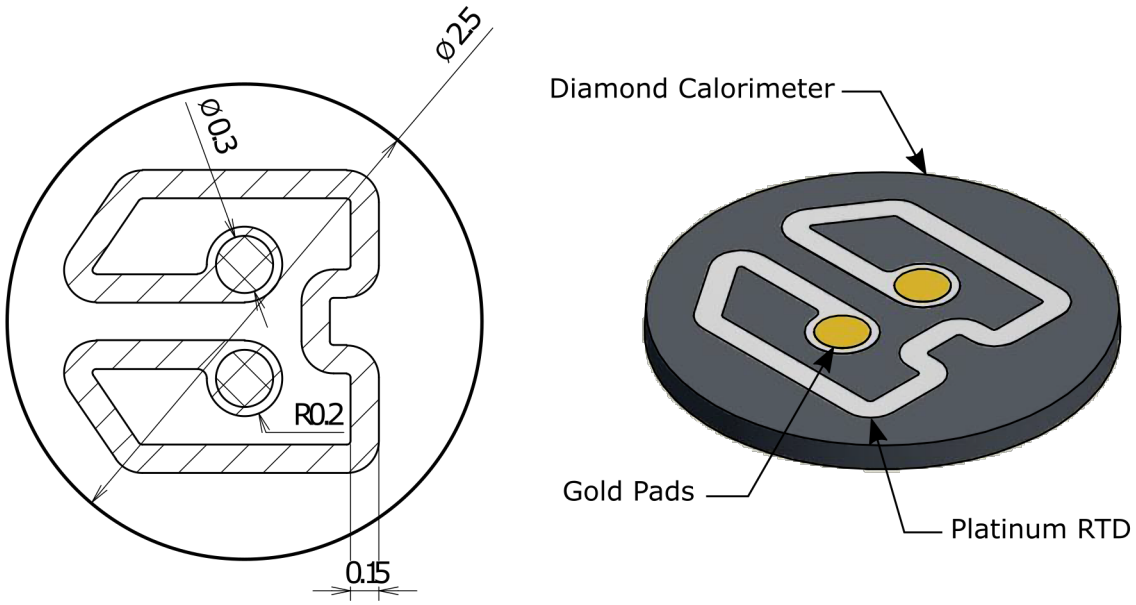


Figure 3.8: Drawing of the diamond calorimeter with dimensions in mm. Dimensions other than thickness are standard across gauge types.

designed in-house, but fabricated by an external manufacturer specialising in the deposition of metallic coatings on diamond, where superior cleaning and surface-finishing processes enabled the direct deposition of the platinum film with more than adequate adhesion.

3.6.2 Housing and Assembly

To produce a DHTG, the calorimeter element described above is bonded into a steel housing using one of the adhesives given in Table 3.2 and signal wires are attached. Details of each DHTG manufactured can be found in Table B.1. Two versions of housing were designed. Cross-sectional drawings and photograph of each version are shown in Figs. 3.9 to 3.10 respectively.

Version 1, used for DHTG numbers A1–A7, 1–22, 29 and 30, is shown in Fig. 3.9a. This version was designed to be installed interchangeably with surface-junction thermocouples in a 4 mm hole to facilitate comparative measurements. The small package size proved difficult to manufacture, and robustness issues arose with the electrical cable junction at the rear of

the gauge during installation for experimental testing. Gauges produced with this design of body later incorporated the epoxy stem seen in Fig. 3.10a which extended beyond the back of the steel body, acting as a cable strain relief.

Version 2, used for DHTG numbers 23–28 and 31–33, was designed around PCB 113-series piezoelectric pressure transducers which are used extensively in pulse-flow facilities. This design greatly improves the ease of use by making the two interchangeable in models and tunnel walls. Additionally, the Version 2 housing features an internal chamfer, designed to minimise the area of adhesive exposed to the flow, while simultaneously minimising lateral conduction from the diamond to the steel housing by providing a greater thickness of adhesive separating the two.

The assembly process follows these steps:

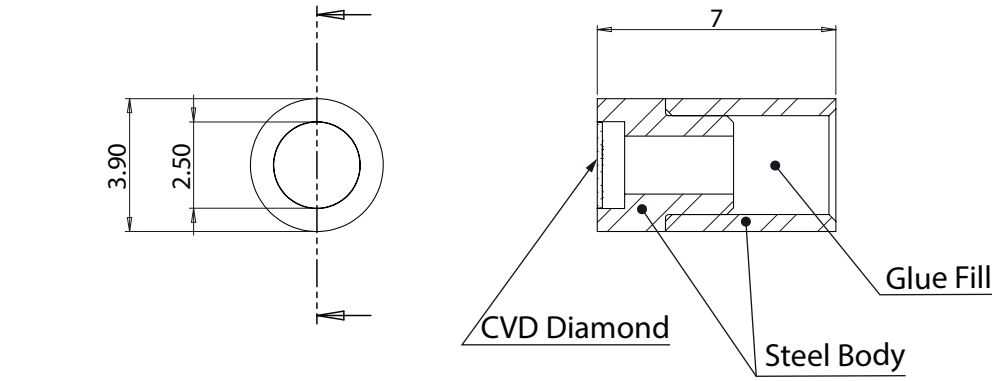
1. The calorimeter element, consisting of the diamond, the thin-film, and its gold wires, is potted using the selected adhesive (see Table 3.2) in the front section of housing;

2. Larger diameter electrical leads are soldered onto the gold leads at low temperature ($<$280 °C);

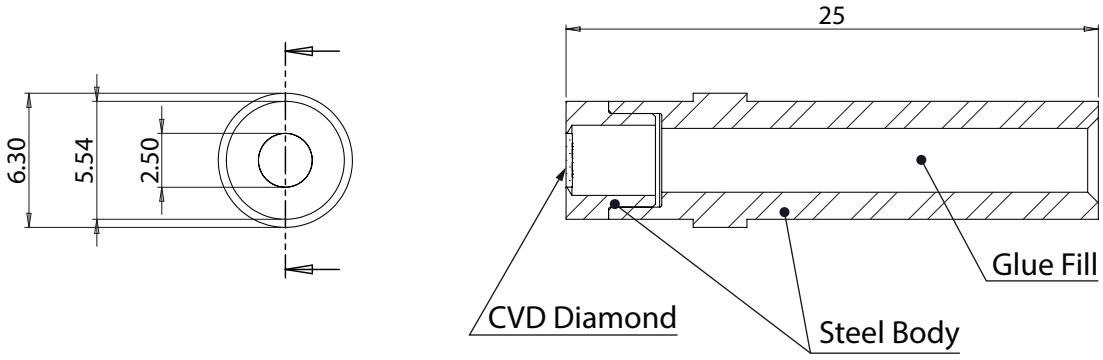
3. The rear section of housing is slid onto the assembly;

4. The internal bore is back-filled with adhesive.

The maximum operating temperature of a DHTG is limited by two criteria: 1) the maximum operating temperature of the adhesive used, as given in Table 3.2; and 2) the solder joint between the gold leads and the signal wires, which will melt at 280 °C due to a eutectic formed by gold and tin. Because the solder joint is located at a depth inside the gauge whereas the adhesive is located near the surface, which of these conditions is the limiting factor depends on the thermal penetration depth, and therefore the test-duration.



(a) Version 1.



(b) Version 2.

Figure 3.9: Drawings of version 1 and version 2 of the DHTG housing.



(a) Version 1 housing, DHTG20.



(b) Version 2 housing, DHTG26.

Figure 3.10: Photographs of the two versions of the DHTG sensor with the serpentine platinum RTD track visible through the transparent PCD diamond calorimeter layer in both.

3.7 Evaluation of DHTG Performance

In the preceding sections, the performance of a calorimeter gauge has been investigated analytically using one-dimensional assumptions, resulting in data reduction equations and estimates of response time for the DHTG. As the physical DHTG is not one-dimensional, there exists a conceptual error in the application of the data reduction equations which is quantified in this section.

In this section, transient heat conduction through a two-dimensional axisymmetric Finite Element (FE) model of all four types of DHTG are modelled using Comsol Multiphysics [118]. From the temperature response to a step in surface heat flux, the data reduction equations Eq. (3.5) and Eq. (3.6) are used to estimate the surface heat flux with the same thermophysical properties and calorimeter thickness as used in the FE model. The estimated heat flux is then compared to the applied heat flux, revealing the conceptual error from the data reduction method. Because the studies of each type of DHTG are very similar, differing only in calorimeter thickness and material, details are given for the Type 1 DHTG in greater depth, and then the final results are compared for all types.

3.7.1 Finite Element Model

Figure 3.11 shows the simulation domain for the Type 1 DHTG, with material regions labelled. The domains for Type 2–4 differed only in the diamond thickness and thermal conductivity, resulting from the different grade of diamond. The axis of symmetry is at $r = 0$. The two 60 µm diameter gold signal wires in the real DHTG are modelled as a single wire of 84.85 µm, thus preserving cross-sectional area. The thermophysical properties used are given in Table 3.5. A constant heat flux of $1\,\mathrm{MW{\cdot}m^{-2}}$ was used as the boundary condition across the entire top surface of the domain and a simulation duration of 10 ms was chosen, adequately covering the typical test-duration of both reflected shock tunnels and expansion tunnels.

Table 3.5: Thermophysical properties used in the FE study.

Region	ρ, kg·m^{-3})	c_p, J·kg^{-1}·K^{-1}	k, W·m^{-1}·K^{-1}
Steel [119]	7850	475	44.5
Epoxy[(a)]	1500	1100	0.55
Diamond[(b)]	3514	$c_p(T)$	$k(T)$
Gold [119]	19 300	129	314.0

[(a)] Properties of Permabond ES550, see Table 3.2.
[(b)] Dependent on diamond type and temperature see Section 3.5.

The thermal penetration depth x_p into the gold lead at the end of the simulation was estimated to be 2.0 mm using the equation $x_p = 4\sqrt{\alpha t}$ [30], where $t = 10$ ms. Only this depth below the diamond layer was modelled, and an adiabatic boundary condition was applied on the rear surface. Similarly, an adiabatic boundary condition was used on the surface at $r = 2$ mm because the radial thermal penetration depth through the steel is less than the radial thickness of this region at the end of the test time.

The mesh consisted of 15,500 triangular elements, with a higher density in the diamond region and towards the top surface of the gauge. Mesh convergence was demonstrated by doubling the number of elements and observing less than a 0.1 % change to both the peak magnitude of the temperature response and the peak magnitude of the time derivative of the temperature response on the rear surface of the diamond layer.

3.7.2 Temperature Response

The surface integral of temperature across the front and rear sides of the diamond from the FE simulation of the Type 1 DHTG are plotted in Fig. 3.12. For this simulation, the difference in temperature across the diamond layer does not exceed 0.05 K. The largest temperature difference was seen for the Type 3 DHTG, where the difference was 0.11 K. The spatial difference in diamond properties is therefore negligible, and the assumption that $T_L = \overline{T}$ used to derive the data reduction equations is valid.

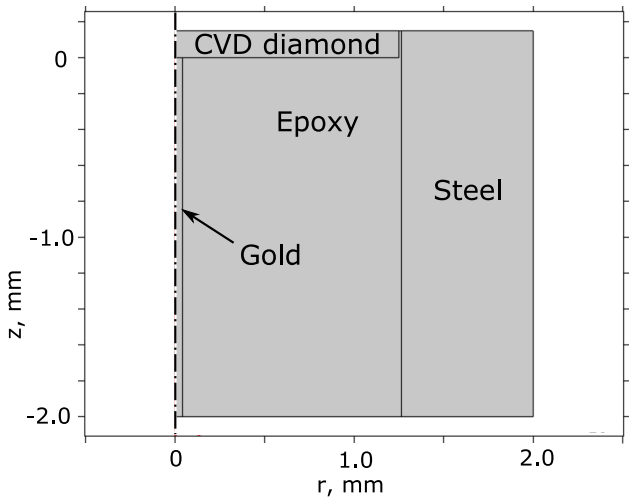


Figure 3.11: The simulation domain for the Type 1 DHTG with material regions labelled.

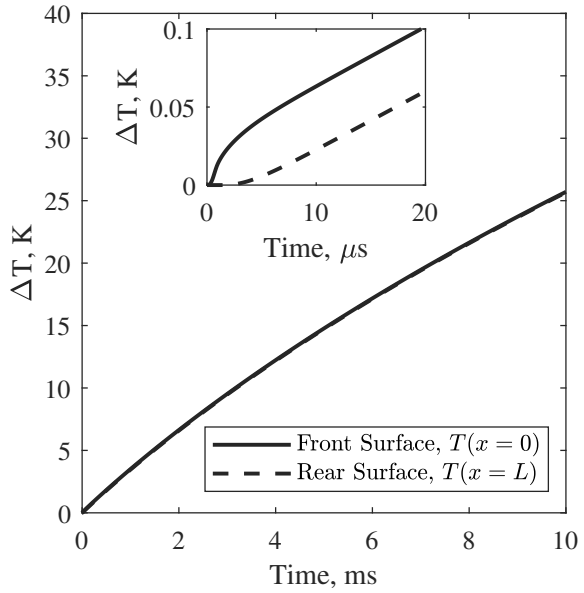


Figure 3.12: Spatially averaged temperature rise across the front and rear surface of the diamond layer in the FE model, in response to a $1\,\mathrm{MW{\cdot}m^{-2}}$ step in heat flux applied at the surface.

3.7.3 Heat Flux Results

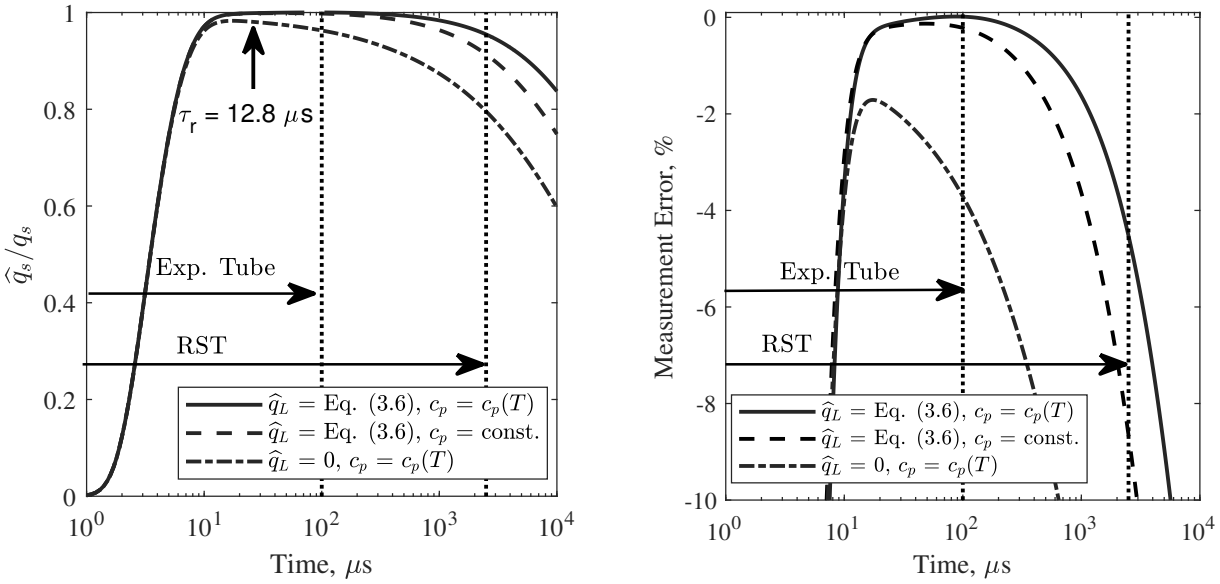
The estimated ("measured") surface heat flux $\widehat{q}_s$ was found by substituting the rear surface temperature rise from the FE model into the calorimeter data reduction equations, Eq. (3.5) and Eq. (3.6), with the diamond and substrate layer material properties given in Table 3.5. Detailed results are given for the Type 1 DHTG, followed by results and conclusions for all types.

3.7.3.1 Results for a Type 1 DHTG

For the Type 1 DHTG, Fig. 3.13a shows the estimated heat flux $\widehat{q}_s$ normalised by the applied heat flux q_s, and Fig. 3.13b shows the relative error between the two which is referred to as the measurement error. A typical expansion tube test time of 100 µs and shorter RST test time of 2.5 ms are indicated, although a longer RST test-time may be up to the full 10 ms shown. On both plots, three heat flux solutions are shown, each calculated using variant of the calorimeter data reduction method.

One heat flux solution is calculated using temperature dependent diamond properties and Eq. (3.6) to account for losses from the calorimeter to the semi-infinite substrate. After the initial rise-time, the estimated heat flux is shown to be accurate to within 0.2 % for the expansion tunnel test-time, and 4.5 % for the 2.5 ms RST test-time indicated. For longer test-durations, the accuracy deteriorates rapidly to more than 10 %. The error grows with time because only losses through axial conduction are accounted for in the data reduction method, but losses due to lateral conduction are also present in the FE model. Additionally, apart from a thin layer of adhesive, the lateral conduction is into steel, which has a significantly higher thermal effusivity than the adhesive, meaning it conducts heat away from the diamond more effectively, thus contributing to the measurement error.

A second heat flux solution uses the same correction for losses as the blue line, but with constant diamond thermophysical properties, fixed at the starting temperature. Significant



(a) Normalised by applied heat flux.

(b) Relative measurement error.

Figure 3.13: The estimated heat flux for the Type 1 DHTG, calculated from the rear surface temperature rise shown in Fig. 3.12.

measurement error is introduced if the change of specific heat capacity with temperature is not accounted for. The third heat flux solution is calculated with temperature-dependent diamond properties but with no correction for any losses from the calorimeter, demonstrating the importance of correcting for losses, even on short time-scales.

3.7.3.2 Results for All DHTG Types

The data reduction error for all four types of DHTG is shown in Fig. 3.14, calculated using temperature-dependent specific heat capacity for the diamond and Eq. (3.6) to correct for conductive losses. The same typical test-times which were indicated for the Type 1 DHTG results in Fig. 3.13 are also given here. Additionally, horizontal lines indicating -1 % and -5 % error are shown.

The time during which the transient measurement error is less than -1 % and -5 % is used to define the two operating windows for each type of DHTG given in Table 3.6. For 1 % level of accuracy, the DHTGs have maximum test-times of 520 µs to 720 µs, covering use

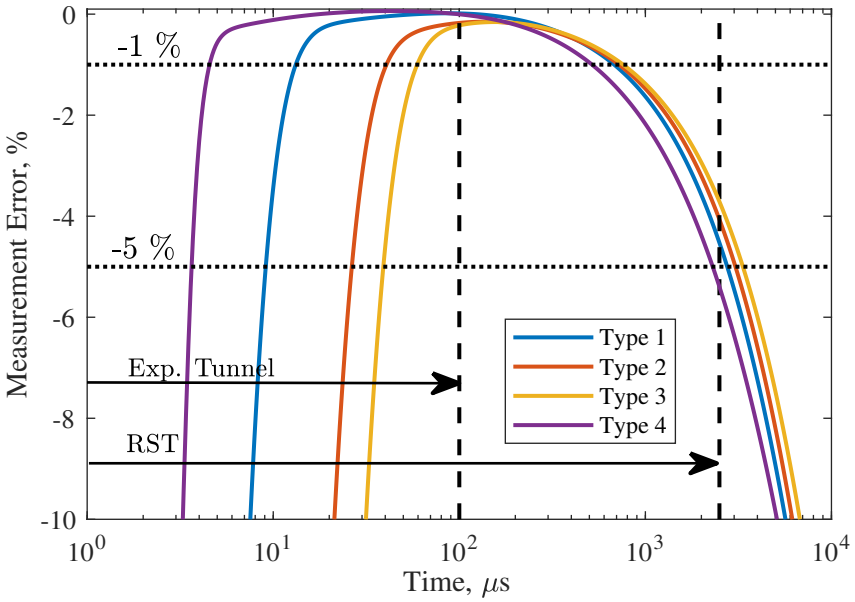


Figure 3.14: Relative measurement error for all four types of DHTG in response to a $1\,\mathrm{MW{\cdot}m^{-2}}$ step in surface heating.

in expansion tunnels but only the shortest of RST test-times. For a 5 % level of accuracy, a 2.5 ms test-time is covered, but for longer test-times the error increases rapidly. The values found for the start of the 1 % window indicate slightly slower rise times than those given in Table 3.3. However, Eq. (3.8) used to calculate those values is a rule-of-thumb, and therefore exact agreement is not expected.

As mentioned above in the discussion of the Type 1 DHTG results, the long-term error is dominated by radial conduction into the steel body. For this reason, the useful windows given here, which were calculated from models of DHTGs with Version 1 housings serves as a conservative estimate for Version 2 housings, where there is a thicker layer of adhesive between the diamond and steel.

The analysis presented in this section is based on the response to a step in heat flux, so to determine the applicability of a DHTG for a given application should be used in conjunction with the amplitude-frequency response analysis presented in Section 3.5.3.

Table 3.6: rise-time estimated from the FE model compared to the estimate calculated using Eq. (3.8).

DHTG Type	1 % Window	5 % Window
Type 1 (150 µm)	12.8 µs to 680 µs	9.1 µs to 2760 µs
Type 2 (220 µm)	40.5 µs to 720 µs	26.3 µs to 3080 µs
Type 3 (325 µm)	59.3 µs to 720 µs	39.1 µs to 3640 µs
Type 4 (75 µm)	3.3 µs to 520 µs	2.3 µs to 2300 µs

3.8 Heat Flux Measurement Uncertainty

The previous section presented an evaluation of the conceptual error of the data reduction method. In this section, the measurement uncertainty from the parameters used in the data reduction equations is estimated, i.e. uncertainty in material properties and the thickness of the calorimeter. The temperature measurement uncertainty is not considered at this point because it depends on the specific experimental set-up, such as amplifiers, the operation of the RTD, and data acquisition systems. In subsequent chapters where experimental measurements are presented, the temperature uncertainty is combined with the results presented here. Additionally, only systematic uncertainty is considered; random uncertainty should be estimated from multiple experimental measurements.

Following the overview of the theory of uncertainty analysis presented in Appendix C, the systematic relative uncertainty is calculated as:

$$\left(\frac{b_{\widehat{q}_s}}{\widehat{q}_s}\right) = \sqrt{\sum_{i=1}^{N}\left(\frac{X_i}{\widehat{q}_s}\frac{\partial \widehat{q}_s}{\partial X_i}\right)^2\left(\frac{b_{X_i}}{X_i}\right)^2} \tag{3.12}$$

where X_i are the fundamental measurements in the data reduction equation, and b_{X_i} are their respective systematic uncertainties. The cross-correlation error term is not present in Eq. (3.12) because the only variable that has correlated systematic errors in the data reduction equation is T_L, but the error in this variable is assumed to be zero. Table 3.7 gives the values of X_i and their respective relative uncertainties for the 95 % confidence interval,

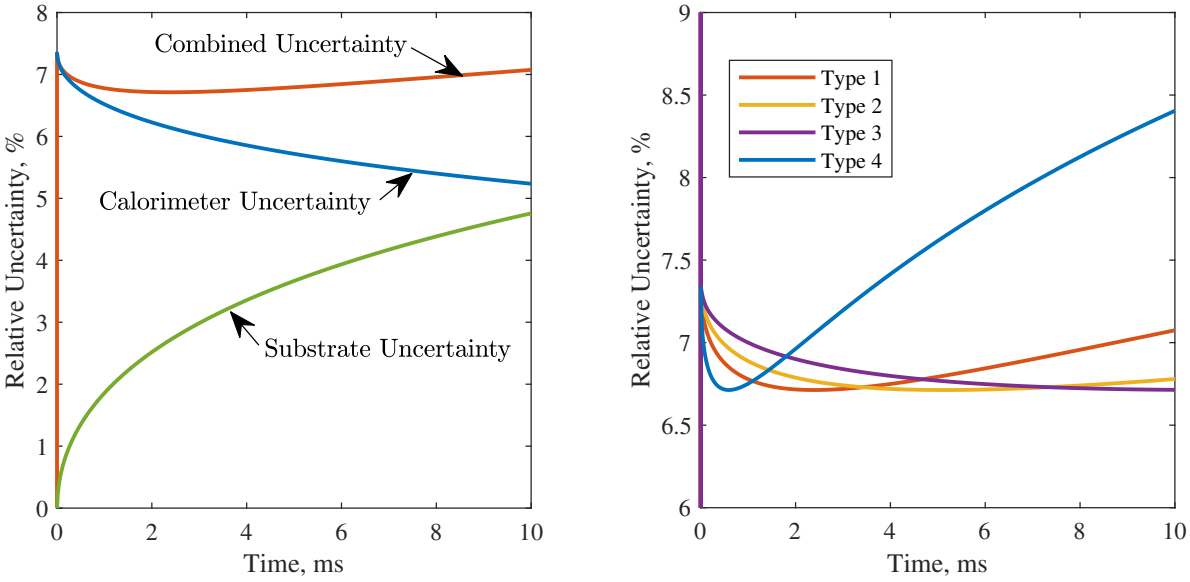
Table 3.7: Systematic uncertainty for each variable in the data reduction equation for heat flux, valid for all types of DHTG.

X_i	Typical Value	Units	Relative Uncertainty, $(\mathcal{X}_{X_i})$, %
ρ_1	3514	$\mathrm{kg{\cdot}m^{-3}}$	2
$c_{p,1}$	$c_{p,1}(T)$	$\mathrm{J{\cdot}kg^{-1}{\cdot}K^{-1}}$	7
L	75 to 325	µm	2
ρ_2	1500	$\mathrm{kg{\cdot}m^{-3}}$	10
$c_{p,2}$	1100	$\mathrm{J{\cdot}kg^{-1}{\cdot}K^{-1}}$	30
k_2	0.55	$\mathrm{W{\cdot}m^{-1}{\cdot}K^{-1}}$	10

i.e. two times the standard deviation [120]. The uncertainty in diamond material properties are presented in Section 3.5. The relative uncertainty in the thickness of the calorimeter was obtained from a sample of measurements and was found to be consistent across types of DHTG. The epoxy material properties given are for Permabond ES550 as this is the adhesive used for the majority of the DHTGs. The material properties provided by manufacturers lack an indication of uncertainty, and therefore an estimate is used. It is assumed that the relative uncertainty in each property is constant across all types of diamond and adhesive. Hence, the same values can be used in the uncertainty analysis for all types of DHTG.

Figure 3.13a showed that the estimated heat flux $\widehat{q}_s$ is time-dependent in response to a step in applied heat flux. Therefore, the measurement uncertainty calculated using Eq. (3.12) is also a function of time. Figure 3.15a shows the measurement uncertainty for the response from the Type 1 DHTG. The overall relative measurement uncertainty, called the Combined Uncertainty, is a result of the uncertainty due to the properties of the calorimeter and properties of the substrate, i.e. the first and second terms in Eq. (3.5) respectively. The calorimeter uncertainty scales with the lumped value of $\rho_1 c_{p,1} L$, calculated to be 7.3 %. The substrate heat flux uncertainty scales with the lumped value of $\sqrt{\rho_2 c_{p,2} k_2}$, calculated to be 17 %.

Immediately following the step in heat flux at $t = 0$, very little heat is lost to the substrate, so the combined uncertainty is dominated by the calorimeter uncertainty, calculated to be



(a) Type 1 DHTG.

(b) All types of DHTG.

Figure 3.15: Measurement uncertainty as a function of time.

7.3 % for all DHTG types. With increased time, as the temperature of the calorimeter rises, the magnitude of the heat flux lost to the substrate increases, and so does its contribution to the combined uncertainty. During the 10 ms shown, the relative uncertainty for the Type 1 ranges from a maximum of 7.3 % to a minimum of 6.7 %.

Figure 3.15b shows the combined relative uncertainty for all four types of DHTG as a function of time. To simplify the reporting of the measurement uncertainty, for DHTG types 1, 2 and 3, the uncertainty over the 10 ms time shown can be conservatively stated as a constant 7.3 %. The actual values are shown to temporarily fall below this, but only by 0.5 %. The measurement uncertainty of the Type 4 DHTG increases rapidly with time. The calorimeter is thinner, meaning that for the same applied heat flux, the temperature rise is larger. This results in a higher conductive heat flux into the substrate and therefore higher substrate uncertainty. However, over the initial 2.5 ms which adequately covers a test-times in smaller RST facilities, it is valid to assume a constant uncertainty of 7.3 %.

Figure 3.16 shows the uncertainty bounds given in Fig. 3.15a superimposed upon the data reduction error presented in Fig. 3.13a for the Type 1 DHTG in response to the ap-

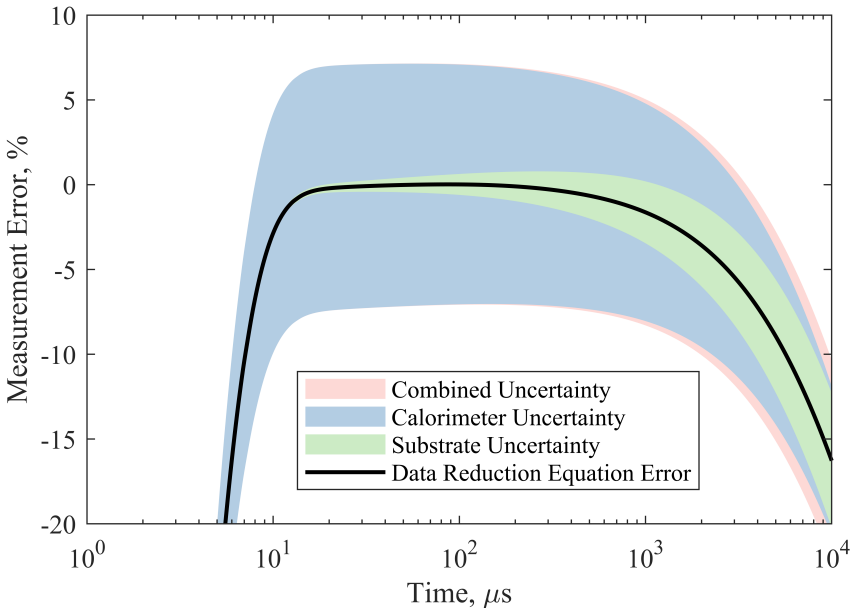


Figure 3.16: Uncertainty superimposed upon data reduction error for the Type 1 DHTG in response to a step in surface heat flux.

plied $1\,\mathrm{MW{\cdot}m^{-2}}$ surface heat flux. This figure illustrates the transient bounds which an experimental measurement of this applied heat flux could be expected to fall between.

3.9 Chapter Summary

This chapter has presented the design and manufacture of a new heat transfer gauge, named the Diamond Heat Transfer Gauge (DHTG). Four types of DHTG have been manufactured using three grades of diamond and thicknesses spanning 75 µm to 325 µm. A one-dimensional model of the gauge is used to provide a data reduction method and to evaluate the rise-time, amplitude-frequency response, and sensitivity of each DHTG type. A two-dimensional axisymmetric FE model of the DHTG was used to evaluate the transient accuracy of the one-dimensional data reduction method.

This chapter began by setting out three objectives for the design of a new heat transfer gauge for use in pulse-flow facilities. Below is a summary of how well the designed DHTGs theoretically achieve these goals.

1. **Response Time:** Based on the one-dimensional heat conduction model, the theoretical response time, amplitude-frequency response, and measurement sensitivity of the gauge have been calculated. The response times, ranging from 2.4 µs to 54.4 µs, are sufficiently fast to make measurements within both shock tubes, expansion tubes, and reflected shock tunnels[1].

2. **Accuracy:** A study using an axisymmetric FE model of all four types of DHTG was used to estimate the transient error associated with the data reduction method. From this, maximum operating windows for the DHTGs were defined. Based on a criteria of less than 1 % error, these are in the range 520 µs to 720 µs. Therefore, for longer duration pulse-flow facilities such as RSTs, an improved data reduction method is required, and is the motivation for the following chapter. The measurement uncertainty resulting from the material properties used is calculated to be 7.3 %, which is competitive with existing instrumentation.

3. **Robustness:** The robustness of the DHTG has not been discussed in this chapter; it requires experimental evaluation and is covered in Chapters 6 and 7.

[1]Type 4 DHTGs have been manufactured and used to make measurements in low-enthalpy hypersonic facilities [117], but results from these studies is beyond the scope of this thesis and are therefore not presented.

CHAPTER 4

Development of an Impulse-Response Based Data Reduction Method

Contents

4.1 Introduction 61
4.2 The Inverse Heat Conduction Problem 62
4.3 The SFSM Algorithm 65
4.4 Obtaining Impulse Response 68
4.5 Comparison of Data Reduction Methods 72
4.6 Chapter Summary 91

4.1 Introduction

In the previous chapter, an analysis of the performance of the DHTG started from the viewpoint of designing a typical calorimeter, for which the the measured heat flux is proportional to the rate of change of temperature of an isothermal slug. In this chapter, the data reduction process for the DHTG is considered more generally by solving what is known as the Inverse Heat Conduction Problem (IHCP). This chapter begins with an introduction to the IHCP and the problem of regularisation. This is followed by the presentation of an

algorithm to solve the IHCP named the Sequential Function Specification Method (SFSM), with a modification to allow for non-linearity due to the temperature dependent thermo-physical properties of diamond. The subsequent section compares the unit impulse response of a DHTG, which is an input required in the SFSM method, found from three models of increasing fidelity on three time-scales representing different types of experimental facility.

The last section of this chapter presents a complete data reduction method for the DHTG, making use of the SFSM algorithm, the L-Curve method to select the optimal regularisation parameter, and the design of an optimal low-pass filter. A Finite Element model of a DHTG is used to provide a mock experimental temperature response to two heat flux profiles which are representative of pulse-flow facilities. Representative noise is added to the signals, and subsequently the estimated heat flux from both the SFSM-based method and the calorimeter-based method (as presented in Chapter 3) are compared.

4.2 The Inverse Heat Conduction Problem

4.2.1 The IHCP

The IHCP is a well-known ill-posed inverse problem in thermal engineering. The topic is covered by a vast amount of literature, but a good overview of the problem is given by Beck [31]. To summarise, the problem involves the determination of a boundary condition of temperature or heat flux when given one or more in-depth temperature measurements. In the context of the DHTG, this means calculating surface heat flux when given the measurement of temperature on the rear side of the diamond calorimeter surface. A well-posed problem is one which satisfies three conditions: existence of solution, uniqueness of solution, and stability of solution to small changes in input. The IHCP is an ill-posed problem, meaning that one or more of these conditions is not met. The first condition, the existence of a solution, is satisfied by considering the physics of the problem: that if a change in temperature is measured then a heat flux must have produced it. The second two conditions, uniqueness

and stability, are not met; solutions are highly sensitive to imperfect data i.e. measurement noise, and any solution is an estimate.

Experimental data is always imperfect to some degree due to contamination from random noise and from electrical interference. Instability in the solution produced by noise is a function of both sampling rate and magnitude: both the fundamental heat diffusion equation (Eq. (3.1)) and the basic calorimeter equation (Eq. (3.5)) show that time differentiation of temperature takes place, thus, increasing sampling rate increases instability. Regularisation is required to stabilise the solution.

4.2.2 Regularisation

The "amount" of regularisation applied, often described by a regularisation parameter R, has a significant impact on the solution. Too little regularisation leads to overly noisy and unstable solutions, while too much regularisation leads to over-smoothed solutions and therefore removes information. The amount of regularisation required depends on the parameters the degree to which the problem is ill-posed. To illustrate this, consider a homogenous slab of material with a heat flux applied at the surface and a single internal temperature measurement. The further from the surface the measurement is made, the more damped the response will be, and so the more ill-posed the problem becomes, thus requiring more regularisation.

The aim of a scheme to find the optimal regularisation parameter is to find a balance between rejecting noise without affecting the signal. An example of a simple regularisation scheme is a low-pass filter: signal content at higher frequencies which contribute more to instability are attenuated more than lower frequency signal content. However, if the cut-off frequency is too low, then signal content will be lost. More complex regularisation schemes all fundamentally have a filtering effect, with the regularisation parameter representing the strength of the filter and cut-off frequency. There are many methods in the literature for finding the optimum regularisation parameter, see for example Refs. [121, 122, 75, 50].

4.2.3 The Forward Problem

Before moving to the inverse problem, the forward problem is discussed. If a surface heat flux is the input to a system, and a measured temperature is the output, then the system is fully defined by its impulse response, h. This is true if the system is Linear and Time-Invariant (LTI). The relationship is defined by the convolution integral:

$$T(t) = q(t) * h(t) = \int_0^t q(\tau)h(t-\tau)d\tau \tag{4.1}$$

This formulation of the problem can be tied to the calorimeter analysis of Chapter 3 by considering the impulse response of an isothermal calorimeter surrounded by a perfect insulator: $h = 1/(\rho c_p L)$. Thus, Eq. (4.1) reduces to Eq. (3.5), which was the heat flux data reduction equation given for a calorimeter without losses.

The forward problem involves solving Eq. (4.1), given the impulse response and a surface heat flux. Following the discrete form of Duhamel's integral, with discretised signals consisting of N components, sampled at intervals of Δt, such that $t_i = t_{i-1} + \Delta t$, the integral can be replaced with a summation, and an equation for the Mth component of temperature calculated from the heat flux history can be written as:

$$T_M = T_0 + \sum_{n=1}^{M} q_n h_{M-n} \Delta t \tag{4.2}$$

The inverse problem, i.e. the IHCP, involves solving Eq. (4.1) for the surface heat flux given a temperature rise. The equation has the form of a Volterra integral of the first kind, where the impulse response is the kernel [75]. This form of integral equation is known to be ill-posed, and hence unstable in the presence of imperfect data. In an experimental setting where some amount of measurement noise is inevitable, the measured temperature Y will be the sum of the real temperature rise T, and the noise ϵ:

$$Y = T + \epsilon \tag{4.3}$$

The SFSM algorithm presented in the following section provides regularisation, and hence stability to the solution, and can therefore be used to solve Eq. (4.2) for the surface heat flux in the presence of imperfect data.

4.3 The SFSM Algorithm

The Sequential Function Specification Method (SFSM) algorithm, originally presented by Beck [31], solves the IHCP by estimating each component of a discretised signal consecutively. If a heat flux signal has elements $\widehat{q}_1, \widehat{q}_2, ..., \widehat{q}_{M-1}$ which have already been found, then the aim is to find $\widehat{q}_M$. The estimated temperature at the current time-step, calculated from the previously estimated heat fluxes with $\widehat{q}_M = 0$ is:

$$T_{M|q_M=0} = T_0 + \sum_{i=1}^{M-1} q_i h_{M-n} \Delta t \tag{4.4}$$

Following this, it can be reasoned that the heat flux $\widehat{q}_M$ must produce a temperature rise to make up the difference between $T_{M|\widehat{q}_M=0}$ and the measured temperature Y_M:

$$\widehat{q}_{s,M} = \frac{Y_M - T_{M|q_M=0} - T_0}{h_1 \Delta t} = \frac{Y_M - \sum_{i=1}^{M-1} q_i h_{M-n} \Delta t - T_0}{h_1 \Delta t} \tag{4.5}$$

For an in-depth temperature measurement, as sampling frequency increases, the first element of h_1 decreases, tending to zero. Division by this small number leads to solution instability. At the cost of information, stability can be achieved by drastically reducing the sampling frequency. The SFSM method applies regularisation by assuming a functional form of the heat flux over a number of samples. The algorithm, as given by Beck [31] and Woodbury [123], is as follows:

1. A functional form for $q(t)$ is assumed for times $t_M, t_{M+1}, ..., t_{M+R-1}$ (the heat flux is

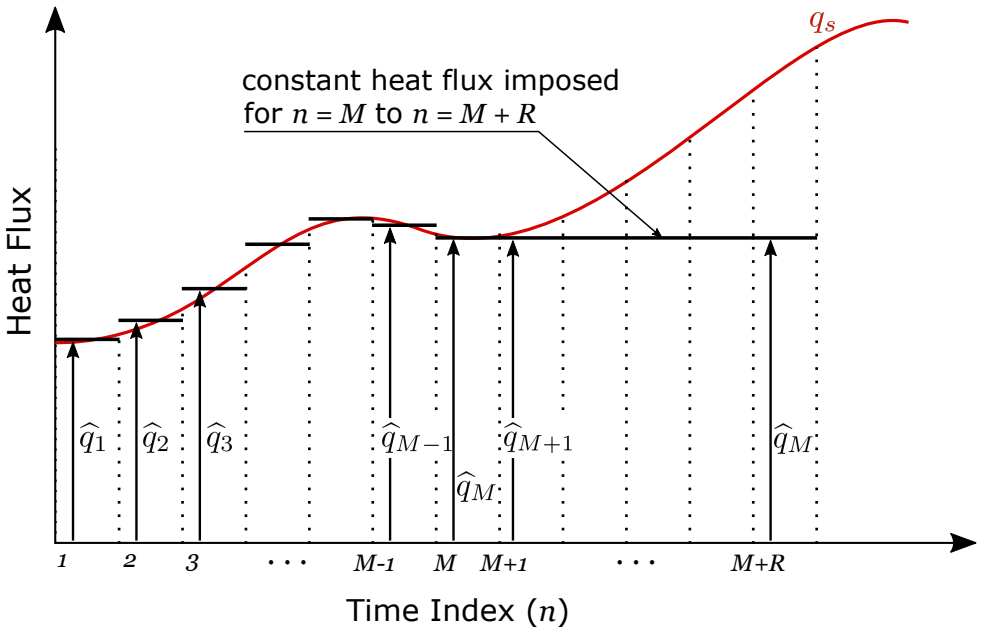


Figure 4.1: Schematic of the SFSM algorithm showing the real heat flux and the discretised components of estimated heat flux.

known for $t < t_{M-1}$).

2. A sum of squares function is used for these times and involves squares of difference between the measured and the corresponding calculated temperatures.

3. The heat flux components are estimated for the assumed functional form.

4. Only the first heat flux component, q_M, is retained.

5. M is increased by one and the procedure is repeated.

If the functional form of the heat flux imposed is constant, then $q_M = q_{M=1} = q_{M+2} = ... = q_{M+R}$. The variable R, the regularisation parameter, defines how many future time-steps of heat flux are held constant. q_M must be found which minimises the difference between the measured temperature (Y) and the calculated temperature ($\widehat{T}$) over the regularisation period. That is to say, the heat flux is that which in a least squares sense minimises the objective function:

$$S = \sum_{i=1}^{R} (Y_{M+i-1} - T_{M+i-1})^2 = \sum_{i=1}^{R} (Y_{M+i-1} - \widehat{T}_{M+i-1|q=0} - h_i \Delta t q_M)^2 \tag{4.6}$$

By minimising the objective function with respect to the estimated heat flux, i.e. $dS/dq_{s,M} = 0$, an equation for the estimated heat flux can be written as:

$$\widehat{q}_{s,M} = \sum_{i=1}^{R} K_j \left(T_M + \sum_{j=1}^{M-1} q_j h_{M-j+i-1} \Delta t - T_0 \right) \tag{4.7}$$

where

$$K_i = \frac{h_i \Delta t}{\sum_{j=1}^{R} (h_j \Delta t)^2} \tag{4.8}$$

As mentioned previously, this algorithm is only valid for LTI systems, those in which the impulse response does not change with time. This is not the case for the DHTG because the thermal properties change with temperature, and therefore the impulse response changes. The algorithm can be adapted to account for changing thermal properties if two assumptions are made: firstly that the properties are constant for the duration of each time-step[124]; secondly that the diamond layer is isothermal so that the impulse response can easily be updated at each time-step according to the measured temperature. Under these conditions the equation for the forward problem (Eq. (4.2)) can be re-written with temperature dependencies as:

$$T_M = T_0 + \sum_{n=1}^{M} q_n h_{M-n}(T_j) \Delta t \tag{4.9}$$

and Eqs. (4.7) to (4.8) as:

$$\widehat{q}_{s,M} = \sum_{i=1}^{R} K_j \left(T_M + \sum_{j=1}^{M-1} q_j h(T_j)_{M-j+i-1} \Delta t - T_0 \right) \tag{4.10}$$

where

$$K_i = \frac{h_i(T_j)\Delta t}{\sum_{j=1}^{R} \left(h_j(T_j)\Delta t\right)^2} \tag{4.11}$$

The "amount" of regularisation which the parameter R represents depends on sampling frequency, f_s. To remove the sampling frequency dependency, and therefore allow for the comparison of the amount of regularisation used across data sets where sampling frequency may not be constant, the regularisation parameter can be defined, with units of time, as:

$$\lambda_R = \frac{1}{fs} R \tag{4.12}$$

In summary, the SFSM algorithm takes a discretised temperature signal and sequentially estimates the heat flux at each time-step by assuming that the heat flux over R future time-steps is constant. Increasing the value of R has a stabilising effect on the solution by including more future time-steps of data into the calculation of the current heat flux, resulting in damping of high frequency components of the solution. Changes in thermophysical properties can be accounted for by updating the impulse response at each time-step. An advantage of the SFSM is that an impulse response, found either experimentally or computed once using a high fidelity numerical model, can be used directly in the calculation of surface heat flux.

4.4 Obtaining Impulse Response

The impulse response of a DHTG is required to calculate surface heat flux using the SFSM method. In this section the impulse response from three models of a DHTG is calculated and compared over a duration of 100 ms. The aim of this comparison is to show how increased fidelity of model is required for longer test-durations. Unless otherwise stated, the impulse response referred to is the unit impulse response: the temperature response of the gauge to a Dirac delta function heat flux boundary condition, delivering a total energy of $1\,\mathrm{J/m^2}$. The unit impulse response is therefore measured in units of K. All methods compare the response

of a Type 2 DHTG (220 µm Opaque PCD calorimeter) in a Version 2 housing (although the type of housing is only relevant for the two-dimensional model), with the material properties of Ceramabond 670 used as the substrate (see Table 3.2). Similar analyses could be performed for the other types of gauge, however this case was chosen to match the type of gauge used in the experiments to measure the impulse response in Chapter 5.

4.4.1 Models for Obtaining Impulse Response

The three models are:

Model 1: Zero-Dimensional Model

Treating the diamond layer as a perfect isothermal calorimeter with no losses gives an impulse response of:

$$h_{0D}(t) = \frac{1}{\rho_1 c_1 L} \tag{4.13}$$

Model 2: One-Dimensional Analytical Model

The analytical solution for the conduction of heat through a two-layer medium presented in Appendix A results in an expression for the time derivative of temperature of the rear surface of the calorimeter in response to a step in surface heat flux. The impulse response is the derivative of the step response, so substituting q_s =1 W/m^2 into Eq. (A.24) gives:

$$h_{1D}(t) = \left.\frac{\partial T(L,t)}{\partial t}\right|_{q_s=1} = \frac{2\sqrt{\alpha_1}}{(1+a)k_1\sqrt{\pi t}} \sum_{n=0}^{\infty} \left(\frac{1-a}{1+a}\right)^n \exp\left(-\frac{L^2}{\alpha_1 t}\left(n+\frac{1}{2}\right)^2\right) \tag{4.14}$$

Model 3: Two-Dimensional Axisymmetric Finite-Element Model

The domain of the FE model is shown in Fig. 3.11. The model is similar to that presented in the previous chapter (Section 3.7). However, in this case a Type 2 DHTG (220 µm, OPCD) with a Version 2 housing is modelled. The gauge has a nominal 99 % rise time of 50 µs. The temperature dependent material properties of the diamond used are that of Opaque PCD given in Table 3.1 and Fig. 3.4. The substrate was modelled as Ceramabond 670, the properties of which are given in Table 3.2. As in Section 3.7, to allow an axisymmetric simulation, two gold leads were modelled as a single 84.9 µm lead to preserve cross-sectional area. The axial and radial dimensions of the domain are sufficient to assume semi-infinite conditions, i.e. adiabatic boundaries, up to a test-time of 2.5 ms. The thin-film gauge itself was not modelled, so the temperature response of the gauge is taken as the spatially averaged temperature across the rear surface of the diamond region.

To obtain the impulse response, a temporally Gaussian pulse of heat flux with a full-width at half maximum duration of 5 ns was applied across the entire top surface boundary, delivering a total energy of $1\,\mathrm{J/m^2}$. The duration of the pulse is four orders of magnitude less than the response time of the gauge. It is therefore valid to assume that the temperature response is equivalent to the impulse response. The simulation was run for two different boundary conditions on the rear and side boundaries: adiabatic and fixed temperature. These two conditions provide limiting cases, bounding the real DHTG response. If the semi-infinite assumptions hold, then by definition this boundary condition has no effect on the measured temperature response. However, for longer time-scales as considered here, this is not the case. If the heat pulse reaches either the side or rear boundary, then the properties of the surrounding material and its thermal contact to the gauge must be considered.

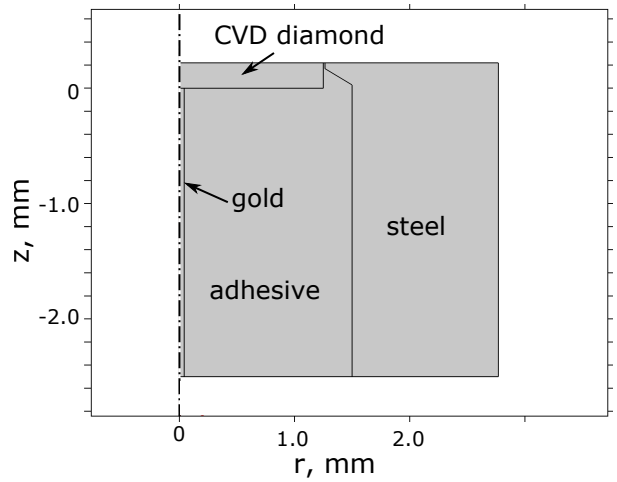


Figure 4.2: The domain used for the FE model. The axis of symmetry is at $r = 0$.

4.4.2 Comparison of Impulse Responses

Impulse responses from the three models are shown in Fig. 4.3 for an initial isothermal temperature of 25 °C for three time-scales, corresponding roughly to the test duration of an expansion tube (up to 250 µs), a small reflected shock tunnel (up to 2.5 ms), and a longer duration facility (up to 100 ms).

For the shortest time-scale (Expansion tube), there is little loss from the calorimeter. After the rise time, the difference between the zero-dimensional model with no losses and the FE model is only 5 %. The difference between the one-dimensional model and the two FE model responses is negligible, meaning the use of the impulse response from any of these could be used in the SFSM algorithm with little change to the measured heat flux. On this time-scale the heat pulse at the surface propagates a very small distance into the substrate, so the response is insensitive to the accurate modelling of losses, and entirely independent of the boundary conditions applied to the external edges.

Moving to the 2.5 ms times-scale (Reflected Shock Tunnel), the importance of modelling the losses more accurately becomes apparent. In this case the heat pulse propagates much further into the substrate and steel body. The difference between the one-dimensional and axisymmetric models is noticeable, and is a result of radial conduction. The response from the

FE model for the two different types of boundary condition are indistinguishable, because the thermal penetration depth on this timescale is still less than the distance to the boundaries.

For the 100 ms time-scale (longer duration facility), the difference between the three models is significant: full modelling of heat conduction in the gauge is of utmost importance for the calculation of the impulse response. For a test duration of more than 20 ms, the difference between the two responses from the FE model show that how the boundaries are modelled is important. These two responses are limiting cases, representing perfectly insulating boundaries and perfectly conducting boundaries respectively, so a real material would produce a response somewhere between the two.

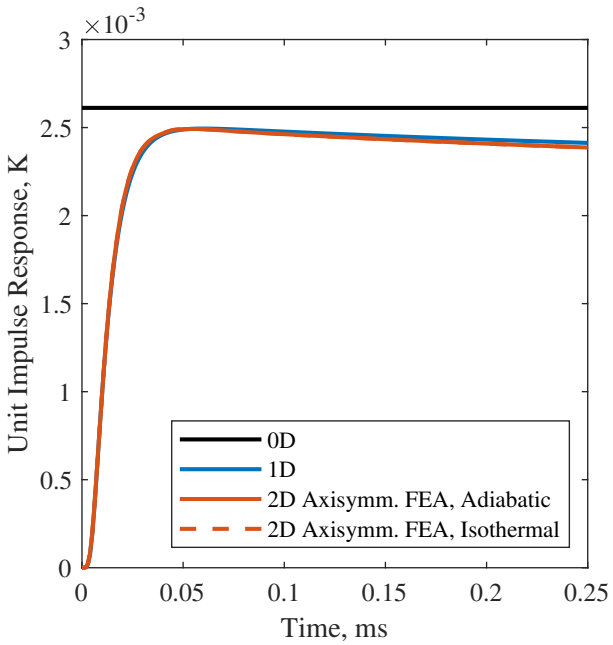
Figure 4.4 shows the impulse response from model 3 across a range of initial temperatures from 293 K to 343 K, i.e. a rise of 50 K from room temperature, spanning a typical temperature rise in a pulse-flow facility experiment. A decrease in magnitude of impulse response is observed with increasing temperature, following the temperature dependence of the specific heat capacity of diamond shown in Fig. 3.4.

4.5 Comparison of Data Reduction Methods

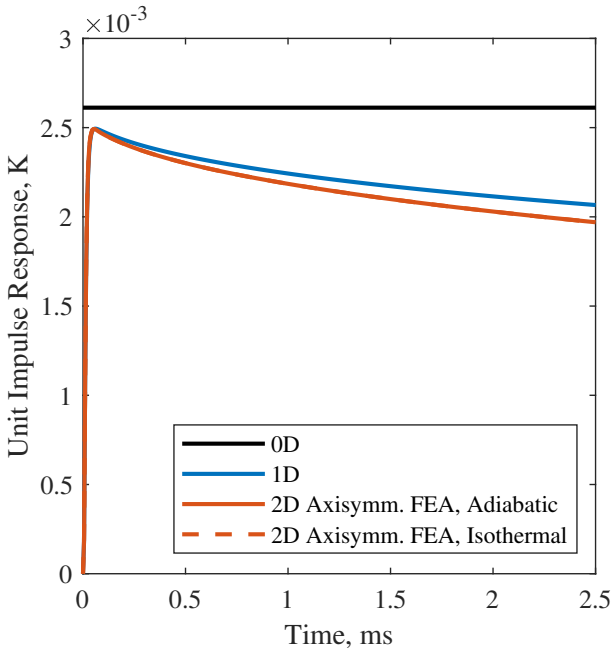
This section describes a study that was performed both to evaluate the accuracy of the SFSM method compared to the calorimeter-based method, and to demonstrate the full data reduction process for each method from a measurement of temperature with noise, through to the final heat flux solution.

Figure 4.5 shows a flow-chart of the steps the study follows. The first steps produce mock experimental data, T_n. Two surface heat flux profiles are defined, $q_{s,1}$ and $q_{s,2}$, representing measured heat fluxes in pulse-flow facilities. The FE model of a Type 2 DHTG described in Section 4.4.1 is used to provide the temperature response to the two heat flux profiles, T. Noise is added to the temperature responses to give T_n.

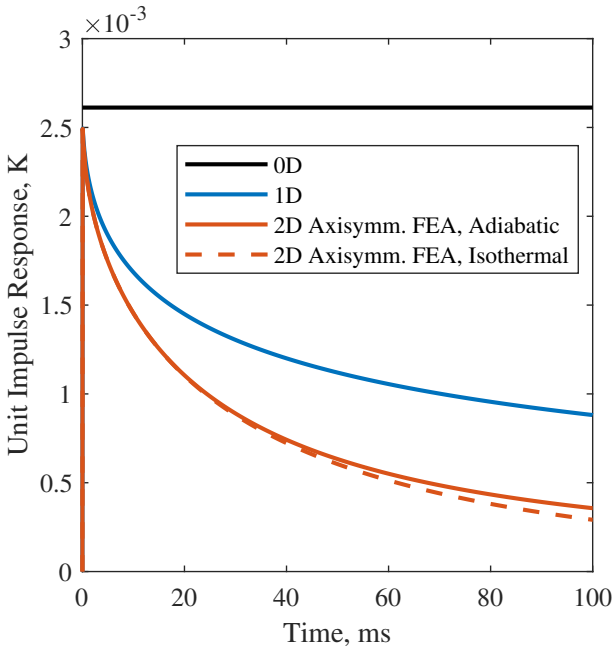
Both the calorimeter-based data reduction method and the SFSM data reduction method



(a) Expansion Tube or Shock Tube.



(b) Reflected Shock Tunnel.



(c) Long-duration facility.

Figure 4.3: The unit impulse response for three time-scales, representing typical test-times of three types of hypersonic facility.

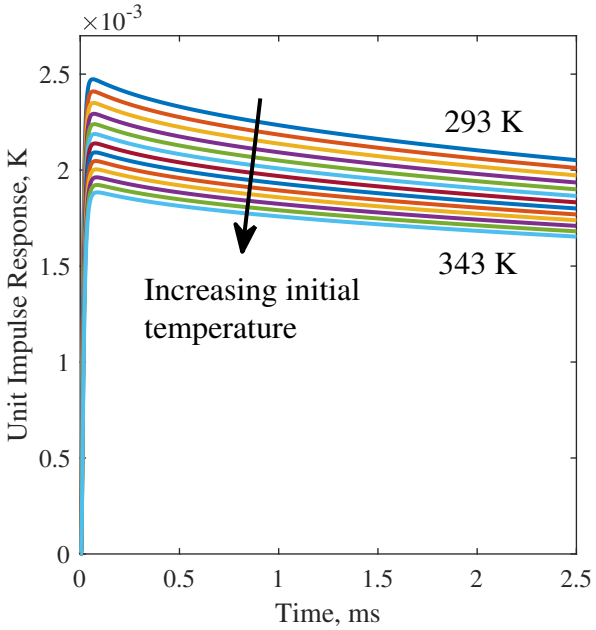


Figure 4.4: The unit impulse response of a Type 2 DHTG from the FE model, plotted for a range of initial isothermal temperatures.

are used to calculate surface heat flux from T_n. The impulse response for the SFSM method is derived from the same FE model as the temperature responses and the thermophysical properties of the DHTG used in data reduction equations are the same as in the FE model. A method known as the L-Curve[121] is used to select the optimum regularisation parameter for the SFSM method, and then an optimal low-pass filter Φ is designed and implemented for both methods. The dashed boxes on the flow chart denote the full steps of the two data reduction methods. These sets of steps are those that are implemented to calculate heat flux from an experimental measurement of temperature rise.

4.5.1 Producing Mock Experimental Data

4.5.1.1 Heat Flux Profiles and Temperature Response

The piece-wise constant heat flux profiles described by Eq. (4.15) and Eq. (4.16) were used as the boundary condition across the top surface of the FE model described in Section 4.4.1. The heat fluxes and corresponding temperature responses from the FE model are shown in

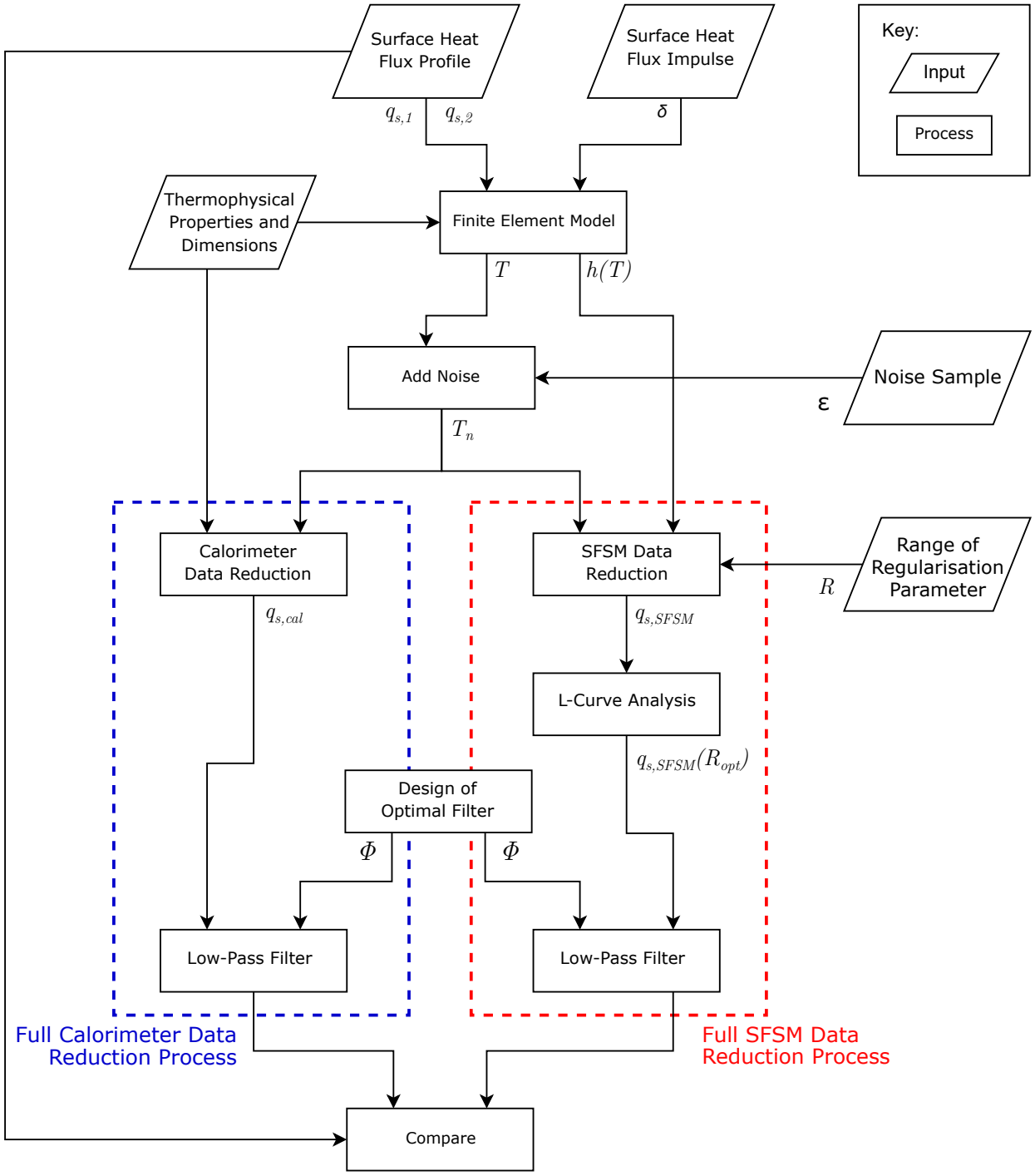
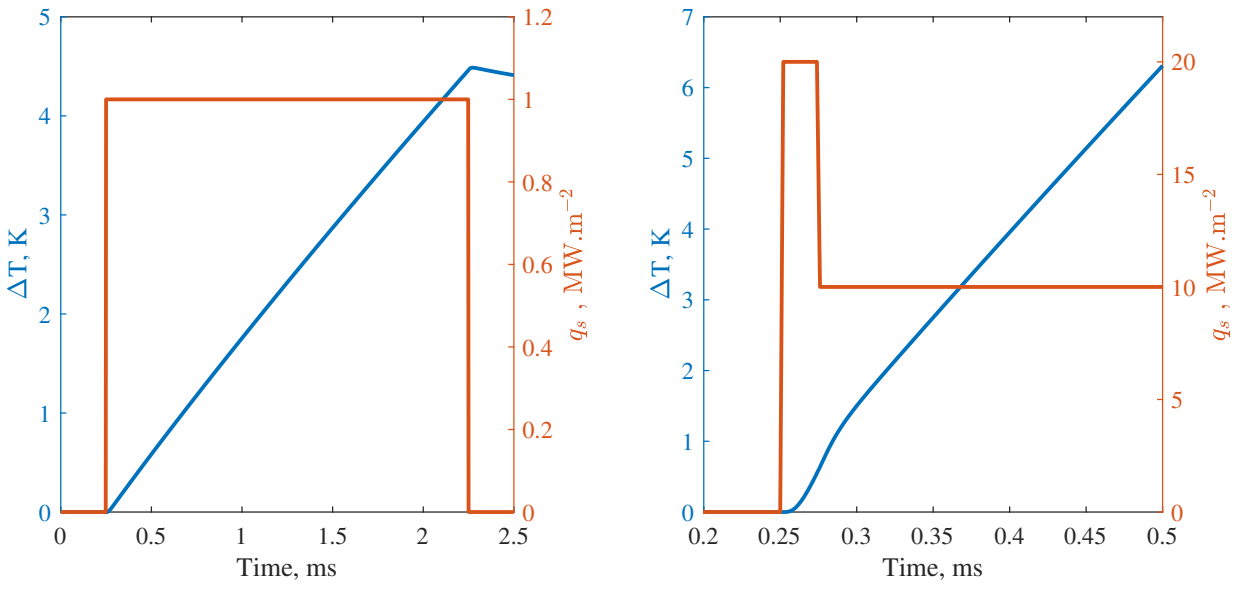


Figure 4.5: A flow chart of the study performed to compare the calorimeter and SFSM reduction methods.

Fig. 4.6.

$$q_{s,1} = \begin{cases} 0\,\mathrm{MW/m^2} & 0\,\mathrm{ms} \leq t < 0.25\,\mathrm{ms} \\ 1\,\mathrm{MW/m^2} & 0.25\,\mathrm{ms} < t < 2.25\,\mathrm{ms} \\ 0\,\mathrm{MW/m^2} & 2.25\,\mathrm{ms} < t < 2.5\,\mathrm{ms} \end{cases} \tag{4.15}$$

$$q_{s,2} = \begin{cases} 0\,\mathrm{MW/m^2} & 0\,\mathrm{ms} \leq t < 0.25\,\mathrm{ms} \\ 20\,\mathrm{MW/m^2} & 0.25\,\mathrm{ms} < t < 0.275\,\mathrm{ms} \\ 10\,\mathrm{MW/m^2} & 0.275\,\mathrm{ms} < t < 0.5\,\mathrm{ms} \end{cases} \tag{4.16}$$



(a) Case 1. (b) Case 2.

Figure 4.6: Input heat flux and temperature response from the FE model.

Case 1 represents stagnation point heating in a Reflected shock tunnel with a total test-time of 2.5 ms[1]. The profile is a box-car function with a peak magnitude of 1 MW·m^{-2}. In a real experiment, it would not be expected that the heat flux drop to zero at the end of the test time, but this feature was included to investigate how the calculated heat flux responds

[1]An RST test-time of 2.5 ms is typical of high enthalpy test-conditions or smaller facilities.

to a sharp step down, as well as the step up at the start.

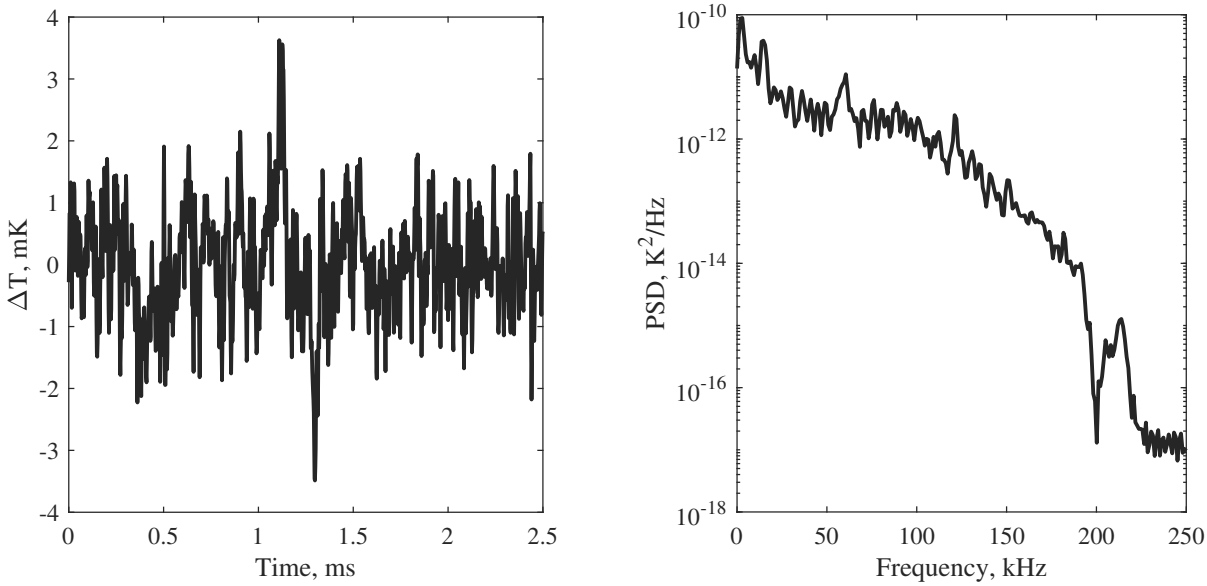
Case 2 represents stagnation point heat flux in an expansion tunnel. It has an initial $20\,\mathrm{MW{\cdot}m^{-2}}$ peak lasting 25 µs followed by a steady period of $10\,\mathrm{MW{\cdot}m^{-2}}$ lasting 225 µs. A similar initial peak is seen in experimental data [26]. There is a period of 0.25 ms where the heat flux is zero at the start for both cases because the SFSM method requires R data points at isothermal conditions before the flow arrives because in the calculation of the heat flux at each time-step the algorithm uses the measured temperature at R samples ahead. In an experimental setting this is not an issue, as recording data before the start of the experiment is standard practice.

The temperature responses from the FE model were sampled at a constant rate of 500 kHz. At this, and each subsequent step of comparison in this section, the two cases of heat flux are compared side-by-side in figures, with Case 1 (RST) on the left, and Case 2 (Expansion Tunnel) on the right.

4.5.1.2 Addition of Measurement Noise

The sample of noise shown in Fig. 4.7 was recorded from a DHTG mounted in the test section of the T6 Reflected Shock Tunnel in Oxford during no-flow conditions. An HTA3 amplifier was used with a constant current of approximately 10 mA. The data was recorded at a sampling rate of 2 MHz but was down-sampled (and anti-alias filtered) to 500 kHz to match the sampling rate of the current numerical investigation. Figure 4.7b shows the Power-Spectral Density (PSD) of the sample and demonstrates how the energy content falls with frequency. If white noise were used, the PSD would be constant across the frequency spectrum and would therefore present a different problem for the regularisation of the solution.

To investigate the effect of different noise levels, the noise sample was multiplied by a factor, N_F, before being added to the temperature responses from the FE model to produce T_n, the mock experimental data to be fed into the data reduction methods. Noise Factors of 0, 1, 5, and 10 were used, producing noise samples with standard deviations as given in



(a) Temperature noise.

(b) Temperature noise spectrum.

Figure 4.7: Experimentally recorded temperature noise and its Power Spectral Density, i.e. for $N_f = 1$.

Table 4.1.

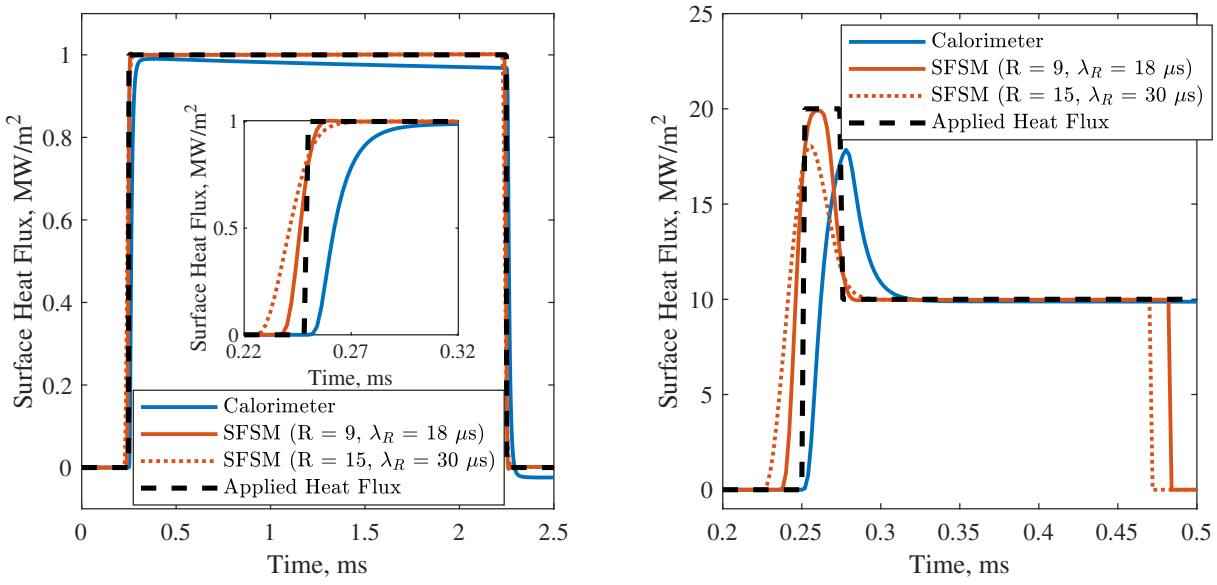
Table 4.1: Standard deviation of noise sample for each case of N_F.

N_F	σ_{T_n}, mK
0	0
1	0.89
5	4.45
10	8.90

4.5.2 Solution Without Noise, $N_F = 0$

To compare the measurement error from the data reduction methods in isolation, heat flux solutions using perfect data are presented before the addition of noise is considered. Figure 4.8 shows the surface heat flux calculated using both data reduction methods with noise-free data, i.e. $N_F = 0$, without any filtering of the signals. Figure 4.9 shows the relative error between these solutions and the applied heat flux. For the SFSM method, results for regu-

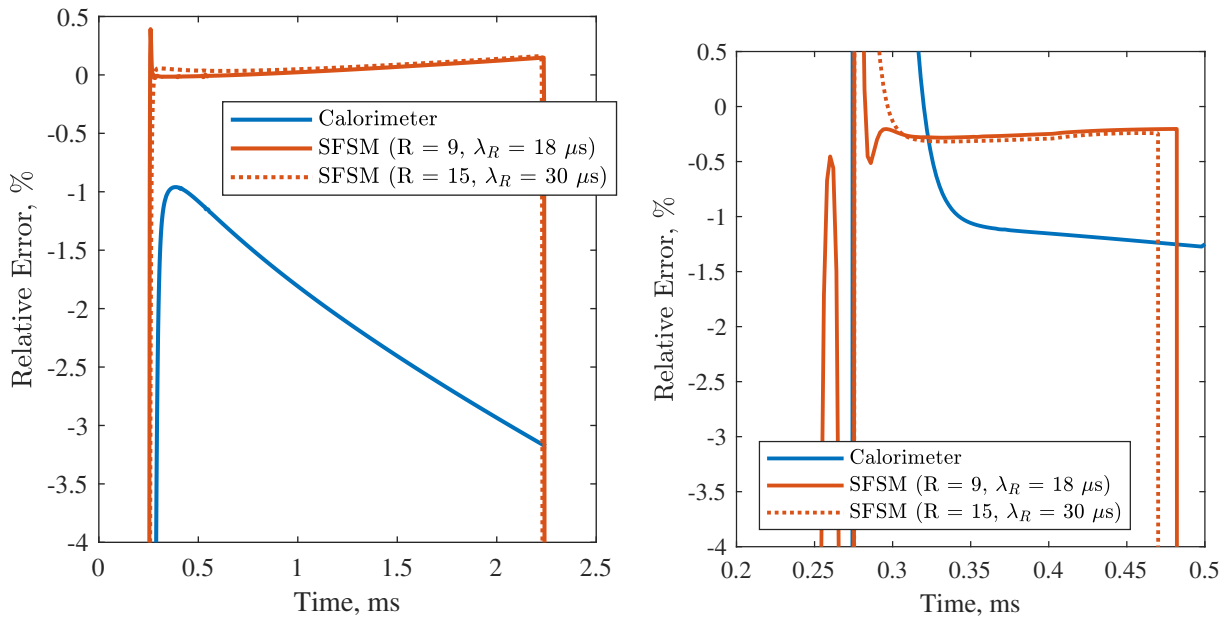
larisation parameters of $R = 9$ and $R = 15$ are shown. The former was chosen to represent a best-case solution with the least amount of regularisation possible, but even without the addition of noise, the numerical error from the simulation is sufficient to produce instability for $R < 9$, and would result in significant over-shoot and ringing in response to the step in heat flux at $t = 0.25\,\text{ms}$. The solution for $R = 15$ was chosen to match the rise-time of the calorimeter solution most closely, and therefore provides a like-for-like comparison of the response. However, at each time-step, the SFSM algorithm uses data R time-steps into the future. This "look-ahead" property of the algorithm results in a time-shift compared to the calorimeter solution.



(a) Case 1. (b) Case 2.

Figure 4.8: Heat flux solutions without any noise added to the temperature signal.

For Case 1, the test-time is long in comparison to the rise-time of the gauge, so small changes to the rise-time are not important compared to the long-term accuracy. The advantage that the SFSM method provides for long-term accuracy is seen most clearly in Fig. 4.9a: while the relative error of the calorimeter solution is in the range $-1\,\%$ to $-3\,\%$ and would increase rapidly for longer test-times, the error for the SFSM method is less than 0.25 %. This is because the impulse response used in the SFSM method accurately encapsulates three-



(a) Case 1. (b) Case 2.

Figure 4.9: Relative measurement error in the heat flux solutions without any noise added to the temperature signal.

dimensional conduction, whereas the calorimeter method only accounts for one-dimensional axial conduction. Therefore, the SFSM method is able to reconstruct the heat flux more accurately in the long-term.

For Case 2, the difference in long-term accuracy between the calorimeter method and the SFSM method is small: less than 1 % as shown on Fig. 4.9b. There is insufficient time for conductive losses to become significant, and therefore the difference in how the losses are modelled between the two methods has less impact on the solution compared to Case 1. However, the difference is significant during the transient response to the step changes at $t = 0.25\,\text{ms}$ and $t = 0.275\,\text{ms}$ where large relative errors are evident in Fig. 4.9 due to temporal misalignment between the solutions and the applied heat flux. Figure 4.8b shows that the SFSM solution for $R = 9$ is able to resolve the short-duration peak, where both the calorimeter method and the solution for $R = 15$ show a significantly attenuated peak value.

This analysis demonstrates using noise-free data that not only can the SFSM method improve the long-term accuracy of the heat flux solution compared to the calorimeter method,

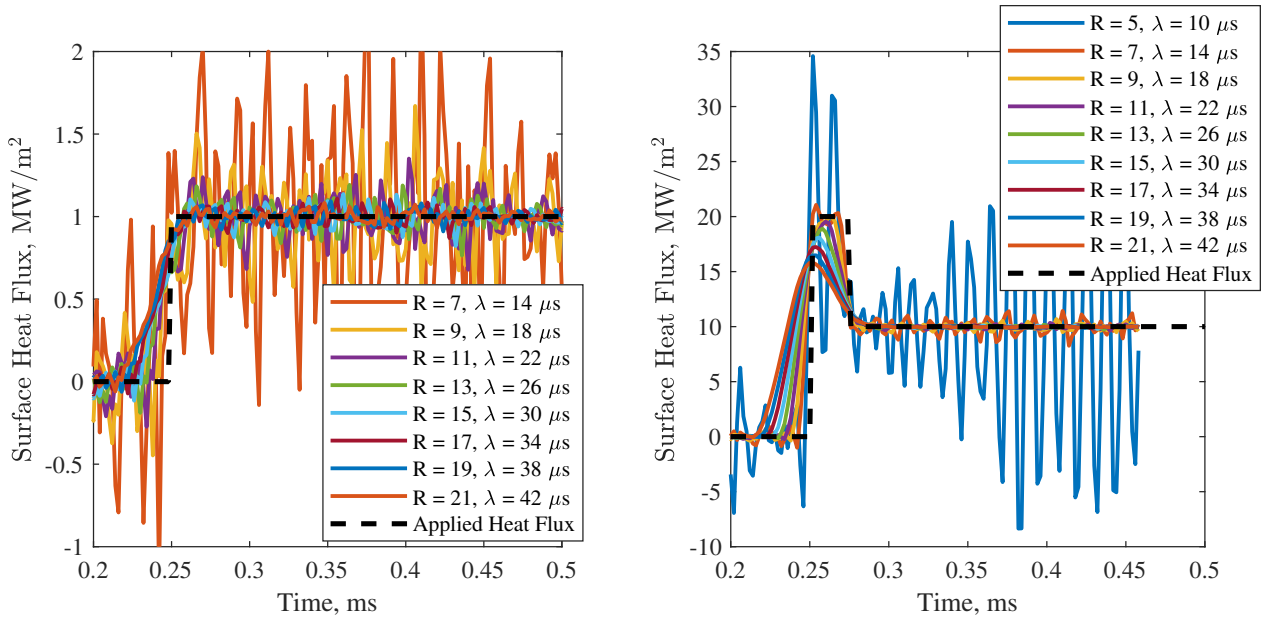
but it can also reduce the rise time of the gauge, thus improving the transient accuracy of the gauge.

4.5.3 SFSM Solutions With Noise

Figure 4.10 shows surface heat fluxes calculated using the SFSM method, with noisy temperature data for $N_F = 1$, for $R = 7$ to $R = 21$. The signals are shown over shortened time-scales because the effect of varying the regularisation parameter is most clearly seen at areas with large gradients in heat flux, i.e. at the step changes. At low values of R, the solution resolves the step changes more accurately, but at the cost of increased oscillation. As the regularisation parameter is increased, the magnitude of these oscillations decreases, and increased smoothing of the step-response is seen, thus illustrating the low-pass filtering effect of regularisation. For the same value of regularisation parameter, $\widehat{q}_s$ seems much more oscillatory for Case 1 than for Case 2. However this is simply a product of the scale of the vertical axis. With the same absolute level of noise for both cases, the Signal-To-Noise Ratio (SNR) is higher for Case 2. The solution for $R = 5$ for Case 2 is seen to grow with time, indicating that the solution is unstable; given more time the solution will keep growing indefinitely. Similar trends are seen for higher noise levels, $N_F = 5$ and $N_F = 10$, although the magnitude of the oscillations at a given R value are larger.

4.5.4 Selection of the Optimum Regularisation Parameter

To produce a heat flux solution that can be considered the output of the SFSM method from the spectrum of results presented above, an optimum value of regularisation parameter must be selected. By performing this numerical study, information is available which would not be in an experiment: notably, the applied heat flux q_s, and the heat flux calculated using temperature data without the addition of noise, denoted $\widehat{q}'_s$. With these, the effect of the regularisation parameter on the accuracy of the solution can be investigated. The solution error can be broken down into two parts: perturbation error and bias error. The perturbation



(a) Case 1. (b) Case 2.

Figure 4.10: Heat flux solutions using the SFSM method for a spectrum of values of the regularisation parameter, for $N_F = 1$.

error is a product of the amplification of perturbations, i.e. noise, in the temperature signal. This can be defined as the variance of the solution, and is a function of the difference between the solution with and without added noise:

$$Var[\widehat{q}_s(R)] = \sqrt{\frac{1}{N}\sum\left(\widehat{q}_s(R) - \widehat{q}'_s(R)\right)^2} \tag{4.17}$$

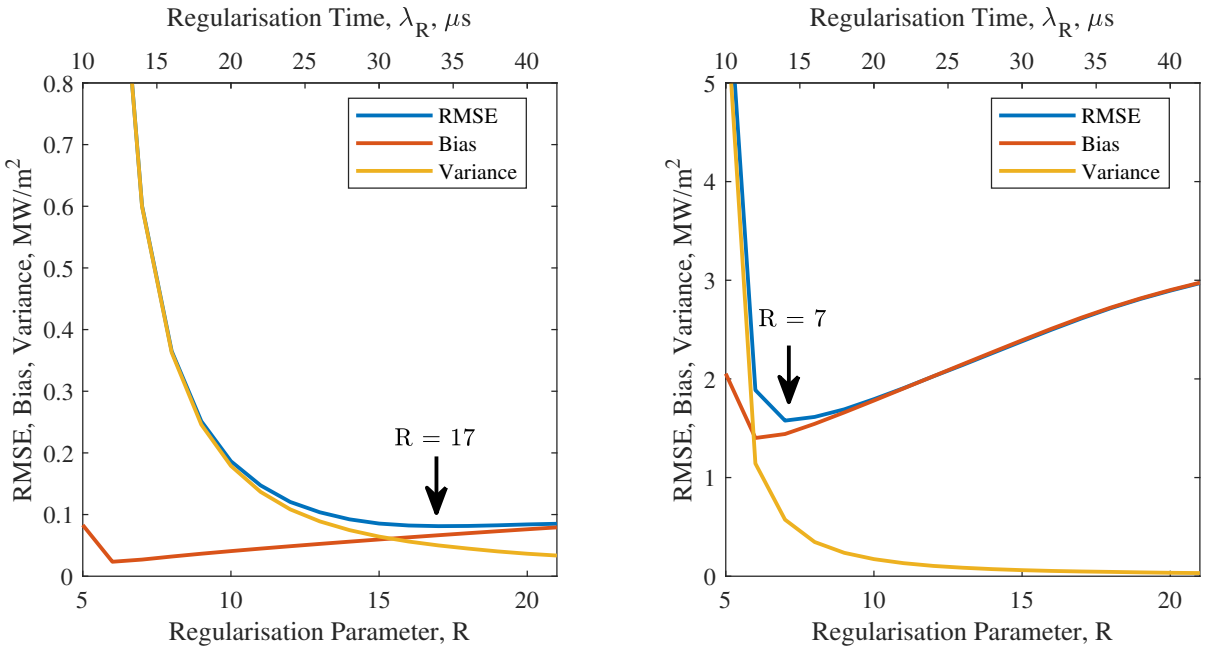
The bias error, sometimes called the regularisation error, is a function of the difference between the solution without noise and the applied heat flux:

$$Bias[\widehat{q}_s(R)] = \sqrt{\frac{1}{N}\sum\left(\widehat{q}'_s(R) - q_s(R)\right)^2} \tag{4.18}$$

The overall error can be defined as the Root-Mean Squared difference between the input and calculated heat fluxes. This can also be calculated as the sum in quadrature of the variance and the bias:

$$RMSE[\widehat{q}_s(R)] = \sqrt{\frac{1}{N}\sum\left(\widehat{q}_s(R) - q_s(R)\right)^2} = \sqrt{Var[\widehat{q}_s(R)]^2 + Bias[\widehat{q}_s(R)]^2} \tag{4.19}$$

These metrics are shown in Figure 4.11 for $N_F = 1$ as a function of the regularisation parameter. For low values of R, the overall error is dominated by variance, as can be seen in the solutions shown in Fig. 4.10. As R is increased, the bias error grows with the increasing filtering effect of regularisation. An increase in bias for $R = 5$ is seen due to solution instability. These figures clearly demonstrate the bias-variance trade-off which is inherent to all regularisation problems. For both cases there is a value of R which minimises the RMSE: for Case 1 it is $R = 17$, and for Case 2 it is $R = 7$. The method for finding the optimum R using experimentally available data is successful if it is close to these values.



(a) Case 1.

(b) Case 2.

Figure 4.11: Root-Mean-Squared Error, Bias, and Variance as a function of the regularisation parameter for $N_F = 1$. The point of minimum RMSE is labelled.

In an experiment however, neither q_s nor $\widehat{q}_s$ are known, and therefore, other metrics of accuracy which use available information must be employed. The most logical metric

to calculate, and minimise, is a residual based on the difference between the measured temperature and the temperature found by solving the forward problem with the solution heat flux as a boundary condition:

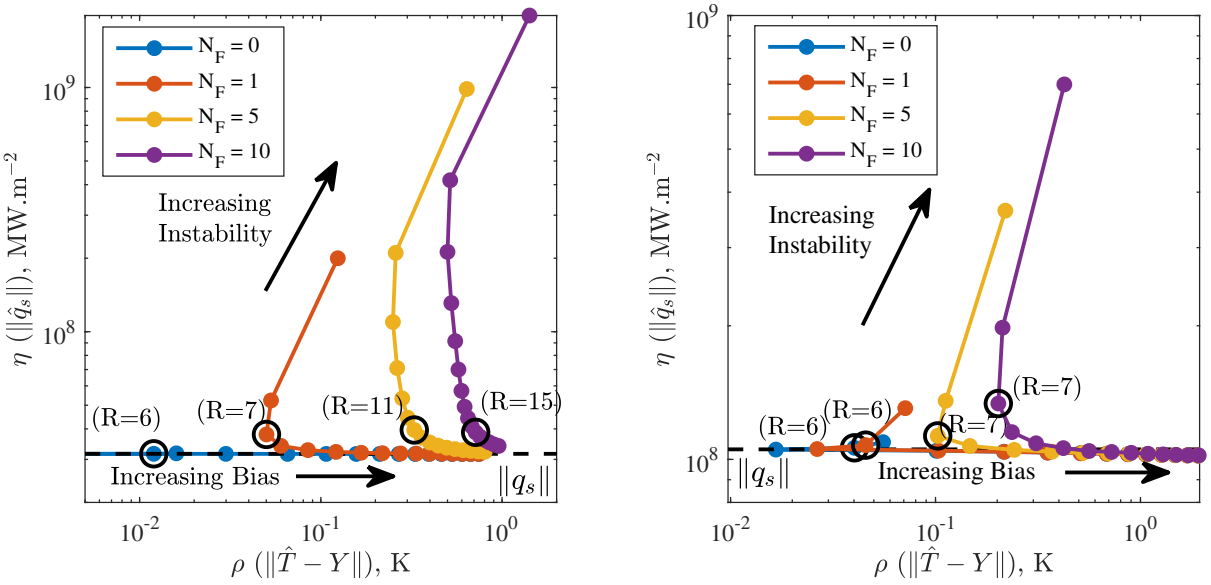
$$\rho(R) = ||\widehat{T}(R) - Y|| = \sqrt{\sum_{k=1}^{n} \left(\widehat{T}(R) - Y\right)^2} \tag{4.20}$$

Minimisation of this residual alone would lead to a solution with low bias and large variance, because $\widehat{T}$ is insensitive to fluctuations in q_s due to the smoothing, dampening effect of sub-surface temperature measurements. A competing metric, which if minimised would lead to an over-smoothed (high bias error) solution, is the Root-Mean-Squared size of the solution:

$$\eta(R) = ||\widehat{q}_s(R)|| = \sqrt{\sum_{k=1}^{n} \left(\widehat{q}_s(R)\right)^2} \tag{4.21}$$

With these two parameters, the L-Curve [121] can be formed. The L-Curve is a parametric plot of $\rho(R)$ against $\eta(R)$: the bias of the solution against the magnitude of the solution. Figure 4.12 shows L-curves for all four values of N_F with log scales for both axes. The bias-variance trade-off is seen in the L-Curves, as previously seen in Fig. 4.11. As R is reduced from the corner, the solution size grows rapidly, and as R is increased, the solution bias grows. The circled and labelled values of R are the points of maximum curvature; these are the points at which the rate of change from variance-dominated error to bias-dominated error is greatest. This is the standard criteria for the selection of the optimum value of R, and should ideally be close to the value of R that gives the minimum RMSE, as shown in Fig. 4.11.

The location of the corner, in terms of R, is a function of the signal-to-noise ratio, which implicitly involves the design of the gauge: a DHTG with a thicker calorimeter is less sensitive and hence for the same surface heat flux has a lower signal. For higher levels of noise, i.e. higher N_F, more regularisation is needed to stabilise the solution. This is seen



(a) Case 1. (b) Case 2.

Figure 4.12: L-Curves with the point of maximum curvature labelled.

more clearly for Case 1, where the signal-to-noise ratio is worse. For Case 2, the increased need for regularisation between each case is lost in the discretisation of the spectrum of R. The L-Curve for Case 2 shows a more pronounced reduction in solution size for $R > 7$ because the calculated heat flux does not resolve the short peak in q_s, as can be seen in Fig. 4.10.

The optimum value of R found as the point of maximum curvature of the L-Curve is known to result in solutions which may look overly oscillatory [121]. The selected solution of $R = 7$ for $N_F = 1$ can be seen on Fig. 4.10 to have oscillations of larger magnitude than the steady state value, however, the intended use for the measurement must be considered. If a test-time average measurement is the final result, then an oscillatory solution with zero-mean noise and little bias will be more accurate, as long as enough periods of oscillation are averaged. On the other hand, for the presentation of transient heat flux data, or if the averaging period is short compared to the oscillation period, it may be advantageous to low-pass filter the results.

4.5.5 Design of an Optimal Low-Pass Filter

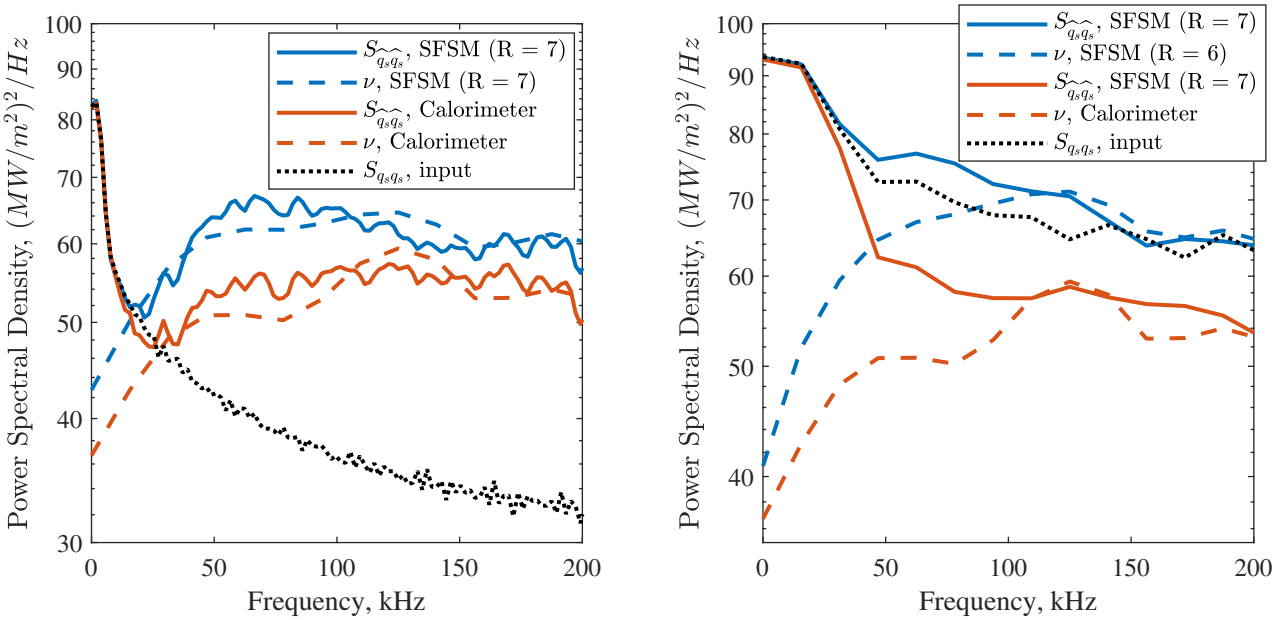
Fundamentally, it is not possible to distinguish, with certainty, signal from noise for an experimental measurement. However, if the noise is considered to be a stationary process, i.e. its mean and variance are constant over time, then a filter Φ_q for a heat flux solution q which rejects noise without compromising signal content [125] can be given as

$$\Phi_q(f) = \frac{S_{q_s q_s}(f) - \nu(f)}{S_{qq}(f)} \tag{4.22}$$

where S_{qq} is the PSD (Power-Spectral Density) of the heat flux q and ν is the PSD of the noise. Making the assumption that the noise is a stationary process implies that S_{qq} is a super-position of the PSD of the signal and ν, where the latter can be calculated as the PSD of the heat flux solution for $t < 0$, i.e. over the period of time during which the heat flux is zero. In an experiment, this can be calculated from the initial portion of data before the flow arrives, which is known as pre-trigger data, or pre-trigger noise.

Figure 4.13 shows the PSD of the SFSM heat flux solution for $N_f = 1$ for the optimum value of R given from the L-curve, of the calorimeter heat flux solution, and of the applied heat flux (which has no noise). For the heat flux solutions, $\nu(f)$ is also shown. The PSDs were estimated using Welch's method [126]. For frequencies below 10 kHz, the magnitude of the PSD for both the calorimeter and SFSM solutions is greater than that of the noise. As frequency increases, the two spectra begin to converge, indicating a reducing signal-to-noise ratio. If at any point $\nu(f) = S_{\widehat{qq}}(f)$, then the signal-to-noise ratio is unity, and therefore the optimal filter is zero ($\Phi = 0$) because there is no useful signal. Given a perfect estimation of the PSD, the two lines would gradually converge without ever touching or crossing. However variance is unavoidable in the calculation of discrete Fourier transforms, hence, some oscillation and crossing of the lines is present.

Figure 4.14 shows $\Phi(f)$ calculated using the PSDs given in Fig. 4.13 and similar PSDs for all four cases of N_f. Without any noise, $\Phi(f) = 1$ across the entire frequency range

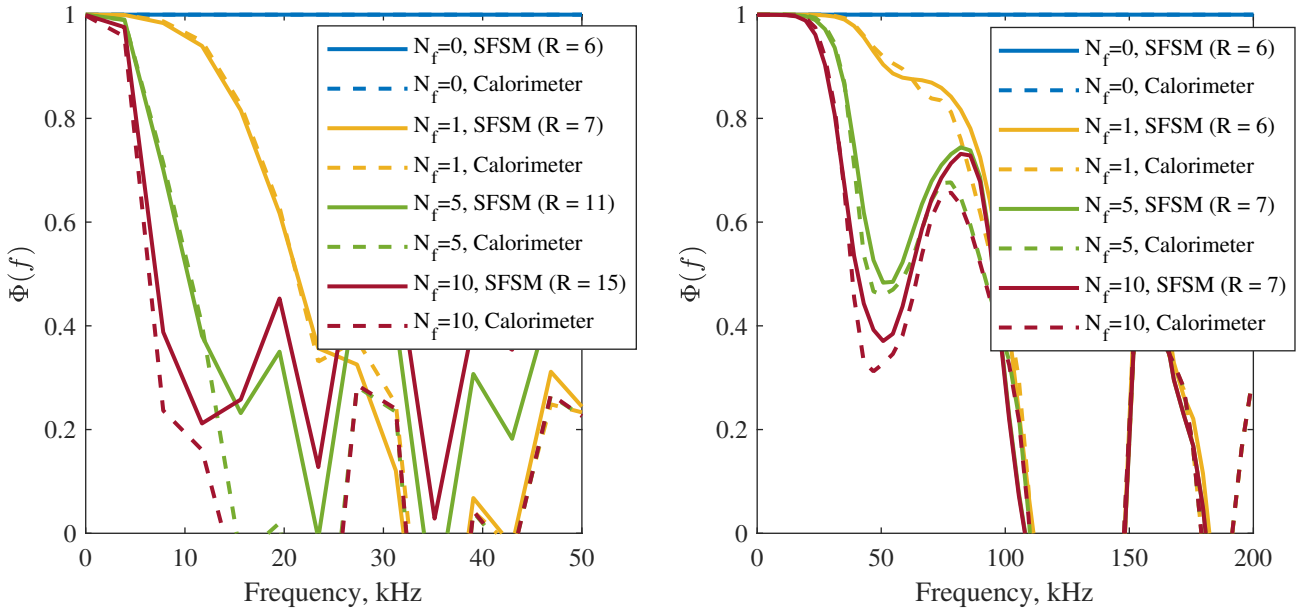


(a) Case 1. (b) Case 2.

Figure 4.13: PSD of the heat flux solution $S_{\widehat{q}_s\widehat{q}_s}$, of the noise ν, and of the applied heat flux $S_{q_sq_s}$.

shown. As the magnitude of the noise increases, the optimal filter shows a decreasing cut-off frequency. For Case 2 the cut-off frequency is higher than for Case 1 because the applied heat flux is an order of magnitude larger, meaning the signal-to-noise ratio is higher. An important conclusion drawn from this analysis is that the realisable bandwidth of a sensor is a function of the magnitude of the signal, the magnitude and nature of the noise, and the sensitivity of the gauge as a function of frequency (see Section 3.5.3). The measurement bandwidth of a sensor, as might be defined from the theoretical rise time or purely analytical methods, is not necessarily attainable in an experiment.

Due to the oscillations in Φ at higher frequencies, it is impractical to use it directly as a filter. Instead, low-pass filters should be designed to match the response of Φ at low frequencies, and provide a smooth level of attenuation at higher frequencies. This is shown for $N_f = 1$ in Fig. 4.15 using second-order Butterworth filters with cut-off frequencies given in Table 4.2. These filters are applied to give the final heat flux solutions in the following section.



(a) Case 1. (b) Case 2.

Figure 4.14: PSD of the heat flux solution $S_{\widehat{q}_s\widehat{q}_s}$, of the noise ν, and of the applied heat flux $S_{q_sq_s}$.

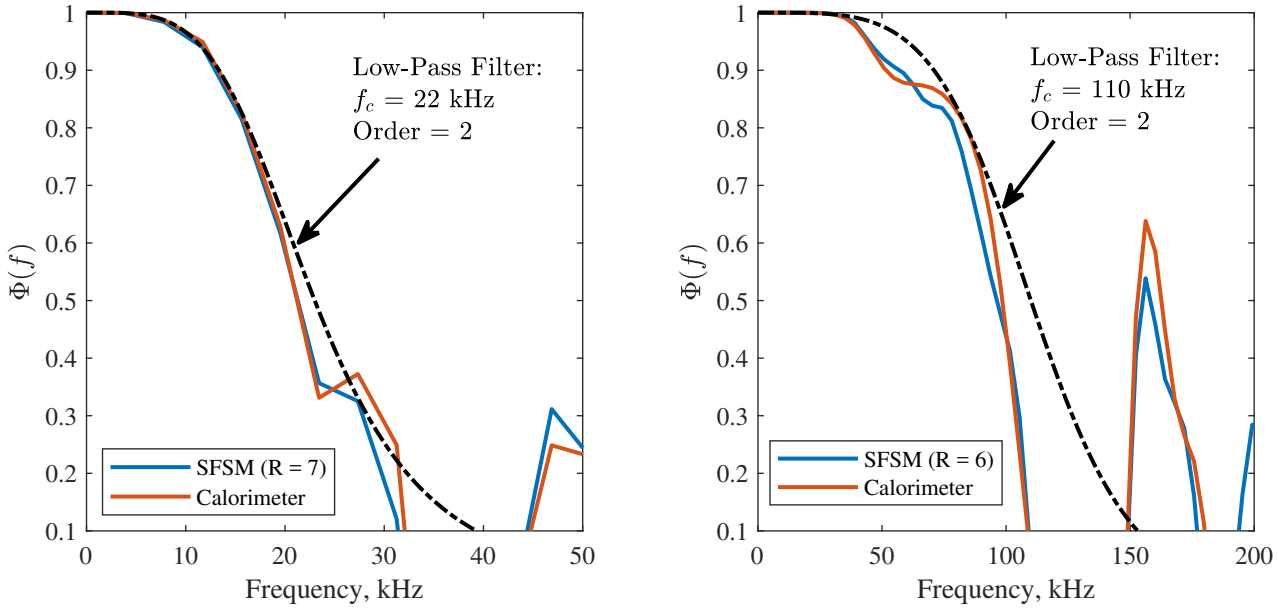
Table 4.2: Cut-off frequencies for second-order low-pass filters designed around the optimal filter Φ.

Case	$f_{c,SFSM}$, kHz	$f_{c,calorimeter}$, kHz
1	22	22
2	110	110

4.5.6 Comparison of Final Heat Fluxes

The final heat fluxes from this study for $N_F = 1$ are shown in Fig. 4.16. For the heat fluxes from the SFSM method, the optimum value of R has been chosen using the point of maximum curvature on the L-Curve. Both the SFSM and calorimeter solutions have been filtered using the low-pass filters described in the previous section.

For Case 1, the advantage that the SFSM method offers in terms of long-term accuracy and response time is almost hidden in the noise, but the growing inaccuracy with time of the calorimeter method can be seen toward the end of the test-time and was seen more clearly



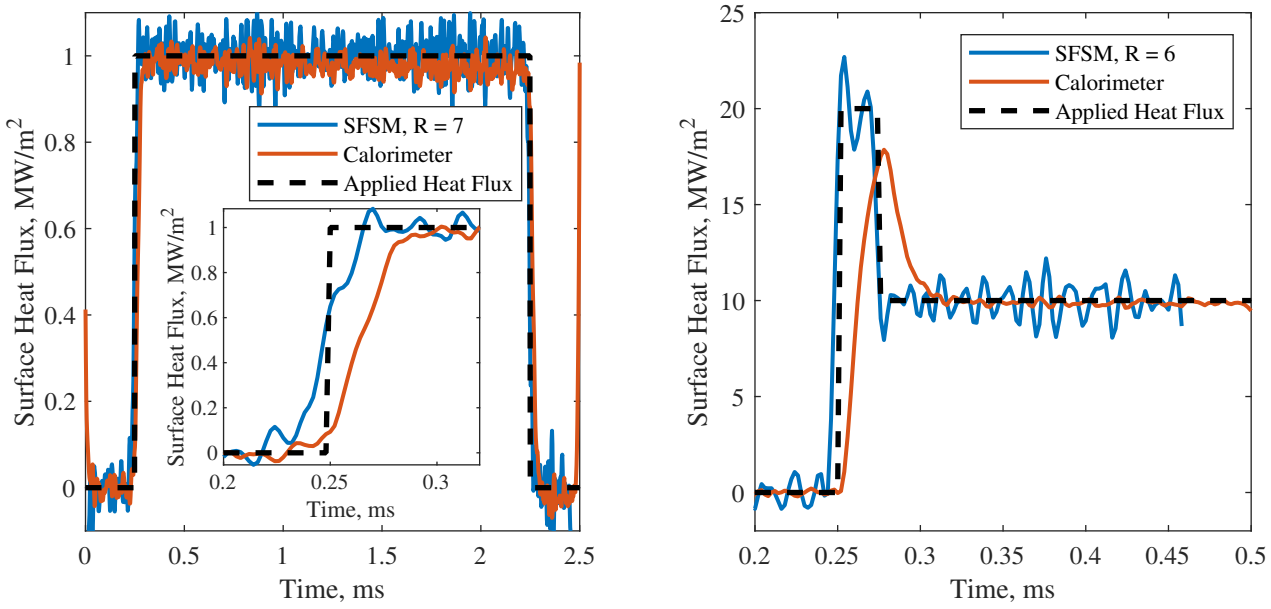
(a) Case 1. (b) Case 2.

Figure 4.15: Design of the optimal filter $\Phi(f)$.

for the noise-free case in Section 4.5.2. The rise time of the measurements is shown to be very similar in the inset plot in Fig. 4.16a because the solutions from both methods have been filtered at 22 kHz.

For Case 2, as for the noise-free case, the SFSM shows superior transient accuracy, more accurately resolving the initial peak and reaching the subsequent steady state period faster. The trade-off for the improved rise-time of the SFSM method is increased variance in the solution. However, whether this increase is a matter of concern depends on the purpose: if a test-time average heat flux measurement is the aim, then a solution with higher variance but faster rise time can only lead to more accurate measurements, provided the solution is not numerically unstable. For the presentation of transient data, additional low-pass filters can be applied to improve legibility and help to reveal trends.

For cases of N_f with higher levels of noise, the advantage the SFSM method provides to the transient accuracy decreases. Higher levels of noise mean that the optimal filter designed in the previous section has a lower-cut-off frequency, thus limiting the rise time of the SFSM



(a) Case 1. (b) Case 2.

Figure 4.16: Final heat fluxes from the SFSM method and the calorimeter method for $N_f = 1$. Both signals have been low-pass filtered using the optimal filter Φ.

solution.

4.6 Chapter Summary

This chapter has presented a data reduction method for the DHTG using an adapted version of the SFSM algorithm to solve the IHCP with temperature dependent thermophysical properties. A full set of steps in the data reduction processes from a measured temperature change signal to heat flux are given in Fig. 4.5. A study was performed to compare the new data reduction method to the calorimeter-based method given in the previous chapter using an FE model of a Type 2 DHTG (220 µm thick calorimeter made from Opaque PCD) to provide both a mock experimental temperature response to two heat flux profiles, and the impulse response required for the SFSM algorithm. An experimentally recorded sample of noise was added to the temperature response to more accurately replicate the use of the methods with experimental data.

Increased accuracy of the SFSM method over the calorimeter method was demonstrated, both in terms of improved response time, meaning reduced transient measurement error, and long-term steady-state measurement accuracy. A method to design an optimal low-pass filter for experimental data was presented, leading to a conclusion that the realisable bandwidth of a measurement technique can be significantly lower than the theoretical bandwidth. While this study focussed entirely on a Type 2 DHTG, the methodology presented is equally applicable to all types of DHTG.

To determine the uncertainty of an experimental measurement, uncertainty in the values of material properties and gauge geometry used in the determination of impulse response must be considered. An experimental measurement of impulse response could reduce these uncertainties and by using it directly in the SFSM method will allow a parameter-free calculation of heat flux. This is the motivation for the following chapter.

CHAPTER 5

Experimental Measurement of Impulse Response

Contents

5.1 Introduction 92
5.2 Experimental Set-up 93
5.3 Data Reduction 96
5.4 Experimental Measurement Uncertainty 97
5.5 Experimental Results 99
5.6 Tuning FE Model to Experimental Data 102
5.7 Chapter Summary 106

5.1 Introduction

This chapter details an experiment designed to directly measure the unit impulse response of a DHTG at a range of initial temperatures with micro-second time resolution using a pulsed UV laser to apply a short-duration burst of high intensity heat flux to its surface. The experiment is similar to the standard laser-flash method used to determine the thermal diffusivity of materials, e.g. Baba and Ono [127], and to the heat transfer gauge impulse

response measurements described by Buttsworth [61] and Palmer [73]. However, the current work differs from these latter experiments in that the absolute magnitude of the absorbed heat flux is calculated, allowing an absolute measurement of impulse response to be found. In this chapter, the experimental set-up is described, followed by an explanation of how the unit impulse response was calculated from the experimental data, and a subsequent uncertainty analysis. The effect of spatial non-uniformity of the laser beam intensity is investigated, and finally, the thermophysical properties of the diamond and substrate are estimated by tuning the response of a simulation of the experiment to match the experimental response.

5.2 Experimental Set-up

Figure 5.1 shows a schematic of the experimental set-up. The gauge tested was DHTG24, a Type 2 DHTG with a 220 µm thick OPCD diamond calorimeter. Incident radiation at 266 nm is strongly absorbed by OPCD [128] and can therefore be considered purely as surface heating. The Nd:YAG laser emits a beam with a combination of its primary and secondary harmonics: 1064 nm and 532 nm. A selective mirror was used to separate the two wavelengths, sending the 1064 nm to a beam dump and the 532 nm to a frequency-doubling non-linear caesium lithium borate (CLBO) crystal, thus achieving frequency quadrupling of the primary wavelength produced by the laser, and introducing 266 nm to the beam. Another selective mirror was used to remove the 532 nm portion of the beam. Note that DHTGs with transparent PCD calorimeters cannot be used with this set-up because PCD has low absorptivity at 266 nm. For the calibration of transparent PCD calorimeters, the incident wavelength must be further reduced to below 210 nm.

The laser provided 5 ns pulses at a repetition rate of 10 Hz. The duration of the pulses delivered is more than 3 orders of magnitude less than the typical response time of the gauge and so for analysis purposes can be considered an impulse. The incident energy was found by measuring the energy of a fraction of the beam using a beam sampler and a THORLABS

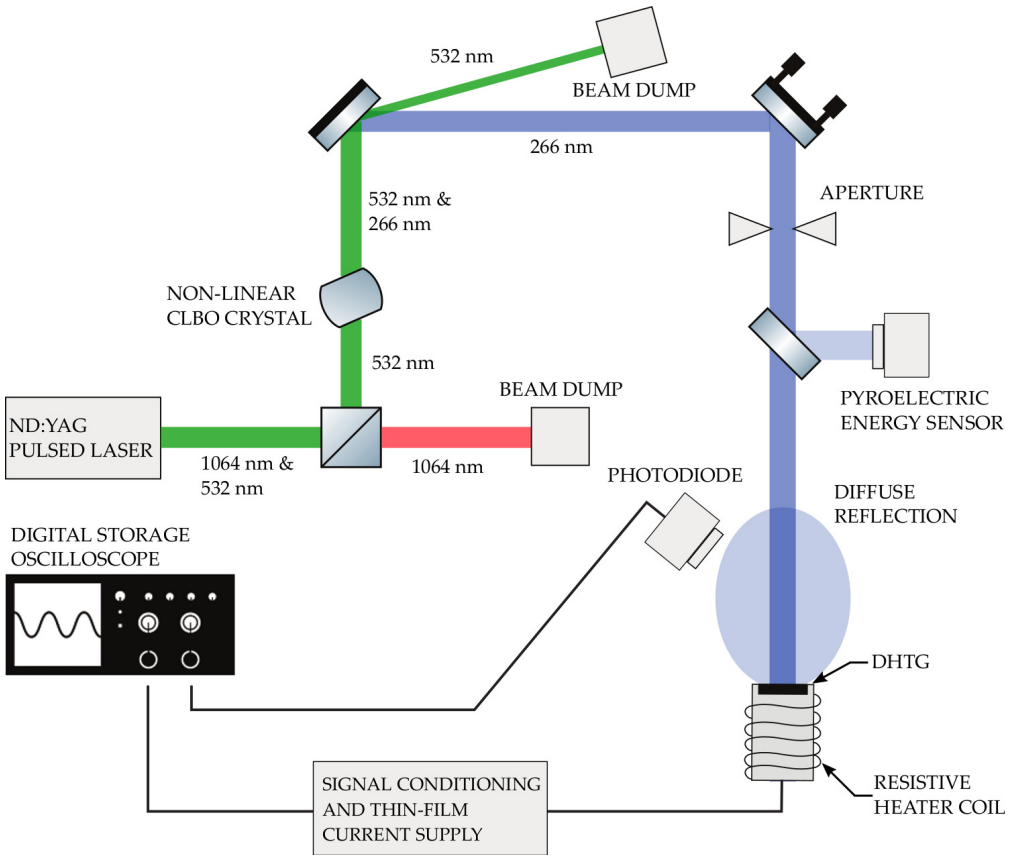


Figure 5.1: Schematic of the experimental set-up for the impulse response measurement.

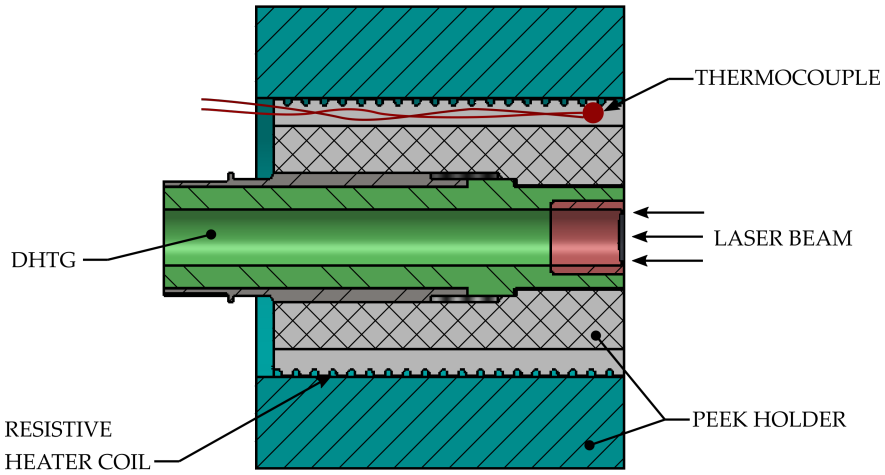


Figure 5.2: Cross-sectional view of the DHTG mounted in its heater.

ES111C Pyroelectric Energy Sensor with a broadband absorptive coating. A digital storage oscilloscope was used to record the response of the DHTG and a high-speed photodiode; the latter was used to detect diffuse reflection from the gauge surface and trigger the data acquisition.

The DHTG was mounted inside a PEEK (Polyether Ether Ketone) holder with an embedded resistive heater coil and thermocouple, as shown in Fig. 5.2. The resistive wire is wound around the helical cut in the inner piece with wires exiting through the rear. A DC power supply was used to supply the coil with a constant current to raise the initial temperature of the DHTG. The thermocouple was used as an indicator of the temperature of the gauge during the experiments, but in the analysis of the results the temperature measured by the platinum RTD in the DHTG was used. Nominal initial temperatures of 25 °C, 45 °C, and 65 °C were used, covering a range of expected temperature rises in expansion tube or reflected shock tunnel testing.

An HTA3 amplifier [129] was used to provide a constant current supply to the RTD in the DHTG and to amplify the voltage response. To allow an absolute measurement of temperature with the RTD, a reading of the voltage across the gauge (V_{ref}) was recorded at an isothermal temperature T_{ref}, as measured by the thermocouple. The set-up was left

overnight to allow full equilibration with the thermocouple.

The following procedure was used to perform an experiment, resulting in a single transient measurement of impulse response:

1. Block the laser beam from hitting the DHTG with a shutter;
2. Turn on laser and allow an hour to reach steady state;
3. Turn on power supply to heater coil and wait until indicated thermocouple temperature has reached steady state;
4. Briefly open shutter, allowing a pulse from the laser to hit the DHTG;
5. Allow 5 min for the DHTG temperature to equilibrate before repeating.

An intensity map of the laser beam at the same location as the DHTG was captured using a THORLABS CCD Camera Beam Profiler immediately before and after this procedure.

5.3 Data Reduction

The temperature rise of the DHTG, $\Delta T_{exp}(t)$, was calculated from the recorded voltage response by first removing the gain of the amplifier, and then using the equations for temperature rise with an implicit calculation of constant current which are given in Appendix D. The full equation is shown here in terms of the slope and intercept from the RTD calibration experiment for clarity, and for use in the evaluation of uncertainty.

$$\Delta T_{exp}(t) = \frac{(V(t) - V_1)(R_l + c_{RTD} + m_{RTD}(T_1 - T_0))}{mV_1} \tag{5.1}$$

The transient unit impulse response is calculated by normalising the transient temperature rise by the absorbed energy (E_a) per unit area:

$$h_{exp}(t) = \frac{\Delta T_{exp}(t)}{E_a/A} \tag{5.2}$$

where

$$E_a = \frac{E_{EM} F_D (1 - R_D)}{\overline{E_{s,c}}/\overline{E_{t,c}}} \tag{5.3}$$

in which: E_{EM} is the measured pulse energy of the sampled beam; R_D is the reflectivity of the diamond, which is taken to be 20 % based on multiple sources in the literature for polished surfaces with normal incidence at a wavelength of 266 nm [128, 130]; and the values of $\overline{E_{s,c}}$ and $\overline{E_{t,c}}$ are the mean energy of 200 pulses measured using the energy meter on the sampled and transmitted side of the beam sampler respectively. The ratio $\overline{E_{s,c}}/\overline{E_{t,c}}$ represents the reflectivity of the beam sampler and was found to be 1.39 %.

The full data reduction equation can therefore be written as:

$$h_{exp}(t) = \frac{\Delta T_{exp}(t)}{E_a/A} = \frac{\Delta T_{exp}(t) A}{E_{EM} F_D (1 - R_D)} \left(\frac{\overline{E_{s,c}}}{\overline{E_{t,c}}} \right) \tag{5.4}$$

5.4 Experimental Measurement Uncertainty

The overall relative systematic uncertainty at the 95 % confident interval in the unit impulse response was calculated to be $B_{h_{exp}}/h_{exp} = 11.2\,\%$ by evaluating Eq. (5.5)[1] with the typical measured values and respective uncertainties given in Table 5.1. The diamond in these experiments has a manufacturer-quoted RMS surface roughness of $Ra = 250\,\text{nm}$, whereas the values of reflectivity taken from the literature were found using diamond surfaces with $Ra = 10\,\text{nm}$ [128]. An estimated uncertainty of 30 % for B_{R_D}/R_D is applied. The systematic uncertainty of 5 % for the measurements taken using the energy meter is the value quoted by the manufacturer. The random uncertainties for $\overline{E_{s,c}}$ and $\overline{E_{t,c}}$ are given as two times the standard deviation of the measured values. The systematic errors in the energy measurement are taken to be correlated because each measurement was taken using the same energy meter. The uncertainty associated with misaligning the beam to the diamond, and therefore the

[1] See Appendix C for details on uncertainty analysis.

Table 5.1: Uncertainty analysis for the experimentally measured impulse response.

X_i	Typical Value	B_{X_i}/X_i, %	S_{X_i}/X_i, %
ΔT_{exp}	0.7 K	1.5	n/a
A	4.91 mm^2	0.16	n/a
$\overline{E_{s,c}}$	7.0 µJ	5	5.5
$\overline{E_{t,c}}$	503.0 µJ	5	0.8
E_{EM}	33 µJ	5	n/a
F_D	0.738	3.5	n/a
R_D	0.2	30	n/a
h_{exp}	2.52 mK	11.2	n/a

calculation of F_D, was estimated to be 3.5 % by adding an estimated alignment accuracy offset of 0.25 mm to the assumed centre-point of the profile and re-calculating the fraction of energy which would be incident onto the diamond. The uncertainty in the measured temperature was found to be 1.5 %.

$$\begin{aligned}\left(\frac{B_{h_{exp}}}{h_{exp}}\right)^2 = &\left(\frac{\Delta T}{h_{exp}}\frac{\partial h_{exp}}{\partial \Delta T}\right)^2\left(\frac{B_{\Delta T}}{\Delta T}\right)^2 + \left(\frac{A}{h_{exp}}\frac{\partial h_{exp}}{\partial A}\right)^2\left(\frac{B_A}{A}\right)^2 \\ &+ \left(\frac{E_{sc}}{h_{exp}}\frac{\partial h_{exp}}{\partial E_{sc}}\right)^2\left(\left(\frac{B_{E_{sc}}}{E_{sc}}\right)^2 + \left(\frac{S_{E_{sc}}}{E_{sc}}\right)^2\right) \\ &+ \left(\frac{E_{tc}}{h_{exp}}\frac{\partial h_{exp}}{\partial E_{tc}}\right)^2\left(\left(\frac{B_{E_{tc}}}{E_{tc}}\right)^2 + \left(\frac{S_{E_{tc}}}{E_{tc}}\right)^2\right) \\ &+ \left(\frac{E_{EM}}{h_{exp}}\frac{\partial h_{exp}}{\partial E_{EM}}\right)^2\left(\left(\frac{B_{E_{EM}}}{E_{EM}}\right)^2 + \left(\frac{S_{E_{EM}}}{E_{EM}}\right)^2\right) \\ &+ \left(\frac{F_D}{h_{exp}}\frac{\partial h_{exp}}{\partial F_D}\right)^2\left(\frac{B_{F_D}}{F_D}\right)^2 + \left(\frac{R_D}{h_{exp}}\frac{\partial h_{exp}}{\partial R_D}\right)^2\left(\frac{B_{R_D}}{R_D}\right)^2 \\ &+ 2\left(\frac{\partial h_{exp}}{\partial E_{EM}}\right)\left(\frac{\partial h_{exp}}{\partial E_{sc}}\right)\frac{(B_{E_{EM}})\,(B_{E_{sc}})}{(h_{exp})^2} \\ &+ 2\left(\frac{\partial h_{exp}}{\partial E_{EM}}\right)\left(\frac{\partial h_{exp}}{\partial E_{tc}}\right)\frac{(B_{E_{EM}})\,(B_{E_{tc}})}{(h_{exp})^2} \\ &+ 2\left(\frac{\partial h_{exp}}{\partial E_{sc}}\right)\left(\frac{\partial h_{exp}}{\partial E_{tc}}\right)\frac{(B_{E_{sc}})\,(B_{E_{tc}})}{(h_{exp})^2}\end{aligned} \tag{5.5}$$

The magnitude of each term in Eq. (5.5) is given in Table 5.2 to illuminate how each variable in the data reduction equation (Eq. (5.4)) contributes to the overall uncertainty.

Table 5.2: Uncertainty analysis for the experimentally measured impulse response.

Term in Eq. (5.5)	Implicated Variables	Value $\times 10^3$
1	ΔT	0.225
2	A	0.003
3	E_{sc}	5.525
4	E_{tc}	2.564
5	E_{EM}	2.500
6	F_D	1.225
7	R_D	5.625
8	E_{EM},E_{sc}	−5.000
9	E_{EM},E_{tc}	5.000
10	E_{sc},E_{tc}	−5.000

It is not possible to calculate the standard parameters of Uncertainty Magnification Factor and Uncertainty Contribution Percentage for this case because correlated uncertainties are present. The largest contributor to the overall uncertainty is the reflectivity of diamond, followed by each of the terms relating to measurements made with the energy meter. However, the effect of the correlated uncertainty between the energy meter measurements is to reduce the overall uncertainty.

5.5 Experimental Results

5.5.1 Experimental Temperature Response

Fig. 5.3 shows the experimentally measured unit impulse response of DHTG24 at three initial isothermal temperatures of 25 °C, 45 °C, and 65 °C. The bold line for each temperature is the average of four repeat experiments at the same nominal condition. The individual experiments are the semi-transparent lines of the same colour. The temperature stated in the legend is the mean of the initial temperature measured by the RTD across the four experiments. The mean pulse energy absorbed by the calorimeter across all tests was 1.84 mJ, producing peak temperature rises of around 0.7 K. The experimental uncertainty is indicated

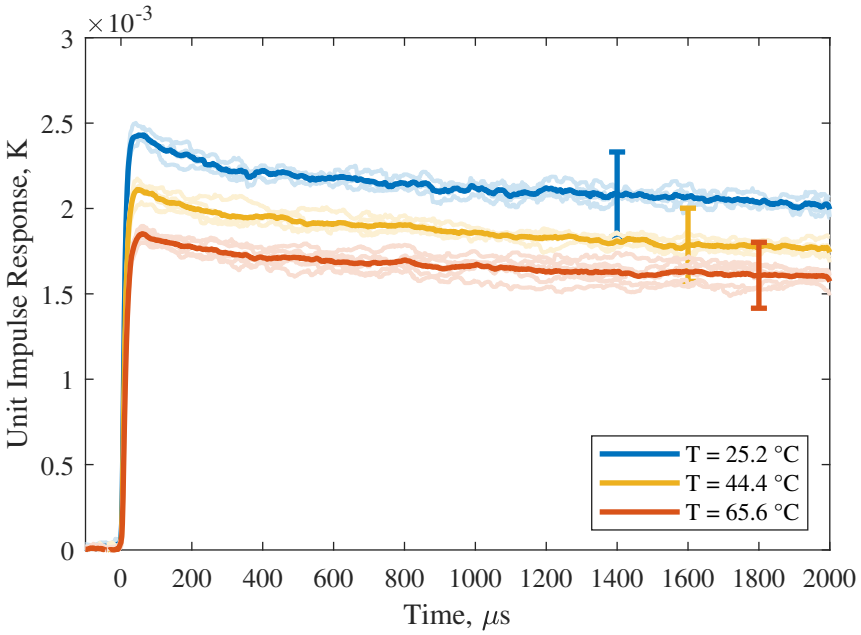


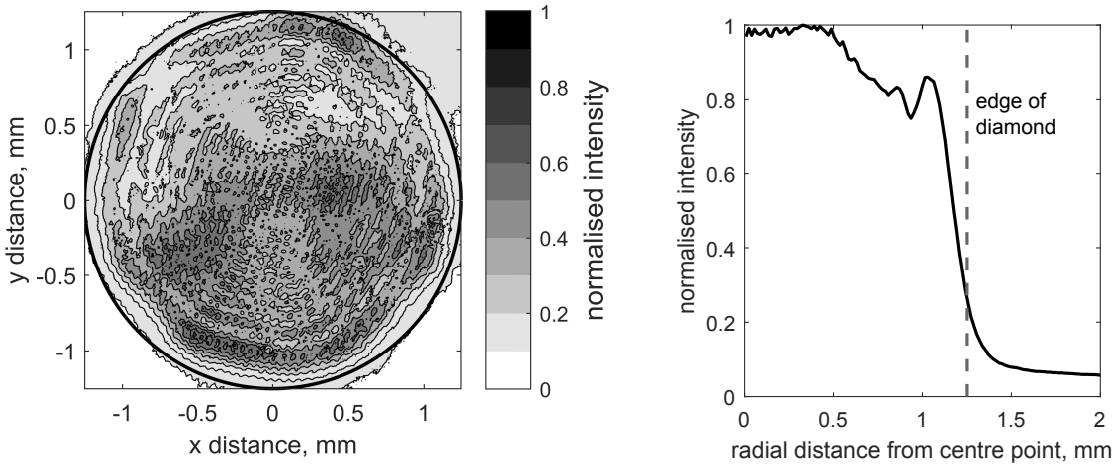
Figure 5.3: Unit impulse response of DHTG24 at three initial temperatures. Bold lines represent the average across all pulses at the indicated temperature.

by a single error bar for the averaged line at each temperature. The data has been filtered using a 20 µs moving median filter to remove noise.

5.5.2 Beam Non-Uniformity

The map of normalised intensity of the laser beam shown in Fig. 5.4b was recorded immediately after the experimental data had been gathered. Figure 5.4 shows the two-dimensional profile averaged, and projected onto a single line of radius. The normalised intensity was calculated by first subtracting the background intensity, found by averaging a small window at the edge of the CCD detector area, and then dividing by the maximum intensity. The intensity varies by 20 % over the central 1.1 mm radius of the diamond surface, with a sharp drop-off outside of this. The radial profile shows that an appreciable amount of energy is incident on the gauge body rather than the diamond, i.e. outside the the 1.25 mm radius marked on Fig. 5.4b. The fraction of the total pulse energy which is incident on the diamond was calculated to be 73.8 % i.e. $F_D = 0.738$ in Eq. (5.4) .

Non-uniformity in the applied heat flux means that immediately following the laser pulse,



(a) (b)

Figure 5.4: (a) Two-dimensional map of beam intensity taken immediately after experiments were performed. The edge of the diamond is indicated by the 2.5 mm diameter circle. (b) The intensity map averaged and projected onto a line of radius.

radial temperature gradients exist across the diamond. The time taken for the diamond to reach isothermal conditions can be approximated using the equation for the 99 % rise time of a calorimeter given by Schultz and Jones [30] as $\tau_R = x^2/(2\alpha)$ (see Section 3.4.2). Following the arrival of the laser pulse, it takes approximately 50 µs ($x = 220$ µm) for the rear surface to equilibrate with the front surface, and 511 µs ($x = 0.75$ mm) for the temperature to equilibrate radially from the edge of the high intensity peak to the edge of the diamond.

The concentration of incident energy toward the centre of the diamond combined with the fact that the thin-film track is not uniformly distributed on the rear surface of the diamond (see Fig. 5.5) mean that on short time-scales, i.e. $t < 511$ µs), the measured temperature response is not equal to what would be measured in response to uniform heating. In an experiment using the DHTG to measure a heat flux it is assumed that the heat flux is spatially uniform over the diamond surface, therefore the experimental measurements of impulse response presented in Fig. 5.3 are not valid for the calculation of experimental heat flux using the SFSM method presented in Chapter 4.

The following section presents a study in which the experimental results are used to tune

the response of a finite element model of the gauge, from which the impulse response of the DHTG with uniform surface heating can be found, thus producing an impulse response which can be used in the calculation of heat flux.

5.6 Tuning FE Model to Experimental Data

5.6.1 Modifications to FE Model

With changes to the surface heat flux boundary condition and how the temperature response of the DHTG is calculated, the axisymmetric FE model described in Chapter 4 was used as the basis for a simulation to model how the DHTG responds to a non-uniform heat flux. Instead of using a spatially uniform pulse as used previously, the intensity profile shown in Fig. 5.4b was used to adjust the heat flux boundary condition applied across the top surface. In the previous study, the temperature response of the DHTG was taken as the integrated temperature across the rear surface of the diamond. This is valid for uniform heating, but, because the RTD in the real gauge is a serpentine track, it is not valid for the highly non-uniform heat flux which the laser produces.

Since the platinum RTD shows linear sensitivity to temperature over the calibrated range, the temperature measured by the RTD in an experiment can be calculated as an integral along the path of the thin-film. The centre-line of the thin-film path was discretised into n sections of equal arc length and parametrised in terms of radial distance from the centre r_n, as shown in Fig. 5.5. The temperature measured by the RTD, as simulated by the FE model, can then be written as:

$$T_{RTD} = \sum_{1}^{N} \frac{T_n(r)}{N} \tag{5.6}$$

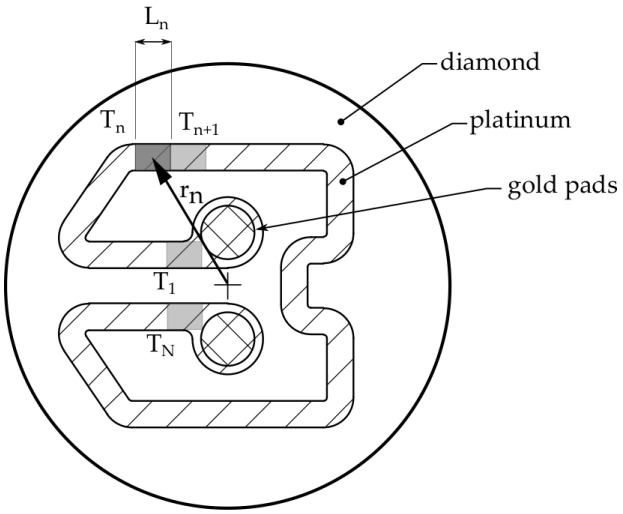


Figure 5.5: The discretisation of the thin-film track into N elements of equal arc-length. Each element measures a temperature T_n and is located at a radial distance r_n from the centre-point.

5.6.2 Results from FE Model

At each of the three nominal isothermal temperatures which the experiment was performed at, the FE simulation was run with varying values of specific heat capacity of the diamond and thermal effusivity of the adhesive until the simulated response matched the experimental response. For the diamond, the density was held constant at the value given in Section 3.5, and only the specific heat capacity was adjusted because the values of density for diamond in the literature show very little variability compared to the specific heat capacity. The thermal conductivity was not adjusted because accurate knowledge of the thermal conductivity is not necessary when calculating a measured heat flux with the DHTG. Considering the adhesive substrate as a semi-infinite medium, the long-term rate of decay of the impulse response is a function of the thermal effusivity. In reality, there is radial conduction and conduction through the gold electrical leads, so simply adjusting the adhesive properties to match the rate of decay of the response finds an effective value which also encapsulates error in the assumed thermophysical properties of the steel and gold.

Figure 5.6 shows, for each initial temperature, the experimental response and the response

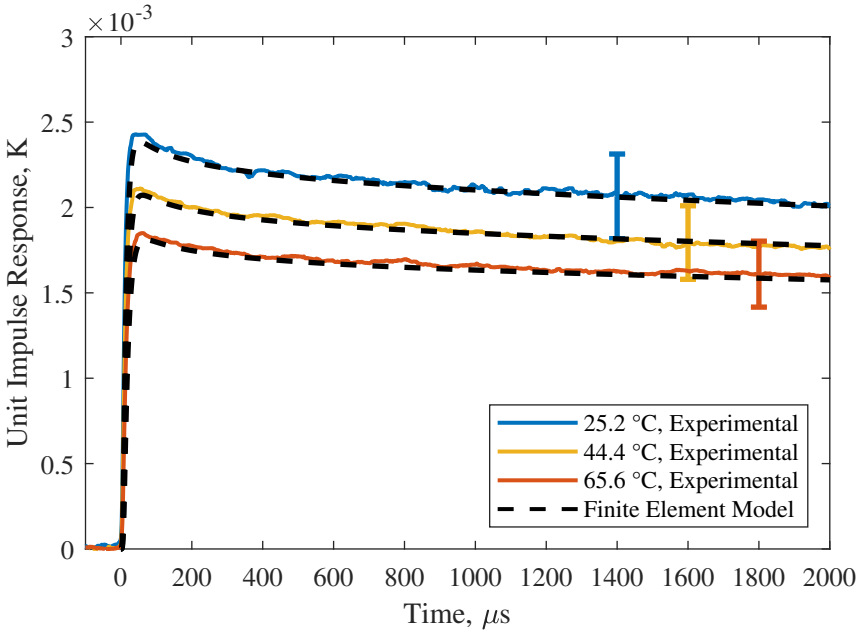


Figure 5.6: The unit impulse response at three initial temperatures with the tuned response from the FE model.

Table 5.3: Comparison of the specific heat capacity of diamond from sources in the literature and that found by tuning the FE model response to experimental response. The uncertainty in the experimental values is the systematic experimental measurement uncertainty. Units are $J{\cdot}kg^{-1}{\cdot}K^{-1}$.

T, °C	Literature c_p	Experimental c_p
25.2	499.8 ± 35.9	535.8 ± 55.2
44.4	559.7 ± 40.4	617.8 ± 63.6
65.6	630.9 ± 45.3	707.5 ± 72.9

from the FE model in which the thermophysical properties have been tuned as described above. The values of specific heat capacity found from the FE model are given in Table 5.3 with the mean values from multiple sources in the literature as given in Section 3.5.1. The same data is plotted in Fig. 5.7, where the difference between the current experiments and the values from the literature can be seen graphically. The values estimated from the current experiments are higher than the literature, but the confidence intervals overlap by a sufficient percentage to conclude that there is no statistically significant difference between the data sets [131].

By tuning the FE model, the effective thermal effusivity of the substrate was estimated

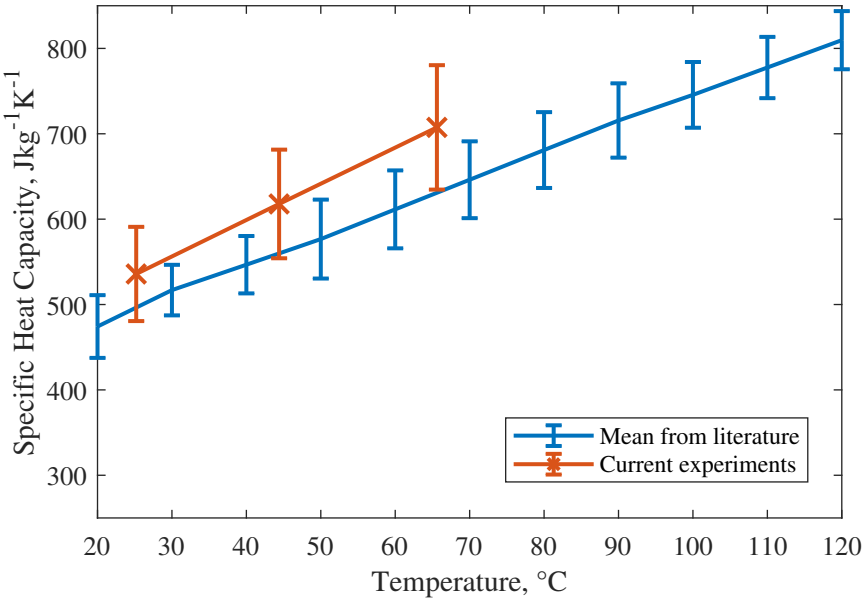


Figure 5.7: Values of specific heat capacity from the current experiments compared to the mean of values from the literature.

to be 866.0 $\mathrm{J{\cdot}m^{-2}{\cdot}K^{-1}{\cdot}s^{-1/2}}$, i.e. 36 % lower than the value of 1370.0 $\mathrm{J{\cdot}m^{-2}{\cdot}K^{-1}{\cdot}s^{-1/2}}$ given in Table 3.2 from the manufacturer material properties. This does not necessarily mean that the thermal properties of the bulk substrate material are different from the value stated by the manufacturer because the value found in this study is an effective value, encapsulating the real conductive loss from the calorimeter. For example, the difference could be due to imperfect thermal contact between the diamond and the adhesive.

The non-uniformity of the beam profile means that the experimental impulse response is different to that which would be measured were a spatially uniform heat flux applied across the full surface of the gauge. Using the material properties derived by matching the finite element simulation to the experiment, the simulations were run again, but with a spatially uniform heat flux distribution. The resulting responses are shown in Fig. 5.8. In the first 200 µs, the non-uniform response over-shoots the uniform response as expected. The long term non-uniform response shows a steeper decay because a larger radial temperature gradient exists for this heating case, resulting in higher radial conductive losses from the calorimeter.

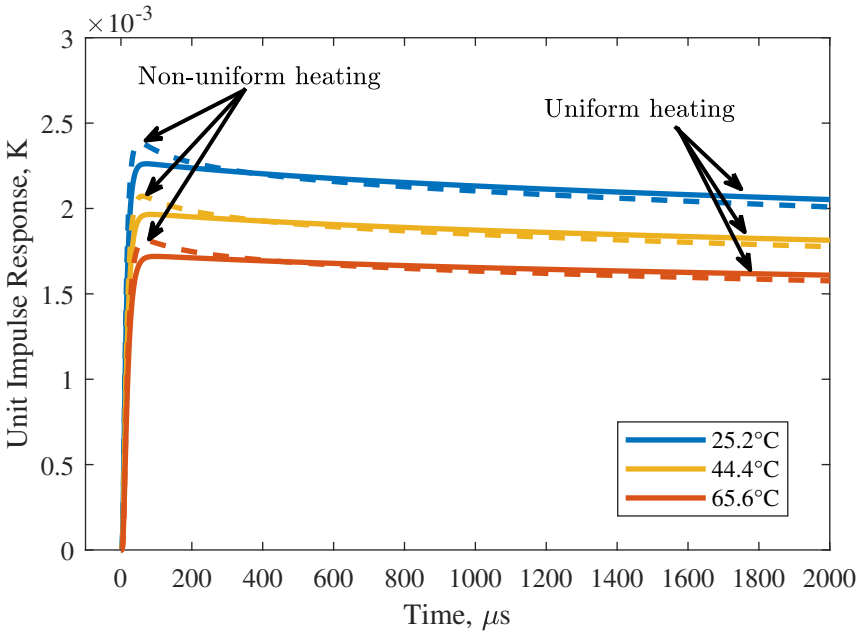


Figure 5.8: Impulse responses from the FE model with both a spatially uniform heating profile, and the non-uniform heating profile given in Fig. 5.4b.

5.7 Chapter Summary

The response of a DHTG to a short-duration pulse of heat flux from a laser has been measured at three initial isothermal temperatures covering a temperature rise which might be seen in pulse-flow facility. Due to spatial non-uniformity in the laser beam intensity, the response measured is not usable for experimental heat flux data reduction using the SFSM method. For this, the impulse response to spatially uniform heating is required.

The experiment was simulated using a Finite Element model, and the specific heat capacity of the diamond and effective thermal diffusivity of the substrate were found by tuning the response from the model to match the experimental response. Using the tuned model, the impulse response was found by applying a spatially uniform heat flux intensity. The specific heat capacity found from the study showed no statistically significant difference when compared to values given in the literature. For this reason, it is recommended that because the data set is more complete, the thermophysical properties from the literature are used to produce impulse responses for experimental data reduction.

5.7. CHAPTER SUMMARY

The two largest contributing factors to the uncertainty in the measured impulse response are due to uncertainty in the reflectivity of the diamond and the measurements taken using the energy meter. Reduction in one or both of these uncertainties would improve the utility of the experiments presented in this chapter, and along with improvement of the spatial uniformity of the beam, would enable the experimental response to be used directly in the SFSM data reduction method.

CHAPTER 6

Experiments in the X2 Expansion Tunnel

Contents

6.1 Introduction **108**
6.2 Experimental Set-up **109**
6.3 Data Reduction and Measurement Uncertainty **111**
6.4 Heat Flux Results **112**
6.5 Robustness Results **118**
6.6 Chapter Summary **122**

6.1 Introduction

This chapter describes an experimental campaign conducted in the X2 expansion tunnel, at the University of Queensland. The two primary aims were: firstly, to evaluate the robustness of DHTGs in an extremely harsh environment, and secondly, to compare the heat transfer measurements with those from existing gauges, and predicted values obtained from empirical correlations. Experiments were performed at a range of flow conditions, with total enthalpies ranging from $25\,\mathrm{MJ{\cdot}kg^{-1}}$ to $70\,\mathrm{MJ{\cdot}kg^{-1}}$, and at a range of angles of attack, from 0° on a flat plate, through to stagnation point. The chapter describes the facility and flow

Table 6.1: Details of the flow conditions for the experimental campaign in X2. All conditions used air as the test gas.

Condition	h_0 MJ·kg^{-1}	V_∞ km·s^{-1}	ρ_∞ g·m^{-3}	p_∞ kPa	T_∞ K	M_∞	Leading Edge	Shot Numbers
A1 [135]	25.3	7.0	1.7	0.62	1300	9.9	Sharp	x2s3482 - x2s3484
A2 [135]	25.3	7.0	1.7	0.62	1300	9.9	Blunt	x2s3504 - x2s3506
B [10]	39.6	8.7	1.0	0.58	2000	10.3	Sharp	x2s3490 - x2s3491
C [136]	53.4	10.1	2.0	1.07	1900	12.2	Sharp	x2s3492 - x2s3494
D [137]	70.7	11.4	1.9	1.99	3150	10.3	Sharp	x2s3495 - x2s3498
E [138]	50.0	8.3	15.3	35.04	5850	5.2	Blunt	x2s3507 - x2s3510

conditions, the experimental model, and gives an analysis of the results in terms of heat transfer measurements and gauge robustness.

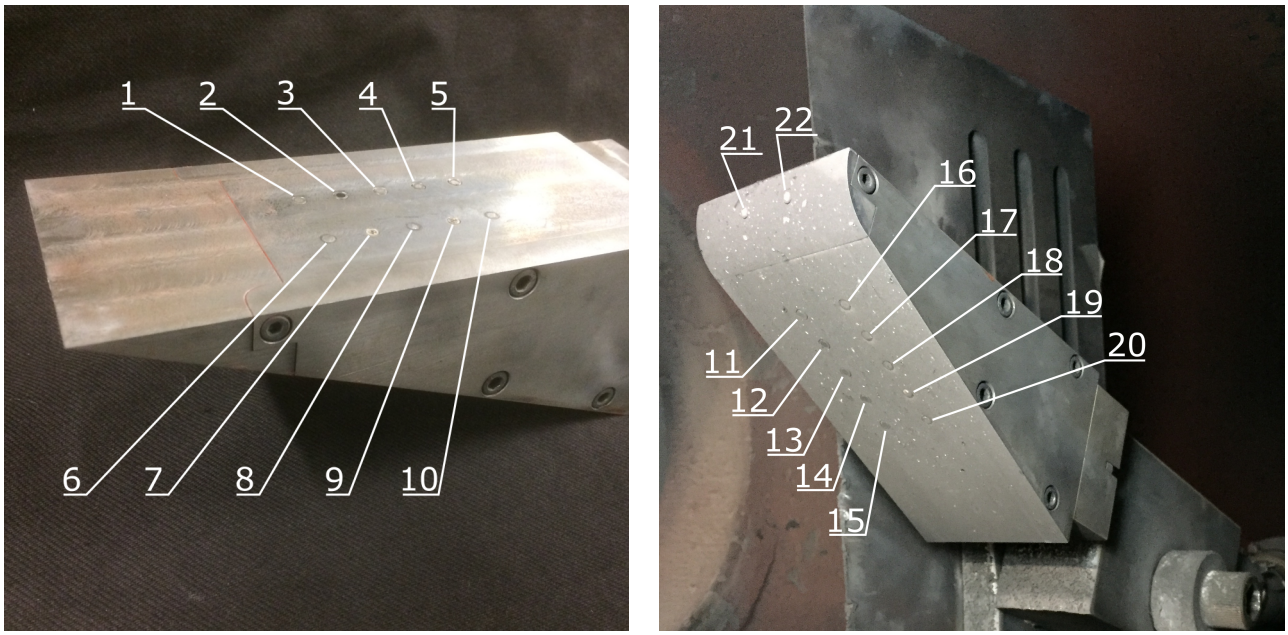
6.2 Experimental Set-up

6.2.1 Facility and Conditions

The X2 facility is a free-piston driven impulse flow wind tunnel which can produce scaled test flow conditions representative of atmospheric entry into most planets in our solar system [132]. The facility was configured as an expansion tunnel with a single driver and a diverging nozzle at the test section entrance. Details of X2 can be found in Gildfind et al. [133]. The nominal test section flow properties for each condition used are shown in Table 6.1. h_0 is the total enthalpy and the subscript ∞ indicates free-stream properties. The flow conditions were calculated from facility fill-pressures and experimentally measured shock speeds using PITOT, a University of Queensland in-house facility simulation code [134]. In addition to the shots mentioned in the table, shots were performed at each condition with a Pitot-pressure probe in the test section to validate the flow conditions.

6.2.2 Model and Instrumentation

The test model used had two configurations shown in Fig. 6.1 with labelled hole numbers indicating the location of heat transfer gauges. The first configuration is a 140 mm long, 22.5° sharp wedge, mounted such that the top side was at 0° angle of attack. The second configuration has a blunt nose with a radius of 21.7 mm and was angled such that the bottom side was at 45° angle of attack.



(a) Sharp leading edge.

(b) Blunt leading edge.

Figure 6.1: Photos of the model used for experimental testing in X2 with hole numbers labelled.

The model was instrumented with 10 DHTGs, 8 coaxial surface-junction thermocouples, and 2 thin-film heat transfer gauges. The top side had five DHTGs (holes 1 to 5), three thermocouples (holes 6, 8, and 10), and two thin-film gauges (holes 7 and 9). The underside had five DHTGs (holes 11 to 15) and five thermocouples (holes 16 to 20). Two additional DHTGs were mounted on the stagnation point when the blunt leading edge was attached (holes 21 and 22). The thermocouples, which were manufactured at the University of Southern Queensland, have an outer diameter of 3.2 mm, are Type-E (chromel-constantan). The

surface junction was made by scratching the surface of the gauge twice with the probe tip of a multi-meter, producing an "X" pattern. Further details about the gauges can be found in Ref. [26]. During the experimental campaign DHTGs which were significantly damaged or broken were replaced whereas the thermocouples were glued permanently into the model and were not moved or replaced.

6.3 Data Reduction and Measurement Uncertainty

Constant current supply and signal amplification for the DHTGs was provided by the University of Queensland HTG3 amplifiers which have a bandwidth of 350 kHz. After removing the amplifier gain, the voltage recorded for the DHTGs was processed into temperature using Eq. (D.2). The heat flux was calculated using the calorimeter-based data reduction method presented in Section 3.4.1 (i.e. Eq. (3.5)). The specific heat capacity of the diamond used in the data reduction equation was updated at each time-step according to the measured thin-film temperature using the temperature-dependent properties presented in Fig. 3.4a. The SFSM method was not used because analysis in Section 3.7.3.2 showed that the calorimeter method is sufficiently accurate for the short test-durations of up to 200 µs in X2. Additionally, high levels of measurement noise meant the improvement the SFSM method can provide to response time was negligible (see Section 4.5.5 for a discussion of the effect of noise magnitude on data reduction).

An in-house thermocouple amplifier with a quoted response time of 1 µs [135] was used to amplify the thermocouple response. Temperature rise was calculated using a sensitivity of 62.5 $\mu V \cdot K^{-1}$ [56]. To calculate the heat flux, the impulse response method developed by Oldfield [36] was applied, using the standard assumption of one-dimensional semi-infinite conduction into a homogenous medium. The effective value of thermal effusivity was taken to be 8900 $J \cdot m^{-2} \cdot K^{-1} \cdot s^{-1/2}$ [56]. This value is believed to be correct for junctions made by scratches [26], but could be an over-estimate on the short test-times of the current experi-

ments, as discussed in Section 2.3,

Data was recorded at a sampling rate of 2.5 MHz for all sensors. The heat flux signals from the DHTGs and thermocouples were filtered using low-pass filters with cut-off frequencies at the approximate bandwidth of each type of sensor. A cut-off frequency of 50 kHz was used for the DHTGs. Based on a response time of 1 µs to 2 µs [56], a cut-off frequency of 350 kHz was used for the thermocouples.

The measurement uncertainty for the DHTGs in this experiment is equivalent to the analysis presented in Appendix D.3, which was 7.3 %, with the addition of uncertainty in the measured temperature change, estimated to be $\mathcal{X}_{\Delta T} = 1.5\,\%$. Combining these, the overall measurement error excluding the conceptual error due to the data reduction equation, is 7.5 %. As discussed in Chapter 2, the uncertainty in the heat flux measured by the thermocouples depends on a large number of factors and changes with the time-scale of interest. Simple analyses in the literature which do not take into account time-dependent errors give a best-case uncertainty of approximately 10 % [66, 70], although transient errors on the time-scale of the testing presented will be significantly higher.

6.4 Heat Flux Results

6.4.1 Example Measurement

Figure 6.2 shows a trace of test-section Pitot pressure from shot x2s3485 along with temperature rise, and heat flux from shot x2s3504, from a DHTG on the stagnation point. Both shots were nominally the same, at Condition A2, but the Pitot pressure rake and model could not be mounted simultaneously. When a shot is fired, the gas in the acceleration tube is the first to enter the test section and is seen as the initial peak in the heat flux and pressure traces. The test gas then arrives and there is a period of relatively steady pressure which is the useful test time and is indicated on this plot, and all subsequent plots of heat transfer, as the area between the grey regions. During the first half of test time, the measured heat

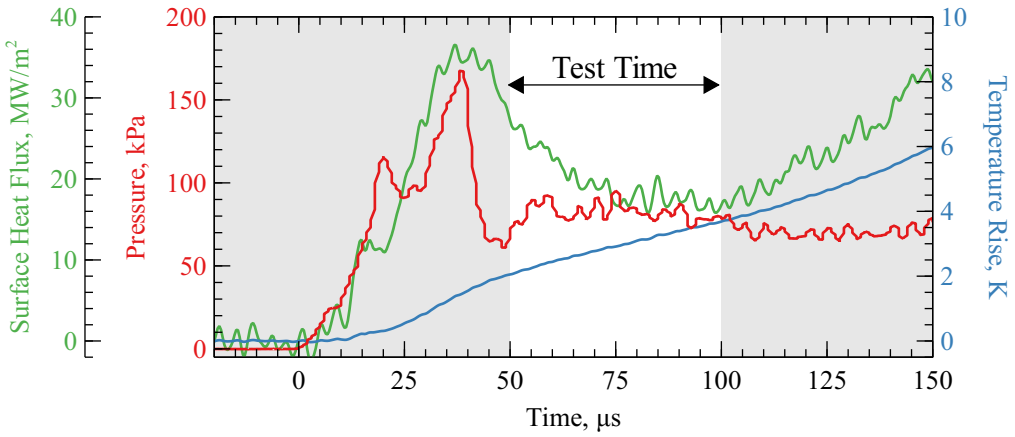


Figure 6.2: Pitot pressure from shot x2s3485. Stagnation point temperature rise and heat flux for DHTG7, shot x2s3504.

flux is still falling from the initial peak. Due to the finite response time of the gauge, only the end portion of the measurement during the test time will be accurate. The end of the test time is dictated by the arrival of the unsteady expansion which processed the test gas and is seen as a gradual rise in measured heat flux.

6.4.2 Results at Each Flow Condition

The surface heat flux measured by a DHTG and a thermocouple at an equal distance from the leading edge are compared in Fig. 6.3 for one of the shots performed at each flow condition. Note that DHTG7 is used for Conditions A2, B, D and E, while DHTG13 is used for condition A1, and DHTG14 is used for condition C. Table 6.2 gives the the test-time averages of these measurements, and shows the percentage difference between the two types of gauge. For each shot, the DHTGs measure a lower initial peak when the accelerator gas arrives due to a slower response time than the thermocouples. The test-time follows, where there is agreement between the two types of gauge to within 10 % for all conditions except condition A1 and E, where the TC measures a significantly higher heat flux.

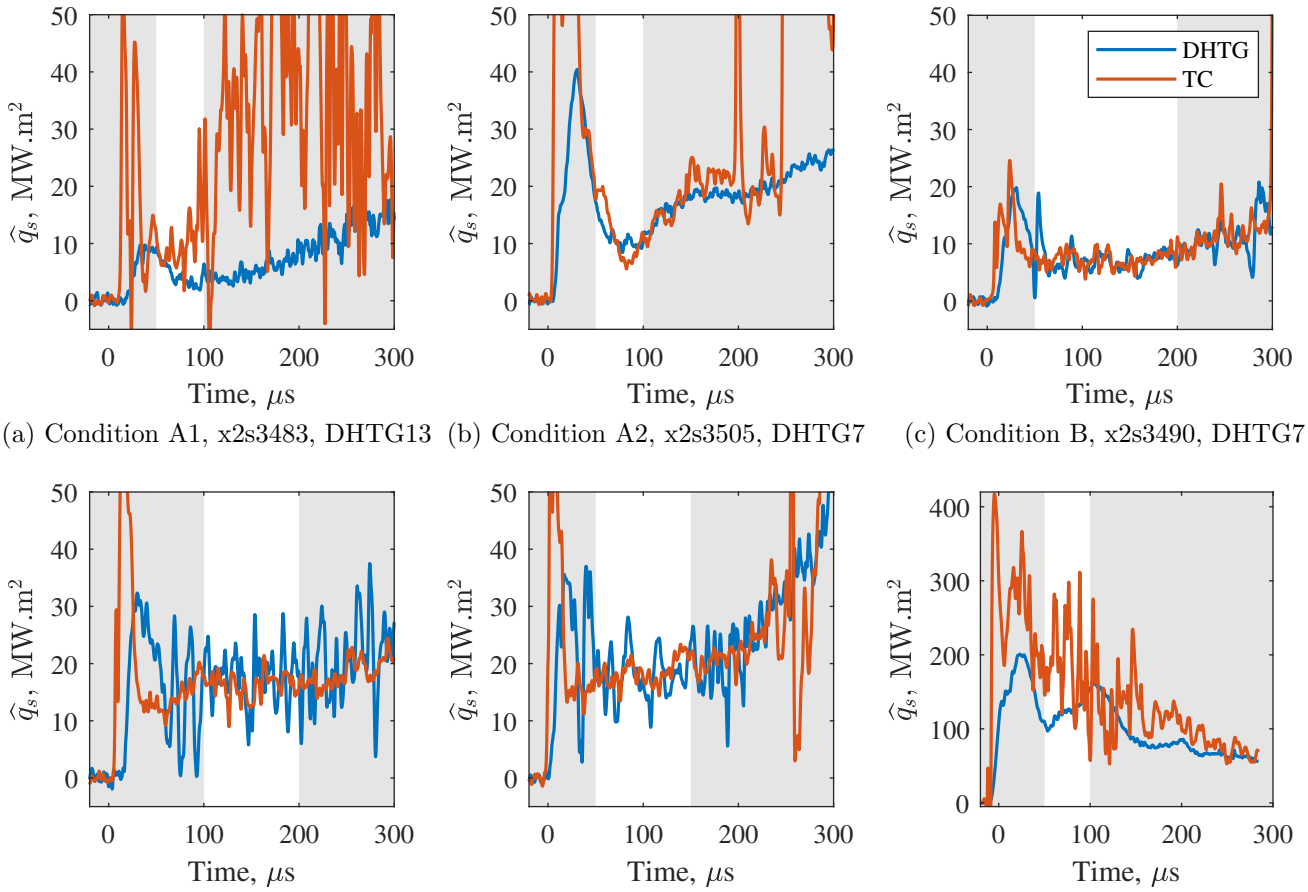
Stagnation point heat flux scales with $V_\infty^3\sqrt{\rho_\infty/R_n}$, and on the flat under-side of the model the heat flux also scales with the angle of attack. These trends are shown in the results:

Table 6.2: Test-time average heat fluxes of the data presented in Fig. 6.3. Percentage differences are in reference to the DHTG.

Condition	DHTG $MW \cdot m^{-2}$	TC $MW \cdot m^{-2}$	Difference %
A1	4.1	10.5	154.5
A2	10.2	11.5	12.3
B	7.4	7.2	−2.5
C	17.8	16.1	−9.2
D	18.4	18.5	0.6
E	129.0	185.1	43.5

an increase in average heat flux during the test time is seen moving through Condition A1, B, C, D, which represents an increase in flow enthalpy at roughly constant density, and at a constant angle of attack. When the angle of attack is increased and the blunt leading edge is used, the measured heat flux increases, as seen by comparing Condition A1 to A2. Comparing the two conditions with the blunt leading edge, the heat flux of Condition E is an order or magnitude greater than that of Condition A2 due to the increase in enthalpy and free-stream density.

The measured heat flux from both types of heat transfer gauge have large oscillations for some shots. This is most noticeable for the DHTGs at conditions C and D, and for conditions A1 and E and for the TC. The oscillations for the DHTG are thought to be due either due to poor signal to noise ratio, possibly from an intermittent electrical fault leading to poor grounding or shielding, or from vibrations in the model giving spurious readings. It is believed that for condition A1, the thermocouple was damaged in some way, or an electrical contact was made during the shot leading to the erroneously large heat flux measurement. The oscillations seen for condition E were also seen on many other shots at this condition, which are not presented here. The faster response time of the thermocouples means that they are able to measure higher frequency heat flux content than the DHTGs, meaning it is possible that the oscillations are caused by surface heating that the thermocouples can resolve but the DHTGs cannot. However, the post-shock temperature for Condition E was estimated to



(a) Condition A1, x2s3483, DHTG13 (b) Condition A2, x2s3505, DHTG7 (c) Condition B, x2s3490, DHTG7

(d) Condition C, x2s3492, DHTG14 (e) Condition D, x2s3495, DHTG7 (f) Condition E, x2s3507, DHTG7

Figure 6.3: Measured heat flux from a DHTG and a thermocouple for one shot at each condition.

be greater than 11 000 K and contain ionised species and free electrons. These species could interfere with the exposed metallic junctions and produce the oscillations. Previous authors using similar gauges have also noted noisy measurements after repeated high enthalpy shots, and suggest it may be due to surface damage [56], although the mechanism for this is unclear.

6.4.3 Results for Condition A2

In Fig. 6.4, the experimental stagnation point heat flux measurements from all three shots at Condition A2 are compared to an estimate calculated using the Fay and Riddell equation [139] for equilibrium flow with a two-dimensional stagnation line given in Appendix E.

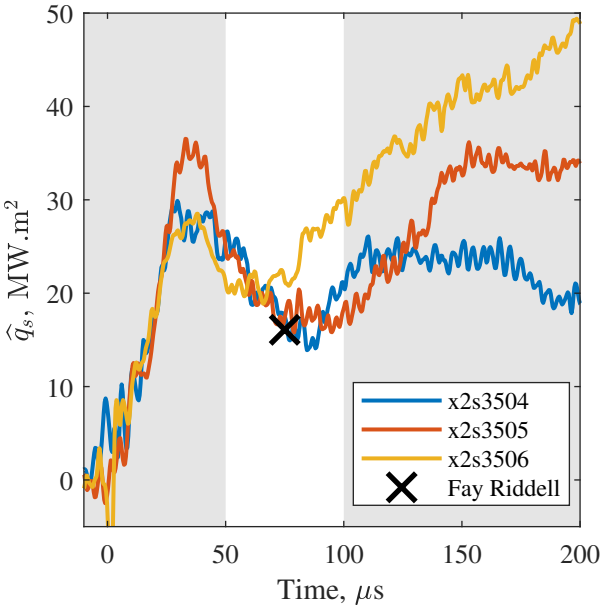
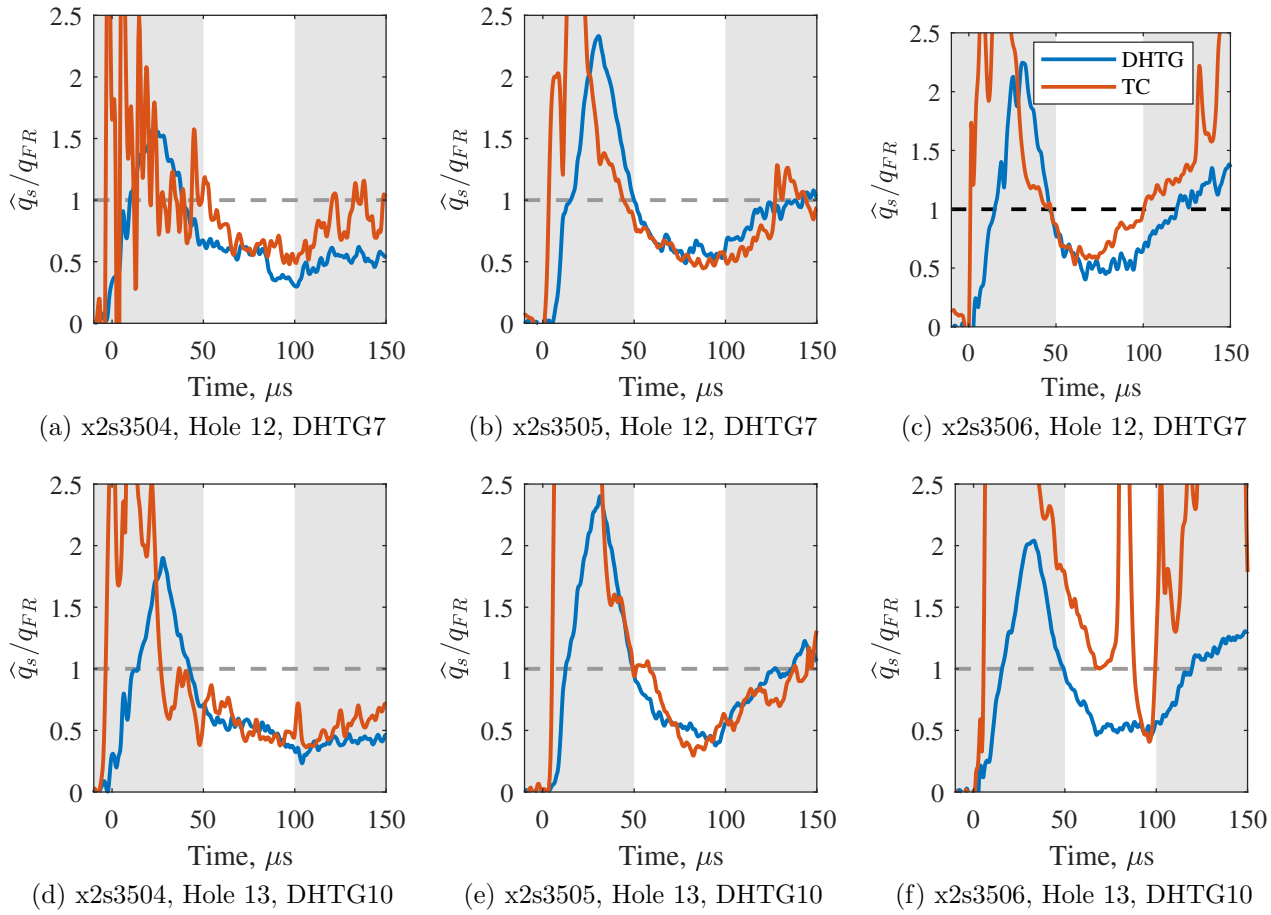


Figure 6.4: Stagnation point heat flux from DHTG11 and the Fay-Riddell prediction for three shots at Condition A2.

The NASA CEA code [140] was used to calculate equilibrium flow properties for each flow state in the calculation of q_{FR}. DHTG11 is a Type 3 DHTG with 99 % response time of 54.4 µs and a 95 % response time of 39.1 µs (see Section 3.7.3.2), so only the latter portion of the 50 µs test time should be compared to the predicted value. This is shown to agree well for the first two shots, but for the third shot, x2s3406, the DHTG measurement is erroneously high due to damage to the gauge which is discussed in the following section.

Figure 6.5 shows the measured heat fluxes at two locations along models for Condition A2 normalised by the Fay Riddell estimate of stagnation point heat flux. In each plot, the measured heat flux from a DHTG and a thermocouple at equal distances from the leading edge are shown. For most of the shots, the agreement between the gauges is good with the notable exception of the final plot, shot x2s3506. For this shot, the thermocouple measures a significantly higher heat flux than the DHTG. The reason for the discrepancy is unclear, but it can be assumed that the sharp spike in heat flux at 80 µs is not physical and is most likely the result of a brief electrical fault. As in previous figures, the initial peak measured by the thermocouple is significantly higher due to their shorter response time.



(a) x2s3504, Hole 12, DHTG7 (b) x2s3505, Hole 12, DHTG7 (c) x2s3506, Hole 12, DHTG7

(d) x2s3504, Hole 13, DHTG10 (e) x2s3505, Hole 13, DHTG10 (f) x2s3506, Hole 13, DHTG10

Figure 6.5: Heat flux from a DHTG and a TC for Condition A2, normalised by the Fay and Riddell stagnation point value. Each column is a distinct shot number. Each row is a constant axial distance from the leading edge.

6.4.4 A Note on Thermocouple Effective Thermal Effusivity

In Chapter 2, the result of studies into the effective thermal effusivity of surface-junction thermocouples on short time-scales were presented. Many studies were shown to concur that due to the proximity of the junctions to the insulation layer between the two thermocouple elements, the value of effective thermal effusivity could be significantly lower than the average of the bulk materials, by 5 % to 60 % (see, for example, Marineau [63], Li [64], Buttsworth [61]). Apart from the two cases discussed above, good agreement is shown between the heat flux measurements from the thermocouples and DHTGs despite the use of bulk value of thermal effusivity for the thermocouples. The agreement lends weight to the theory suggested by Buttsworth [66] and James [26], that the effective thermal effusivity of thermocouples with scratched junctions, as used here, is closer to the bulk value than other methods.

6.5 Robustness Results

Before each shot in the experimental campaign, a photo was taken of the surface of each heat transfer gauge and the electrical resistance was measured. A change in resistance indicates that damage has propagated through the diamond layer and damaged the thin-film. If this happens, then the static calibration used to calculate the temperature rise may no longer be valid. The survival rate for DHTGs on the flat plate side of the model was 100 %, with no visual signs of damage seen and no change in resistance detected. Of the eight DHTGs that were used at an angle of attack, four ended the campaign having been used for 17 shots with visual surface damage but without a change in resistance. Four gauges were destroyed, surviving between one and four shots. The sample size was not large enough to draw conclusions about the effect of diamond thickness on robustness.

To illustrate how damage can be seen through the measurement of resistance and visually through surface damage, the final seven shots of the campaign are considered, Conditions A2

and E. The resistance measured for these shots is shown in Fig. 6.6. The measurements were taken immediately before the labelled shot was fired. The resistance of DHTG7 changes negligibly during these shots. This gauge had been in use since the beginning of the campaign without resistance change. Figure 6.7 shows a photograph before the campaign and at the end of the campaign when the gauge had been in use for 17 shots. Signs of surface abrasion can be seen, but not of large impacts. DHTG10 on the other hand shows a very dramatic change in resistance during shot x2s3508. Figure 6.8 shows a photograph of the surface before and after this shot. A direct impact from a diaphragm fragment is clear on the latter photograph. This impact must have significantly damaged the thin-film. DHTG11 was mounted on the stagnation point, where the most damaged would be expected. The resistance is shown to change with every shot, indicating repeated impacts which did not fully sever the thin-film. The photos in Fig. 6.9 compare the surface before being used, and after 6 shots, with signs of multiple impacts visible. The calibration described in Appendix D was repeated for this gauge after shot x2s3510. The results were significantly different to those obtained from the calibration prior to the experimental campaign, confirming that change in resistance at room-temperature is a good indication that the heat transfer data is not useful.

The analysis presented suggests that a singular large impact from a diaphragm fragment can break the thin-film on the rear surface of the diamond, whilst many smaller impacts have the effect of surface abrasion and damage does not propagate to the rear surface and affect the thin-film. The thermocouples required the surface junction to be re-scratched between some shots, however all but one of the thermocouples used was still functional at the end of the campaign.

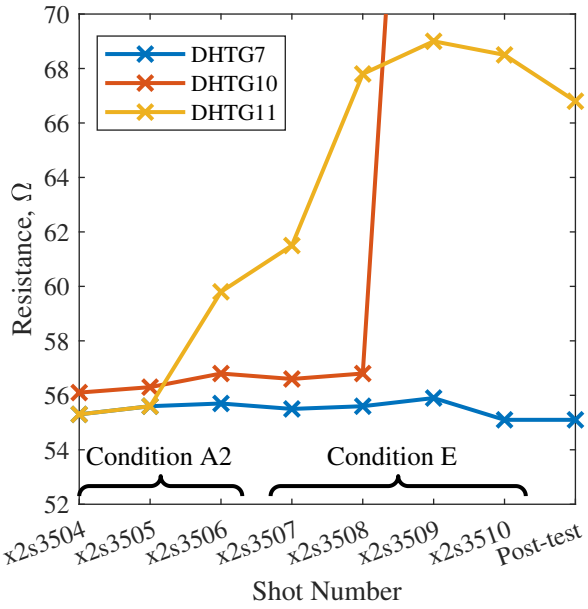
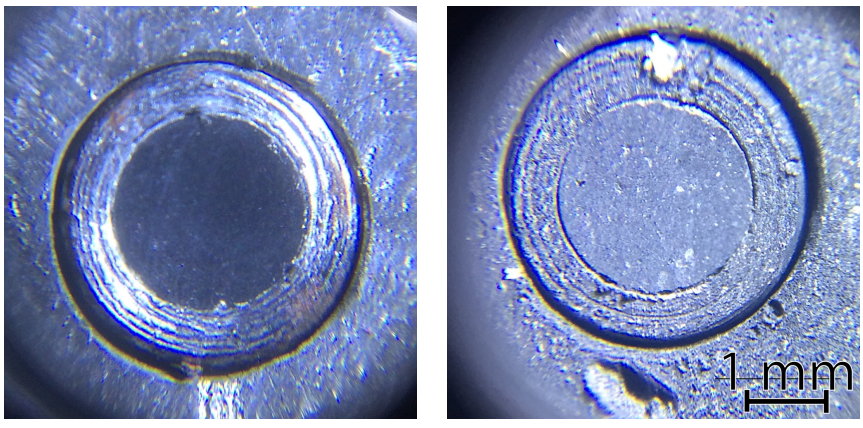
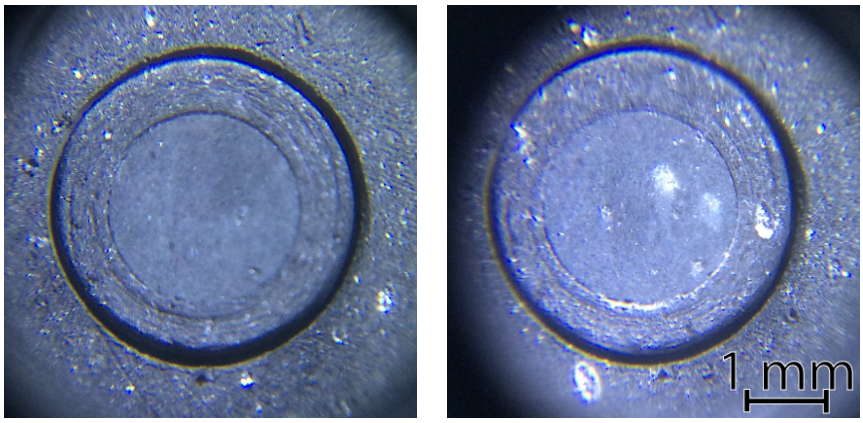


Figure 6.6: Electrical resistance measured immediately before the labelled shot number.



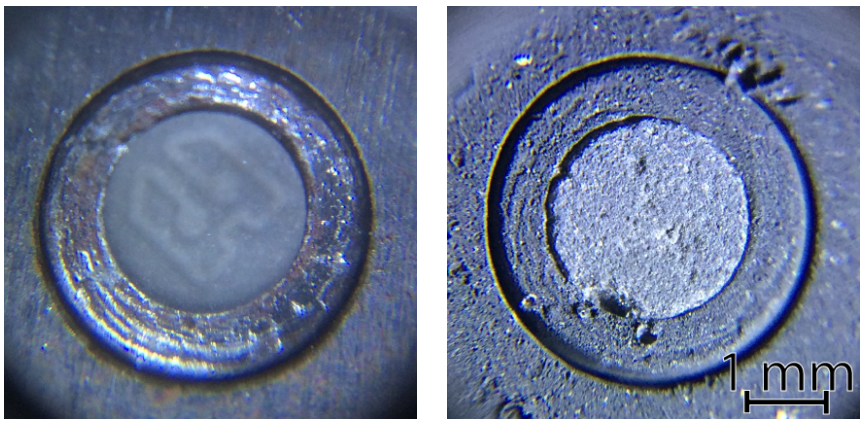
(a) Pre-Testing (0 shots). (b) Post-Testing (17 shots).

Figure 6.7: Photos of the surface of DHTG7.



(a) Post-x2s3507 (4 shots). (b) Post-x2s3508 (5 shots).

Figure 6.8: Photos of the surface of DHTG10.



(a) Pre-x2s3504 (0 shots). (b) Post-x2s3510 (6 shots).

Figure 6.9: Photos of the surface of DHTG11, which was located on the stagnation point.

6.6 Chapter Summary

The DHTG is shown to be a viable method of measuring surface heat fluxes in an expansion tunnel. Heat fluxes measured by a DHTG and a coaxial surface-junction thermocouple are shown to agree within 12 % across the majority of the conditions tested at. The exceptions were Conditions A1 and E, where the reason for the discrepancy between the two types of gauge requires further investigation. Stagnation point measurements made by the DHTG are shown to agree with the Fay and Riddell equation [139], for two shots before the gauge is damaged.

DHTGs mounted at 0° remained undamaged throughout the campaign. While four DHTGs survived up to 17 shots at a variety of flow conditions at angles of attack of either 12.5°, 22.5°, 45° and 90°, the remaining four were destroyed within four shots. This demonstrates that DHTGs are robust, but more susceptible to damage from diaphragm particles than coaxial thermocouples when mounted at angles of attack in an expansion tube environment.

CHAPTER 7

Experiments in the T6 Reflected Shock Tunnel

Contents

7.1 Introduction **123**
7.2 Experimental Set-Up **124**
7.3 Fill Conditions, Flow Conditions, and Test-Time **127**
7.4 Data Reduction and Measurement Uncertainty **131**
7.5 Robustness Results **133**
7.6 Heat Flux Results **137**
7.7 Chapter Summary **145**

7.1 Introduction

The aim of the experiments presented in this section was to evaluate and compare the use of DHTGs in a reflected shock tunnel to current standard instrumentation: thin-film gauges and surface-junction thermocouples. Previous experiments in the X2 expansion tube, a much more destructive environment, showed that the DHTGs were not damaged at all when mounted on a flat plate, so the experiments here focus on stagnation point measurements only. The three types of heat transfer gauge were flush-mounted in cylindrical probes with

rounded corners which were installed in a rake in the T6 test-section, alongside Pitot-pressure probes. This chapter firstly presents the set-up of the experiments, followed by details of the fill conditions, flow conditions, and the determination of the useful test-time. Then, the heat flux measured by the three types of gauges are compared to each other, and to the Fay Riddell [139] stagnation point heating correlation. Finally, the robustness of the gauges is analysed by looking at measurements of electrical resistance of each gauge between shots and microscope photographs of each gauge surface before and after testing.

7.2 Experimental Set-Up

7.2.1 The T6 Facility

The experiments presented in this chapter were performed in the T6 Stalker Tunnel at Oxford University. A brief description of the operation of the facility follows, but more information regarding the history, operation, and commissioning can be found in Refs. [141, 18, 24, 142]. The facility is a multi-mode free-piston driven pulse-flow wind tunnel, configured as a Reflected Shock Tunnel for the current experiments. A CAD schematic of T6 is shown in Fig. 7.1. The free-piston driver is used to drive a strong shock into the driven tubes by bursting the primary diaphragm, which was 1.2 mm thick stainless steel with a 0.45 mm score depth for all shots presented here. The shock travels down the driven tubes and is reflected from the end-wall at the secondary diaphragm station, just upstream of the nozzle's geometric throat. The gas processed by the reflected shock is now in a quasi-steady state, known as the nozzle supply condition. This hot, high pressure gas bursts the secondary Mylar diaphragm separating the driven tubes from the evacuated test-section and dump-tank, and begins to flow through the nozzle and into the test-section. The useful test-time begins once the flow through the nozzle reaches a steady state. The nominally Mach 7 nozzle was designed using perfect-gas equations and is therefore only strictly a Mach 7 nozzle for low-enthalpy flows. It has a throat diameter of 18.3 mm and an exit diameter of 211.1 mm,

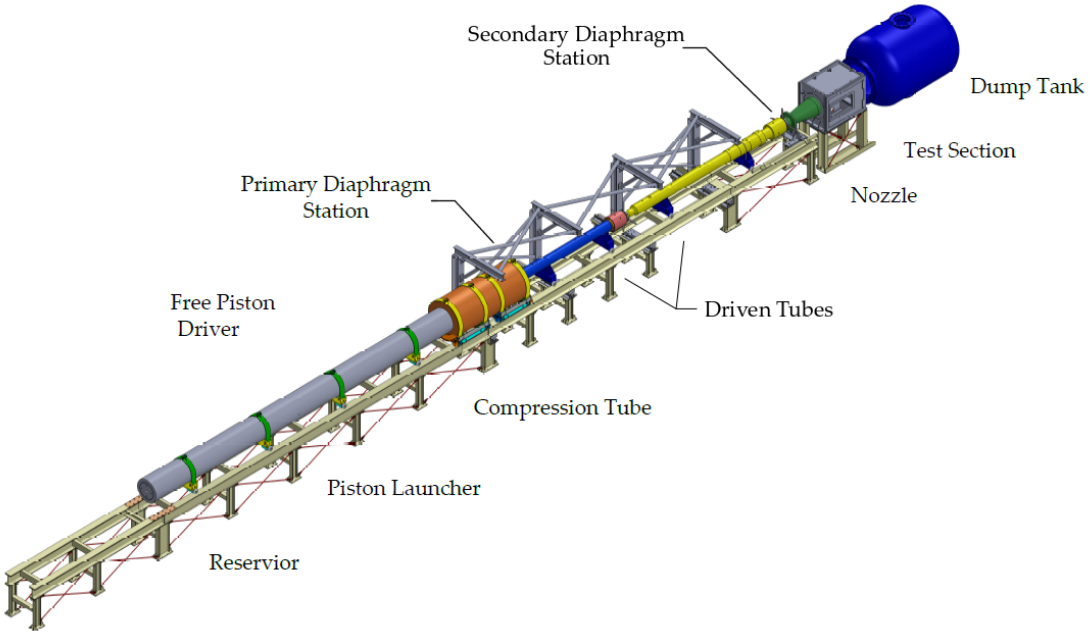


Figure 7.1: CAD schematic of T6 configured as a reflected shock tunnel, adapted from McGilvray et al. [24].

giving a geometric area ratio of 133.1.

7.2.2 Heat Transfer Instrumentation

Table 7.1 gives details of the three heat transfer gauges used in the current experiments. DHTG31 is a Type 2 gauge with a calorimeter thickness of 220 µm. The thin-film gauge was manufactured at the University of Queensland. The temperature sensitive element is a strip of nickel which is sputtered on the surface of a 3.9 mm diameter quartz cylinder. Refs. [43, 143, 56] provide further information on the design and construction of the TFG. The thermocouple is the same as that used in the experiments in X2 presented in the previous chapter: it is a coaxial Type E thermocouple which uses a thin oxide layer for electrical insulation between the elements. For the current experiments, the surface junction was made by abrasion with 400 grit sandpaper. The thermocouple was manufactured at the University of Southern Queensland, more information can be found in Refs. [61, 26].

The sensitivity and value of R_0 for the DHTG and TFG were obtained using the water-

Table 7.1: Details of the heat transfer gauges used in the experiments presented in this section.

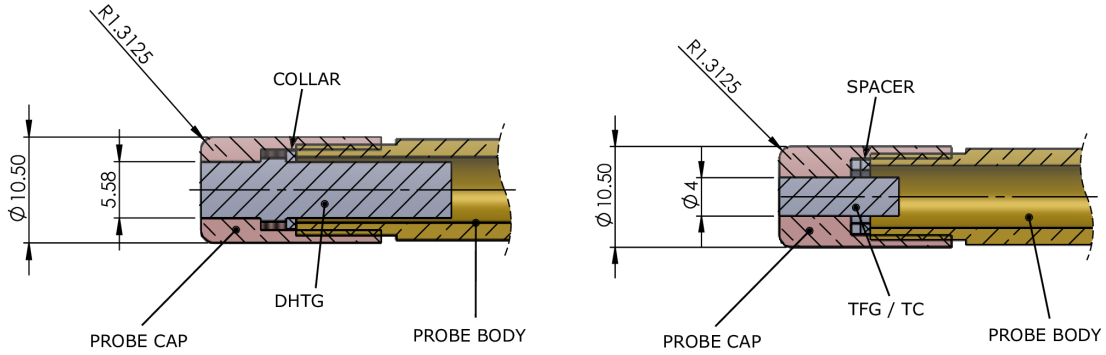
Gauge	Sensitivity	R_0, Ω	$\sqrt{\rho ck}$, J·m^{-2}·K^{-1}·s$^{-1/2}$	Serial Number
DHTG	$m = 0.1349\,\Omega\cdot\mathrm{K}^{-1}$	50.5	n/a	DHTG31
TFG	$m = 0.0413\,\Omega\cdot\mathrm{K}^{-1}$	29.49	1540 [43]	LW36702
TC	$S = 62.5\,\mu\mathrm{V}\cdot\mathrm{K}^{-1}$ [145]	n/a	8900 [145]	n/a

bath calibration method given in Appendix D.2. Values of thermal effusivity ($\sqrt{\rho ck}$) are given for the TFG and TC as they are required to calculate heat flux from a measured temperature change one-dimensional semi-infinite analysis.

An HTA3 amplifier [129, 36] was used to provide a constant current supply and amplify the response of the DHTG and the TFG. The HTA3 amplifier has bandwidth of 340 kHz and gain profile that rises with frequency to counteract the falling sensitivity of the heat flux gauges (this behaviour is discussed in Section 3.5.4), and hence reduce digitisation errors. A FYLDE FE-351-UA [144] differential amplifier with a gain of 1000 and a bandwidth of 100 kHz was used to amplify the thermocouple response.

7.2.3 Probe Design

The heat transfer gauges were mounted in brass caps with a base radius of $R_b = 5.25\,\mathrm{mm}$ and a corner radius of $R_c = 1.31\,\mathrm{mm}$, i.e. $R_c/R_b = 1/4$. Cross-sectional drawings of the caps are shown in Fig. 7.2. While the DHTG is held into its cap mechanically, both the TC and thin-film had to be fixed into their cap using epoxy. The thermocouple and thin-film gauge have the same radius, and so were mounted in identical caps. Kemp [146] showed that for a body of this geometry in flows with partially dissociated air and Mach numbers ranging from 7 to 10, the heat flux is constant from $r = 0$ to $r = R_b/2$, where r is the radial distance from the centre of the cap. The area with constant heat flux covers the sensing area of all three types of gauge, meaning the heat flux measured should be the same.



(a) DHTG. (b) TC and TFG.

Figure 7.2: Drawings of the stagnation point probe caps.

7.2.4 Experimental Installation

Figure 7.3 shows a photograph of the rake installed in the T6 test-section. Each hole in the rake is numbered, and an indication of the type of gauge is given. Each location either had a PCB pressure transducer, or a heat transfer gauge. Details of the specific gauges and the distance from the centreline are given in Table 7.2. Electrical cables exit the rake through the hollow sting, and through cable feed-throughs on the side of the test-section.

7.3 Fill Conditions, Flow Conditions, and Test-Time

Table 7.3 gives details of the fill conditions of the driven tube (state 1), the fill conditions of the driver (state 4), the nozzle supply conditions (state 5), and the nozzle exit conditions (state 7). Details about the development of the condition can be found in Ref. [142]. The nozzle supply and nozzle exit conditions were found using the ESTCj (Equilibrium Shock Tube Conditions, junior) program [147]. The program calculates flow properties using zero-dimensional state-to-state modelling of the processes in the driven tube and assumes thermochemical equilibrium compositions at all stages. The nozzle supply state is calculated by processing the gas initially in the driven tube through an incident shock and reflected shock. The velocity of the incident shock, V_{ss}, is measured experimentally using fast-response

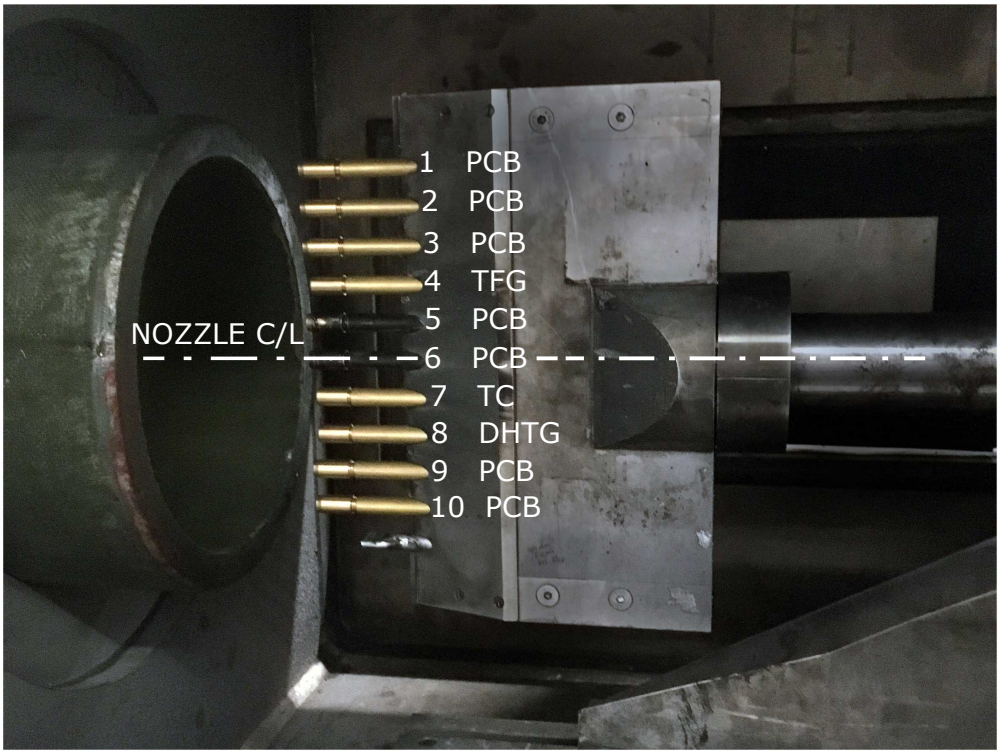


Figure 7.3: Photograph of the rake in the T6 test-section with rake positions and gauge types labelled. The nozzle exit can be seen on the left.

piezoelectric pressure transducers located at intervals along the length of the driven tube. The resulting gas state is isentropically expanded until the pressure matches that measured by transducers located closest to the end-wall (at the entrance to the nozzle) . The nozzle exit state is calculated by processing the nozzle supply gas through an isentropic expansion until the calculated Pitot pressure matches the experimental measurement from pressure transducers in the rake. The geometric area ratio of the nozzle is not used, eliminating error due to uncertainty in the effective area ratio as a result of the boundary layer.

A full uncertainty analysis has not yet been conducted for the flow conditions in T6. However comprehensive studies using the same methodology to calculate the free-stream properties, i.e. ESTCj, exist for T4 at the University of Queensland [148, 149]. Given that T4 [150] is a very similar facility to T6 and uses much the same instrumentation for shock timing, stagnation pressure, and Pitot pressure measurements, uncertainties from T4 can serve as an initial estimate for T6, and are given in Table 7.3. A comprehensive study to

Table 7.2: Details of the pressure sensors and heat flux gauges in the rake. Location numbers correspond to those labelled on Fig. 7.3.

Location Number	Distance to Centreline (mm)	Gauge Type	Serial Number
1	100	PCB 113B21	LW36702
2	80	PCB 113B27	36463
3	60	PCB 113B27	36464
4	40	TFG	L6702
5	20	PCB 113B27	36465
6	0	PCB 113B27	36466
7	-20	TC	n/a
8	-40	DHTG	DHTG31
9	-60	PCB 113B27	36472
10	-80	PCB 113B27	36473
11	-100	-	-

characterise the flow conditions in T6 will require calibration of the pressure transducers, an evaluation of the attenuation of the incident shock speed in the driven tube, additional pitot rake surveys of the test flow, and CFD modelling of the flow through the nozzle.

Experimentally recorded Pitot pressure from the pressure transducer on the centre-line of the nozzle (location 6), is shown in Fig. 7.4. The useful test-time is indicated from 300 µs to 800 µs. The test-time begins once the flow is stable following nozzle start-up processes. The test-time ends when an expansion wave arrives, originating from the diaphragm bursting and reflected from the piston. This can be seen as a gradual decrease in Pitot pressure. Oscillations in the Pitot pressure trace are a result of Helmholtz resonance in the cap used to shield the pressure transducer from fragments in the flow [151].

Figure 7.5 shows images taken using a Photron FASTCAM Mini AX 200 high-speed camera, recording at a frame-rate of 12.5 kHz. The stagnation flow-field can be seen because it is hot enough to radiate. The shock stand-off distance can be seen to be generally stable over the useful test-time. After the test-time is over, at $t = 1120$ µs, diaphragm particles can be seen hitting sensors, and following this, hot radiating driver gas arrives and saturates the image. The core flow was found to be greater than 160 mm in diameter [142]: all of the heat

Table 7.3: Fill and flow conditions for the shots performed in T6.

	Units	T6s87	T6s88	T6s89	Uncertainty, ±%
			Fill Conditions		
p_1 [a]	kPa	200	180	180	1.5 [d]
T_1 [a]	K	293	293	293	2 [d]
p_4 [a]	kPa	120	120	120	–
$\chi_{He,4}$ [a]	–	0.19	0.19	0.19	–
$\chi_{Ar,4}$ [a]	–	0.81	0.81	0.81	–
			Nozzle Supply Conditions		
V_{ss} [b]	m·s^{-1}	1478	1577	1505	5 [e]
p_{5s} [b]	MPa	24.31	23.86	24.02	5 [e]
T_{5s} [c]	K	2180.0	2368.2	2356.4	5.1 [d]
ρ_{5s} [c]	kg·m^{-3}	38.85	35.10	35.51	6.1 [d]
$h_{0,5s}$ [c]	MJ·kg^{-1}	2.52	2.78	2.77	7.3 [d]
			Nozzle Exit Conditions		
$p_{p,7}$ [b]	kPa	351.28	342.15	342.77	8 [e]
p_7 [c]	Pa	6121.3	6081.8	6069.9	15 [e]
T_7 [c]	K	257.8	289.7	287.0	12 [e]
ρ_7 [c]	g·m^{-3}	80.27	73.14	73.69	13 [e]
V_7 [c]	m·s^{-1}	2125.3	2228.8	2222.7	5 [e]
M_7 [c]	–	6.60	6.53	6.54	5 [e]
AR_{eff} [c]	–	115.9	117.4	117.9	–

[a] Nominal value.
[b] Experimentally measured value.
[c] Calculated value, using ESTCj.
[d] Value from Doherty for T4 [149].
[e] Value from Mee for T4 [148].

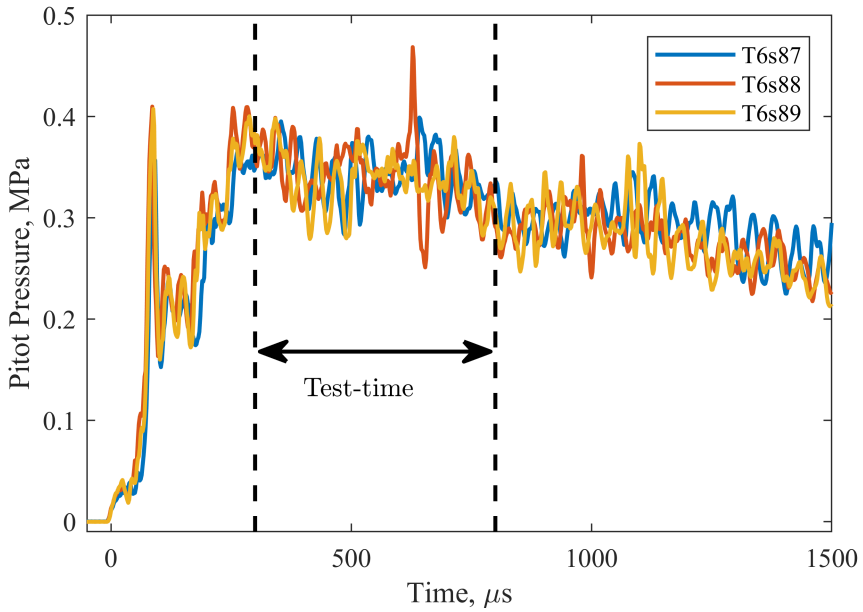
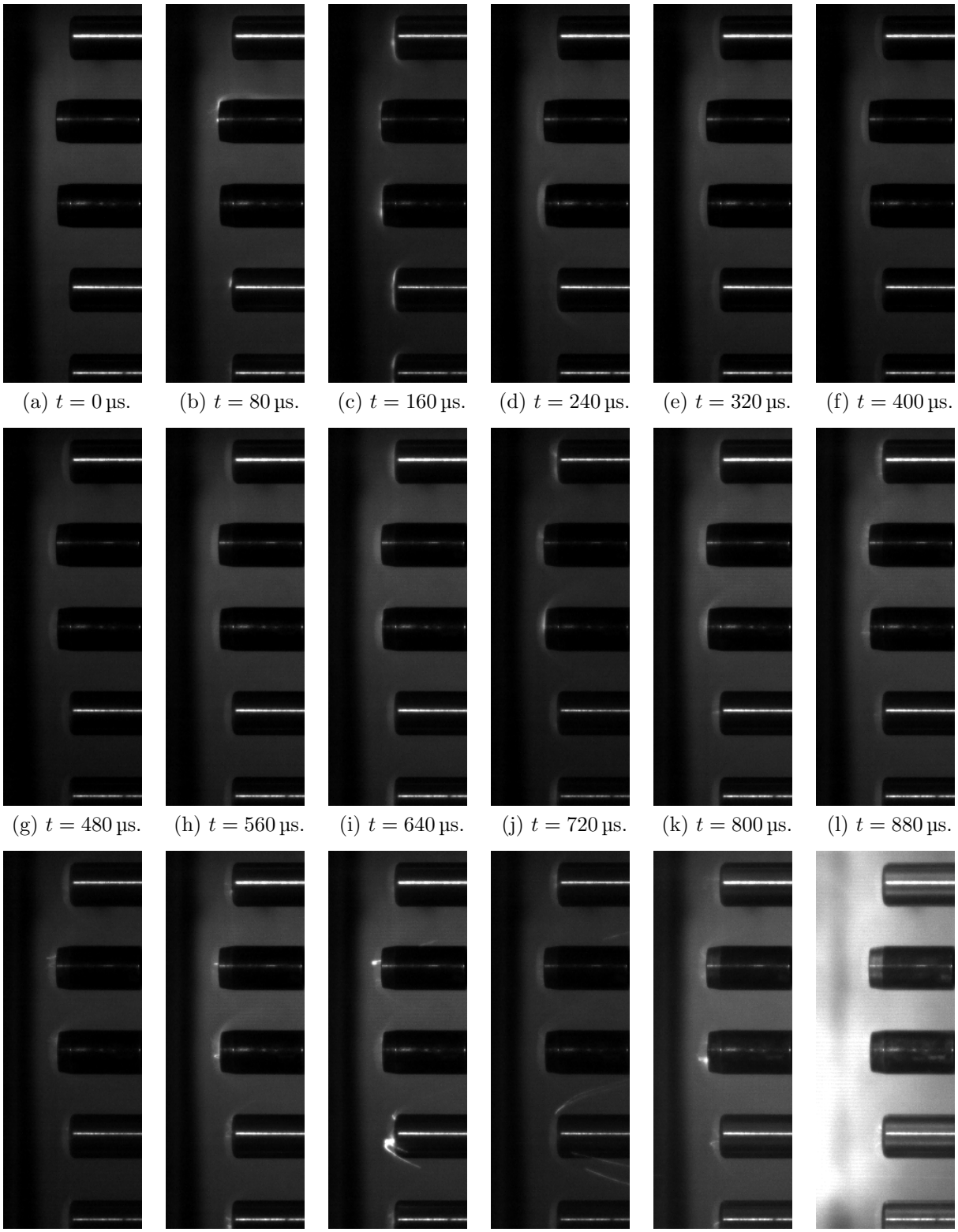


Figure 7.4: Pitot pressure from the PCB on the centre-line of nozzle (location 6 in the rake).

transfer gauges are within the core flow; only rake locations 1 and 11 are outside.

7.4 Data Reduction and Measurement Uncertainty

The voltage response from the heat transfer gauges was recorded at 1 MHz. After removing the gain of the amplifiers, the temperature change was calculated for the DHTG and TFG using Eq. (D.2), and for the TC using the sensitivity given in Table 7.1. For the DHTG, surface heat flux was then calculated using both the SFSM method (see Chapter 4) and the calorimeter method (see Chapter 3). The temperature-dependent impulse response for the SFSM method was obtained from the FE model described in Section 4.4, and shown in Fig. 4.4. The result of the calibration experiment presented in Chapter 6 was not used, for reasons discussed therein. The L-Curve method (see Section 4.5) was used to find the optimum value of the regularisation parameter for the SFSM method. The material properties used in the calorimeter method are the same as those used in the FE model. For the TC and TFG, the impulse response method given by Oldfield [36] was used with the respective



(a) $t = 0\,\mu s$. (b) $t = 80\,\mu s$. (c) $t = 160\,\mu s$. (d) $t = 240\,\mu s$. (e) $t = 320\,\mu s$. (f) $t = 400\,\mu s$.

(g) $t = 480\,\mu s$. (h) $t = 560\,\mu s$. (i) $t = 640\,\mu s$. (j) $t = 720\,\mu s$. (k) $t = 800\,\mu s$. (l) $t = 880\,\mu s$.

(m) $t = 960\,\mu s$. (n) $t = 1040\,\mu s$. (o) $t = 1120\,\mu s$. (p) $t = 1200\,\mu s$. (q) $t = 1280\,\mu s$. (r) $t = 1360\,\mu s$.

Figure 7.5: Frames recorded by the high-speed camera from shot T6s89. The first frame, marked $t = 0\,\mu s$, is the last frame before the flow is seen to arrive at the rake. The steady test-time is from $300\,\mu s$ to $800\,\mu s$.

values of thermal effusivity given in Table 7.1.

The measurement uncertainty for the DHTG and TC in the current experiments is the same as that presented in the previous chapter. To summarise, for the DHTG, the uncertainty due to material properties is 7.3 %, the uncertainty in the value of temperature change is 1.5 %, giving an overall measurement error of 7.5 %. Note that these values do not include conceptual error from the data reduction method, meaning the uncertainty for both the SFSM and calorimeter methods are taken to be the same. The measurement uncertainty for the TC is estimated to be at least 10 % [66, 70, 56, 26], although this does not include uncertainty in the effective value of thermal product, which changes with time. The measurement uncertainty for the TFG has not been calculated as no heat flux data is presented for this gauge due to damage, as discussed in the following section.

7.5 Robustness Results

In a pulse-flow facility, damage to instrumentation and models is a result of impacts from fragments, produced when the diaphragms bursts, that are then entrained in the flow. Fragments of the secondary (Mylar) diaphragm, which is burst by the incident shock, pass through the test-section before the useful test-duration. While it is possible that pieces of Mylar damage instrumentation, it is fragments from the primary steel diaphragm that are most damaging, producing visible impact craters on model surfaces in the test-section. These steel fragments pass through the test-section with the driver gas, after the useful test-duration.

Photographs of the surface of each gauge were taken between each shot using a small handheld microscope to check for significant surface damage. Higher quality photographs were taken with a larger microscope before and after the campaign, shown for the DHTG in Fig. 7.7, for the TFG in Fig. 7.8, and for the TC in Fig. 7.9. The surface of the DHTG shows a sand-blasted effect: it has been roughened, but not significantly damaged, although there is evidence of some slightly larger impacts, seen as lighter spots. Unfortunately a

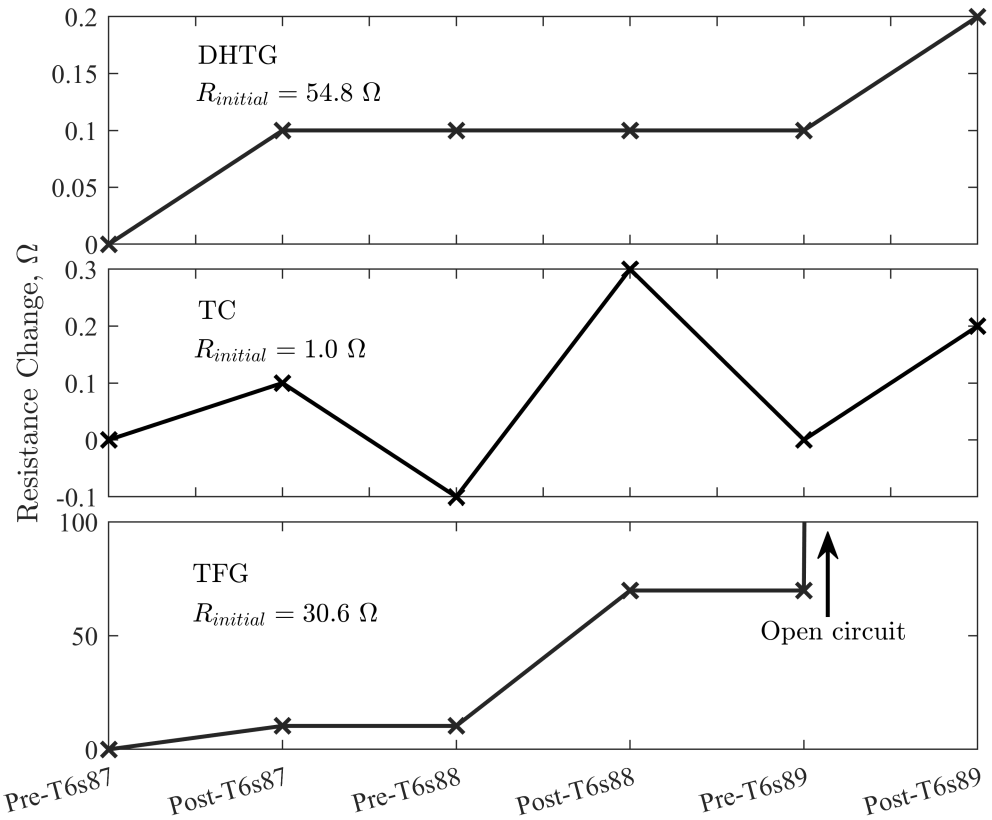
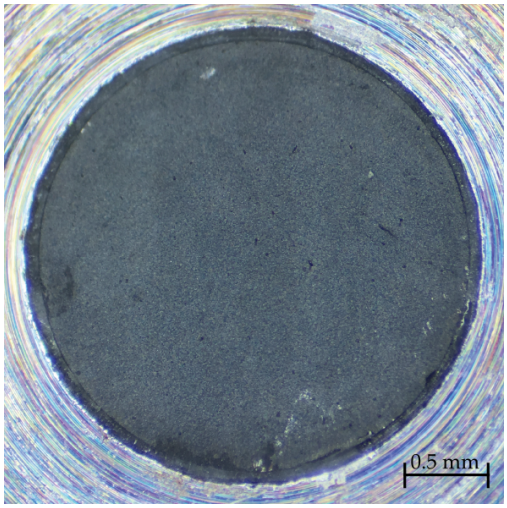


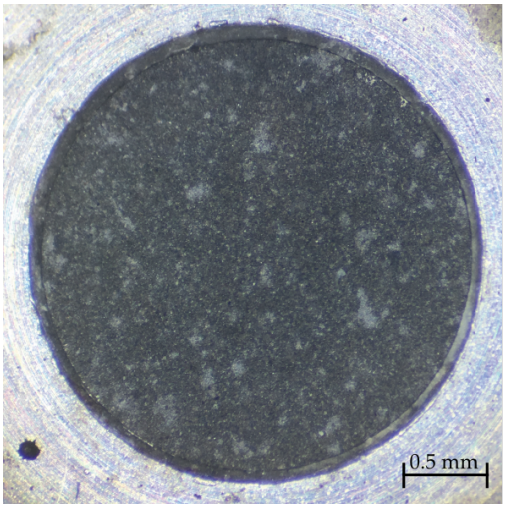
Figure 7.6: Change in resistance, measured before and after each shot, referenced to the pre-T6s87 measurement.

photograph was not taken of the TFG surface before testing, so a gauge with nominally identical construction is shown. There are significant signs of damage after the testing: the gold tabs on either side have been eroded considerably, as has the thin RTD film. Evidence of a large impact crater in the quartz substrate is seen on left hand side. Small amounts of pitting are also evident on the surface of the TC, but the most significant damage is erosion of the heat shrink tubing and epoxy adhesive surrounding the gauge, this is most notable toward the bottom left of Fig. 7.9b. Evidence of particles hitting both the TC and the TFG can be seen in the high-speed camera frames, specifically Figs. 7.5n to 7.5q.

The electrical resistance of each gauge was also recorded between each shot, as shown in Fig. 7.6. The resistance change for the DHTG is small, making it unlikely that the change was caused by damage to the gauge. It is more likely to be caused by random measurement error or slight changes to the ambient temperature. For the TC, during each shot the resistance increased slightly, and the surface was re-abraded with sandpaper before the subsequent shot. It is possible that this was not necessary for every shot, as other investigations using the same gauges have used resistances up to $10\,\Omega$ [26]. The increase in resistance is due to erosion of the shallow electrical junctions created by the sandpaper. In contrast, the resistance of the TFG changed significantly during the first shot: by $10.3\,\Omega$, a change of 33.7 % from the initial value. This change in resistance means that the calibration of the gauge was no longer valid, and so an accurate measurement of temperature change could no longer be made. For this reason, no heat transfer data from the TFG is presented in the following sections. The measurement of resistance of the TFG after shot T6s89 was open-circuit, meaning that the damage seen in Fig. 7.8b was significant enough to sever the continuity of the electrical connection across the film.

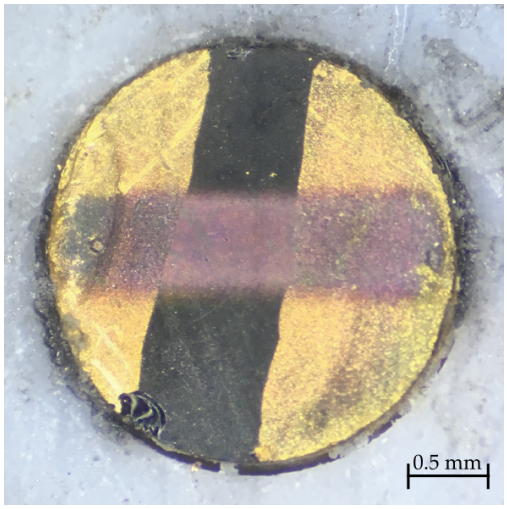


(a) Before.

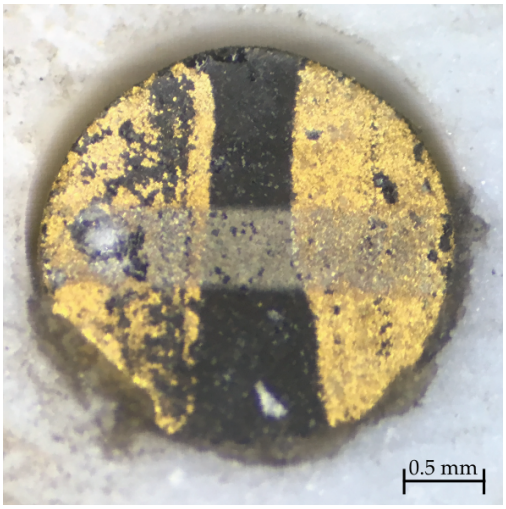


(b) After.

Figure 7.7: Microscope photographs of the surface of DHTG31 before and after testing in T6.

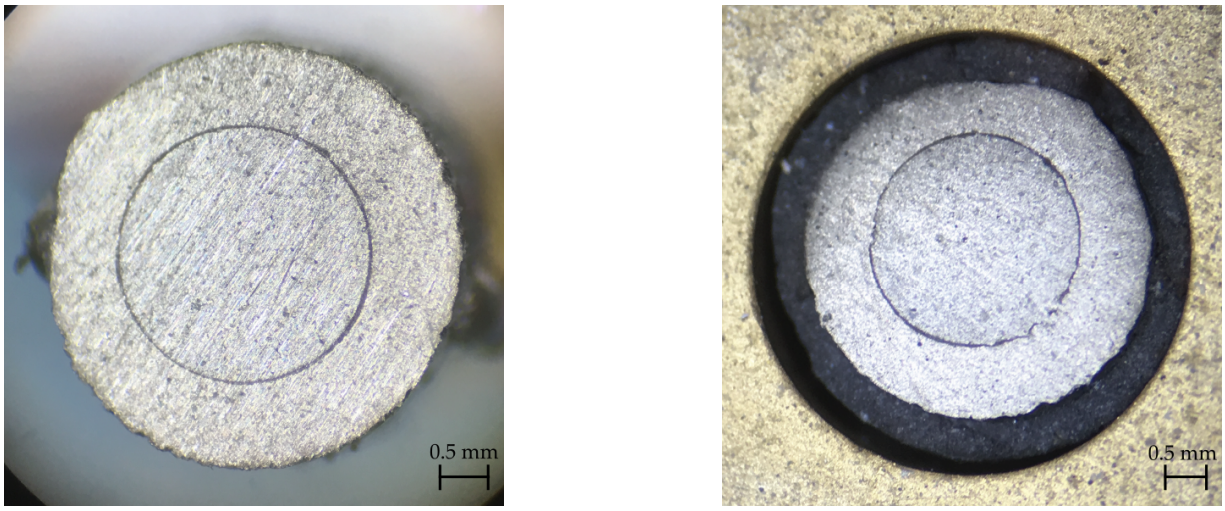


(a) Before (S/N LW6706).



(b) After (S/N LW36702).

Figure 7.8: Microscope photographs of the surface of a new TFG, and the TFG used in T6 after testing. Note that these are not the same gauge but have nominally identical construction.



(a) Before. (b) After.

Figure 7.9: A microscope photograph of the surface of the TC before and after testing in T6.

7.6 Heat Flux Results

7.6.1 Fay and Riddell Heat Flux Estimation

An estimate of the stagnation point heat flux for each shot was calculated using the Fay Riddell [139] equation (given as Eq. (E.1) in Appendix E) with the free-stream properties given in Table 7.3. Zoby and Sullivan [152] give a correction factor to adjust the body radius to account for deviation from the hemispherical geometry which is assumed in the Fay Riddell equation: for a flat-faced cylindrical probe of base radius 5.25 mm and a corner radius of 1.31 mm, a correction factor of 0.345 is given, resulting in an effective radius of $R_{eff} = 15.22\,\text{mm}$.

The implementation of the calculation of q_{FR} requires the free-stream flow properties p_7, T_7, and V_7, from which the flow properties required at each state are calculated assuming equilibrium conditions, using the NASA CEA program [140]. However, to calculate the uncertainty in q_{FR} its sensitivity to the fundamental measurements must be considered. Using the method given in Appendix C, the relative uncertainty can be found by evaluating

Table 7.4: Details of the uncertainty in the elemental measurements used to calculate, $\mathcal{X}_{q_{FR}}$, the overall relative uncertainty in the Fay Riddell heat flux. The typical values of pressure and shock speed are for T6s89.

X_i	Typical Value	$\mathcal{X}_{X_i}$	U_{X_i}	UMF_{X_i}	UPC_{X_i}
R_{eff}	15.22 mm	5 %	0.525 mm	0.50	22.1 %
V_{ss}	1505 m·s^{-1}	5 %	78.35 m·s^{-1}	1.48	48.9 %
$p_{p,7}$	342.77 kPa	8 %	27.42 kPa	0.51	14.4 %
$p_{5,s}$	24.02 MPa	5 %	1.20 MPa	0.81	14.4 %
p_1	180 kPa	1.5 %	2.7 kPa	0.35	0.3 %

Eq. (7.1) with the relevant values given in Table 7.4. All stated values of uncertainty are given as the overall uncertainty at the 95 % confidence interval. A value of uncertainty correction factor used to calculate the value of R_{eff} is not given by the authors of the paper it is taken from. The value of 5 % for the uncertainty in R_{eff} was estimated, and includes uncertainty in both the actual radius r_b, and the correction factor. The values of UPC calculated show that the largest contributor to the overall uncertainty is the value of shock speed. Since the maximum estimated stagnation temperature is 2368 K, there is negligible free-stream dissociation, meaning $h_D = 0\,\text{MJ·kg}^{-1}$, and so it is not necessary to consider uncertainty in Le (the Lewis number). The resulting uncertainty is: $\mathcal{X}_{q_{FR}} = U_{q_{FR}}/q_{FR} = 10.6$ %.

$$\left(\frac{U_{q_{FR}}}{q_{FR}}\right)^2 = \left(\frac{R_{eff}}{q_{FR}}\frac{\partial q_{FR}}{\partial R_{eff}}\right)^2\left(\frac{U_{R_{eff}}}{R_{eff}}\right)^2 + \left(\frac{V_{ss}}{q_{FR}}\frac{\partial q_{FR}}{\partial V_{ss}}\right)^2\left(\frac{U_{V_{ss}}}{V_{ss}}\right)^2 + \left(\frac{p_{p,7}}{q_{FR}}\frac{\partial q_{FR}}{\partial p_{p,7}}\right)^2\left(\frac{U_{p_{p,7}}}{p_{p,7}}\right)^2 + \left(\frac{p_{5,s}}{q_{FR}}\frac{\partial q_{FR}}{\partial p_{5,s}}\right)^2\left(\frac{U_{p_{5,s}}}{p_{5,s}}\right)^2 + \left(\frac{p_1}{q_{FR}}\frac{\partial q_{FR}}{\partial p_1}\right)^2\left(\frac{U_{p_1}}{p_1}\right)^2 \tag{7.1}$$

7.6.2 Experimental Heat Flux Results

Figure 7.10 shows the heat flux measured by the DHTG and the TC for each of the three shots, normalised by the respective values of q_{FR} given in Table 7.5, where measured test-time average heat fluxes are also given. For the DHTG, the heat flux calculated using both the SFSM method and the calorimeter method are shown. The heat flux from the TFG is

not shown, owing to the damage discussed in Section 7.5. A second-order low-pass filter with a cut-off frequency of 120 kHz has been applied to the signals in accordance with the analysis given in the following section. All of the measured heat fluxes show the same general pattern: firstly, there are peaks upon first arrival of the flow, during the nozzle start-up and flow establishment period; then, the useful test-time begins, characterised by relatively steady heat flux; toward the end of the test-time and beyond, the heat flux gradually decreases, following the gradual decrease of Pitot pressure shown in Fig. 7.4.

The test-time average heat fluxes and q_{FR} are shown in Table 7.5, and displayed graphically with measurement uncertainties in Figure 7.11. The heat flux measured by the DHTG using the SFSM method is between 2.8 % and 3.8 % higher than that using the calorimeter method. This difference is expected because the superior transient accuracy of the SFSM method, i.e. the SFSM estimation is a closer representation of reality, as demonstrated in Chapter 4. The test-time average measurement from the TC is between 19.8 % and 39.5 % higher than for the DHTG. However, it is believed that the particularly high value of heat flux obtained for shot T6s88 was not due to heat flux from the flow, but may be due to an impact from a diaphragm fragment: in Fig. 7.10c temporary large increases in heat flux can be seen at $t = 600\,\mu s$ and at $t = 800\,\mu s$. Unfortunately no evidence of impacts at these times could be seen in the high-speed camera footage to corroborate this theory. The spike in heat flux at $t = 1200\,\mu s$ for the DHTG heat flux in Fig. 7.10a and Fig. 7.10b is also presumed to be caused by an impact.

Table 7.5: Test-time average heat fluxes in units of $MW{\cdot}m^{-2}$. The percentage differences are in reference to the DHTG (SFSM) measurement.

	T6s87		T6s87		T6s89	
	$\widehat{q_s}$	% Diff.	$\widehat{q_s}$	% Diff.	$\widehat{q_s}$	% Diff.
DHTG (SFSM)	3.24	–	3.62	–	3.63	–
DHTG (Calorimeter)	3.12	−3.7	3.52	−2.8	3.53	−2.8
TC	3.88	19.8	5.05	39.5	4.38	20.7
Fay Riddell [139]	3.55	9.6	3.95	9.1	3.93	8.3

The uncertainties given for the measurements are the 95 % confidence interval of the systematic uncertainties, i.e. there is a 5 % probability that the true value is outside the uncertainty bounds. Note that the test-time average is taken to be a single measurement, i.e. the uncertainty given is purely due to systematic error. [1] The uncertainty bounds of the DHTG (SFSM) measurement and the TC measurement do not overlap for any of the shots. Therefore, there is a statistically significant difference between the measurements, for which there are three possible explanations:

1. The true heat flux the gauges experienced is not equal;

2. There is an error in the data reduction method for one or both of the gauges;

3. The measurement uncertainty is under-estimated for one or both of the gauges.

It is believed that the difference in true heat flux is not significant: a uniform core flow for the shots numbers presented here is shown by Subiah [142] and the probe diameters are accurate to within 0.1 mm. Since $q_s \propto 1/\sqrt{R}$, this geometric uncertainty would only result in a difference of 1 % in measured heat flux.

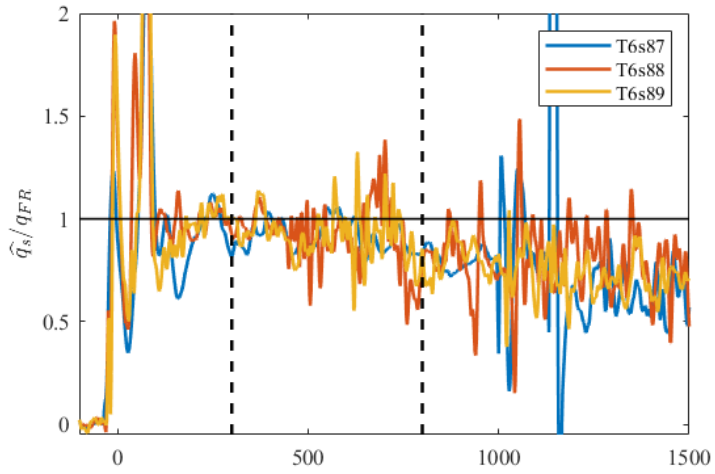
The discrepancy between the DHTG and TC measurements could be explained by uncertainty, or error, in the value of thermal effusivity used in the data reduction for the TC. A discussion of literature in Section 2.3 concluded that the effective thermal effusivity of a surface-junction thermocouple must be calibrated for the specific junction geometry used, and the time-scale of the measurements made. The value of thermal effusivity used here was found from long-duration calibration experiments [56] not accounting for the transient effect on heat conduction of the insulation between the thermocouple elements. However, the measured heat fluxes from the DHTG and the TC presented in the previous chapter agree to within 10 % for four of the conditions presented, and the thermocouples used in these experiments are nominally the same across the two sets of experiments, as are the DHTGs.

[1] A measure of random variation should be taken from the variation of this mean value over multiple shots, instead of variation during the test-time, see Section 5-3 in Coleman and Steele [120] for further discussion of this practice.

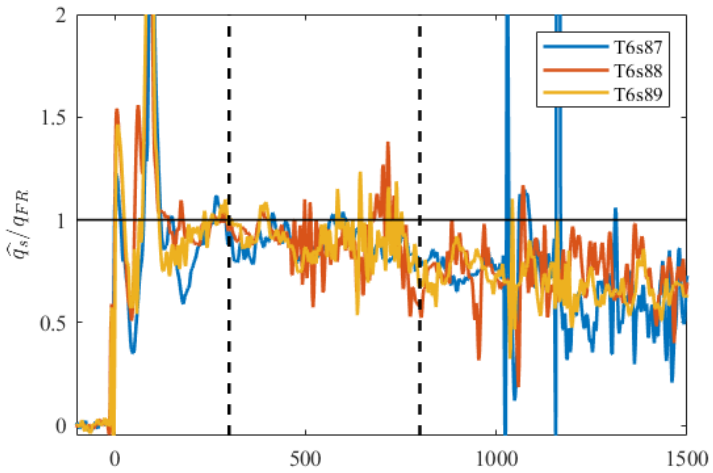
Aside from a difference in amplifiers and data acquisition systems, which are deemed unlikely to make such a difference in measured heat flux, the only fundamental difference between the instrumentation in each of the sets of experiments is the way in which the thermocouple junctions were made. In X2, the junctions were made by scratching twice, in an "X" pattern, across the surface of the gauge with the probe tip of a multimeter, whereas in T6 the junctions were made by abrading the surface with 400 grit sandpaper. Buttsworth [66] noted that the effective thermal effusivity of junctions made using scalpel scratches were closer to the average value of the bulk materials than those made using abrasive paper, due to the depth of the junction and its location further away from the insulating layer.

In a study using the same type of thermocouple as in this thesis, James [26] used an effective thermal effusivity based on average bulk material properties of $8900\,\mathrm{J{\cdot}m^{-2}{\cdot}K^{-1}{\cdot}s^{-1/2}}$ for scratched junctions, and based on the results of a calibration experiment in a shock tube, used a value of $4360\,\mathrm{J{\cdot}m^{-2}{\cdot}K^{-1}{\cdot}s^{-1/2}}$ for abraded junctions. Using the latter value would result in a difference to the test-time average heat flux of $-50\,\%$ when compared to the former. However, this latter value is based on a time-scale of tens of microseconds, and is therefore not applicable to the current timescale of more than $500\,\mu\mathrm{s}$. The true value of effective thermal effusivity of the thermocouple lies between these bounds.

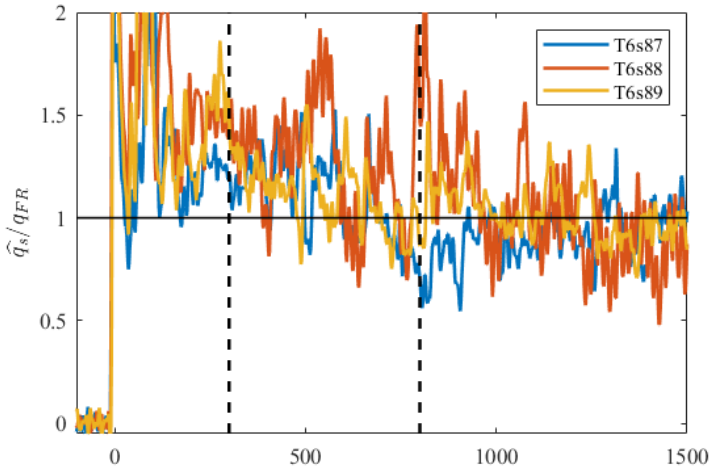
In summary, the discrepancy between the measured heat fluxes can be explained by the fact that an incorrect value of thermal effusivity has been used to calculate the heat flux for the thermocouple. This highlights the need for calibration experiments to give time-dependent effective thermal effusivity, and an increase in the reported measurement uncertainties.



(a) DHTG, processed using SFSM.



(b) DHTG, processed as a calorimeter.



(c) TC.

Figure 7.10: Experimental heat fluxes normalised by the heat flux calculated using the Fay Riddell equation.

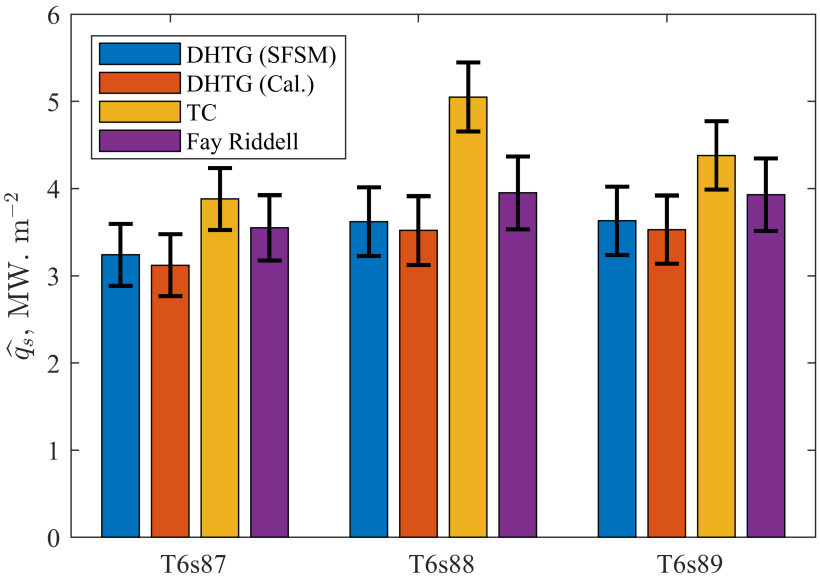


Figure 7.11: Test-time average heat fluxes.

7.6.3 Noise and Filtering

In Section 4.5.5 a method was presented which used the PSD of the full solution, S_{qq}, and the PSD of the pre-trigger noise, ν, to inform the design of a low-pass filter. This method is applied to the heat flux data from T6, the resulting PSDs for shot T6s87 are shown in Fig. 7.12a. In this case, the pre-trigger noise was defined as the signal over the period $-1200\,\mu s < t < 0\,\mu s$, and the full solution as $0\,\mu s < t < 1200\,\mu s$. The optimal filter, Φ, is shown in Fig. 7.12b with the amplitude response of a second-order low-pass Butterworth filter with cut-off frequency of 120 kHz which was designed to roughly match the response of Φ over the lower range of frequencies plotted. The amplifier used for the TC has a quoted bandwidth of 100 kHz, so it is expected that there is little signal at frequencies above this. The same filter was applied to both the TC and the DHTG heat fluxes, as it showed good agreement to the respective optimal filters, and allows for a like-for-like comparison of noise levels. This analysis was performed for shots T6s88 and T6s89, the results were consistent, so the same filter was used for all shots.

Table 7.6 gives the standard deviation of the pre-trigger noise of the measured heat fluxes, after the low-pass filter has been applied. These values are of interest because they are the measurement noise floor, giving an indication of the smallest fluctuations which can reasonably be measured by each gauge. By comparing the noise floor to the predicted heat flux in a future experiment, the suitability of each gauge for the measurement can be determined. The noise of the TFG is the lowest by over an order of magnitude, and the noise floor of the DHTG is consistently smaller than that of the TC. Both the DHTG and the

Table 7.6: Standard deviation of the pre-trigger noise in units of $kW \cdot m^{-2}$.

	T6s87	T6s88	T6s89
DHTG (SFSM)	22.3	47.7	47.3
DHTG (Calorimeter)	40.6	42.2	43.3
TC	119.8	237.6	162.1
TFG	0.8	n/a	n/a

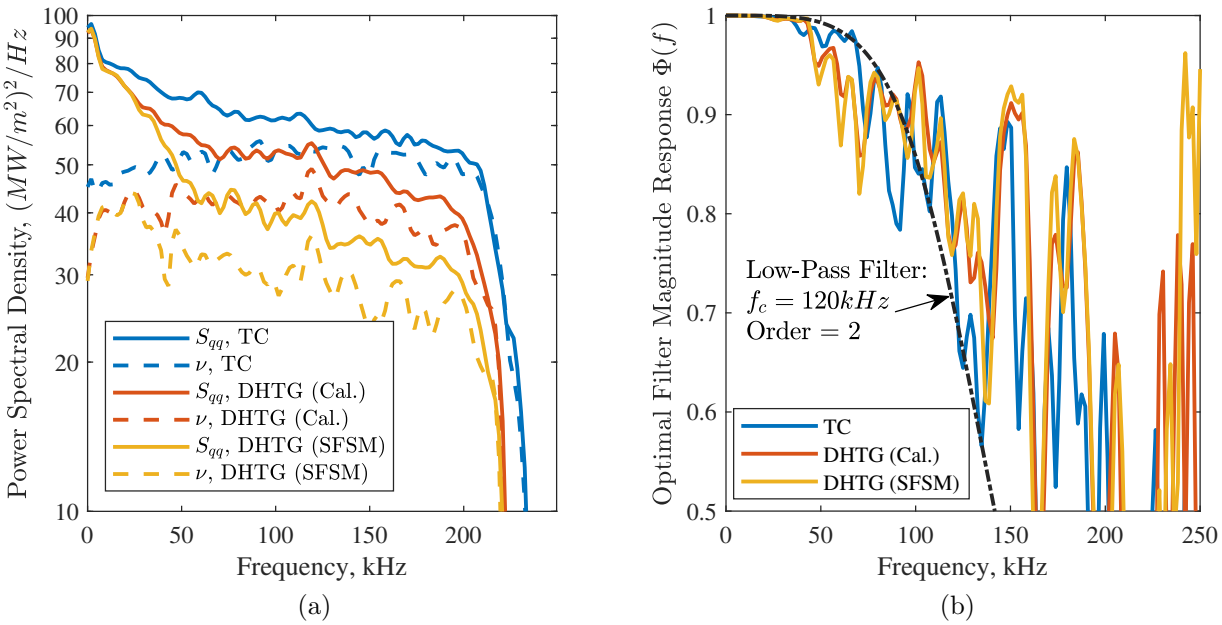


Figure 7.12: a) Power-spectral density of the signal and of the noise before the flow arrives. b) Design of the optimal low-pass filter.

TFG use nominally the same wiring, amplifier, and method of measuring temperature; the discrepancy is due to the difference in measurement sensitivity, as compared in Section 3.5.4.

7.7 Chapter Summary

The experiments presented in this chapter have shown that the DHTG is a viable method for the measurement heat fluxes in reflected shock tunnels. The heat flux measured by the DHTG was around 20 % lower than the TC, and around 9 % lower than the predicted value using the Fay Riddell correlation. The discrepancy between the DHTG and the TC cannot be explained by the current estimate of measurement uncertainty; the most likely explanation is that the effective value of thermal effusivity used to calculate the heat flux for the TC is too high, due to the proximity of the junctions made by surface abrasion to the electrically (and thermally) insulating layer between the two thermocouple metals.

Regarding robustness: while a standard thin-film gauge was rendered useless after a single

shot due to a large change in resistance, minimal surface damage was observed to the DHTG after three shots with no significant change in resistance. The surface-abraded thermocouple was not damaged during these shots either, but did require re-abrading between shots, whereas no maintenance at all was required for the DHTG. Since the stagnation point is the location where most damage will occur, the robustness results mean that the DHTG is suitable for measurements on any surface or orientation in a reflected shock tunnel.

CHAPTER 8

Conclusions and Recommendations

The aim of this thesis was to improve on the accuracy and robustness of heat flux measurement techniques currently used in pulse-flow hypersonic and hypervelocity wind tunnels. To this end, the development of a novel heat transfer gauge is presented: the Diamond Heat Transfer Gauge. This thesis has described the design and manufacture of the gauge, the development of data reduction methods, the results of calibration experiments, and two experimental campaigns in pulse-flow facilities. This chapter discusses the main findings and conclusions of the body of work, and makes recommendations for how it should be continued and built upon.

8.1 Conclusions

8.1.1 Development of the DHTG

Diamond Heat Transfer Gauges using synthetic CVD diamond as a calorimeter material with a platinum thin-film resistance temperature detector on the rear surface have been successfully manufactured and used to measure heat fluxes for the first time. Four types of

gauge have been produced, with diamond thicknesses of 75 µm, 150 µm, 220 µm and 325 µm. Analysis using both a one-dimensional heat conduction model and a Finite Element model showed that these DHTGs have rise times of 2.4 µs, 11.6 µs, 36.3 µs, and 54.4 µs respectively, indicating that these gauges have sufficiently fast response times for measurements in pulse-flow facilities.

The transient accuracy of a calorimeter-based data reduction method was shown to be accurate to within 1 % for test-times less than 500 µs to 700 µs, after the initial rise time, depending on the calorimeter thickness. For longer test-durations, the accuracy of this method decreases due to radial conduction that the one-dimensional model does not account for. A data reduction method based on the Sequential Function Specification Method (SFSM) showed a pronounced improvement in accuracy for longer test durations because the impulse response of the gauge used in this method can encapsulate three-dimensional conduction effects. An error of less than 0.5 % was demonstrated for a typical 2.5 ms Reflected Shock Tunnel test-time. Additionally, for measurements with a high signal-to-noise ratio, the SFSM method can improve the response time of the DHTG compared to the calorimeter method.

The measurement uncertainty of the DHTG is comparable to that of current instrumentation: an uncertainty of ± 7.5 % was calculated for the heat flux measurements presented in this thesis, with the largest contributor to this value being an uncertainty of 7 % in the specific heat capacity of the diamond. Sources in the literature give values ranging between ± 7 % and ± 11 % for surface-junction thermocouples and ± 6 % and ± 10 % for thin-film gauges. However, the transient error for thermocouples may be significantly higher if the thermal effusivity is not calibrated for the measurement time-scale of interest and the specific junction geometry, meaning that in reality, it is expected that the DHTGs are significantly more accurate than coaxial thermocouples.

The response of a DHTG to a short duration laser pulse applied to its surface was measured. Spatial non-uniformity in the beam intensity meant that the measured response is not usable as the impulse response input to the SFSM data reduction method. The

uncertainty in the measured response was 11.2 %, primarily driven by uncertainty in the reflectivity of the diamond surface and multiple measurements with an energy meter. The specific heat capacity of diamond was estimated by tuning the response of a simulation, using a Finite Element model, to match the experimental response. No significant difference was found between the results obtained from this experiment and values given in the literature.

8.1.2 Experiments in an Expansion Tunnel

An experimental campaign was performed in the X2 expansion tunnel at the University of Queensland. DHTGs and surface-junction thermocouples were used to measure surface heat fluxes on blunt- and sharp-nosed wedge models with the gauges mounted at angles of attack of 0°, 12.5°, 45° and 90°. Five flow conditions were used, with total enthalpies ranging from $25\,\mathrm{MJ{\cdot}kg^{-1}}$ to $70\,\mathrm{MJ{\cdot}kg^{-1}}$ and heat fluxes up to $129\,\mathrm{MW{\cdot}m^{-2}}$ were measured by the DHTG. Test-time average measurement discrepancy between the DHTG and thermocouples was less than 12 %, i.e. within the measurement uncertainties, for all but two conditions where the thermocouple measured significantly higher heat fluxes. It was concluded that these thermocouple measurements were erroneous because the signal was significantly noisier than in other shots and may have been affected by electrical interference from ionised species. On the stagnation point, measurements from the DHTG were shown to agree with a value predicted using the Fay and Riddell equations over multiple shots.

No DHTGs mounted at 0° angle of attack were damaged in X2. Those mounted at higher angles survived between 1 and 17 shots, with four out of eight gauges still operational at the end of the campaign, however, even those not destroyed showed significant surface damage. DHTGs with thicknesses of 150 µm, 220 µm and 325 µm were all used, but no conclusions could be drawn regarding the relationship between diamond thickness and robustness.

The DHTG is shown to be a viable technique for measuring heat fluxes in an expansion tunnel. However, DHTGs are more susceptible to damage from diaphragm fragments than coaxial thermocouples, particularly at high angles of attack or on stagnation points. At

low angles of attack, and for a limited number of shots at higher angles of attack, DHTGs can provide a second measurement technique to corroborate measurements made by surface-junction thermocouples in expansion tunnels.

8.1.3 Experiments in a Reflected Shock Tunnel

A second experimental campaign was performed in the T6 Reflected Shock Tunnel at Oxford University. The campaign consisted of three shots where the total enthalpy of the flow was $2.5\,\mathrm{MJ{\cdot}kg^{-1}}$ to $2.8\,\mathrm{MJ{\cdot}kg^{-1}}$. Stagnation point heat flux measurements were made on cylindrical probes with rounded corners using a DHTG, a thin-film gauge, and the same type of thermocouple as was used in X2. An observed difference of approximately 20 % between the heat fluxes measured by the DHTG and TC could not be explained by measurement uncertainty.

The reason for why the DHTG and TC measurements agree in X2 and not in T6 is not clear, but may be due to the different methods used to form the surface junctions in each set of experiments leading to an unaccounted for difference in the value of effective thermal effusivity used to calculate heat flux for the thermocouple. In X2 the junction was made by scratching across the surface with the tip of a multi-meter probe, whereas in T6 it was made by abrasion with sandpaper. The measurements made by both types of gauge agree individually with an estimate of heat flux calculated using the Fay and Riddell equation.

In terms of robustness, DHTGs were proven to be superior to thin-film gauges for stagnation point measurements. The thin-film gauge was damaged after a single shot, rendering further measurements without recalibration useless, and was completely destroyed after three shots. At the end of the campaign, the DHTG and TC were operational and showed signs of small impacts, but no substantial damage.

For experiments in a Reflected Shock Tunnel, the DHTG provides an alternative measurement technique to surface junction thermocouples for use on windward model faces and stagnation points, where thin-film gauges would be damaged. Despite the faster response

time of surface junction thermocouples, DHTGs can provide superior measurements for smaller heat fluxes due to a lower noise-floor.

8.2 Recommendations for Future Work

Future efforts to continue the work of this thesis should:

1) Repeat the experiments to measure the impulse response of the DHTG with a spatially uniform laser beam intensity, thus removing the need to tune the response of a computational model to the experimental response to find the true impulse response. Achieving this will reduce the heat flux measurement uncertainty of the DHTG by allowing the use of the experimentally measured impulse response to be used directly with the SFSM data reduction method.

2) As for 1), but additionally use a DHTG with a mirror-polished diamond surface ($Ra < 10\,\text{nm}$). This will result in specular reflection and allow the reflected energy to be measured directly or calculated more accurately using values of reflectivity from the literature.

3) Continue the experimental campaign in T6 to determine the number of shots before a DHTG is damaged beyond use in a Reflected Shock Tunnel.

4) Investigate the catalytic efficiency of diamond for the dissociated species of air, and other planetary atmospheres. Knowledge of this will increase the accuracy of measurements in hypervelocity facilities with highly non-equilibrium flows.

5) Investigate applications of the DHTG outside of pulse-flow facilities, where high speed measurements are needed in harsh environments.[1]

[1]Published work by the author presents the use of a DHTG to make heat flux measurements in a high enthalpy plasma wind-tunnel, see Penty Geraets et al. [88]

References

[1] Heppenheimer, T. A. *Facing the heat barrier: a history of hypersonics*. Vol. 4232. Government Printing Office, 2009.

[2] Desai, P. N., Lyons, D. T., Tooley, J., et al. "Entry, descent, and landing operations analysis for the Stardust entry capsule". In: *Journal of Spacecraft and Rockets* 45.6 (2008), pp. 1262–1268. DOI: 10.2514/6.2006-6410.

[3] Davies, C. and Arcadi, M. *Planetary mission entry vehicles quick reference guide. Version 3.0*. Tech. rep. NASA SP-2006-3401. NASA, 2006.

[4] Anderson, J. D. *Modern Compressible Flow: with Historical Perspective, Third Edition*. Vol. 12. McGraw-Hill New York, 2004.

[5] Stalker, R. J. "Hypervelocity aerodynamics with chemical nonequilibrium". In: *Annual Review of Fluid Mechanics* 21.1 (1989), pp. 37–60. DOI: 10.1146/annurev.fluid.21.1.37.

[6] Lu, F. K. M. and Marren, D. "Principles of Hypersonic Test Facility Development". In: American Institute of Aeronautics and Astronautics, 2002. Chap. 2, pp. 17–27.

[7] Neely, A. and Morgan, R. "Measurement of heating rates for Earth entry at 13 km/s". In: *25th Plasmadynamics and Lasers Conference, Fluid Dynamics and Co-located Conferences*. 11; M1: 0; doi:10.2514/6.1994-2606. American Institute of Aeronautics and Astronautics, June 1994. DOI: 10.2514/6.1994-2606.

[8] Brandis, A. M. and Johnston, C. O. "Characterization of stagnation-point heat flux for earth entry". In: *45th AIAA Plasmadynamics and Lasers Conference*. 2014, p. 2374. DOI: 10.2514/6.2014-2374.

[9] Holden, M. S., Wadhams, T. P., MacLean, M. G., et al. "Measurements of real gas effects on regions of laminar shock wave/boundary layer interaction in hypervelocity flows for "blind'code validation studies". In: *21st AIAA Computational Fluid Dynamics Conference*. 2013, p. 2837. DOI: 10.2514/6.2013-2837.

[10] Zander, F., Morgan, R., Sheikh, U., et al. "Hot-wall reentry testing in hypersonic impulse facilities". In: *AIAA journal* 51.2 (2013), pp. 476–484. DOI: 10.2514/1.j051867.

[11] Knight, D., Longo, J., Drikakis, D., et al. "Assessment of CFD capability for prediction of hypersonic shock interactions". In: *Progress in Aerospace Sciences* 48 (2012), pp. 8–26. DOI: 10.1016/j.paerosci.2011.10.001.

[12] Johnston, C. "A comparison of EAST shock-tube radiation measurements with a new air radiation model". In: *46th AIAA Aerospace Sciences Meeting and Exhibit*. 2008, p. 1245. DOI: 10.2514/6.2008-1245.

[13] Wilder, M. C., Prabhu, D. K., and Reda, D. "The Effects of Surface Roughness on Turbulent Heat Transfer Measured in Hypersonic Free Flight". In: *52nd Aerospace Sciences Meeting*. 2014, p. 0512. DOI: 10.2514/6.2014-0512.

[14] Wise, D. J. and Smart, M. K. "Roughness-Induced Transition of Hypervelocity Boundary Layers". In: *Journal of Spacecraft and Rockets* 51.3 (2014), pp. 847–854. DOI: 10.2514/1.a32674.

[15] Olivier, H. "An improved method to determine free stream conditions in hypersonic facilities". In: *Shock Waves* 3.2 (1993), pp. 129–139. DOI: 10.1007/bf02115892.

[16] Ilich, Z., Grossir, G., and Chazot, O. "Evaluation of the stagnation-point velocity gradient in low-enthalpy hypersonic flows". In: *33rd AIAA Aerodynamic Measurement Technology and Ground Testing Conference*. 2017, p. 3984. DOI: 10.2514/6.2017-3984.

[17] Marineau, E. and Hornung, H. "Heat flux calibration of t5 hypervelocity shock tunnel conical nozzle in air". In: *47th AIAA Aerospace Sciences Meeting including The New Horizons Forum and Aerospace Exposition*. 2009, p. 1158. DOI: 10.2514/6.2009-1158.

[18] Collen, P. L., Doherty, L., McGilvray, M., et al. "Commissioning of the T6 Stalker Tunnel". In: *AIAA Scitech 2019 Forum*. 2019, p. 1941. DOI: 10.2514/6.2019-1941.

[19] Hornung, H. "Experimental hypervelocity flow simulation, needs, achievements and limitations". In: *Pacific International Conference on Aerospace Science and Technology, National Cheng Kung University, Tainan, Taiwan*. 1993, pp. 1–10.

[20] Hornung, H. G. "28th Lanchester Memorial Lecture — Experimental real-gas hypersonics". In: *The Aeronautical Journal* 92 (920 Dec. 1988), pp. 379–389. ISSN: 2059-6464. DOI: 10.1017/s0001924000016511. URL: http://journals.cambridge.org/article_S0001924000016511.

[21] Hannemann, K. and Karl, S. "Recent extensions to the high enthalpy shock tunnel Göttingen (HEG)". In: *Proceedings of the 2nd International ARA Days "Ten Years after ARD"*. 2008, pp. 21–23.

[22] Hornung, H., Sturtevant, B., Belanger, J., et al. "Performance data of the new free-piston shock tunnel T5 at GALCIT". In: *Shock Waves*. Springer, 1992, pp. 603–610.

[23] Stalker, R., Paull, A., Mee, D., et al. "Scramjets and shock tunnels—the Queensland experience". In: *Progress in Aerospace Sciences* 41.6 (2005), pp. 471–513. DOI: 10.1016/j.paerosci.2005.08.002.

[24] McGilvray, M., Doherty, L. J., Morgan, R. G., et al. "T6: The Oxford University Stalker Tunnel". In: *20th AIAA International Space Planes and Hypersonic Systems and Technologies Conference*. 2015, p. 3545. DOI: 10.2514/6.2015-3545.

[25] Tanno, H., Komuro, T., Sato, K., et al. "Aeroheating measurement of Apollo shaped capsule with boundary layer trip in the free-piston shock tunnel HIEST". In: *52nd Aerospace Sciences Meeting*. 2014, p. 0434. DOI: 10.2514/6.2014-0434.

[26] James, C. M., Birch, B., Smith, D. R., et al. "Testing of Ultra Fast Response, Durable Co-axial Thermocouples for High Enthalpy Impulse Facilities". In: *AIAA Aviation 2019 Forum*. 2019, p. 3007. DOI: 10.2514/6.2019-3007.

[27] Stalker, R. "Modern developments in hypersonic wind tunnels". In: *The Aeronautical Journal* 110.1103 (2006), pp. 21–39. DOI: 10.1017/s0001924000004346.

[28] Roediger, T., Knauss, H., Kraemer, E., et al. "The Atomic Layer Thermopile—A Fast Heat Flux Sensor for Measuring High Heat Loads in Short Duration Hypersonic Ground Testing Facilities". In: *Proc. ICMAR* (2007), pp. 154–166.

[29] Diller, T. E. "Advances in heat flux measurements". In: *Advances in heat transfer*. Vol. 23. Elsevier, 1993, pp. 279–368. DOI: 10.1016/s0065-2717(08)70008-x.

[30] Schultz, D. L. and Jones, T. *Heat-Transfer Measurements in Short-Duration Hypersonic Facilities.* Tech. rep. DTIC Document, 1973.

[31] Beck, J. V., Blackwell, B., and Clair Jr, C. R. S. *Inverse heat conduction: Ill-posed problems*. James Beck, 1985.

[32] Woodbury, K. A. *Inverse engineering handbook*. CRC Press, 2002.

[33] Vidal, R. *Model instrumentation techniques for heat transfer and force measurements in a hypersonic shock tunnel*. Tech. rep. WADC technical note 56-315. Cornell Aeronautical Laboratory, 1956.

[34] Rabinowicz, J., Jessey, M., and Bartsch, C. "Resistance Thermometer for Transient High-Temperature Studies". In: *Journal of Applied Physics* 27.1 (1956), pp. 97–98. DOI: 10.1063/1.1722210.

[35] Hogendoorn, C., De Lange, H., and Van Steenhoven, A. "Design optimization for fast heat-transfer gauges". In: *Measurement Science and Technology* 9.3 (1998), p. 428. DOI: 10.1088/0957-0233/9/3/017.

[36] Oldfield, M. L. G. "Impulse Response Processing of Transient Heat Transfer Gauge Signals". In: *Journal of Turbomachinery* 130 (2008). DOI: 10.1115/1.2752188.

[37] Simmons, J. "Measurement techniques in high-enthalpy hypersonic facilities". In: *Experimental thermal and fluid science* 10.4 (1995), pp. 454–469. DOI: 10.1016/0894-1777(94)00066-h.

[38] Rose, P. H. and Stark, W. I. "Stagnation point heat-transfer measurements in dissociated air". In: *Journal of the Aerospace Sciences* 25.2 (1958), pp. 86–97. DOI: 10.2514/8.7519.

[39] Flaherty, W. and Austin, J. "Comparative surface heat transfer measurements in hypervelocity flow". In: *Journal of Thermophysics and Heat Transfer* 25.1 (2011), pp. 180–183. DOI: 10.2514/1.50450.

[40] Miller III, C. G. *Comparison of thin-film resistance heat-transfer gages with thin-skin transient calorimeter gages in conventional hypersonic wind tunnels*. Tech. rep. NASA Technical Memorandum 83197. NASA, 1981.

[41] Jahn, R. G. and Weimer, D. "On the Performance of Thin-Film Gauges in High-Temperature Shock Tube Flows". In: *Journal of Applied Physics* 29.4 (1958), pp. 741–742. DOI: 10.1063/1.1723270.

[42] Marrone, P. and Hartunian, R. "Thin-Film Thermometer Measurements In Partially Ionized Shock-Tube Flows". In: *The Physics of Fluids* 2.6 (1959), pp. 719–721. DOI: 10.1063/1.1705982.

[43] Wise, D. "Experimental Investigation of a Three Dimensional Scramjet Engine at Hypervelocity Conditions". PhD thesis. The University of Queensland, 2014. DOI: 10.14264/uql.2015.465.

[44] Cook, W. J. and Felderman, E. J. "Reduction of data from thin-film heat-transfer gages - A concise numerical technique". In: *AIAA journal* 4.3 (1966), pp. 561–562. DOI: 10.2514/3.3486.

[45] Hartunian, R. and Varwig, R. "On Thin-Film Heat-Transfer Measurements in Shock Tubes and Shock Tunnels". In: *The Physics of Fluids* 5.2 (1962), pp. 169–174. DOI: 10.1063/1.1706592.

[46] Bertolazzi, E., Battisti, L., and Trivellato, F. "Numerical processing of thin-film thermometer data for determining transient heat fluxes". In: *Applied Mathematical Modelling* 36.8 (2012), pp. 3645–3662. DOI: 10.1016/j.apm.2011.09.089.

[47] Buttsworth, D. R. *A finite difference routine for the solution of transient one dimensional heat conduction problems with curvature and temperature-dependent thermal properties*. Tech. rep. OUEL Report Number 2130/97. University of Oxford, 1997.

[48] Buttsworth, D. R. and Jones, T. V. "Transient thin film heat flux measurements with finite thin film thickness". In: *21st International Symposium on Shock Waves, Great Keppel Island, Australia*. 1661. 1997.

[49] Wise, D. J. and Smart, M. K. "Experimental Investigation of a Three-Dimensional Scramjet Engine at Mach 12". In: *20th AIAA International Space Planes and Hypersonic Systems and Technologies Conference*. 2015, p. 3650. DOI: 10.2514/6.2015-3650.

[50] Frankel, J. I. and Chen, H. h. "Heat Flux Data Reduction using a Natural Filter Test Function". In: *AIAA Scitech 2019 Forum*. 2019, p. 1553. DOI: 10.2514/6.2019-1553.

[51] Collins, M., Chana, K., and Povey, T. "New technique for the fabrication of miniature thin film heat flux gauges". In: *Measurement Science and Technology* 26.2 (2015), p. 025303. DOI: 10.1088/0957-0233/26/2/025303.

[52] Lu, F. K. and Kinnear, K. M. "Characterization of thin-film heat-flux gauges". In: *Journal of thermophysics and heat transfer* 13.4 (1999), pp. 548–549. DOI: 10.2514/2.6477.

[53] Lyons, P. and Gai, S. "A method for the accurate determination of the thermal product (ρck) 1/2 for thin film heat transfer or surface thermocouple gauges". In: *Journal of Physics E: Scientific Instruments* 21.5 (1988), p. 445. DOI: 10.1088/0022-3735/21/5/005.

[54] Gatowski, J. A., Smith, M. K., and Alkidas, A. C. "An experimental investigation of surface thermometry and heat flux". In: *Experimental Thermal and Fluid Science* 2.3 (1989), pp. 280–292. DOI: 10.1016/0894-1777(89)90017-4.

[55] Epstein, A., Guenette, G., Norton, R., et al. "High-frequency response heat-flux gauge". In: *Review of Scientific Instruments* 57.4 (1986), pp. 639–649. DOI: 10.1063/1.1138882.

[56] Capra, B. R. "Aerothermodynamic Simulation of Subscale Models of the FIRE II and Titan Explorer Vehicles in Expansion Tubes". PhD thesis. The University Of Queensland, 2006.

[57] Kinnear, K. and Lu, F. "Design, calibration and testing of transient thin film heat transfer gauges". In: *20th AIAA Advanced Measurement and Ground Testing Technology Conference*. 1997, p. 2504. DOI: 10.2514/6.1998-2504.

[58] Kovács, Á. and Mesler, R. B. "Making and testing small surface thermocouples for fast response". In: *Review of Scientific Instruments* 35.4 (1964), pp. 485–488. DOI: 10.1063/1.1718852.

[59] Gai, S. and Mudford, N. "Stagnation point heat flux in hypersonic high enthalpy flow". In: *Shock Waves* 2.1 (1992), pp. 43–47. DOI: 10.1007/bf01414420.

[60] Mohammed, H., Salleh, H., and Yusoff, M. Z. "Design and fabrication of coaxial surface junction thermocouples for transient heat transfer measurements". In: *International Communications in Heat and Mass Transfer* 35.7 (2008), pp. 853–859. DOI: 10.1016/j.icheatmasstransfer.2008.03.009.

[61] Buttsworth, D. R., Stevens, R., and Stone, C. R. "Eroding ribbon thermocouples: impulse response and transient heat flux analysis". In: *Measurement Science and Technology* 16.7 (2005), p. 1487. DOI: 10.1088/0957-0233/16/7/011.

[62] Sanderson, S. R. and Sturtevant, B. "Transient heat flux measurement using a surface junction thermocouple". In: *Review of Scientific Instruments* 73.7 (2002), p. 2781. DOI: 10.1063/1.1484255.

[63] Marineau, E. and Hornung, H. "Modeling and calibration of fast-response coaxial heat flux gages". In: *47th AIAA Aerospace Sciences Meeting including The New Horizons Forum and Aerospace Exposition*. 2009, p. 737. DOI: 10.2514/6.2009-737.

[64] Li, J., Chen, H., Zhang, S., et al. "On the response of coaxial surface thermocouples for transient aerodynamic heating measurements". In: *Experimental Thermal and Fluid Science* 86 (2017), pp. 141–148. DOI: 10.1016/j.expthermflusci.2017.04.011.

[65] Buttsworth, D. R. "Transient response of an erodable heat flux gauge using finite element analysis". In: *Proceedings of the Institution of Mechanical Engineers, Part D: Journal of Automobile Engineering* 216.8 (2002), pp. 701–706. DOI: 10.1177/095440700221600808.

[66] Buttsworth, D. R. "Assessment of effective thermal product of surface junction thermocouples on millisecond and microsecond time scales". In: *Experimental Thermal and Fluid Science* 25.6 (2001), pp. 409–420. DOI: 10.1016/s0894-1777(01)00093-0.

[67] Sundqvist, B. "Thermal diffusivity and thermal conductivity of Chromel, Alumel, and Constantan in the range 100–450 K". In: *Journal of applied physics* 72.2 (1992), pp. 539–545. DOI: 10.1063/1.351885.

[68] Davis, J.-P. "High-enthalpy shock/boundary-layer interaction on a double wedge". PhD thesis. California Institute of Technology, 1999.

[69] Mohammed, H., Salleh, H., and Yusoff, M. "Fast response surface temperature sensor for hypersonic vehicles". In: *Instruments and Experimental Techniques* 53.1 (2010), pp. 153–159. DOI: 10.1134/s0020441210010288.

[70] Mohammed, H., Salleh, H., Yusoff, M., et al. "Thermal product of type-E fast response temperature sensors". In: *Journal of Thermal Science* 19.4 (2010), pp. 364–371. DOI: 10.1007/s11630-010-0395-8.

[71] Irimpan, K. J., Mannil, N., Arya, H., et al. "Performance evaluation of coaxial thermocouple against platinum thin film gauge for heat flux measurement in shock tunnel". In: *Measurement* 61 (2015), pp. 291–298. DOI: 10.1016/j.measurement.2014.10.056.

[72] Gülhan, A. *Heat flux measurements in high enthalpy flows*. Tech. rep. German Aerospace Centre (DLR) Cologne, 2000.

[73] Palmer, R. A. "Measurement of Heat Transfer in Superorbital Flows". PhD thesis. University of Queensland, 1999.

[74] Rose, P. H. "Development of the calorimeter heat transfer gauge for use in shock tubes". In: *Review of Scientific Instruments* 29.7 (1958), pp. 557–564. DOI: 10.1063/1.1716258.

[75] Frankel, J., Keyhani, M., and Elkins, B. "Surface heat flux prediction through physics-based calibration, part 1: theory". In: *Journal of Thermophysics and Heat Transfer* 27.2 (2013), pp. 189–205. DOI: 10.2514/1.t3917.

[76] Frankel, J. I., Geraets, R. T. P., McGilvray, M., et al. "New Data Reduction Equation for Thin-Film Diamond Slug Calorimeters". In: *Submitted* (2019).

[77] Frankel, J., Chen, H., and Keyhani, M. "New step response formulation for inverse heat conduction". In: *Journal of Thermophysics and Heat Transfer* 31.4 (2017), pp. 989–996. DOI: 10.2514/1.t5067.

[78] Elkins, B. E., Keyhani, M., and Frankel, J. I. "Surface Heat Flux Prediction Through Physics-Based Calibration, Part 2: Experimental Validation". In: *Journal of Thermophysics and Heat Transfer* 27.2 (2013), pp. 206–216. DOI: 10.2514/6.2012-223.

[79] Palmer, R., Morgan, R., Palmer, R., et al. "Stagnation point heat transfer in superorbital expansion tubes". In: *35th Aerospace Sciences Meeting and Exhibit*. 1997, p. 280. DOI: 10.2514/6.1997-280.

[80] Ledford, R. *A Device for Measuring Heat Transfer Rates in Arc-Discharge Hypervelocity Wind Tunnels*. Tech. rep. AEDC-TDR-62-64. ARO INC ARNOLD AFS TN, 1962.

[81] Cary Jr, A. M. *Turbulent-boundary-layer heat-transfer and transition measurements with surface cooling at Mach 6*. Tech. rep. TN D-5863. NASA, 1970.

[82] Starner, K. and Varwig, R. *Thick film thermocouple gauges for roughened model heat flux measurements*. Tech. rep. Aerodynamics and Propulsion Research Laboratory, 1969.

[83] Sprinks, T. "On the Calibration of Calorimeter Heat-Transfer Gages". In: *AIAA Journal* 1.2 (1963), pp. 464–464. DOI: 10.2514/3.54837.

[84] Battaglia, J.-L., Cois, O., Puigsegur, L., et al. "Solving an inverse heat conduction problem using a non-integer identified model". In: *International Journal of Heat and Mass Transfer* 44.14 (2001), pp. 2671–2680. DOI: 10.1016/s0017-9310(00)00310-0.

[85] Lohle, S. "Characterisation of a heat flux sensor using short pulse laser calibration". In: *Review of Scientific Instruments* 78 (2007). DOI: 10.1063/1.2736388.

[86] Loehle, S., Battaglia, J.-L., Jullien, P., et al. "Improvement of High Heat Flux Measurement Using a Null-Point Calorimeter". In: *Journal of Spacecraft and Rockets* 45.1 (2008), pp. 76–81. DOI: 10.2514/1.30092.

[87] Loehle, S., Nawaz, A., Herdrich, G. H., et al. "Comparison of Heat Flux Gages for High Enthalpy Flows-NASA Ames and IRS". In: *46th AIAA Thermophysics Conference*. 2016, p. 4422. DOI: 10.2514/6.2016-4422.

[88] Penty Geraets, R., McGilvray, M., Loehle, S., et al. "Stagnation Point Heat Flux Measurements in a Plasma Wind Tunnel Using a Diamond Heat Transfer Gauge". In: *AIAA Scitech 2019 Forum*. 2019. DOI: 10.2514/6.2019-0535.

[89] Nagayama, T., Nagai, H., Tanno, H., et al. "Global heat flux measurement using temperature-sensitive paint in high-enthalpy shock tunnel HIEST". In: *55th AIAA Aerospace Sciences Meeting*. 2017, p. 1682. DOI: 10.2514/6.2017-1682.

[90] Ozawa, H., Laurence, S. J., Schramm, J. M., et al. "Fast-response temperature-sensitive-paint measurements on a hypersonic transition cone". In: *Experiments in Fluids* 56.1 (2015), pp. 1–13. DOI: 10.1007/s00348-014-1853-y.

[91] Beck, W. H., Klein, C., Henne, U., et al. "Application of temperature and pressure sensitive paints to DLR hypersonic facilities: "lessons learned"". In: *53rd AIAA Aerospace Sciences Meeting*. 2015, p. 0023. DOI: 10.2514/6.2015-0023.

[92] Laurence, S., Ozawa, H., Schramm, J. M., et al. "Heat-flux measurements on a hypersonic inlet ramp using fast-response temperature-sensitive paint". In: *Experiments in Fluids* 60.4 (2019), p. 70. DOI: 10.1007/s00348-019-2711-8.

[93] Nakakita, K., Osafune, T., and Asai, K. "Global heat transfer measurement in a hypersonic shock tunnel using temperature-sensitive paint". In: *41st Aerospace Sciences Meeting and Exhibit*. 2003, p. 743. DOI: 10.2514/6.2003-743.

[94] Hubner, J., Carroll, B., Schanze, K., et al. "Temperature-and pressure-sensitive paint measurements in short-duration hypersonic flow". In: *AIAA journal* 39.4 (2001), pp. 654–659. DOI: 10.2514/2.1358.

[95] Schramm, J. M., Edzards, F., and Hannemann, K. "Calibration of Fast-Response Temperature Sensitive Paints for Their Application in Hypersonic High Enthalpy Flows". In: *New Results in Numerical and Experimental Fluid Mechanics XI*. Cham: Springer International Publishing, 2018, pp. 141–151. DOI: 10.1007/978-3-319-64519-3_13.

[96] Ohmi, S., Nagai, H., Asai, K., et al. "Effect of temperature-sensitive-paint thickness on global heat transfer measurement in hypersonic flow". In: *Journal of Thermophysics and Heat Transfer* 22.3 (2008), pp. 373–381. DOI: 10.2514/1.34152.

[97] Choudhury, R., Fuata, J., Stern, N., et al. "Surface Convective Heating Rates for a Double Swept-Wedge Configuration at Mach 6". In: *20th Australasian Fluid Mechanics Conferenced*. 2016.

[98] Reda, D. C., Wilder, M. C., and Prabhu, D. K. "Transition experiments on blunt bodies with isolated roughness elements in hypersonic flight". In: *Journal of Spacecraft and Rockets* 47.5 (2010), pp. 828–835.

[99] Le Sant, Y., Marchand, M., Millan, P., et al. "An overview of infrared thermography techniques used in large wind tunnels". In: *Aerospace Science and Technology* 6.5 (2002), pp. 355–366. DOI: 10.1016/s1270-9638(02)01172-0.

[100] Cullen, T., Gollan, R., and Morgan, R. "Application of Infrared Thermography in an Expansion Tunnel". In: *32nd International Symposium on Shock Waves (ISSW32)*. 2019.

[101] Ramesh, R., Kelly, R., Cullen, T. G., et al. "Shock Layer Radiation Measurements at a Mars Entry Condition for Infrared Thermography". In: *AIAA Aviation 2019 Forum*. 2019, p. 3006. DOI: 10.2514/6.2019-3006.

[102] Follador, R., Minucci, M., Toro, P., et al. "Preliminary study of CVD diamond film to improve the performance of heat flux sensors for hypersonic experiments". In: *Diamond and related materials* 14.3 (2005), pp. 637–640. DOI: 10.1016/j.diamond.2004.11.026.

[103] Clark, T. "The Development of a Diamond-Shielded Heat Transfer Gauge for Hypersonic Test Facilities". MA thesis. University of Queensland, 2015.

[104] Vanyai, T. "Dynamic Calibration of Heat Transfer Gauges". MA thesis. University of Oxford, 2015.

[105] Wort, C., Sweeney, C., Cooper, M., et al. "Thermal properties of bulk polycrystalline CVD diamond". In: *Diamond and Related Materials* 3.9 (1994), pp. 1158–1167. DOI: 10.1016/0925-9635(94)90162-7.

[106] Graebner, J. "Measurements of specific heat and mass density in CVD diamond". In: *Diamond and related materials* 5.11 (1996), pp. 1366–1370. DOI: 10.1016/0925-9635(96)00550-x.

[107] Coe, S. and Sussmann, R. "Optical, thermal and mechanical properties of CVD diamond". In: *Diamond and Related Materials* 9.9-10 (2000), pp. 1726–1729. DOI: 10.1016/s0925-9635(00)00298-3.

[108] Smithells, C. J. *Metals reference book*. Elsevier, 2013.

[109] Moelle, C., Werner, M., SzuÈcs, F., et al. "Specific heat of single-, poly-and nanocrystalline diamond". In: *Diamond and related materials* 7.2-5 (1998), pp. 499–503. DOI: 10.1016/s0925-9635(97)00202-1.

[110] Kaye, G., Laby, T., Noyes, J., et al. *Tables of Physical and Chemical Constants, 1995*. New York: Longman Scientific and Technical, 2008.

[111] Barin, I. and Platzki, G. *Thermochemical data of pure substances*. Vol. 304. 334. Wiley Online Library, 1989. DOI: 10.1002/9783527619825.

[112] Twitchen, D., Pickles, C., Coe, S., et al. "Thermal conductivity measurements on CVD diamond". In: *Diamond and related materials* 10.3-7 (2001), pp. 731–735. DOI: 10.1016/s0925-9635(00)00515-x.

[113] Huntsman. *Aradlite 5861 A/B Epoxy Adhesive Technical Data Sheet*. Accessed: Dec 2019. URL: https://us.aralditeadhesives.com/us/adhesives/request-a-tds/172-araldite-5861-us-e-new/file.html.

[114] Epoxy Technolgy. *EPO-TEK H77 Technical Data Sheet*. Accessed: Dec 2019. URL: http://www.epotek.com/site/administrator/components/com_products/assets/files/Style_Uploads/H77.pdf.

[115] Permabond. *Permabond ES550 Technical Data Sheet*. Accessed: Dec 2019. URL: https://www.permabond.com/wp-content/uploads/2016/04/ES550_TDS.pdf.

[116] Aremco. *High Temperature Ceramic & Graphite Adhesives Technical Bulletin A2*. Accessed: Dec 2019. URL: https://www.aremco.com/wp-content/uploads/2015/04/A02_15.pdf.

[117] Wylie, S. "Hypersonic Boundary Layer Instability Measurements at Low and High Angles of Attack". PhD thesis. University of Oxford, 2019.

[118] *COMSOL Multiphysics v. 5.2a*. COMSOL AB, Stockholm, Sweden. 2016. URL: www.comsol.com.

[119] Brandes, E. A. and Brook, G. B. *Smithells metals reference book*. Elsevier, 2013.

[120] Coleman, H. W. and Steele, W. G. *Experimentation, validation, and uncertainty analysis for engineers*. John Wiley & Sons, 2009. DOI: 10.1002/9780470485682.

[121] Hansen, P. C. and O'Leary, D. P. "The use of the L-curve in the regularization of discrete ill-posed problems". In: *SIAM Journal on Scientific Computing* 14.6 (1993), pp. 1487–1503. DOI: 10.1137/0914086.

[122] Golub, G. H., Hansen, P. C., and O'Leary, D. P. "Tikhonov regularization and total least squares". In: *SIAM Journal on Matrix Analysis and Applications* 21.1 (1999), pp. 185–194. DOI: 10.1137/s0895479897326432.

[123] Woodbury, K. A. and Thakur, S. K. "Redundant data and future times in the inverse heat conduction problem". In: *Inverse Problems in Engineering* 2.4 (1996), pp. 319–333. DOI: 10.1080/174159796088027610.

[124] Beck, J. V., Litkouhi, B., and Clair Jr, C. R. S. "Efficient sequential solution of the nonlinear inverse heat conduction problem". In: *Numerical Heat Transfer, Part A Applications* 5.3 (1982), pp. 275–286.

[125] Sanderson, S. R. and Simmons, J. M. "Drag Balance for Hypervelocity Impulse Facilties". In: *AIAA Journal* 29.12 (1991). DOI: 10.2514/3.10858.

[126] Welch, P. "The use of fast Fourier transform for the estimation of power spectra: a method based on time averaging over short, modified periodograms". In: *IEEE Transactions on audio and electroacoustics* 15.2 (1967), pp. 70–73.

[127] Baba, T. and Ono, A. "Improvement of the laser flash method to reduce uncertainty in thermal diffusivity measurements". In: *Measurement Science and Technology* 12.12 (2001), p. 2046. DOI: 10.1088/0957-0233/12/12/304.

[128] Pace, E., Pini, A., Corti, G., et al. "CVD diamond optics for ultraviolet". In: *Diamond and related materials* 10.3-7 (2001), pp. 736–743. DOI: 10.1016/s0925-9635(00)00602-6.

[129] Anthony, R. J., Oldfield, M. L. G., Jones, T. V., et al. "Development of high-density arrays of thin film heat transfer gauges". In: *5th ASME/JSME Thermal Engineering Joint Conference, San Diego, CA*. 1999.

[130] Thomas, M. E. and Tropf, W. J. "Optical properties of diamond". In: *Johns Hopkins APL Technical Digest* 14 (1993), pp. 16–23. DOI: 10.1117/12.187336.

[131] Austin, P. C. and Hux, J. E. "A brief note on overlapping confidence intervals". In: *Journal of vascular surgery* 36.1 (2002), pp. 194–195.

[132] James, C., Gildfind, D., Morgan, R. G., et al. "Designing and simulating high enthalpy expansion tube conditions". In: *2013 Asia-Pacific International Symposium on Aerospace Technology*. Japan Society for Aeronautical and Space Sciences. 2013, pp. 1–10.

[133] Gildfind, D. E., Morgan, R. G., and Jacobs, P. A. "Expansion tubes in Australia". In: *Experimental Methods of Shock Wave Research*. Springer, 2016, pp. 399–431. DOI: 10.1007/978-3-319-23745-9_13.

[134] James, C. M., Gildfind, D. E., Lewis, S. W., et al. "Implementation of a state-to-state analytical framework for the calculation of expansion tube flow properties". In: *Shock Waves* (Nov. 2017). ISSN: 1432-2153. DOI: 10.1007/s00193-017-0763-3.

[135] Vella, S. "Expansion Tunnel Heat Transfer Measurements of the ESA-IXV Re-entry Vehicle". B.E. Honours thesis. The University of Queensland, 2016. DOI: 10.14264/uql.2017.203.

[136] Fahy, E., Buttsworth, D., Gollan, R., et al. "Experimental and Computational Fluid Dynamics Studies of Superorbital Earth Re-entry". In: *46th AIAA Thermophysics Conference*. 2016, p. 3532. DOI: 10.2514/6.2016-3532.

[137] Sheikh, U. A., Morgan, R. G., and McIntyre, T. J. "Vacuum Ultraviolet Spectral Measurements for Superorbital Earth Entry in X2 Expansion Tube". In: *Aiaa Journal* 53.12 (2015), pp. 3589–3602. DOI: 10.2514/1.j054027.

[138] Cullen, T., James, C., Gollan, R., et al. "Development of a Total Enthalpy and Reynolds Number Matched Apollo Re-entry Condition in the X2 Expansion Tunnel". In: *31st International Symposium on Shock Waves*. Springer. Cham, 2017, pp. 197–204. DOI: 10.1007/978-3-319-91017-8_24.

[139] Fay, J. A. and Riddell, F. R. "Theory of stagnation point heat transfer in dissociated air". In: *Journal of the Aerospace Sciences* 25.2 (1958), pp. 73–85. DOI: 10.2514/8.7517.

[140] Gordon, S. and McBride, B. J. *Computer program for calculation of complex chemical equilibrium compositions and applications. Part 1: Analysis*. Tech. rep. NASA-RP-1311. NASA, 1994.

[141] Stalker, R. J. "A study of the free-piston shock tunnel". In: *AIAA Journal* 5.12 (1967), pp. 2160–2165.

[142] Subiah, S., Collen, P., Doherty, L., et al. "Condition Development and Commissioning of the Oxford T6 Stalker Tunnel in Reflected Shock Tunnel Mode". In: *International Conference on Flight vehicles, Aerothermodynamics and Re-entry Missions and Engineering, Monopoli, Italy*. ESA Conference Bureau. 2019.

[143] Mee, D. J. *Transition measurements on a 5 degree cone in the T4 shock tunnel*. Tech. rep. Research Report Number 2001-2. University of Queensland, 2001.

[144] Fylde Electronic Laboratories Ltd. *FE-351-U Auniversal amplifier*. Accessed: 2019-11-04. 2018. URL: https://www.fylde.com/wp-content/uploads/2018/03/FE351UA.pdf.

[145] Capra, B. R., Morgan, R. G., and Leyland, P. "Heat Transfer Measurements of the First Experimental Layer of the FIRE II Reentry Vehicle in Expansion Tubes". In: *Fifth European Symposium on Aerothermodynamics for Space Vehicles*. Vol. 563. 2005, p. 243.

[146] Kemp, N. H. "Laminar heat transfer around blunt bodies in dissociated air". In: *Journal of the aerospace sciences* 26.7 (1959), pp. 421–430. DOI: 10.2514/8.8128.

[147] Jacobs, P., Gardner, A., and Hannemann, K. *Gas-dynamic modelling of the HEG shock tunnel*. Tech. rep. DLR-IB 224-2003. Deutsche Zentrum für Luft- und Raumfahrt e.V., 2003.

[148] Mee, D. J. *Uncertainty analysis of conditions in the test section of the T4 shock tunnel*. Tech. rep. Research Report No. 4/93. Department of Mechanical Engineering, The University of Queensland, 1993.

[149] Doherty, L. J. "An experimental investigation of an airframe integrated three-dimensional scramjet engine at a Mach 10 flight condition". PhD thesis. The University of Queensland, 2014.

[150] Stalker, R. J. and Morgan, R. G. "The University of Queensland free piston shock tunnel T-4: Initial operation and preliminary calibration". In: *Fourth National Space Engineering Symposium: Preprints of Papers*. Institution of Engineers, Australia. 1988, p. 182.

[151] McGilvray, M., Jacobs, P. A., Morgan, R. G., et al. "Helmholtz resonance of pitot pressure measurements in impulsive hypersonic test facilities". In: *AIAA Journal* 47.10 (2009), pp. 2430–2439. DOI: 10.2514/6.2009-1157.

[152] Zoby, E. V. and Sullivan, E. M. "Effects of corner radius on stagnation-point velocity gradients on blunt axisymmetric bodies". In: *Journal of Spacecraft and Rockets* 3.10 (1966), pp. 1567–1567. DOI: 10.2514/3.59538.

[153] Platinum Metals Review. "Thermophysical Data on Platinum". In: *Platinum Metals Review* (1984), p. 164.

[154] Crabtree, L. F., Dommett, R. L., and Woodley, J. G. *Estimation of heat transfer to flat plates, cones and blunt bodies*. Tech. rep. Reports and Memoranda No. 3637. R.A.E. Farnborough: Aeronautical Research Council, 1965.

[155] Beckwith, I. E. *Similar solutions for the compressible boundary layer on a yawed cylinder with transpiration cooling*. Tech. rep. Technical Note 4345. National Advisory Committee for Aeronautics, 1958.

[156] Ellison, J. C. *Experimental stagnation point velocity gradients and heat transfer coefficients for a family of blunt bodies at Mach 8 and angles of attack*. Tech. rep. National Aeronatuics and Space Administration, 1969.

APPENDIX A

Solution of Heat Diffusion Equations

A.1 Temperature Solution

The heat diffusion equation for the one-dimensional two-layer system with a semi-infinite substrate shown in Fig. 3.2 with constant thermophysical properties is:

$$\frac{\partial T_n}{\partial t} = \frac{1}{\alpha_n}\frac{\partial^2 T_n}{\partial x^2} \tag{A.1}$$

for $n = 1, 2$, where the temperature T is taken to be the reduced temperature, i.e. $T(t = 0) = 0$.

This can be solved to find the temperature at any depth x in response to a surface heat flux. The following analysis is given by Schultz and Jones [30], but due to a typographical error in the resulting equations it is reproduced here for completeness. The boundary conditions are the surface heat flux:

$$-k_1\frac{\partial T_1}{\partial x} = q_s \ \text{ at } \ x = 0 \tag{A.2}$$

continuity between layers:

$$-k_1\frac{\partial T_1}{\partial x} = -k_2\frac{\partial T_2}{\partial x} \text{ at } x = L \tag{A.3}$$

$$T_1 = T_2 \text{ at } x = L \tag{A.4}$$

and a semi-infinite substrate provides an adiabatic boundary condition:

$$T_2 = T_2(t = 0) = 0 \text{ at } x = \infty \tag{A.5}$$

Denoting the Laplace transform in general as $\mathscr{L}(f(t)) = \mathscr{F}$, and taking Laplace transforms of Eq. (3.1) for $n = 1, 2$ gives

$$\frac{\partial \mathscr{T}_1}{\partial x^2} = \frac{s}{\alpha_1}\mathscr{T}_1 \tag{A.6}$$

$$\frac{\partial \mathscr{T}_2}{\partial x^2} = \frac{s}{\alpha_2}\mathscr{T}_2 \tag{A.7}$$

to which the general solutions are:

$$\mathscr{T}_1 = A\exp\left(x\sqrt{s/\alpha_1}\right) + B\exp\left(-x\sqrt{s/\alpha_1}\right) \tag{A.8}$$

$$\mathscr{T}_2 = A\exp\left(x\sqrt{s/\alpha_2}\right) + B\exp\left(-x\sqrt{s/\alpha_2}\right) \tag{A.9}$$

Taking Laplace transforms of the boundary conditions (Eqs. (A.2) to (A.4)) gives:

$$-k_1\frac{\partial \mathscr{T}_1}{\partial x} = \mathcal{Q}_s \text{ at } x = 0 \tag{A.10}$$

$$-k_1\frac{\partial \mathscr{T}_1}{\partial x} = -k_2\frac{\partial \mathscr{T}_2}{\partial x} \text{ at } x = L \tag{A.11}$$

$$\mathscr{T}_1 = 0 \text{ at } x = \infty \tag{A.12}$$

The constants in the general solutions (Eq. (A.8) and Eq. (A.9)) can be eliminated to give

$$\mathscr{T}_1 = \frac{\mathcal{Q}_s\sqrt{\alpha_1}\left[(1+a)\exp\left(-(x-L)\sqrt{s/\alpha_1}\right)+(1-a)\exp\left((x-L)\sqrt{s/\alpha_1}\right)\right]}{k_1\sqrt{s}\left[(1+a)\exp\left(L\sqrt{s/\alpha_1}\right)-(1-a)\exp\left(-L\sqrt{s/\alpha_1}\right)\right]} \tag{A.13}$$

$$\mathscr{T}_2 = \frac{2\mathcal{Q}_s\sqrt{\alpha_1}\exp\left((L-x)\sqrt{s/\alpha_2}\right)}{k_1\sqrt{s}\left[(1+a)\exp\left(L\sqrt{s/\alpha_1}\right)-(1-a)\exp\left(-L\sqrt{s/\alpha_1}\right)\right]} \tag{A.14}$$

where a is the ratio of thermal effusivities:

$$a = \sqrt{\frac{\rho_2 c_{p,2} k_2}{\rho_1 c_{p,1} k_1}} \tag{A.15}$$

A.2 Heat Flux at $x = L$

If the temperature at T_L is known, i.e. the temperature at $x = L$, the conductive heat flux entering the substrate $\widehat{q}_L$ is independent of layer 1. Either Eq. (A.1) can be solved again with modified boundary conditions, or more simply, the existing solutions can be modified. Substituting $L = 0$ a new coordinate system $u = x + L$ into either Eq. (A.13) or Eq. (A.14) gives

$$\mathscr{T}(u) = \frac{1}{\sqrt{\rho_2 c_{p,2} k_2}}\frac{\mathcal{Q}_L}{\sqrt{s}}\exp\left(-u\sqrt{s/\alpha_2}\right) \tag{A.16}$$

and so at $u = 0$

$$\mathscr{T}_L = \frac{1}{\sqrt{\rho_2 c_{p,2} k_2}} \frac{\mathcal{Q}_L}{\sqrt{s}} \tag{A.17}$$

Rearranging for $\mathcal{Q}_L$ and taking the inverse Laplace transform, gives:

$$q_L = \frac{\sqrt{\rho_2 c_{p,2} k_2}}{\sqrt{\pi}} \int_0^t \frac{dT_L/d\tau(\tau)}{(t-\tau)^{1/2}} d\tau \tag{A.18}$$

This form is not convenient for numerical implementation as it involves differentiation of the surface temperature [30]. Schultz and Jones [30] give another form of the equation without the explicit differentiation of temperature as:

$$\widehat{q}_s(t) = \frac{\sqrt{\rho_1 c_1 k_1}}{\sqrt{\pi}} \left[\frac{T_1(t)}{\sqrt{t}} + \int_{\tau=0}^t \frac{T_1(t) - T_1(\tau)}{(t-\tau)^{3/2}} d\tau \right] \tag{A.19}$$

The numerical implementation of this equation as a data reduction method is discussed in Section 2.2.2.

A.3 Solution with Constant Surface Heat Flux

A.3.1 Temperature

An analytical expression for temperature as a function of depth into the calorimeter can be found for the case of a step in surface heat flux of magnitude $q_{s,0}$ by substituting $\mathcal{Q}_s = q_{s,0}/s$ into Eq. (A.13) and taking inverse Laplace transforms. The temperature in the first layer is:

$$T_1(X,\tau) = A \sum_{n=0}^{\infty} \left(\frac{1-a}{1+a}\right)^n \left\{ \frac{\tau}{\sqrt{\pi}} \exp\left(-\frac{1}{\tau^2}\left(n+\frac{X}{2}\right)^2\right) - \left(n+\frac{X}{2}\right) \operatorname{erfc}\left(\frac{1}{\tau}\left(n+\frac{X}{2}\right)\right) \right.$$
$$\left. + \left(\frac{1-a}{1+a}\right) \left[\frac{\tau}{\sqrt{\pi}} \exp\left(-\frac{1}{\tau^2}\left(n+1-\frac{X}{2}\right)^2\right) - \left(n+1-\frac{X}{2}\right) \operatorname{erfc}\left(\frac{1}{\tau}\left(n+1-\frac{X}{2}\right)\right) \right] \right\} \tag{A.20}$$

Where

$$A = \frac{2q_{s,0}L}{k_1} \qquad X = \frac{x}{L} \qquad \tau = \frac{\sqrt{\alpha_1 t}}{L}$$

A.3.2 Time Derivative of Temperature

Equation (A.20) can be differentiated to give:

$$\frac{\partial T_1}{\partial t}(X,\tau) = \frac{B}{\tau}\sum_{\infty}^{n=0}\left(\frac{1-a}{1+a}\right)^n\left[\exp\left(-\frac{1}{\tau^2}\left(n+\frac{X}{2}\right)^2\right)+\left(\frac{1-a}{1+a}\right)\left(\exp\left(-\frac{1}{\tau^2}\left(n+1-\frac{X}{2}\right)^2\right)\right)\right] \tag{A.21}$$

where

$$B = \frac{q_s\alpha_1}{k_1 L}\sqrt{\pi} \tag{A.22}$$

Evaluating Section A.3.2 at $x = 0$ and $x = L$ gives Eq. (A.23) and Eq. (A.24) respectively. Note that both of these equations are given incorrectly as Equations (105) and (106) in Schultz and Jones [30].

$$\frac{\partial T_1}{\partial t}(X=0,\tau) = \frac{B}{\tau}\left(1+2\sum_{\infty}^{n=0}\left(\frac{1-a}{1+a}\right)^n\exp\left(-\frac{n^2}{\tau^2}\right)^2\right) \tag{A.23}$$

$$\frac{\partial T_1}{\partial t}(X=1,\tau) = \frac{2}{1+a}\frac{B}{\tau}\sum_{\infty}^{n=0}\left(\frac{1-a}{1+a}\right)^n\exp\left(-\frac{1}{\tau^2}\left(n+\frac{1}{2}\right)^2\right) \tag{A.24}$$

APPENDIX B

Table of DHTG Details

DHTG No.	Material	Thickness, µm	Housing Version	Adhesive	Purpose	m, $\Omega{\cdot}K^{-1}$	U_m, $\Omega{\cdot}K^{-1}$	c (R_0), Ω	U_c, Ω	α_R, K^{-1}	Calib. Date
A1	PCD	150	1	Araldite	Shock Tube	0.1220	0.0002	43.11	0.66	2.83×10^{-3}	27/06/16
A2	PCD	150	1	Araldite	X2 2017	0.1208	0.0010	41.18	0.66	2.93×10^{-3}	31/08/16
A3	PCD	150	1	Araldite	X2 2017	0.1211	0.0043	40.50	0.66	2.99×10^{-3}	31/08/16
A4	PCD	150	1	Araldite	X2 2017	0.1205	0.0002	41.17	0.66	2.93×10^{-3}	31/08/16
A5	PCD	150	1	Araldite	X2 2017 (IXV)	n/a	n/a	n/a	n/a	n/a	n/a
A6	PCD	150	1	Araldite	X2 2017 (IXV)	n/a	n/a	n/a	n/a	n/a	n/a
A7	PCD	150	1	Araldite	X2 2017 (IXV)	n/a	n/a	n/a	n/a	n/a	n/a
1	PCD	150	1	Araldite	X2 2018	0.1185	0.0005	41.12	0.65	2.88×10^{-3}	02/02/17
2	PCD	150	1	Araldite	X2 2018	0.1194	0.0009	41.48	0.66	2.88×10^{-3}	02/02/17
3	PCD	150	1	Permabond ES550	X2 2018	0.1186	0.0010	40.81	0.66	2.91×10^{-3}	02/02/17
4	PCD	150	1	Permabond ES550	X2 2018	0.1190	0.0010	42.64	0.66	2.79×10^{-3}	02/02/17
5	PCD	150	1	Fortafix Flameseal	X2 2018	0.1191	0.0005	41.99	0.66	2.84×10^{-3}	02/02/17
6	OPCD	200	1	Permabond ES550	X2 2018	0.1317	0.0009	50.57	0.67	2.60×10^{-3}	06/02/17
7	OPCD	200	1	Permabond ES550	X2 2018	0.1325	0.0005	50.03	0.67	2.65×10^{-3}	06/02/17
8	OPCD	200	1	Permabond ES550	X2 2018	0.1309	0.0006	49.53	0.67	2.64×10^{-3}	06/02/17
9	OPCD	200	1	Permabond ES550	X2 2018	0.1339	0.0005	50.62	0.67	2.65×10^{-3}	06/02/17
10	OPCD	200	1	Permabond ES550	X2 2018	0.1347	0.0005	50.81	0.67	2.65×10^{-3}	06/02/17
11	PCD	300	1	Permabond ES550	X2 2018	0.1233	0.0005	47.40	0.66	2.60×10^{-3}	06/02/17
12	PCD	300	1	Permabond ES550	X2 2018	0.1231	0.0004	47.25	0.66	2.60×10^{-3}	06/02/17
13	PCD	300	1	Permabond ES550	X2 2018	0.1206	0.0006	46.95	0.66	2.57×10^{-3}	06/02/17
14	PCD	300	1	Permabond ES550	X2 2018	0.1194	0.0004	46.12	0.66	2.59×10^{-3}	06/02/17
15	PCD	300	1	Permabond ES550	X2 2018	0.1207	0.0003	46.67	0.66	2.59×10^{-3}	06/02/17
16	PCD	150	1	Permabond ES550	X2 2018	0.1371	0.0043	57.48	0.70	2.39×10^{-3}	08/02/17
17	PCD	150	1	Permabond ES550	X2 2018	0.0522	0.0891	207.96	3.87	2.51×10^{-4}	08/02/17
18	PCD	300	1	Permabond ES550	n/a	0.1191	0.0006	46.09	0.66	2.58×10^{-3}	19/04/17
19	OPCD	200	1	Permabond ES550	n/a	0.1360	0.0004	51.40	0.67	2.65×10^{-3}	19/04/17
20	PCD	300	1	Permabond ES550	n/a	0.1213	0.0003	47.65	0.66	2.55×10^{-3}	06/07/17
21	SCD	75	1	Permabond ES550	HDT 2017 (Cone)	0.1586	0.0004	55.51	0.69	2.86×10^{-3}	06/07/17
22	SCD	75	1	Permabond ES550	HDT 2017 (Cone)	0.1531	0.0016	55.00	0.69	2.78×10^{-3}	06/07/17
23	OPCD	220	2	Ceramabond 670	Laser Pulse Calib.	0.1404	0.0005	53.39	0.68	2.63×10^{-3}	09/05/18
24	OPCD	219	2	Ceramabond 670	Laser Pulse Calib.	0.1376	0.0002	51.25	0.67	2.69×10^{-3}	09/05/18

25	OPCD	224	2	Ceramabond 670	Laser Pulse Calib.	0.1359	0.0004	51.22	0.67	2.65×10^{-3}	09/05/18
26	PCD	324	2	Ceramabond 670	PWK4 (IRS)	n/a	n/a	47.12	n/a	2.50×10^{-3}	04/10/18
27	PCD	326	2	Ceramabond 670	PWK4 (IRS)	n/a	n/a	46.86	n/a	2.55×10^{-3}	04/10/18
28	PCD	324	2	Ceramabond 670	PWK4 (IRS)	n/a	n/a	46.47	n/a	2.51×10^{-3}	04/10/18
29	OPCD	221	1	Permabond ES550	HDT 2018 (Cone)	n/a	n/a	n/a	n/a	n/a	n/a
30	PCD	322	1	Permabond ES550	HDT 2018 (Cone)	n/a	n/a	n/a	n/a	n/a	n/a
31	OPCD	222	2	Epotek H77	T6 2019	0.1349	0.0006	50.50	0.67	2.67×10^{-3}	01/06/19
32	OPCD	219	2	Epotek H77	T6 2019	0.1334	0.0005	50.61	0.67	2.63×10^{-3}	01/06/19
33	PCD	323	2	Epotek H77	T6 2019	0.1372	0.0010	51.97	0.67	2.64×10^{-3}	01/06/19

APPENDIX C

Uncertainty Analysis

The first section of this appendix presents a generalised uncertainty analysis that multiple chapters of this thesis make use of. The analysis is a succinct version of the relevant aspects of that given by Coleman and Steele [120]. The second section is a brief note on how the general uncertainty analysis can be applied to a linear regression.

C.1 Uncertainty in a Calculated Value

Consider a general data reduction equation which is a function of N fundamental measurements X_i:

$$f = f(X_1, X_2, X_3, ..., X_N) \tag{C.1}$$

Then the general equation for the total absolute uncertainty U_f of the calculated value, f is:

$$U_f^2 = \sum_{i=1}^{N} \left(\frac{\partial f}{\partial X_i} \right)^2 U_{X_i}^2 + 2 \sum_{i=1}^{N-1} \sum_{k=i+1}^{N} \left(\frac{\partial f}{\partial X_i} \right) \left(\frac{\partial f}{\partial X_k} \right) U_{X_i X_k} \tag{C.2}$$

where U_{X_i} is the expanded uncertainty at the 95 % confidence interval in each fundamental measurement X_i, and $U_{X_iX_k}$ is the covariance estimator for correlated errors in the X_i and X_k variables. The partial derivatives $\partial f/\partial X_i$ are known as sensitivity coefficients. If the standard random and systematic uncertainties are s_{X_i} and b_{X_i} respectively, then the expanded uncertainty is given by:

$$U_{X_i} = 2\left(s_{X_i}^2 + b_{X_i}^2\right)^{1/2} \tag{C.3}$$

If the random and systematic uncertainties were given as expanded uncertainties at the 95 % confidence interval, i.e. as S_{X_i} and B_{X_i}, then an equivalent expression can also be written as:

$$U_{X_i} = \left(S_{X_i}^2 + B_{X_i}^2\right)^{1/2} \tag{C.4}$$

Following from Eq. (C.3), equations for the random and systematic uncertainties can be written as:

$$s_f^2 = \sum_{i=1}^{N}\left(\frac{\partial f}{\partial X_i}\right)^2 s_{X_i}^2 + 2\sum_{i=1}^{N-1}\sum_{k=i+1}^{N}\left(\frac{\partial f}{\partial X_i}\right)\left(\frac{\partial f}{\partial X_k}\right) s_{X_iX_k} \tag{C.5}$$

$$b_f^2 = \sum_{i=1}^{N}\left(\frac{\partial f}{\partial X_i}\right)^2 b_{X_i}^2 + 2\sum_{i=1}^{N-1}\sum_{k=i+1}^{N}\left(\frac{\partial f}{\partial X_i}\right)\left(\frac{\partial f}{\partial X_k}\right) b_{X_iX_k} \tag{C.6}$$

If there are p uncorrelated elemental sources of error contributing to each of the random and systematic uncertainty terms, then

$$s_{X_i}^2 = \sum_{1}^{p} {s_{X_i}}_p^2 \tag{C.7}$$

and

$$b_{X_i}^2 = \sum_{1}^{p} {b_{X_i p}}^2 \tag{C.8}$$

where $s_{X_i p}$ and $b_{X_i p}$ are the elemental error sources. The covariance estimators in Eq. (C.2) cannot be calculated exactly, but can be estimated. If there are L common elemental error sources, then:

$$b_{X_i X_k} = \sum_{\alpha=1}^{L} (b_{X_{i,\alpha}})(b_{X_{k,\alpha}}) \tag{C.9}$$

$$s_{X_i X_k} = \sum_{\alpha=1}^{L} (s_{X_{i,\alpha}})(s_{X_{k,\alpha}}) \tag{C.10}$$

C.2 Numerical Evaluation of Sensitivity Coefficients

If a simple analytical expression for the data reduction equation can be written, then it may be possible to analytically evaluate the partial derivatives (known as sensitivity coefficients) required in Eq. (C.2) and Eqs. (C.5) to (C.6). However, it may be more convenient, or necessary, to evaluate the partial derivatives using a finite difference method. For example, a central difference scheme can be implement as:

$$\frac{\partial f}{\partial X_i} \approx \frac{f(X_1, X_2, ..., X_i + \Delta X_i, ..., X_N) - f(X_1, X_2, ..., X_i - \Delta X_i, ..., X_N))}{2\Delta X_i} = \tag{C.11}$$

Coleman and Steele [120] recommend starting with a the value of ΔX_i around $0.01 X_i$, and then iteratively reducing it until the calculated derivative converges.

C.3 Non-Dimensional Uncertainty

The relative (non-dimensional) uncertainty $\mathcal{X}_f$ is found by dividing Eq. (C.2) by the expected value f:

$$\mathcal{X}_f^2 = \left(\frac{U_f}{f}\right)^2 = \sum_{i=1}^{N} \left(\frac{X_i}{f}\frac{\partial f}{\partial X_i}\right)^2 \left(\frac{U_{X_i}}{X_i}\right)^2 = \sum_{i=1}^{N} \left(\frac{X_i}{f}\frac{\partial f}{\partial X_i}\right)^2 \left(\mathcal{X}_f^2\right) \tag{C.12}$$

where $\mathcal{X}_{X_i}$ is the relative uncertainty of each fundamental measurement.

Two additional non-dimensional parameters can be defined. Firstly, the Uncertainty Magnification Factor:

$$UMF_i = \frac{X_i}{f}\frac{\partial f}{\partial X_i} \tag{C.13}$$

which indicates the factor by which each fundamental uncertainty is magnified ($UMF > 1$) or attenuated ($UMF > 1$) through the data reduction equation. This parameter is useful at the design stage of an experiment for identifying which fundamental measurements it is most important to focus on reducing the uncertainty of.

Secondly, the Uncertainty Contribution Percentage (UPC) is a measure of how much each fundamental uncertainty contributes to the overall uncertainty, defined as:

$$UPC_i = \left(\frac{\partial f}{\partial X_i}\right)^2 \frac{U_{X_i}^2}{U_f^2} = \left(UMF_i \frac{\mathcal{X}_{X_i}}{\mathcal{X}_f}\right)^2 \times 100 \tag{C.14}$$

C.4 Uncertainty in a Linear Regression

If a linear regression is performed on a data set consisting of N measurements of two variables, X and Y, then the computed gradient and intercept can be considered data reduction equations:

$$m = m(X_1, X_2, X_3, ..., X_N, Y_1, Y_2, Y_3, ..., Y_N) \tag{C.15}$$

and

$$c = c(X_1, X_2, X_3, ..., X_N, Y_1, Y_2, Y_3, ..., Y_N) \tag{C.16}$$

Equations (C.5) to (C.6) can now be used with these data reduction equations, with the elemental systematic and random uncertainties in the measured variables, to estimate the overall uncertainty. Note that it is vital to include the covariance estimators. Sections 7-3 and 7-4 of Coleman and Steele [120] cover this topic in greater detail.

APPENDIX D

RTD Operation and Calibration

This appendix describes the theoretical operation and calibration of the platinum RTDs used as the temperature transducers in each DHTG. Details of the calibration results for each DHTG can be found in Appendix B.

D.1 RTD Operation

The electrical resistance of an RTD element changes with temperature according to:

$$\Delta R = \alpha_R R_0 \Delta T \tag{D.1}$$

where α_R is the temperature coefficient of resistance with units K^{-1}, and R_0 is the resistance at a reference temperature T_0. A two-wire configuration is used to measure temperature in experiments. If the film is supplied with a constant current I_c, typically around 10 mA, then by applying Ohm's law, the change in resistance can be detected as a change in voltage. The temperature change is:

$$\Delta T(t) = \frac{(R(t) - R_1)}{\alpha_R R_0} = \frac{(R(t) - R_1)I_c}{\alpha_R R_0 I_c} = \frac{(V(t) - V_1)}{\alpha_R R_0 I_c} \tag{D.2}$$

where subscript 1 indicates an isothermal condition prior to an experiment. The values of α_R and R_0 are determined from the result of a calibration experiment which described below. The current can be calculated as:

$$I_c = \frac{V_1}{R_l + R_0(1 + \alpha_R(T_1 - T_0))} \tag{D.3}$$

where R_l is the extra resistance of any additional cabling added in the experimental installation which was not present for the calibration experiment.

The current can also be found through direct measurement by measuring the voltage drop across a high-accuracy resistor. This method allows for changes to the cabling runs between gauges and data acquisition equipment without the need to measure the resistance change, and means that a measurement of the initial temperature of the gauge is not necessary. However, a highly stable current source is required.

D.2 RTD Calibration

Calibration of the gauges is performed in a thermostatic water-bath following a process described by Collins et al. [51]. Each gauge, or set of gauges, is sealed in a water-proof bag and submerged into the bath. The resistance of the gauges are recorded using a digital multi-meter while the temperature is cycled in steps over a range of temperatures covering the expected temperature rise in an experiment. At each step, the temperature of the bath is held constant until the gauges reach isothermal conditions, as determined by the convergence to within a given limit of so-called specimen thermocouples which are attached with good thermal contact to the gauges themselves. A typical temperature range is 20 °C to 60 °C in steps of 5 °C to 10 °C. Over this range, the relationship between resistance and

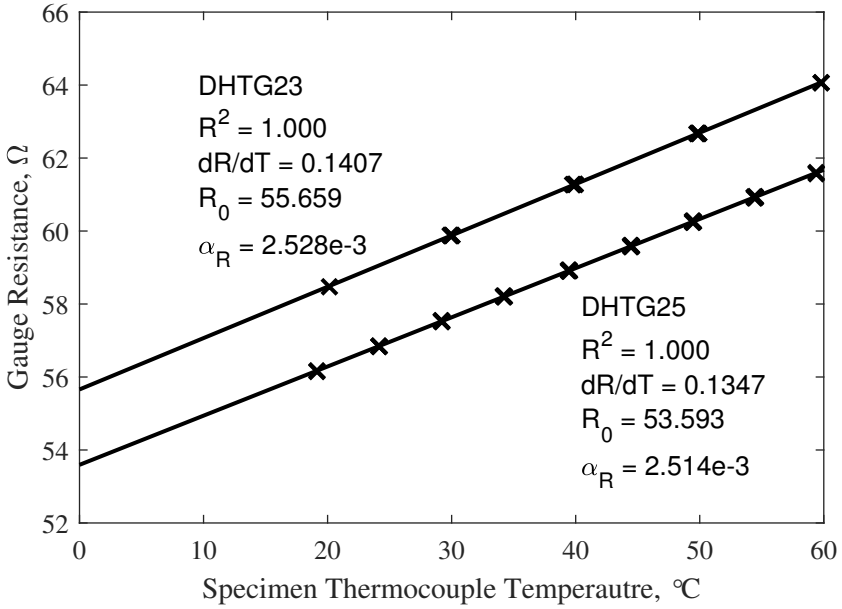


Figure D.1: Typical water-bath calibration data and results.

temperature for platinum is linear [153]. An ordinary least-squares regression is performed on the resistance and specimen temperature data set to fit a straight line and determine its gradient m and intercept c. The value of R_0 is defined as the resistance at 0 °C, i.e.:

$$R_0 = c \tag{D.4}$$

Although care must be taken as calibrations from other sources may choose to define R_0 at 20 °C. The coefficient of resistance with temperature is defined as:

$$\alpha_R = \frac{dR/dT}{R_0} = \frac{m}{c} \tag{D.5}$$

Figure D.1 shows an example of two DHTG calibrations consisting of measurements of temperature and resistance and the results of a linear regression for each data set. Each calibration run cycled through the temperature range twice. This highly linear and repeatable behaviour with no visible hysteresis between heating and cooling cycles is typical for DHTG RTD calibrations.

Table D.1: Mean values of calibration parameters and their respective uncertainties for all DHTGs in Table B.1.

Property	Value	Unit
$\overline{m}$	0.130	$\Omega{\cdot}^{\circ}\mathrm{C}^{-1}$
$\overline{c}$	48.41	Ω
$\overline{\mathcal{X}_m}$	0.21	%
$\overline{\mathcal{X}_c}$	1.32	%

D.3 Uncertainty in Calibrated Parameters

The uncertainty in the calibrated gradient and intercept, U_m and U_c respectively, can be estimated by considering the regression as a data reduction equation, following the analysis described briefly in Appendix C, and more thoroughly in Section 7-3 of Coleman and Steele [120]. The dominant systematic uncertainty in the resistance was estimated to be $0.3\,\Omega$, due to measured variability across the channels of the data acquisition system used for the water bath calibration. The systematic uncertainty in the specimen temperature measurement was taken to be $1.1\,^{\circ}\mathrm{C}$, according to standard error charts for Type K thermocouples. It was assumed that no correlation between errors in measured resistance and temperature exists, and that the systematic uncertainty in each individual measurement of temperature and resistance were correlated.

The calibration results and respective uncertainties for individual DHTGs is given in Appendix B. To give an indication of typical values, Table D.1 shows the mean across all calibrations, and the mean of the relative uncertainties, where $\mathcal{X}_m = U_m/m$. The calibration of DHTG17 has not been included in these means as it was a clear outlier.

APPENDIX E

The Fay and Riddell Stagnation Point Heat Flux Equation

E.1 Hemispherical and Cylindrical Bodies

The Fay and Riddell equation is a stagnation point heat flux correlation developed in 1958 [139]. The correlation is based on a solution of the boundary layer equations for spheres and cylinders in dissociated air, and can be used for flows in thermochemical equilibrium and for "frozen" flows, i.e. where recombinations rates are much slower than the characteristic flow passage duration. For the latter case, the catalytic efficiency of the wall can be accounted for. A non-catalytic wall is one which does not participate in chemical reactions, whereas a "super-catalytic" wall is an infinitely effective collision partner to chemical reactions in the flow, and so an equilibrium state next to the wall is always achieved. In reality, all materials lie somewhere between these two extremes.

The equations for stagnation point heating with an equilibrium boundary layer in the form given by Crabtree [154] is:

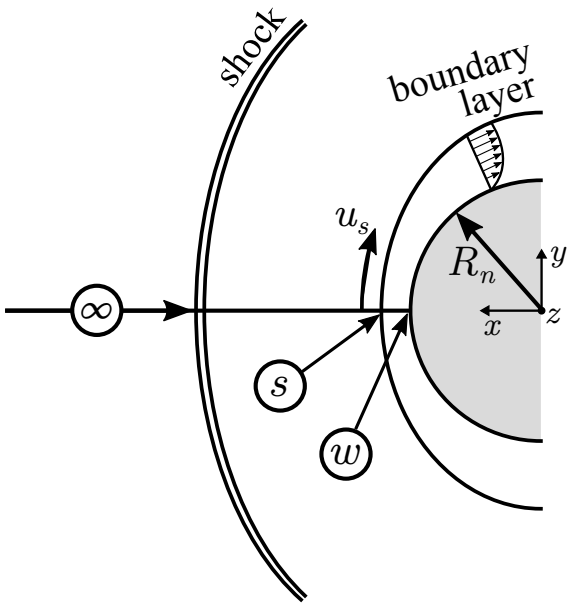


Figure E.1: Stagnation point flow-field with states labelled for the Fay-Riddell equation.

$$q_{FR} = \frac{0.537a}{Pr^{0.6}} \sqrt{1 + \sqrt{\left(\frac{R_x}{R_z}\right)}} \left(h_s - h_w\right) \left[1 + \left(Le^{0.52} - 1\right) \frac{h_D}{h_s}\right] \sqrt{\left(\frac{du}{dy}\right)_s} \tag{E.1}$$

For a frozen boundary layer with a non-catalytic wall:

$$q_{FR} = \frac{0.537a}{Pr^{0.6}} \sqrt{1 + \sqrt{\left(\frac{R_x}{R_z}\right)}} \left(h_s - h_w\right) \left[1 + \frac{h_D}{h_s}\right] \sqrt{\left(\frac{du}{dy}\right)_s} \tag{E.2}$$

For a frozen boundary layer with a catalytic wall:

$$q_{FR} = \frac{0.537a}{Pr^{0.6}} \sqrt{1 + \sqrt{\left(\frac{R_x}{R_z}\right)}} \left(h_s - h_w\right) \left[1 + \left(Le^{0.63} - 1\right) \frac{h_D}{h_s}\right] \sqrt{\left(\frac{du}{dy}\right)_s} \tag{E.3}$$

As labelled on the schematic diagram given in Fig. E.1, the subscripts s, w, and ∞ refer to the stagnation point outside the boundary layer, the wall, and the free-stream conditions respectively. The Lewis number, Le, characterises the ratio of thermal diffusivity to mass

diffusivity, and is estimated by Fay and Riddell to be 1.4 [139]. The enthalpy of dissociation of the free-stream species is h_D, which for low-enthalpy flows may be approximately zero, meaning that both this term and the Lewis number drop out of the equation. The Prandlt number, Pr, is taken to be 0.71.

For the case of an an axisymmetric boundary layer, i.e. a hemisphere, $R_x/R_z = 1$ and Fay and Riddell [139] gives:

$$a = (\rho_s \mu_s)^{0.4} (\rho_w \mu_w)^{0.1} \tag{E.4}$$

For two-dimensional boundary layer, i.e. a cylinder, $R_x/R_z = 0$ and Beckwith [155] gives:

$$a = 1.06 (\rho_s \mu_s)^{0.44} (\rho_w \mu_w)^{0.06} \tag{E.5}$$

The velocity gradient term $(du/dy)_s$ can be evaluated in a number of ways. Illich [16] has conveniently compiled and compared the most common methods used for hypersonic flows. Fay and Riddell originally calculated the velocity gradient assuming a modified Newtonian pressure distribution as:

$$\left(\frac{du}{dy}\right)_s = \frac{1}{R_n}\sqrt{\frac{2(p_s - p_\infty)}{\rho_s}} \tag{E.6}$$

Methods of calculating the velocity gradient based on a measured shock stand-off distance, for example by Olivier [15], may be more accurate for high enthalpy flows where significant deviation from ideal gas behaviour occurs.

E.2 Correction Factors for Non-Hemispherical Bodies

Correction factors to the velocity gradient term in Eqs. (E.1) to (E.3) can be used to provide estimates of stagnation point heat flux to bodies which are not hemispherical or cylindrical. See, for example, Zoby and Sullivan [152] and Ellison [156]. Note that these correction factors

are to a Newtonian velocity gradient, and cannot be used to correct the velocity gradient calculated using a different method.